Journal of Diabetes Research

Molecular and Imaging Biomarkers and Artificial Intelligence in Diabetic Retinopathy

Lead Guest Editor: Honghua Yu
Guest Editors: Lei Liu, Yijun Hu, Tao Li, Jing Luo, and Mingguang He

Molecular and Imaging Biomarkers and Artificial Intelligence in Diabetic Retinopathy

Journal of Diabetes Research

Molecular and Imaging Biomarkers and Artificial Intelligence in Diabetic Retinopathy

Lead Guest Editor: Honghua Yu
Guest Editors: Lei Liu, Yijun Hu, Tao Li, Jing Luo, and Mingguang He

Contents

Hindawi
Journal of Diabetes Research
Volume 2022, Article ID 4663221, 7 pages
https://doi.org/10.1155/2022/4663221

Research Article

Causes and Risk Factors of Repeated Hospitalization among Patients with Diabetic Retinopathy

Yu Xiao,[1,2] **Yingying Liang**,[1,2] **Zhanjie Lin**,[1,3] **Huiqian Kong**,[1] **Zijing Du**,[1] **Yunyan Hu**,[1] **and Shuyi Ouyang**[1]

[1]*Guangdong Eye Institute, Department of Ophthalmology, Guangdong Provincial People's Hospital, Guangdong Academy of Medical Sciences, Guangzhou, China*
[2]*The Second School of Clinical Medicine, Southern Medical University, Guangzhou, China*
[3]*Graduate School, Shantou University Medical College, Shantou, China*

Correspondence should be addressed to Yunyan Hu; 582519472@qq.com and Shuyi Ouyang; 157840281@qq.com

Received 3 September 2021; Revised 20 January 2022; Accepted 5 May 2022; Published 28 May 2022

Academic Editor: Ali Sharif

Purpose. To identify the causes and risk factors of repeated hospitalization among patients with diabetic retinopathy (DR). *Methods.* Our study retrospectively examined the data of DR patients who were readmitted for treatments to the Department of Ophthalmology, Guangdong Provincial People's Hospital between January 2012 and July 2021. We first analyzed the main causes of repeated admissions and then divided the patients into three groups according to the times of readmissions. Ordinal logistic regression was performed to determine the impact of patients' demographic and clinical characteristics. Moreover, comparisons of the length of stay and the hospitalization cost of DR patients with repeated admission causes were conducted. *Results.* Among 2592 hospital discharges of 827 patients who experienced at least two hospitalizations, the major causes of repeated hospitalization were macular edema (30.83%), vitreous hemorrhage (29.09%), cataract (22.76%), proliferative membrane formation (6.91%), silicone oil removal (4.71%), retinal detachment (4.44%), and glaucoma (4.17%). The results of ordinal logistic regression showed that younger patients with medical insurance and local residence have a higher risk of repeated hospitalization ($p < 0.05$). Furthermore, patients readmitted for vitreous hemorrhage, proliferative membrane formation, and retinal detachment experienced longer length of hospital stay and higher hospitalization cost ($p < 0.001$). *Conclusions.* Multiple causes and risk factors contribute to repeated hospitalization, imposing a substantial physical and economic burden on DR patients. A better understanding of these causes and risk factors of readmission may lead to lowering such risks and alleviating patients' burden.

1. Introduction

Diabetic retinopathy (DR) is a common microvascular complication of diabetes mellitus. Patients with any type of diabetes are at the risk of developing DR, and it was found that after 20 years of living with diabetes, regardless of the efficacy of blood sugar management, almost all patients with type 1 diabetes and more than 60% of those with type 2 diabetes would have DR [1]. Furthermore, DR is considered the leading cause of vision loss and global blindness in working-age adults [2]. Despite statistical variations among different researches, a high prevalence of DR (up to 43.1%) was reported in diabetic population in China, contributing to the largest DR population in the world [3–6].

DR not only threatens the vision and life quality of patients, but also brings heavy healthcare and economic burden to their family and society. With worldwide population aging and prolonged life expectancy, the prevalence and burden of DR will continue to escalate [7]. As a progressive disease, DR can be divided into two stages according to its pathophysiology and corresponding severity: nonproliferative and proliferative. DR can be asymptomatic in its early, nonproliferative stage, which, without early detection and timely treatment, will furtively progress to proliferative DR,

causing severe visual impairment [8]. Hence, measures should be taken to delay DR progression and therefore reduce the times of readmission, such as disease prevention and regular screening in the target population, as well as early intervention and patient education among DR patients in order to raise their awareness and compliance [9].

Hospital readmission is an undesirable outcome that may be preventable in DR management [10]. A thorough understanding of the causes and risk factors of repeated admissions is needed to identify high-risk individuals and reduce the readmission rate. Although current evidence has already indicated that long duration of diabetes, poor glycemic control, and high blood pressure are the risk factors of DR progression, the impacts of demographic and clinical characteristics on repeated admissions of DR patients remain unclear [11].

This study aimed to identify the causes and risk factors of repeated hospitalization of DR patients, as well as to compare the length of hospital stay and hospitalization cost by different causes.

2. Methods

2.1. Subjects and Data Collection. In this retrospective study, we examined the electronic medical records (EMRs) of DR patients who were readmitted to the Department of Ophthalmology, Guangdong Provincial People's Hospital (GPPH) between January 1, 2012, and July 31, 2021. Inclusion criteria was patients with the diagnosis of DR defined by an International Classification of Disease, Tenth Revision (ICD-10) code within E10-14. Patients were excluded if they did not receive treatments due to any contraindications or an undocumented reason (no specific reason noted in patient record). All the treatments were performed by senior vitreoretinal specialists in accordance with the uniform operating standards of the surgical team of the Department of Ophthalmology, GPPH.

The following demographic and clinical characteristics of each patient per stay were assessed: age upon the first hospitalization, gender, residence (inside or outside the city of Guangzhou), marital status (single, married, divorced or widowed), payment type (self-pay or medical insurance), times of readmission, length of stay, hospitalization cost, and admission diagnoses including primary diagnosis and secondary diagnoses (e.g., comorbidities and systemic conditions).

Informed consent was waived since our study was based on a retrospective analysis of EMRs, with all patient information deidentified and kept anonymous. Approval of the use of these records for the analysis was provided by the Research Ethics Committee of GPPH (No. GDREC2020229H).

2.2. Outcome Variables. The primary outcomes were the causes and times of repeated hospitalizations. We also identified the associations between patients' demographic and clinical characteristics and the causes of repeated admissions. Furthermore, we analyzed the relationship between the causes and the length of stay, along with their association with inpatient charges.

2.3. Statistical Analysis. The summary of categorical variables (e.g., gender, residence, payment type, and marital status) included counts and percentages. Since no data was normally distributed with regard to all continuous variables (e.g., age, length of stay, and hospitalization charges), medians with interquartile range (IQR) in addition to mean with standard deviation (SD) values were presented.

To analyze the contributing factors to the times of hospitalization, we divided the patients into three groups. Chi-square and Fisher's exact test were performed for categorical variables, while Kruskal-Wallis rank sum test was performed for continuous ones. Variables independently associated with the times of hospitalizations at the $p < 0.05$ level on univariate analysis were retained in the ordinal logistic regression analysis. Odds ratios (OR) with a 95% confidence interval (CI) were reported for the three groups.

In addition, Mann–Whitney U tests were conducted to compare the length of hospital stay and inpatient fees for DR patients with different hospitalization causes and systemic diseases. A p value less than 0.05 was considered statistically significant for all the tests. All statistical analyses were performed using SPSS 26.0 (SPSS. Inc, Chicago, IL, USA).

3. Results

3.1. General Patient Characteristics. A total of 1623 DR patients were identified between January 1, 2012, and July 31, 2021, of which 827 patients (50.96%) experienced at least two hospital admissions. Among DR patients with multiple admissions, 436 (52.72%) were males and 391 (47.38%) were females, and the median follow-up time was 5.03 (IQR: 1.53-13.10) months. Median age of these patients upon the first hospitalization was 56 (IQR: 49-63) years. Most of DR patients were type 2 diabetes (97.58%).

With respect to residence, 308 (37.24%) of patients lived in local neighborhood, while 519 (62.76%) lived outside the city. As for marital status, 744 (89.96%) of patients were married, 24 (2.90%) were single, while 59 (7.13%) were divorced or widowed. Regarding payment type, 178 (21.52%) patients paid by themselves, while 649 (78.48%) patients had medical insurance.

3.2. Reasons for Repeated Hospitalization. 2592 hospital discharges of 827 patients were analyzed. The major causes of repeated hospitalization were macular edema (799, 30.83%), vitreous hemorrhage (754, 29.09%), cataract (590, 22.76%), proliferative membrane formation (179, 6.91%), silicone oil removal (122, 4.71%), retinal detachment (115, 4.44%), and glaucoma (108, 4.17%). The statistic descriptions of repeated admission causes are summarized in Table 1. In addition, we analyzed the repeated admission causes of DR patients in the past 5 years, which has no statistically significant difference to that in the past decade ($p = 0.089$, Table S1 in the supplement).

3.3. Analysis of the Times of Hospitalizations. Among 827 patients who experienced at least two hospitalizations, the median times of hospitalizations was 3 (IQR: 2-4), with the most being 14. The times of hospitalizations of those

Table 1: Repeated admission causes of diabetic retinopathy patients.

Repeated admission causes	Cases (n)	Percentage (%)
Macular edema	799	30.83
Vitreous hemorrhage	754	29.09
Cataract	590	22.76
Proliferative membrane formation	179	6.91
Silicone oil removal	122	4.71
Retinal detachment	115	4.44
Glaucoma	108	4.17

patients were divided into the following categories: 2-3 times, 4-5 times, and >5 times. These breakpoints were established based on their clinical and statistical significance. Additionally, we analyzed the times of hospitalizations of DR patients in the past 5 years, and in the past 10 years, no statistically significant difference was found ($p = 0.813$, Table S2 in the supplement).

Table 2 illustrated the characteristics in association with the times of hospitalizations. Kruskal-Wallis rank sum test indicated that the age of patients was significantly different among three groups. Chi-square test indicated that residence ($p = 0.003$) and payment type ($p = 0.003$) were significantly different in between-group analysis. Fisher's exact test identified that marital status ($p = 0.002$) was different among those groups. However, there was no statistically significant difference between groups for gender ($p = 0.088$).

Factors that were statistically significant on univariate analysis were introduced into the ordinal logistic regression analysis (Table 3). The results showed that younger age of DR patients upon the first hospitalization was a risk factor for increasing the times of admissions (OR = 0.954; 95% CI 0.938 to 0.970; $p < 0.001$). Moreover, DR patients who lived in local neighborhood experienced more admission times compared to those who lived outside the city (OR = 1.948; 95% CI 1.370 to 2.773; $p < 0.001$). Besides, individuals with medical insurance were at higher risk of repeated hospitalization than those who paid the inpatient cost by themselves (OR = 1.797; 95% CI 1.130 to 2.858; $p = 0.013$).

3.4. Hospitalization Causes Associated with Length of Stay and Hospitalization Cost. We further analyzed the length of hospital stay and inpatient fees for DR patients within different hospitalization causes and systemic diseases.

Of 827 patients with 2592 hospital discharges, the median length of hospital stay was 1 (IQR: 1-4) day. The hospitalization charges per admission was 1389.65 (IQR: 955.34-2226.34) USD, while surgical fees accounted for the largest proportion (71.55%) of the total hospitalization charges, followed by medication fees (12.32%).

Regarding comorbid systemic diseases, hypertension was known in 1044 (40.28%), diabetic nephropathy in 302 (11.65%), and chronic kidney disease in 104 (4.01%) of these patients. A history of dyslipidemia was present in 70 (2.70%) of these patients, while 50 (1.93%) and 43 (1.66%) of the patients had the history of stroke and coronary heart disease, respectively.

As summarized in Table 4, we found that length of stay increased in patients with admission causes of proliferative membrane formation, vitreous hemorrhage, retinal detachment, and glaucoma. Meanwhile, patients with admission causes of macular edema and cataract experienced shorter length of stay.

Length of hospital stay was also found to be significantly longer among the DR patients with comorbid systemic diseases (including hypertension, diabetic nephropathy, chronic kidney disease, and dyslipidemia), compared to those without.

As for hospitalization cost, the nonparametric tests showed that DR patients with admission diagnosis of proliferative membrane formation, retinal detachment, and vitreous hemorrhage required higher hospitalization costs, compared to those with macular edema, cataract, glaucoma, and silicone oil removal (Table 5).

Concerning hospitalization cost between those with and without systemic diseases, the nonparametric tests demonstrated significant differences between the two groups. We found that the inpatient fees of patients with comorbid systemic diseases (including hypertension, diabetic nephropathy, chronic kidney disease, and dyslipidemia) were much higher than those without.

4. Discussion

Nowadays, DR poses a major public health burden to Chinese society. This study contributes to the limited number of literature on the investigation of repeated admissions in DR patients. In this study, we first determined the main causes as well as the risk factors of repeated hospitalization. Then, we investigated the association between the length of hospital stay, inpatient charges, and readmission diagnosis in each stay.

The primary diagnosis of readmissions in DR patients were macular edema (30.83%), vitreous hemorrhage (29.09%), cataract (22.76%), proliferative membrane formation (6.91%), silicone oil removal (4.71%), retinal detachment (4.44%), and glaucoma (4.17%). Among these causes, patients with vitreous hemorrhage, proliferative membrane formation, and retinal detachment experienced longer length of hospital stay and higher hospitalization cost. It is known that vitreous hemorrhage, proliferative membrane formation, and retinal detachment were the most frequent and severe complications in proliferative DR, followed by the long-term treatment, high medical cost, and poor prognosis. Hence, early intervention and timely prophylactic treatment play a crucial role in preventing disease progression. However, DR could be initially asymptomatic; thus, a reasonably considerable proportion of diabetic patients might not be actively engaged in early screening and subsequent follow-ups, as they were unaware of the severity of late-stage DR and its concurrent complications. Therefore, intensive patient education is vital to raise patients' awareness and compliance with regular follow-ups throughout DR management [12]. Through thorough ophthalmic examinations,

Table 2: Comparison of characteristics in patients with different times of hospitalizations.

Variables	Times of hospitalizations			p value
	2-3	4-5	>5	
Age, years, median (IQR)	57 (51-64)	53 (48-60)	52 (44-57)	<0.001[a]
Gender, n (%)				0.088[b]
Male	315 (72.25)	79 (18.12)	42 (9.63)	
Female	300 (76.73)	69 (17.65)	22 (5.63)	
Residence, n (%)				0.003[b]
Inside the city	210 (68.18)	64 (20.78)	34 (11.04)	
Outside the city	405 (78.03)	84 (16.18)	30 (5.78)	
Payment type, n (%)				0.003[b]
Self-pay	149 (83.71)	23 (12.92)	6 (3.37)	
Medical insurance	466 (71.8)	125 (19.26)	58 (8.94)	
Marital status, n (%)				0.002[c]
Single	16 (66.67)	1 (4.17)	7 (29.17)	
Married	551 (74.06)	141 (18.95)	52 (6.99)	
Divorced/widowed	48 (81.36)	6 (10.17)	5 (8.47)	

[a]Kruskal-Wallis rank sum test; [b]chi-square test; [c]Fisher's exact test.

Table 3: The ordinal logistic regression of factors associated with the times of hospitalizations.

Variables	β	OR	95% CI		p value
			Lower	Upper	
Age	-0.047	0.954	0.938	0.970	<0.001
Residence					
Outside the city	Ref.				
Inside the city	0.667	1.948	1.370	2.773	<0.001
Payment type					
Self-pay	Ref.				
Medical insurance	0.586	1.797	1.130	2.858	0.013
Marital status					
Divorced/widowed	Ref.				
Single	-0.045	0.956	0.313	2.921	0.938
Married	0.277	1.319	0.665	2.614	0.428

OR: odds ratios; 95CI%: 95% confidence interval.

Table 4: Comparison of length of hospital stay in diabetic retinopathy patients with or without different admission causes and systemic diseases.

	With	Without	p value
Admission causes			
Proliferative membrane formation	6 (3 – 8)	1 (1 – 4)	<0.001
Vitreous hemorrhage	4 (2 – 7)	1 (1 – 3)	<0.001
Retinal detachment	4 (2 – 7)	1 (1 – 4)	<0.001
Glaucoma	4 (2 – 8)	1 (1 – 4)	<0.001
Silicone oil removal	2 (1 – 4)	1 (1 – 4)	0.016
Cataract	1 (1 – 2)	2 (1 – 5)	<0.001
Macular edema	1 (1 – 1)	3 (1 – 5.5)	<0.001
Systemic diseases			
Diabetic nephropathy	3 (1 – 7)	1 (1 – 4)	<0.001
Chronic kidney disease	3 (1 – 7)	1 (1 – 4)	<0.001
Dyslipidemia	3 (1 – 8)	1 (1 – 4)	<0.001
Hypertension	2 (1 – 5)	1 (1 – 4)	<0.001
Coronary heart disease	2 (1 – 4)	1 (1 – 4)	0.879
Stroke	2 (1 – 5)	1 (1 – 4)	0.327

p value was obtained by Mann–Whitney U tests.

even the most subtle lesions of fundus can be detected in time, before some treatments (e.g., retinal laser photocoagulation) can be performed in the early stages of DR to delay its progression, thereby preventing the occurrence of serious complications and reducing the hospitalization times [8].

We observed that macular edema accounted for the largest proportion of hospitalization causes, along with shorter length of hospital stay and lower hospitalization charges per stay. Macular edema is the most common complication of DR in any stage, resulting in vision loss. Currently, inpatient intravitreal (e.g., anti-VEGF agents and dexamethasone implant) is an effective treatment for macular edema [13]. However, considering its high risk of recurrence, patients with macular edema were often required to take multiple injections during the course of treatment, leading to a significant increase in the times of readmission. Therefore, although the hospitalization cost per stay for patients with macular edema is relatively lower, repeated admission still increases the economic burden of patients.

In addition, up to 22.76% of DR patients were readmitted to the hospital due to cataracts, which may be explained as follows. On the one hand, diabetes is a widely observed clinical risk factor of cataract progression. Comparing to nondiabetic patients, cataracts in diabetic patients are associated with earlier age of onset and rapid progress

Table 5: Comparison of hospitalization cost in DR patients with or without different admission causes and systemic diseases.

	With	Without	*p* value
Admission causes			
Proliferative membrane formation	2700.49 (2273.18 – 3449.1)	1320.56 (923.19 – 2116.53)	<0.001
Retinal detachment	2447.18 (2185.14 – 2794.36)	1345.78 (937.07 – 2163.38)	<0.001
Vitreous hemorrhage	2111.48 (1727.95 – 2640.33)	1198.87 (850.74 – 1845.2)	<0.001
Cataract	1375.44 (1155.81 – 1780.64)	1412.83 (752.52 – 2274.82)	0.001
Silicone oil removal	1288.14 (856.46 – 1637.83)	1402.71 (964.47 – 2246.06)	0.013
Glaucoma	1265.26 (679.59 – 1957.61)	1400.08 (967.23 – 2233.89)	0.019
Macular edema	933.39 (528.01 – 1195.01)	1870.08 (1195.93 – 2458.71)	<0.001
Systemic diseases			
Dyslipidemia	1372.96 (1340.43 – 3104.15)	2063.11 (942.23 – 2209.47)	<0.001
Chronic kidney disease	2032.43 (1146.48 – 2510.3)	1372.96 (939.99 – 2206.5)	<0.001
Diabetic nephropathy	1950.16 (1179.24 – 2578.08)	1340.94 (923.71 – 2175.21)	<0.001
Hypertension	1302.12 (1038.63 – 2412.3)	1576.62 (798.53 – 2141.5)	<0.001
Stroke	1847.58 (1124.5 – 2789.00)	1379.92 (948.29 – 2215.63)	0.003
Coronary heart disease	1380.37 (1230.02 – 2410.72)	1908.16 (947.53 – 2221.41)	0.006

p value was obtained by Mann – Whitney *U* tests ; the unit of value : USD.

[14]. On the other hand, cataract surgery may accelerate the progression of DR and induce macular edema [15]. Thus, clinicians are supposed to assess the risk-benefit ratio before cataract surgery and formulate the best surgical protocol to maximize patients' benefit.

We analyzed the comorbid systemic diseases and found that patients with hypertension, diabetic nephropathy, chronic kidney disease, and dyslipidemia are associated with longer length of hospital stay and higher hospitalization cost per stay. Consequently, besides maintaining stable glucose levels, it is necessary to screen for comorbid systemic diseases at the first hospitalization in DR patients and to monitor the condition of comorbidities regularly, so as to improve the efficacy of each hospital admission and to promote the life quality of patient.

According to the ordinal logistic regression analysis, younger age upon the first hospitalization was a risk factor for repeated admissions (OR = 0.954). The age upon the first hospitalization may be related to the onset age of diabetes. Previous studies have reported the correlation between young age at diabetes onset and high complications burden, and a large population study in China has shown a decreased risk of DR with advancing age after adjusting multiple risk factors [16]. Early age of onset is often associated with severe complications and rapid progression of disease [17]. Therefore, more frequent observance and proactive management of diabetic retinopathy are critical for young-onset diabetes patients.

The times of repeated admission was significantly associated with the payment type according to the ordinal logistic regression analysis (OR = 1.797). Comparing to self-paid patients, patients with medical insurance were readmitted more frequently. For patients who were repeatedly hospitalized, the median hospitalization cost reaches 1389.65 USD. Despite the increasing coverage of medical insurance in China, 21.4% of patients still paid the hospitalization bills out-of-pocket in our study. Since DR patients bear a huge economic burden along with the psychological and physical ones, medical insurance plays a crucial role in alleviating their stress and improving their compliance [18]. Therefore, it is suggested that the government and medical insurance agencies at all levels should pay more attention to optimizing medical insurance reimbursement coverage and standards and to providing the best services within the interpretation of current insurance policies.

As for residence of DR patients, the ordinal logistic regression analysis showed that the risk of repeated hospitalization of patients who lived in other places was lower than that of local residence (OR = 1.948). This may be attributed to the complicated process of seeking medical care for patients who lived in other places; hence, treatment compliance was hard to establish well. Some patients may refuse to be admitted to the hospital because of inconspicuous clinical signs, which increased the risk of disease progression. Furthermore, with the acceleration of the urbanization process and the rapid flow of population in China, the medical institutions for readmissions of these patients may change.

This is one of the first studies to evaluate the causes and risk factors of repeated admissions for DR patients. However, there were several limitations in this study. First, it was a single-center study. Since standards for hospitalization can differ between regions and countries, a multicenter study would be preferable. Besides, further study may enhance the reliability by calculating visits in other hospitals recorded in EMRs or performing short interviews through phones. Second, as a retrospective review, its inferences about causality based on these retrospective and observational data are limited, and selection bias may not be entirely ruled out. Moreover, we found it hard to determine whether the readmissions were planned or unplanned. Lastly, this study

has not evaluated the effects of laboratory values on readmissions. Future prospective controlled studies are recommended to investigate laboratory values and other risk factors associated with multiple readmissions.

5. Conclusion

Reasons for repeated admission of DR patients varied, while factors including younger age, medical insurance reimbursement, and living in local neighborhood were identified as risk factors for repeated hospitalization. Hospital readmission among patients with DR poses a large burden on patients and healthcare systems. A better understanding of the causes and risk factors of repeated admission among DR patients may help identify high-risk patients as well as improve interventions to reduce readmission times.

Data Availability

The data used during the current study are available from the corresponding author on reasonable request.

Disclosure

The sponsors or funding organizations had no role in the design or conduct of this research.

Conflicts of Interest

The authors declare that they have no competing interests.

Authors' Contributions

Yu Xiao, Yingying Liang, and Zhanjie Lin contributed equally to this work, and are co-first authors.

Acknowledgments

This study was supported by the Guangzhou Science and Technology Program Key Projects (A2021003 to SO), the Nursing Research Fund of Guangdong Provincial People's Hospital (DFJH2020005 to SO), and the Research Fund of Guangdong Provincial People's Hospital (8210040606 to YH). The authors thank Mr. Qiu Yutao from the Medical Records Department of Guangdong Provincial People's Hospital for his help in obtaining the subjects' data.

Supplementary Materials

Table S1: the readmission reasons of diabetic retinopathy patients in the past 5 years and the past 10 years. Table S2: the times of hospitalizations of diabetic retinopathy patients in the past 5 years and the past 10 years. *(Supplementary Materials)*

References

[1] J. M. Tarr, K. Kaul, M. Chopra, E. M. Kohner, and R. Chibber, "Pathophysiology of diabetic retinopathy," in *ISRN Ophthalmology*, Springer, New York, NY, 2013.

[2] N. Cheung, P. Mitchell, and T. Y. Wong, "Diabetic retinopathy," *Lancet*, vol. 376, no. 9735, pp. 124–136, 2010.

[3] C. Pang, L. Jia, S. Jiang et al., "Determination of diabetic retinopathy prevalence and associated risk factors in Chinese diabetic and pre-diabetic subjects: Shanghai diabetic complications study," *Diabetes/Metabolism Research and Reviews*, vol. 28, no. 3, pp. 276–283, 2012.

[4] F. H. Wang, Y. B. Liang, X. Y. Peng et al., "Risk factors for diabetic retinopathy in a rural Chinese population with type 2 diabetes: the Handan Eye Study," *Acta Ophthalmologica*, vol. 89, no. 4, pp. e336–e343, 2011.

[5] J. Xu, W. B. Wei, M. X. Yuan et al., "Prevalence and risk factors for diabetic retinopathy: the Beijing Communities Diabetes Study 6," *Retina*, vol. 32, no. 2, pp. 322–329, 2012.

[6] G. Zhang, H. Chen, W. Chen, and M. Zhang, "Prevalence and risk factors for diabetic retinopathy in China: a multi-hospital-based cross-sectional study," *The British Journal of Ophthalmology*, vol. 101, no. 12, pp. 1591–1595, 2017.

[7] L. Guariguata, D. R. Whiting, I. Hambleton, J. Beagley, U. Linnenkamp, and J. E. Shaw, "Global estimates of diabetes prevalence for 2013 and projections for 2035," *Diabetes Research and Clinical Practice*, vol. 103, no. 2, pp. 137–149, 2014.

[8] A. Stitt, T. Curtis, M. Chen et al., "The progress in understanding and treatment of diabetic retinopathy," *Progress in Retinal and Eye Research*, vol. 51, pp. 156–186, 2016.

[9] A. Karunakaran, H. Zhao, and D. J. Rubin, "Predischarge and postdischarge risk factors for hospital readmission among patients with diabetes," *Medical Care*, vol. 56, no. 7, pp. 634–642, 2018.

[10] Z. Khair, M. M. Rahman, K. Kazawa et al., "Health education improves referral compliance of persons with probable diabetic retinopathy: a randomized controlled trial," *PLoS One*, vol. 15, no. 11, article e0242047, 2020.

[11] R. Lee, T. Y. Wong, and C. Sabanayagam, "Epidemiology of diabetic retinopathy, diabetic macular edema and related vision loss," *Eye and Vision*, vol. 2, no. 1, 2015.

[12] M. Piyasena, G. V. S. Murthy, J. L. Y. Yip et al., "Systematic review on barriers and enablers for access to diabetic retinopathy screening services in different income settings," *PLoS One*, vol. 14, no. 4, article e0198979, 2019.

[13] J. P. Ehlers, S. Yeh, M. G. Maguire et al., "Intravitreal pharmacotherapies for diabetic macular edema: a report by the American Academy of Ophthalmology," *Ophthalmology*, vol. 129, no. 1, pp. 88–99, 2021.

[14] A. K. Denniston, A. Y. Lee, C. S. Lee et al., "United Kingdom Diabetic Retinopathy Electronic Medical Record (UK DR EMR) Users Group: report 4, real-world data on the impact of deprivation on the presentation of diabetic eye disease at hospital services," *The British Journal of Ophthalmology*, vol. 103, no. 6, pp. 837–843, 2019.

[15] T. Hong, P. Mitchell, T. de Loryn, E. Rochtchina, S. Cugati, and J. J. Wang, "Development and progression of diabetic retinopathy 12 months after phacoemulsification cataract surgery," *Ophthalmology*, vol. 116, no. 8, pp. 1510–1514, 2009.

[16] Y. Liu, J. Yang, L. Tao et al., "Risk factors of diabetic retinopathy and sight-threatening diabetic retinopathy: a cross-sectional study of 13 473 patients with type 2 diabetes mellitus in mainland China," *BMJ Open*, vol. 7, no. 9, article e016280, 2017.

[17] T. L. Middleton, M. I. Constantino, L. Molyneaux et al., "Young-onset type 2 diabetes and younger current age: increased susceptibility to retinopathy in contrast to other complications," *Diabetic Medicine*, vol. 37, no. 6, pp. 991–999, 2020.

[18] J. J. Peavey, S. L. D'amico, B. Y. Kim, S. T. Higgins, D. S. Friedman, and C. J. Brady, "Impact of socioeconomic disadvantage and diabetic retinopathy severity on poor ophthalmic follow-up in a rural Vermont and New York population," *Clinical Ophthalmology*, vol. 14, pp. 2397–2403, 2020.

Hindawi
Journal of Diabetes Research
Volume 2022, Article ID 1193760, 9 pages
https://doi.org/10.1155/2022/1193760

Research Article

Pigment Epithelium-Derived Factor-Loaded PEGylated Nanoparticles as a New Antiangiogenic Therapy for Neovascularization

Feng Zhao,[1,2] **Wenlei Fei**,[1] **Zhouyue Li**,[2] **Hanyang Yu**,[2] **and Lei Xi**[1]

[1]*Guangdong Provincial People's Hospital, Guangdong Academy of Medical Sciences, Guangzhou, Guangdong, China*
[2]*State Key Laboratory of Ophthalmology, Zhongshan Ophthalmic Center, Sun Yat-sen University, Guangzhou, Guangdong, China*

Correspondence should be addressed to Lei Xi; xilei0606@163.com

Received 3 September 2021; Revised 13 March 2022; Accepted 15 March 2022; Published 22 April 2022

Academic Editor: Akira Sugawara

Background. Pathological neovascularization, which involves a disruption in the balance between angiogenic and antiangiogenic factors under pathological conditions, is the basis of many intraocular diseases. Pigment epithelium-derived factor (PEDF) is a potent natural, endogenous inhibitor of neovascularization because of its antiangiogenic and neuroprotective benefits. However, its application is restricted by its instability and short half-life. The present study is aimed at investigating the cytotoxicity and antiangiogenic effects of PEDF-loaded PEGylated nanoparticles (NP-PEG-PEDF) on high glucose-stimulated human umbilical vein endothelial cells (HUVECs). *Methods*. In this study, NP-PEG-PEDF were fabricated using the multiple emulsion method for the first time. HUVECs were cultured in a high concentration of glucose (30 mmol/L D-glucose), simulating diabetic conditions. The antiangiogenic effects of vascular endothelial growth factor (VEGF), pure PEDF, and NP-PEG-PEDF on proliferation, migration, and tube formation were evaluated. VEGF secretion in high glucose-stimulated HUVECs was further tested in vitro. *Results*. NP-PEG-PEDF exhibited low cytotoxicity in HUVECs. Our results indicated that in vitro, NP-PEG-PEDF attenuated diabetes-induced HUVEC proliferation, migration, and tube formation and suppressed VEGF secretion. The apoptosis of diabetes-induced HUVECs occurred in a dose-dependent manner, which showed a statistically significant difference compared with the PEDF treatment group. *Conclusion*. Our study is the first to demonstrate that NP-PEG-PEDF exert antiangiogenic effects on high glucose-stimulated HUVECs and have the potential to alleviate microvascular dysfunction. These data suggest that the NP-PEG-PEDF delivery system may offer an innovative therapeutic strategy for preventing neovascularization of the fundus.

1. Introduction

Pathological neovascularization (NV) in the fundus, such as choroidal NV and retinal NV, is the basic pathological changes in many intraocular diseases, such as age-related macular degeneration (AMD) [1], pathologic myopia [2], and proliferative diabetic retinopathy (PDR) [3]. The reason for the formation of NV remains unclear, but it involves a disruption in the balance between angiogenic and antiangiogenic factors under pathological conditions, such as hypoxia and inflammation [4, 5]. Over the last decade, inhibition of vascular endothelial growth factor A has emerged as a treatment modality for choroidal neovascularization, despite the fact that a considerable number of patients are refractory to anti-VEGF therapy [6]. Additionally, the finding that anti-VEGF therapy may also affect the physiological blood vessels and tissue has raised concerns regarding the long-term adverse effects of this therapy [7]. Developing new antiangiogenic agents to achieve enhanced efficacy and decreased side effects is another option to address these issues.

Pigment epithelium-derived factor (PEDF), which is secreted by the retinal pigment epithelium (RPE) has antiangiogenic, anti-vasopermeability, and antineurotrophic functions, and it is a prospective biomarker that may inhibit the development of diabetic retinopathy (DR) [8–10]. According to current studies, PEDF is regarded as a promising ocular

protecting agent capable of blocking angiogenesis in the choroid and is an essential contributor to maintaining the retinal vascularity status through its antioxidative properties [11–13]. However, difficulty in sustaining it in an active state and lack of an appropriate delivery system limit its application as an antiangiogenic drug in clinical practice.

Polyethylene glycol (PEG) is a type of surface-modifying agent that helps to achieve mucoadhesive, stable, and stealth nanoparticles [14–16]. It has been reported that an optimized PEGylated nanostructured lipid carrier (NLC) could be physically and chemically stable for at least one month as an aqueous dispersion [17]. In this study, we formulated PEDF-loaded PEGylated nanoparticles (NP-PEG-PEDF) and evaluated their cytotoxicity and antiangiogenic effects in vitro with high glucose-treated human umbilical vein endothelial cells (HUVECs). Our results presented a potential strategy for the treatment of NV in the fundus via an NP-PEG-PEDF drug delivery system.

2. Materials and Methods

2.1. Cell Culture. HUVECs were obtained from the American Tissue Culture Collection (ATCC USA) and cultured in Dulbecco's Modified Eagle Medium (DMEM) with 10% fetal bovine serum (FBS; Hyclone, Grand Island, NY, USA) in a 37°C humidified incubator with 5% CO_2 atmosphere.

2.2. Preparation of NP-PEG-PEDF. Lecithin, cholesterol, DSPE-PEG-FA (a PEG derivative containing folic acid), and PEDF were mixed in a chloroform/methanol solution at a mass ratio of 1.7 : 2 : 1.7 : 1. The organic solvent was removed by rotary evaporation, and a thin film of phospholipids was formed on the walls of the round-bottomed flask. Ultrapure water was added to the mixture. A VCX130 ultrasonic crusher was used to ultrasonicate the mixture for 2 min at a frequency of 20 kHz and a power of 130 W to hydrate the film. The nanoparticles were filtered successively through 200 nm and 100 nm polycarbonate filters five times each, followed by three rounds of Amicon Ultra-4 centrifugation (Millipore, USA).

2.3. Characterization of NP-PEG-PEDF. The NP size (diameter, nm), polydispersity index, and surface charge (zeta potential, mV) were measured by quasielastic laser light scattering using a Zeta PALS dynamic light scattering (DLS) detector (Beckman Coulter, San Diego, USA) at 25°C. The dispersion of NPs was diluted to suitable concentration by ultrapure water before measurement. The morphology of NPs was observed by transmission electron microscopy (TEM). NP suspensions (2 mg/mL) were stained with 2% (*w*/*v*) phosphotungstic acid, and then, they were dropped on a 200-mesh copper grid coated with carbon, dried at room temperature, and observed by a TEM instrument at 100 kV (JEOL-1230, Japan).

2.4. HUVEC Viability Assay. HUVECs were used to detect the angiogenic effect of VEGF and the antiangiogenic effects of NP-PEG-PEDF and pure PEDF in vitro using a 3-(4,5-dimethylthiazol-2-yl)-2,5-diphenyltetrazolium (MTT) cell proliferation kit (Sangon, Shanghai, China) assay. HUVECs were combined in DMEM with a high-glucose concentration (30 mmol/L) at a density of 5×10^3 cells per well in 96-well plates overnight without FBS. HUVECs were incubated with VEGF (20 ng/mL) or different concentrations of NP-PEG-PEDF or PEDF (10, 100, and 1000 ng/mL) for 24, 48, and 72 h. After adding the MTT reagent, the cells were incubated at 37°C for another 4 h. The medium was aspirated carefully from each well, and 150 μL of DMSO (Sigma, St. Louis, MO) was added to dissolve formazan, the end product, and the absorbance was read at a wavelength of 540 nm using a plate reader. Cells treated with medium only were set as 100%, and the other experimental groups were calculated using the following formula: viability (%) = (mean optical density [OD] of cells of the experimental group – mean OD of blank) /(mean OD of cells of the control group – mean OD of blank).

To study the angiogenic inhibitory effects of NP-PEG-PEDF under the stimulation of VEGF, 20 ng/mL VEGF was added to the culture medium. PEDF and NP-PEG-PEDF at the same varying concentrations as tested above were incubated for 24, 48, and 72 h, as stated previously. Each experiment was performed in six wells and repeated at least three times.

2.5. Flow Cytometry Analysis of HUVEC Apoptosis. Apoptosis was measured using the FITC Annexin V Apoptosis Detection Kit (Beyotime Technology Ltd. Co., Shanghai, China), according to the manufacturer's instructions. In brief, HUVECs were seeded into 6-well plates and incubated with DMEM with high glucose (30 mmol/L) containing 10% FBS, VEGF (20 ng/mL), NP-PEG-PEDF (10, 100, and 1000 ng/mL), or PEDF (10, 100, and 1000 ng/mL) for 24, 48, and 72 h. The cells were then collected using 0.25% trypsin and stained with propidium iodide (PI) and annexin V for 30 min at 37°C. The early (annexin V^+/PI^-) and late (annexin V^+/PI^+) apoptotic cells were sorted by fluorescence-activated cell sorting (FACS) (BD Biosciences, San Diego, CA).

2.6. Scratch Wound Healing Assay. HUVECs (1×10^5 cells per well) were seeded into 12-well plates and treated with DMEM containing 10% FBS. Once the cells reached approximately 80% confluence, the monolayer was scratched using a sterile p200 pipette tip. Unattached cells were removed by gentle washing. Subsequently, the attached cells were treated with DMEM with high glucose (30 mmol/L) containing 2% FBS and supplemented with VEGF (20 ng/mL), NP-PEG-PEDF (10 ng/mL and 100 ng/mL), or PEDF (10 ng/mL and 100 ng/mL) for 24 h. Cells were imaged at 0 h and 24 h under an inverted microscope. The following formula was used to calculate the wound closure ratio: wound closure (%) = $(A_0 - A_r)/A_0 \times 100$, where A_0 represents the area of the initial wound area and A_r represents the remaining wound area at 24 h.

2.7. Tube Formation Study. The antiangiogenic potentials of VEGF, NP-PEG-PEDF, and PEDF were tested using a tube formation assay under high glucose (30 mmol/L). Aliquots (150 μL) of Matrigel (BD Biosciences) solution were poured into 24-well plates and incubated at 37°C for 30 min in a 5%

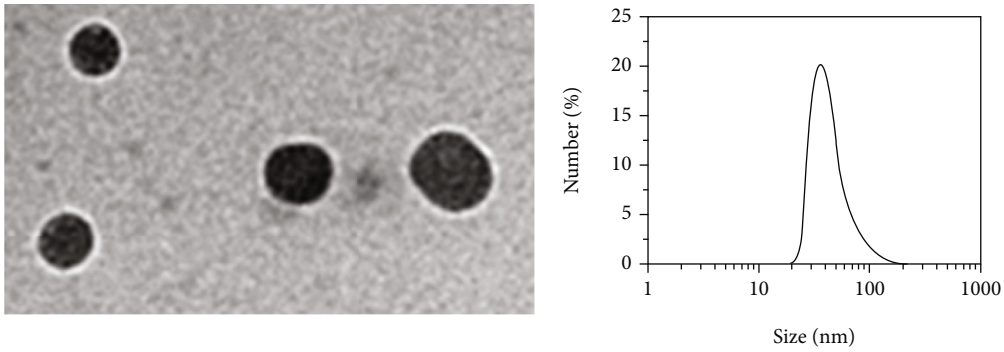

(a) (b)

Figure 1: (a) Transmission electron microscopy image of NP-PEG-PEDF. (b) Size distribution of NP-PEG-PEDF.

CO_2 incubator. HUVECs treated with VEGF (20 ng/mL), NP-PEG-PEDF (10 ng/mL and 100 ng/mL), PEDF (10 ng/mL and 100 ng/mL), or controls were seeded on Matrigel and cultured in DMEM for 8 h. The networks in Matrigel from five randomly chosen fields were counted and photographed under a microscope. All experiments were performed in triplicate.

2.8. VEGF Detection by Enzyme-Linked Immunosorbent Assay. HUVECs were seeded into 96-well plates (1×10^4 per well) with high glucose (30 mmol/L) and incubated at 37°C overnight. After removing the DMEM, NP-PEG-PEDF (10 ng/mL and 100 ng/mL) or PEDF (10 ng/mL and 100 ng/mL) were added to the wells. After 48 and 72 h of incubation, the supernatant of the cell culture was harvested, and the cellular debris was removed by centrifugation. VEGF protein secreted by HUVECs in the culture medium was measured using a VEGF ELISA kit purchased from BOSTER (Wuhan, China) according to the manufacturer's instructions.

2.9. Statistical Analysis. Data analysis was performed using STATA statistical software (version 15.0; StataCorp LLC). All data are presented as mean ± SEM and were evaluated for normality of distribution. Differences were evaluated using analysis of variance, followed by the Student-Newman-Keuls test for multiple comparisons and the Student's *t*-test for pairwise comparisons. Differences were considered statistically significant at $p < 0.05$.

3. Results

3.1. Characterization of NP-PEG-PEDF. Figures 1(a) and 1(b) show the transmission electron microscopy (TEM) image and size distribution of NP-PEG-PEDF, and the NPs were generally spherical in shape with good monodispersity. The zeta potential and hydrodynamic sizes of NP-PEG-PEDF were −11.7 ± 0.87 mV and 44.85 ± 4.78 nm with a polydispersity of 0.183, respectively. The drug encapsulation efficiency (EE) and drug loading efficiency (LE) of the NP-PEG-PEDF were observed at 46.25% and 7.23% which was crucial for clinical application.

3.2. Effect of NP-PEG-PEDF on HUVEC Proliferation. An HUVEC proliferation study was used to evaluate the antiangiogenic effects of NP-PEG-PEDF and pure PEDF in vitro under high glucose (30 mmol/L). HUVECs were incubated for 24, 48, and 72 h at various concentrations (10, 100, and 1000 ng/mL). As shown in Figure 2 and Table 1, the NP-PEG-PEDF-treated groups were statistically different from the PEDF-treated groups at all concentrations and time points. To further evaluate the inhibitory effect of NP-PEG-PEDF on VEGF stimulation, we added 20 ng/mL VEGF to the cell culture medium and found that NP-PEG-PEDF also exhibited better inhibitory effects on HUVEC proliferation (Figure 3 and Table 2).

3.3. Effect of NP-PEG-PEDF on HUVEC Apoptosis. FACS was used to evaluate the effects of early and late apoptosis. As shown in Table 3 and Figure 4, after incubation with PEDF and NP-PEG-PEDF combined with 10% FBS under high glucose (30 mmol/L) for 24, 48, and 72 h, the early and late apoptotic HUVECs showed significant differences in the 10, 100, and 1000 ng/mL-treated groups, with the percentages of apoptotic cells (UR+LR) being significantly higher than those in PEDF-treated cells ($p < 0.05$).

LL: lower left; LR: lower right; UL: upper left; UR: upper right.

3.4. Effect of NP-PEG-PEDF on HUVEC Migration. HUVEC migration was assessed using a cell scratch test under high glucose (30 mmol/L). As shown in Figures 5 and 6, the percent wound closure of the membrane in the NP-PEG-PEDF-treated HUVEC group (10 ng/mL) was significantly lower than that in the PEDF (10 ng/mL) and VEGF (20 ng/mL)-treated groups (p 0.05).

3.5. Effect of NP-PEG-PEDF on HUVEC Tube Formation. In our study, both PEDF- and NP-PEG-PEDF-treated cells exhibited an impaired capacity to form a regular network, and as expected, HUVECs could not form hollow lumens in either group (Figures 7 and 8). Although there was no significant difference between the NP-PEG-PEDF- and PEDF-treated groups (10 ng/mL) in terms of lumen formation, the NP-PEG-PEDF-treated HUVECs showed statistical differences in length compared with the PEDF-treated groups and

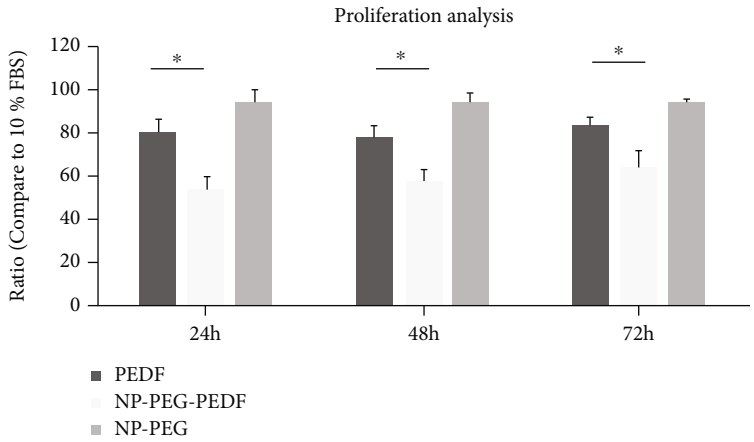

Figure 2: Effects of PEDF and NP-PEG-PEDF on the proliferation of HUVECs in the general culture medium under high glucose (30 mmol/L) at 24, 48, and 72 h. The effective concentrations (1000 ng/mL) at different time points are shown. $^{*}p < 0.05$.

Table 1: Summary of proliferation effects with PEDF and NP-PEG-PEDF-treated HUVECs under high glucose (30 mmol/L).

Time points		10%FBS	NP-PEG 1000 ng/mL	PEDF 1000 ng/mL	PEDF 100 ng/mL	PEDF 10 ng/mL	NP-PEG-PEDF 1000 ng/mL	NP-PEG-PEDF 100 ng/mL	NP-PEG-PEDF 10 ng/mL
24 h	Mean	1	94.27	80.33	77.34	69.15	54.19	45.83	40.34
	SEM		5.41	5.90	2.97	7.25	4.39	4.33	8.92
48 h	Mean	1	91.49	78.26	79.23	80.22	58.13	67.12	61.29
	SEM		6.87	3.69	4.89	5.32	5.02	3.71	10.23
72 h	Mean	1	91.12	83.89	86.13	88.3	64.29	63.12	59.56
	SEM		4.23	4.97	5.65	7.21	3.27	3.92	13.21

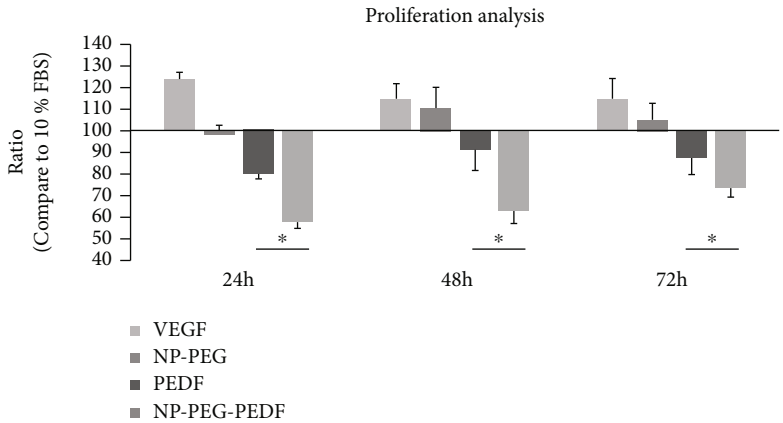

Figure 3: Effects of PEDF and NP-PEG-PEDF on the proliferation of HUVECs with VEGF stimulation under high glucose (30 mmol/L) at 24, 48, and 72 h. The effective concentrations (1000 ng/mL) at different time points are shown. $^{*}p < 0.05$.

presented round morphology with no branches at all, whereas the PEDF-treated group had a tendency to form tubes.

3.6. Effect of NP-PEG-PEDF on HUVECs in terms of the Reduction of VEGF Secretion. As shown in Figure 9 and Table 4, after treatment for 48 and 72 h, VEGF was down-regulated in the PEDF and NP-PEG-PEDF groups under high glucose (30 mmol/L). The NP-PEG-PEDF (100 ng/mL)-treated cells showed less VEGF secretion than the PEDF group at two time points ($p < 0.05$).

4. Discussion

Retinal or choroidal NV is the congenerous pathologic basis of several ocular diseases of the fundus, including PDR and AMD. The current research has shown that glucose metabolism influences the balance of proangiogenesis and antiangiogenesis processes involved in the progression of DR [18, 19]. Therefore, antiangiogenic treatment, especially intravitreal injection of anti-VEGF antibodies, is still the most effective therapeutic strategy throughout the world.

Table 2: Summary of proliferation effects of PEDF and NP-PEG-PEDF combined with VEGF-treated HUVECS under high glucose (30 mmol/L).

Time points		10% FBS	VEGF (20 ng/mL)	NP-PEG 1000 ng/mL	PEDF 1000 ng/mL	PEDF 100 ng/mL	PEDF 10 ng/mL	NP-PEG-PEDF 1000 ng/mL	NP-PEG-PEDF 100 ng/mL	NP-PEG-PEDF 10 ng/mL
24 h	Mean	1	123.61	99.19	79.83	74.57	84.48	57.32	59.48	62.07
	SEM		2.98	3.14	1.67	3.54	3.2	2.3	2.89	1.41
48 h	Mean	1	114.65	110.37	91.19	96.11	97.12	63.12	68.12	62.45
	SEM		6.56	9.24	7.23	5.29	5.81	4.32	5.27	6.82
72 h	Mean	1	115.21	105.25	87.68	90.58	91.03	73.33	79.71	87.82
	SEM		7.89	7.48	6.22	2.73	4.14	6.56	3.59	4.23

Table 3: Summary of flow cytometry data of apoptosis measured by annexin V and PI.

Time point	% of cells	10% FBS		NP-PEG 1000 ng/mL		PEDF 1000 ng/mL		PEDF 100 ng/mL		PEDF 10 ng/mL		NP-PEG-PEDF 1000 ng/mL		NP-PEG-PEDF 100 ng/mL		NP-PEG-PEDF 10 ng/mL	
		Mean	SEM	Mean	SEM	Mean	SEM	Mean	SEM	Mean	SEM	Mean	SEM	Mean	SEM	Mean	SEM
24 h	UL	0.87	0.09	2.29	0.11	2.34	0.15	2.51	0.17	1.65	0.17	1.27	0.07	1.67	0.1	2.26	0.15
	UR	2.16	0.06	2.36	0.17	2.23	0.14	2.43	0.13	1.89	0.19	2.91	0.13	3.23	0.16	2.15	0.22
	LL	95	0.21	93.17	0.23	93.02	0.34	93.33	0.32	94.11	0.39	90.84	0.21	91.12	0.24	91.44	0.23
	LR	1.97	0.12	2.18	0.09	2.41	0.21	1.73	0.09	1.33	0.11	4.98	0.19	3.98	0.22	2.01	0.18
	UR+LR	4.13	0.14	4.54	0.13	4.64	0.23	4.16	0.11	3.22	0.23	7.89	0.26	7.21	0.29	4.16	9.25
48 h	UL	1.39	0.14	1.93	0.07	2.34	0.11	3.44	0.13	2.66	0.21	2.43	0.11	2.89	0.14	2.87	0.15
	UR	1.12	0.13	1.55	0.12	1.56	0.09	1.54	0.09	1.53	0.15	3.97	0.21	2.93	0.24	2.33	0.51
	LL	95.33	0.23	92.54	0.34	92.98	0.38	90.34	0.2	92.25	0.42	83.17	0.34	82.84	0.37	88.21	0.31
	LR	2.16	0.14	3.98	0.25	3.12	0.21	4.68	0.19	2.69	0.45	10.43	0.21	11.34	0.24	4.03	0.17
	UR+LR	3.28	0.33	5.53	0.31	4.68	0.13	6.22	0.23	4.22	0.36	14.4	0.31	14.27	0.34	6.36	0.35
72 h	UL	2.11	0.28	1.91	0.09	1.93	0.11	1.98	0.12	2.32	0.15	2.33	0.11	2.07	0.14	3.00	0.11
	UR	2.03	0.31	2.03	0.11	2.57	0.21	2.63	0.21	2.36	0.13	3.78	0.13	3.13	0.16	3.32	0.24
	LL	91.99	0.26	94.16	0.35	91.52	0.32	92.07	0.34	91.19	0.33	87.12	0.29	87.49	0.32	87.29	0.52
	LR	3.87	0.25	1.9	0.07	3.98	0.08	3.32	0.12	3.31	0.23	6.77	0.13	7.31	0.16	3.21	0.37
	UR+LR	5.9	0.17	3.93	0.11	6.55	0.19	5.95	0.16	5.67	0.28	10.55	0.25	10.44	0.28	6.53	0.48

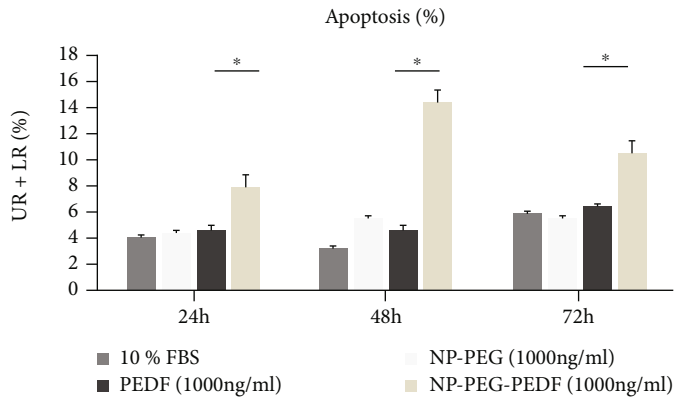

Figure 4: Effects of PEDF and NP-PEG-PEDF on HUVEC apoptosis under high glucose (30 mmol/L). DMEM+10% FBS control was set to 100%. $^{*}p < 0.05$.

However, its potent side effects, such as endophthalmitis, intraocular inflammation, ocular hemorrhage, retinal detachment, thrombosis, and cardiovascular accidents, drive us to look for new alternatives [20–22]. PEDF has been demonstrated to be an important therapeutic adjunct in the management of sight-threatening diseases caused by increased vascular permeability.

PEDF, a 50 kDa endogenously secreted glycoprotein [23], is a versatile protective angiogenic inhibitor for several ocular diseases [24–26]. It is expressed in many different cell

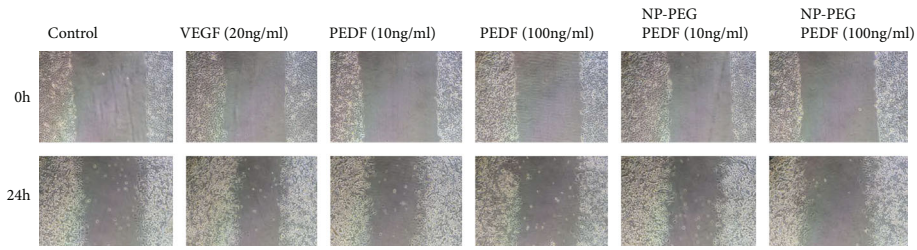

Figure 5: Cell scratch test results. Effects of PEDF and NP-PEG-PEDF on HUVEC scratch wound healing under high glucose (30 mmol/L).

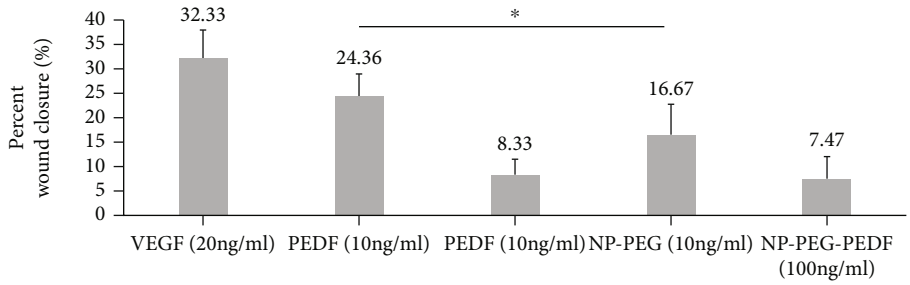

Figure 6: Statistical results of the percent wound closure (%) under different treatments. $^{*}p < 0.05$.

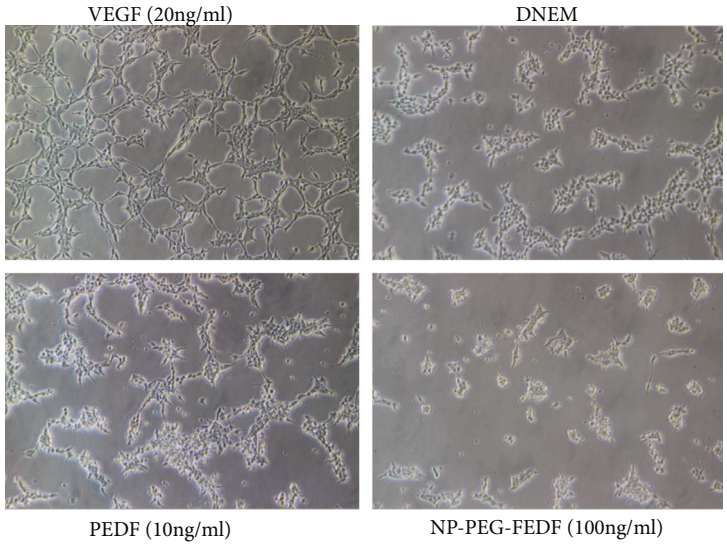

Figure 7: Effects of PEDF and NP-PEG-PEDF on HUVEC tube formation. NP-PEG-PEDF-treated HUVECs presented round morphology and showed no cell branches attempting to form networks.

types in fetal and adult eyes, including the cells of the cornea, lens, and retina. It is a novel agent that can be helpful in inhibiting the occurrence of new fragile blood vessels in the retina [27, 28]. There are many proposed mechanisms by which PEDF may decrease neovascularization and abate neovascular permeability: through inhibition of the VEGF pathway by downregulating mitogen-activated protein kinase-mediated hypoxia-inducible factor 1 activation [29], by enhancing the γ-secretase-dependent cleavage of the C-terminus phosphorylation in VEGF receptor 1 [30, 31], and activating apoptosis by regulating multiple pathways of p38 followed by cleavage of caspase-dependent [32, 33].

In addition, PEDF has nutritional and protective effects on nerves. PEDF can prevent neuronal apoptosis by upregulating the expression of B cell lymphoma 2 (Bcl-2) protein, when oxidative stress damage occurs in PDR [34, 35]. Increased PEDF can decrease H_2O_2-induced disruption of mitochondrial function and cell death in RPE cells by reducing oxidative stress [36]. Moreover, in vivo and in vitro studies revealed that PEDF neuroprotection was achieved by stabilizing photoreceptor degeneration by decreasing intracellular calcium and suppressing apoptotic and inflammatory pathways [37, 38]. In addition, PEDF can distinguish neovascular endothelial cells from normal vascular endothelial cells through Fas-FasL receptors, accomplish selective destruction of abnormal new blood vessels without damaging the normal established retinal blood vessels, and protect and maintain the status of healthy ocular tissues [12, 34, 35].

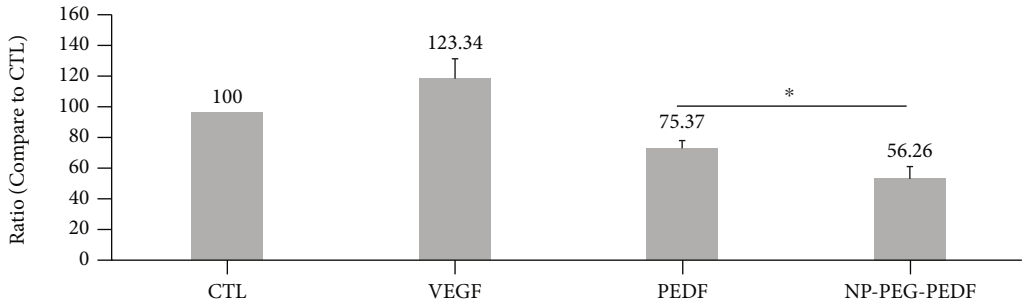

Figure 8: Statistical results of the length of tube formation under different treatments. DMEM+10% FBS control was set to 100%. $^{*}p < 0.05$.

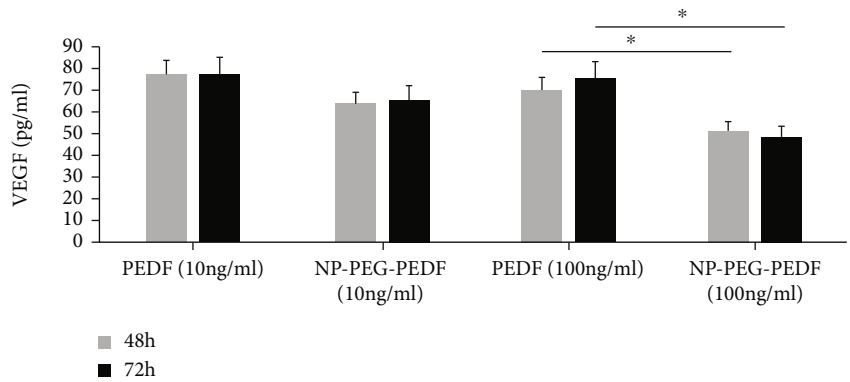

Figure 9: Effects of PEDF and NP-PEG-PEDF treatment on VEGF secretion in HUVECs. The NP-PEG-PEDF-treated group (100 ng/mL) exhibited significant suppression in VEGF secretion at both 48 and 72 h ($p < 0.05$).

Table 4: Summary of VEGF secretion (pg/mL) in PEDF- and NP-PEG-PEDF-treated HUVECs.

Time points		10% FBS	PEDF		NP-PEG-PEDF	
			100 ng/mL	10 ng/mL	100 ng/mL	10 ng/mL
48 h	Mean	1	70.05	76.86	50.23	63.75
	SEM		3.65	6.79	2.76	4.69
72 h	Mean	1	75.81	77.91	47.92	65.78
	SEM		6.34	7.23	4.23	5.12

Because of its antiangiogenic and neuroprotective benefits, PEDF has been used to treat ocular NV. Investigators have evaluated virus-coded PEDF administered by intravitreous or subretinal injection in choroidal NV animal models. They found that overexpression of PEDF can inhibit neovascularization of the choroid and improve the survival of photoreceptors [39–42]. Bai et al. explored PEGylated-PEDF to prevent angiogenesis in HUVECs and in vivo [43]. The results revealed that PEGylated PEDF inhibited HUVEC proliferation, migration, and tube formation in a dose-dependent manner and decreased retinal neovascularization by intravitreous injection in an oxygen-induced retinopathy mouse model. However, there have not been any studies in diabetic models. The instability and short half-life of PEDF restrict its application. In recent years, nanoparticulate dosage forms have emerged as a promising ocular platform to deliver poorly water-soluble compounds because of their enhanced precorneal retention and improved penetration into the ocular tissues [16]. Additionally, nanomedicine has its own properties, including a high surface-to-volume ratio and favorable physicochemical characteristics [44]. PEG is commonly used for nanoparticle modification. The United States Food and Drug Administration has approved the use of PEG in drug modification for several years because of its low toxicity, low cost, and increased solubility [45]. However, it has not been determined if the processes of PEGylation and forming a PEDF-loaded nanostructured lipid altered the stability and toxic activity of PEDF.

In the current study, we developed NP-PEG-PEDF for the first time and evaluated its cytotoxicity and antiangiogenic effects in high-glucose cultured HUVECs. Our results showed that NP-PEG-PEDF inhibited HUVEC proliferation, migration, tube formation, and VEGF secretion and induced HUVEC apoptosis in a dose-dependent manner under diabetic conditions.

5. Conclusion

In summary, our study found, for the first time, that PEDF-loaded PEGylated nanoparticles effectively inhibited NV in

high glucose-stimulated HUVECs in vitro. Because of the neurotrophic and antiangiogenic effects of PEDF, it may be utilized to make a more effective therapeutic treatment of retinal or choroidal NV in the future. Our data suggest that the PEGylated PEDF delivery system could be an extremely promising long-term treatment for PDR or AMD. NP-PEG-PEDF appears to be a safe and effective drug delivery system, and its use may prove to be an innovative approach for future therapeutic strategies against pathologically increased vascular permeability involved in several ocular diseases.

Data Availability

The data used to support the findings of this study are available from the corresponding author upon request.

Conflicts of Interest

All authors declare that there are no conflicts of interest regarding the publication of this paper.

Acknowledgments

The study is supported by the Science and Technology Project of Guangzhou (202102080085) and Guangdong Medical Science Foundation of China (B2021210).

References

[1] S. D. Hobbs and K. Pierce, *Wet age-related macular degeneration (Wet AMD)*, StatPearls [Internet], 2021.

[2] D. Ng, N. Fung, F. Yip, and T. Lai, "Ranibizumab for myopic choroidal neovascularization," *Expert opinion on biological therapy.*, vol. 20, no. 12, pp. 1385–1393, 2020.

[3] T. Y. Wong, C. M. Cheung, M. Larsen, S. Sharma, and R. Simó, "Diabetic retinopathy," *Nature reviews. Disease primers*, vol. 2, no. 1, 2016.

[4] R. O. Schlingemann, "Role of growth factors and the wound healing response in age-related macular degeneration," *Graefe's archive for clinical and experimental ophthalmology = Albrecht von Graefes Archiv für klinische und experimentelle Ophthalmologie*, vol. 242, no. 1, pp. 91–101, 2004.

[5] I. S. Sung, S. Y. Park, K. Y. Jeong, and H. M. Kim, "Investigation of the preventive effect of calcium on inflammation-mediated choroidal neovascularization," *Life sciences*, vol. 233, article 116727, 2019.

[6] C. Campa and S. P. Harding, "Anti-VEGF compounds in the treatment of neovascular age related macular degeneration," *Current drug targets*, vol. 12, no. 2, pp. 173–181, 2011.

[7] A. Carneiro, M. Falcão, A. Pirraco, P. Milheiro-Oliveira, F. Falcão-Reis, and R. Soares, "Comparative effects of bevacizumab, ranibizumab and pegaptanib at intravitreal dose range on endothelial cells," *Experimental eye research*, vol. 88, no. 3, pp. 522–527, 2009.

[8] X. F. Zhu and H. D. Zou, "PEDF in diabetic retinopathy: a protective effect of oxidative stress," *Journal of biomedicine & biotechnology*, vol. 2012, Article ID 580687, 8 pages, 2012.

[9] O. M. Cecilia, C. G. José Alberto, N. P. José et al., "Oxidative stress as the main target in diabetic retinopathy pathophysiology," *Journal of diabetes research*, vol. 2019, Article ID 8562408, 21 pages, 2019.

[10] S. X. Zhang, J. J. Wang, G. Gao, C. Shao, R. Mott, and J. X. Ma, "Pigment epithelium-derived factor (PEDF) is an endogenous antiinflammatory factor," *FASEB journal : official publication of the Federation of American Societies for Experimental Biology.*, vol. 20, no. 2, pp. 323–325, 2006.

[11] K. Nakamura, S. Yamagishi, T. Matsui et al., "Pigment epithelium-derived factor inhibits neointimal hyperplasia after vascular injury by blocking NADPH oxidase-mediated reactive oxygen species generation," *The American journal of pathology.*, vol. 170, no. 6, pp. 2159–2170, 2007.

[12] C. J. Barnstable and J. Tombran-Tink, "Neuroprotective and antiangiogenic actions of PEDF in the eye: molecular targets and therapeutic potential," *Progress in retinal and eye research.*, vol. 23, no. 5, pp. 561–577, 2004.

[13] R. H. Müller, R. Shegokar, and C. M. Keck, "20 years of lipid nanoparticles (SLN & NLC): present state of development & industrial applications," *Current drug discovery technologies*, vol. 8, no. 3, pp. 207–227, 2011.

[14] S. P. Balguri, G. R. Adelli, K. Y. Janga, P. Bhagav, and S. Majumdar, "Ocular disposition of ciprofloxacin from topical, PEGylated nanostructured lipid carriers: effect of molecular weight and density of poly (ethylene) glycol," *International Journal of Pharmaceutics*, vol. 529, no. 1-2, pp. 32–43, 2017.

[15] F. M. Veronese and G. Pasut, "PEGylation, successful approach to drug delivery," *Drug Discovery Today*, vol. 10, no. 21, pp. 1451–1458, 2005.

[16] P. Lakhani, A. Patil, K. W. Wu et al., "Optimization, stabilization, and characterization of amphotericin B loaded nanostructured lipid carriers for ocular drug delivery," *International journal of pharmaceutics*, vol. 572, article 118771, 2019.

[17] J. W. Yau, S. L. Rogers, R. Kawasaki et al., "Global prevalence and major risk factors of diabetic retinopathy," *Diabetes Care*, vol. 35, no. 3, pp. 556–564, 2012.

[18] M. Ponnalagu, M. Subramani, C. Jayadev, R. Shetty, and D. Das, "Retinal pigment epithelium-secretome: a diabetic retinopathy perspective," *Cytokine*, vol. 95, pp. 126–135, 2017.

[19] C. Weigert, U. Friess, K. Brodbeck, H. U. Häring, and E. D. Schleicher, "Glutamine:fructose-6-phosphate aminotransferase enzyme activity is necessary for the induction of TGF-?1 and fibronectin expression in mesangial cells," *Diabetologia*, vol. 46, no. 6, pp. 852–855, 2003.

[20] U. Schraermeyer and S. Julien, "Formation of immune complexes and thrombotic microangiopathy after intravitreal injection of bevacizumab in the primate eye," *Graefe's archive for clinical and experimental ophthalmology = Albrecht von Graefes Archiv für klinische und experimentelle Ophthalmologie*, vol. 250, no. 9, pp. 1303–1313, 2012.

[21] S. Julien, A. Biesemeier, and U. Schraermeyer, "In vitro induction of protein complexes between bevacizumab, VEGF-A165and heparin: explanation for deposits observed on endothelial veins in monkey eyes," *The British journal of ophthalmology*, vol. 97, no. 4, pp. 511–517, 2013.

[22] J. Hanhart, D. S. Comaneshter, Y. Freier-Dror, and S. Vinker, "Mortality associated with bevacizumab intravitreal injections in age-related macular degeneration patients after acute myocardial infarct: a retrospective population-based survival analysis," *Graefe's archive for clinical and experimental ophthalmology = Albrecht von Graefes Archiv für klinische und experimentelle Ophthalmologie*, vol. 256, no. 4, pp. 651–663, 2018.

[23] P. Kozulin, R. Natoli, K. M. Bumsted O'Brien, M. C. Madigan, and J. M. Provis, "The cellular expression of antiangiogenic factors in fetal primate macula," *Investigative ophthalmology & visual science*, vol. 51, no. 8, pp. 4298–4306, 2010.

[24] S. P. Becerra, R. N. Fariss, Y. Q. Wu, L. M. Montuenga, P. Wong, and B. A. Pfeffer, "Pigment epithelium-derived factor in the monkey retinal pigment epithelium and interphotoreceptor matrix: apical secretion and distribution," *Experimental eye research*, vol. 78, no. 2, pp. 223–234, 2004.

[25] Y. Sho-Ichi, "Pigment epithelium-derived factor (PEDF) in health and disease," *Current molecular medicine.*, vol. 10, no. 3, p. 258, 2010.

[26] S. Sheikpranbabu, H. Ravinarayanan, B. Elayappan, P. Jongsun, and S. Gurunathan, "Retracted: Pigment epithelium-derived factor inhibits vascular endothelial growth factor-and interleukin-1beta-induced vascular permeability and angiogenesis in retinal endothelial cells," *Vascular pharmacology.*, vol. 52, no. 1-2, pp. 84–94, 2010.

[27] N. Ogata, M. Wada, T. Otsuji, N. Jo, J. Tombran-Tink, and M. Matsumura, "Expression of pigment epithelium-derived factor in normal adult rat eye and experimental choroidal neovascularization," *Investigative ophthalmology & visual science*, vol. 43, no. 4, pp. 1168–1175, 2002.

[28] L. Xi, "Pigment epithelium-derived factor as a possible treatment agent for choroidal neovascularization," *Oxidative medicine and cellular longevity*, vol. 2020, Article ID 8941057, 11 pages, 2020.

[29] S. X. Zhang, J. J. Wang, G. Gao, K. Parke, and J. X. Ma, "Pigment epithelium-derived factor downregulates vascular endothelial growth factor (VEGF) expression and inhibits VEGF-VEGF receptor 2 binding in diabetic retinopathy," *Journal of molecular endocrinology.*, vol. 37, no. 1, pp. 1–12, 2006.

[30] G. Gao, Y. Li, D. Zhang, S. Gee, C. Crosson, and J. Ma, "Unbalanced expression of VEGF and PEDF in ischemia-induced retinal neovascularization," *FEBS letters*, vol. 489, no. 2-3, pp. 270–276, 2001.

[31] J. Cai, W. G. Jiang, M. B. Grant, and M. Boulton, "Pigment epithelium-derived factor inhibits angiogenesis via regulated intracellular proteolysis of vascular endothelial growth factor receptor 1∗," *The Journal of biological chemistry.*, vol. 281, no. 6, pp. 3604–3613, 2006.

[32] A. Bernard, J. Gao-Li, C. A. Franco, T. Bouceba, A. Huet, and Z. Li, "Laminin receptor involvement in the anti-angiogenic activity of pigment epithelium-derived factor," *The Journal of biological chemistry*, vol. 284, no. 16, pp. 10480–10490, 2009.

[33] H. Liu, J. G. Ren, W. L. Cooper, C. E. Hawkins, M. R. Cowan, and P. Y. Tong, "Identification of the antivasopermeability effect of pigment epithelium-derived factor and its active site," *Proceedings of the National Academy of Sciences of the United States of America*, vol. 101, no. 17, pp. 6605–6610, 2004.

[34] M. Elahy, S. Baindur-Hudson, V. F. Cruzat, P. Newsholme, and C. R. Dass, "Mechanisms of PEDF-mediated protection against reactive oxygen species damage in diabetic retinopathy and neuropathy," *The Journal of endocrinology*, vol. 222, no. 3, pp. R129–R139, 2014.

[35] A. Sanchez, D. Tripathy, X. Yin, J. Luo, J. Martinez, and P. Grammas, "Pigment epithelium-derived factor (PEDF) protects cortical neurons *in vitro* from oxidant injury by activation of extracellular signal-regulated kinase (ERK) 1/2 and induction of Bcl-2," *Neuroscience research*, vol. 72, no. 1, pp. 1–8, 2012.

[36] F. M. Nadal-Nicolas and S. P. Becerra, "Pigment epithelium-derived factor protects retinal pigment epithelial cells against cytotoxicity "in vitro"," *Retinal Degenerative Diseases*, vol. 1074, 2018.

[37] Y. He, K. W. Leung, Y. Ren, J. Pei, J. Ge, and J. Tombran-Tink, "PEDF improves mitochondrial function in RPE cells during oxidative stress," *Investigative ophthalmology & visual science*, vol. 55, no. 10, pp. 6742–6755, 2014.

[38] A. Comitato, P. Subramanian, G. Turchiano, M. Montanari, S. P. Becerra, and V. Marigo, "Pigment epithelium-derived factor hinders photoreceptor cell death by reducing intracellular calcium in the degenerating retina," *Cell death & disease*, vol. 9, no. 5, p. 560, 2018.

[39] A. L. Askou, S. Alsing, J. Benckendorff et al., "Suppression of choroidal neovascularization by AAV-based dual-acting anti-angiogenic gene therapy," *Molecular therapy. Nucleic acids*, vol. 16, pp. 38–50, 2019.

[40] K. Park, J. Jin, Y. Hu, K. Zhou, and J. X. Ma, "Overexpression of pigment epithelium-derived factor inhibits retinal inflammation and neovascularization," *The American journal of pathology*, vol. 178, no. 2, pp. 688–698, 2011.

[41] Y. J. Yu, B. Mo, L. Liu, Y. K. Yue, C. L. Yue, and W. Liu, "Inhibition of choroidal neovascularization by lentivirus-mediated PEDF gene transfer in rats," *International journal of ophthalmology*, vol. 9, no. 8, pp. 1112–1120, 2016.

[42] A. L. Askou, L. Aagaard, C. Kostic et al., "Multigenic lentiviral vectors for combined and tissue-specific expression of miRNA- and protein-based antiangiogenic factors," *Molecular Therapy-Methods & Clinical Development*, vol. 2, p. 14064, 2015.

[43] Y. J. Bai, L. Z. Huang, X. L. Xu et al., "Polyethylene glycol-modified pigment epithelial-derived factor: new prospects for treatment of retinal neovascularization," *The Journal of pharmacology and experimental therapeutics*, vol. 342, no. 1, pp. 131–139, 2012.

[44] Y. Chen, N. Li, B. Xu et al., "Polymer-based nanoparticles for chemo/gene-therapy: evaluation its therapeutic efficacy and toxicity against colorectal carcinoma," *Biomedicine & pharmacotherapy = Biomédecine & pharmacothérapie*, vol. 118, p. 109257, 2019.

[45] H. Liu, M. Zhao, J. Wang et al., "Photodynamic therapy of tumors with pyropheophorbide-*a*-loaded polyethylene glycol–poly (lactic-*co*-glycolic acid) nanoparticles," *International journal of nanomedicine*, vol. 11, pp. 4905–4918, 2016.

Hindawi
Journal of Diabetes Research
Volume 2022, Article ID 5779276, 5 pages
https://doi.org/10.1155/2022/5779276

Research Article

Cross-Camera External Validation for Artificial Intelligence Software in Diagnosis of Diabetic Retinopathy

Meng-Ju Tsai,[1] Yi-Ting Hsieh,[2] Chin-Han Tsai,[3] Mingke Chen,[3] An-Tsz Hsieh,[4,5] Chung-Wen Tsai,[6] and Min-Ling Chen[7]

[1]*Department of Ophthalmology, Taoyuan General Hospital, Ministry of Health and Welfare, Taoyuan, Taiwan*
[2]*Department of Ophthalmology, National Taiwan University Hospital, Taipei, Taiwan*
[3]*Acer Medical Inc., New Taipei, Taiwan*
[4]*Hsieh's Endocrinologic Clinic, New Taipei, Taiwan*
[5]*Department of Internal Medicine, School of Medicine, National Defense Medical Center, Taipei, Taiwan*
[6]*Joy Clinic, Taoyuan, Taiwan*
[7]*Chen Min Ling Medical Clinic, New Taipei, Taiwan*

Correspondence should be addressed to Yi-Ting Hsieh; ythyth@gmail.com

Received 27 June 2021; Revised 12 February 2022; Accepted 17 February 2022; Published 9 March 2022

Academic Editor: Tao Li

Aims. To investigate the applicability of deep learning image assessment software VeriSee DR to different color fundus cameras for the screening of diabetic retinopathy (DR). *Methods*. Color fundus images of diabetes patients taken with three different nonmydriatic fundus cameras, including 477 Topcon TRC-NW400, 459 Topcon TRC-NW8 series, and 471 Kowa nonmyd 8 series that were judged as "gradable" by one ophthalmologist were enrolled for validation. VeriSee DR was then used for the diagnosis of referable DR according to the International Clinical Diabetic Retinopathy Disease Severity Scale. Gradability, sensitivity, and specificity were calculated for each camera model. *Results*. All images (100%) from the three camera models were gradable for VeriSee DR. The sensitivity for diagnosing referable DR in the TRC-NW400, TRC-NW8, and non-myd 8 series was 89.3%, 94.6%, and 95.7%, respectively, while the specificity was 94.2%, 90.4%, and 89.3%, respectively. Neither the sensitivity nor the specificity differed significantly between these camera models and the original camera model used for VeriSee DR development ($p = 0.40$, $p = 0.065$, respectively). *Conclusions*. VeriSee DR was applicable to a variety of color fundus cameras with 100% agreement with ophthalmologists in terms of gradability and good sensitivity and specificity for the diagnosis of referable DR.

1. Introduction

Diabetic retinopathy (DR) is one of the most severe sight-threatening diseases worldwide. Among patients with diabetes, the prevalence was estimated to be 34.6% for any degree of DR, 7.0% for proliferative DR, and 10.2% for vision-threatening DR [1]. The population of patients with diabetes has been increasing in recent years; however, DR awareness and regular evaluation for DR at recommended time points among these individuals remain suboptimal, probably due to poor compliance and limited resources in some areas [2, 3]. Therefore, the development of a cost-effective screening program for DR using fundus photography is an important issue for both patients and healthcare professionals. In recent decades, various computer programs have been developed for automated analysis of color fundus images with acceptable and comparable accuracy to those of human graders [4, 5]. The sensitivity for the detection of referable DR ranged from 85.0% to 96.8% in these studies. Despite the increased efficiency for DR screening, the software used in the automated analysis largely learns explicit disease features taught by specialists, such as the shape and number of dot hemorrhages shown on the photos, to determine DR severity. The application of specified rules to machine learning may limit the detection of undefined features that exist in retinal images.

In recent years, deep learning algorithms have been developed to work through convolutional neural networks (CNNs) and constantly adjust the internal parameters to optimize the predictive capabilities for image analysis and classification with supervised or unsupervised learning. Deep learning algorithms have been proven to be effective in detecting DR using color fundus photographs with good accuracy [6–10]. However, the results of their application in real-world settings may be less satisfactory [11, 12], partially due to image discrepancies among different races or the use of different fundus cameras [13].

The VeriSee DR (Acer Inc., Taiwan) is a certified image assessment software in Taiwan and Thailand, and it uses CNN as the principle of deep learning algorithms for DR screening [14]. During the development of the deep learning models, local image datasets from Taiwan, which contained single-field, 45-degree color fundus photography taken with a nonmydriatic fundus camera (CR-2 series, Canon Inc., Japan) from Taiwanese diabetes patients (mostly East Asians in ethnicity), were incorporated in addition to the open-access dataset EyePACS for model training. The sensitivity (89.2%) and specificity (90.1%) of VeriSee DR in detecting referable DR during the validation stage of model development were good. The accuracy of this software was also good (sensitivity of 95.0% and specificity of 89.9%) for external validation during the subsequent clinical trial in Taiwan. To extend the applicability of the software, this study is aimed at validating the accuracy of VeriSee DR for its application to fundus images taken with different fundus cameras.

2. Methods

2.1. Image Datasets. Color fundus images of diabetes patients taken with nonmydriatic fundus cameras, including the TRC-NW series (TRC-NW400, TRC-NW8, TRC-NW8F, and TRC-NW8F plus, Topcon Inc., Japan) and the nonmyd 8 series (nonmyd 8 and nonmyd 8 s, Kowa Inc., Japan) in three general practice clinics were collected for studies. All images were taken without pupil dilatation, and all participants were Taiwanese (East Asians in ethnicity). The details of the camera specification profiles are presented in Table 1. All images met the criteria for VeriSee DR: single-field, 45- or 50-degree color fundus photographs, JPEG or DICOM as image formats, and a resolution of at least 1024×1024 (1 M) pixels. Such criteria met the standard for DR diagnosis using color fundus photographs. TRC-NW, TRC-NW8, TRC-NW8F, and TRC-NW8F plus used the same camera module and had the same image output formats, except for the additional function of fluorescein angiography in TRC-NW8F and TRC-NW8F plus. Similarly, the nonmyd 8 and nonmyd 8 s had the same camera module and image formats, except for the additional function of anto-fluorescence photography in Kowa nonmyd 8 s. Therefore, the camera models were classified into three categories (TRC-NW400 series, TRC-NW8 series, and nonmyd 8 series) for validation.

After image data collection, only images containing both the disc and central fovea were included. One ophthalmologist then performed the screening process to determine if the image quality was good enough for the diagnosis of DR, and images that were judged as ungradable were excluded. Finally, a total of 1407 fundus photographs were enrolled: 477 of the TRC-NW400 series, 459 of the TRC-NW8 series, and 471 of the nonmyd 8 series. This study adhered to the tenets of the Declaration of Helsinki. It was approved by the National Taiwan University Institutional Review Board (No: 201706108RIPC) with waiver of informed consent.

2.2. Grading for Diabetic Retinopathy. All fundus photographs were graded by three board-certified ophthalmologists based on the International Clinical Diabetic Retinopathy Disease Severity Scale [15]. Referable DR was defined as moderate nonproliferative DR (NPDR) or worse, and the images were judged as either "referable" or "non-referable" by each ophthalmologist. The final diagnosis was based on majority voting from three ophthalmologists, which served as the gold standard for this study.

2.3. Validation. VeriSee DR was applied to all fundus images for the diagnosis of referable DR. First, the VeriSee DR would judge if the image was gradable. VeriSee DR would further determine if the image was either "referable DR" or "non-referable" if the image was gradable; otherwise, the image would be tagged "ungradable." The diagnostic results from VeriSee DR were then compared with those of the gold standard.

2.4. Statistical Analysis. The sensitivity and specificity for the diagnosis made by VeriSee DR were calculated for each image series, and simple asymptotic formulas based on the normal approximation to the binomial distribution were used to estimate the 95% confidence intervals. The results from the three camera models and the results of the original camera model (Canon CR-2 series) were compared using the Chi-square test. The results would be considered as "qualified" if a sensitivity of more than 87% and a specificity of more than 85% were achieved.

3. Results

After enrolment, 1407 fundus photographs were collected, including 477 from the TRC-NW400 series, 459 from the TRC-NW8 series, and 471 from the nonmyd 8 series. All enrolled images (100%) were judged as "gradable" by VeriSee DR and were sent for further diagnosis of referable DR. Among the 1407 fundus photographs, 239 (17.0%) were diagnosed by ophthalmologists as "referable."

3.1. Diagnostic Accuracy among Different Camera Models. According to a previous study, the sensitivity and specificity of the original camera model (CR-2 series) were 95.0% and 89.9%, respectively. As for the results of the three camera models validated in this study, the sensitivity ranged from 89.4% to 95.7%, and the specificity ranged from 89.3% to 94.2% (Table 2). There was no significant difference in sensitivity ($p = 0.40$) or specificity ($p = 0.065$) among the four camera models. All camera models were judged as "qualified" for the use of VeriSee DR in DR diagnosis.

Table 1: Profiles of the color fundus cameras for validation with VeriSee DR.

Brand	Model	Image format	Resolution (pixels)	Angle (degrees)
Topcon	TRC-NW400	DICOM	5 M	45
	TRC-NW8 TRC-NW8F TRC-NW8F plus	JPEG, TIFF, PNG, BMP	20 M	45
Kowa	Nonmyd 8 Nonmyd 8 s	JPEG	24 M	45

Table 2: Sensitivity and specificity of VeriSee DR in diagnosing referable DR in three different camera models.

Fundus camera model	Sensitivity (95% CI)	Specificity (95% CI)
TRC-NW400	89.4% (80.6-98.2%)	94.2% (92.0-96.4%)
TRC-NW8 series	94.7% (89.6-99.8%)	90.4% (87.4-93.3%)
Nomyd 8 series	95.7% (92.1-99.4%)	89.3% (86.0-92.5%)

CI: confidence interval.

Table 3: Sensitivity and specificity of VeriSee DR in diagnosing any DR in three different camera models.

Fundus camera model	Sensitivity (95% CI)	Specificity (95% CI)
TRC-NW400	92.7% (87.5-97.9%)	61.7% (56.8-66.6%)
TRC-NW8 series	92.9% (88.4-97.4%)	73.9% (69.2-78.6%)
Nomyd 8 series	95.1% (92.0-98.2%)	56.9% (51.2-62.7%)

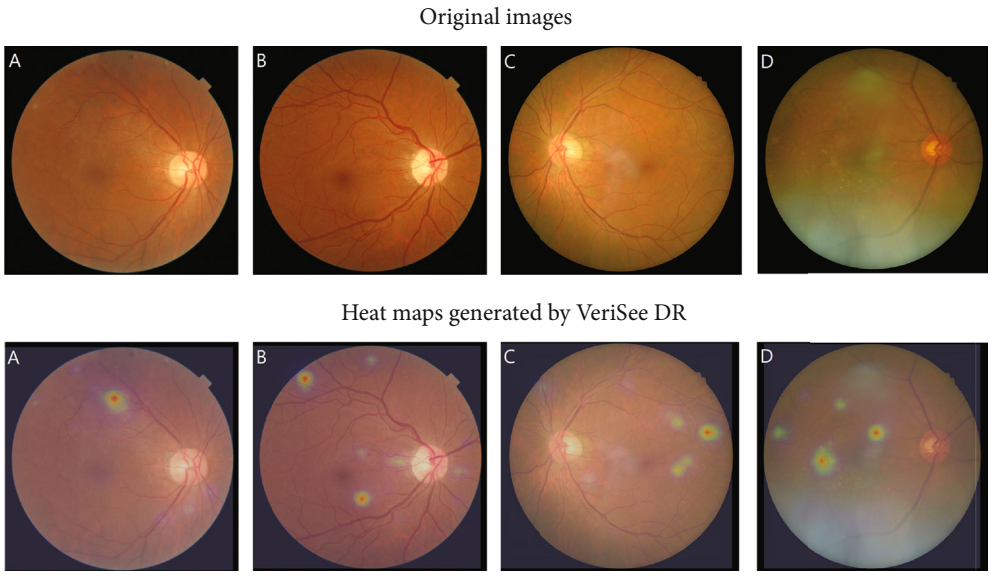

Figure 1: Original images and the heat maps generated by VeriSee DR of 4 cases of proliferative diabetic retinopathy (PDR) or severe nonproliferative diabetic retinopathy (NPDR) that were diagnosed as nonreferable DR by VeriSee DR. (a) A case of psedumed PDR with only suspected laser scars but no microaneurysm or hemorrhage, (b) a case of presumed PDR with atypical neovascularization of the disc and few microaneurysms, (c) a case of branch retinal vein occlusion which was diagnosed as severe NPDR, and (d) a case of age-related macular degeneration and old retinal vein occlusion which was diagnosed as severe NPDR.

4. Discussion

For image-assessment deep learning algorithms, capturing images using different cameras is a primary cause of misidentification [16]. FDA-approved AI-based image-assessment algorithms are usually restricted to images taken with certain machines. Therefore, cross-camera external validation is needed if image assessment software is applied to images of different camera models. In the present study, we demonstrated that the VeriSee DR could be applied to fundus photography taken with other camera models for DR screening with relatively good sensitivity and specificity and is comparable to the original camera model. The gradable rate was 100% for images taken from all camera types.

During the model development stage, a supervised training method was used for the model training of VeriSee DR. Instead of learning the explicit features of DR that have been defined, the deep learning algorithms only received information of the DR staging for each color fundus image. Another feature of the VeriSee DR is that it was pretrained with open-access datasets EYEPACS, which contained images taken from various races using various fundus cameras, and then fine-tuned using the image datasets in Taiwan, which contained images mainly from Taiwanese using the same fundus camera model. Such model training methods not only improve the accuracy but also extend the applicability to various clinical situations and camera models.

It is worth mentioning that all enrolled fundus photographs were judged as "gradable" in the present study, meaning that the VeriSee DR was able to grade all the images that were deemed gradable by the clinicians. During the model training, the algorithms of VeriSee DR also received images recognized as "ungradable" by the ophthalmologists, so it could learn to distinguish if the images were gradable or ungradable, similar to the standard of ophthalmologists. This highlights an important point that this deep learning software acquires the ability to screen images that are not perfect enough, for example, with poor contrast or artifacts. Such images are often encountered in daily practice, but they can often be graded correctly by experienced ophthalmologists. The ability of VeriSee DR to simulate human graders can increase the cost-effectiveness of DR screening. We believe that deep learning algorithms using datasets with mostly high-quality images for model training may not be truly representative of real-world conditions and could possibly result in the overestimation of screening performance [17].

The design for VeriSee DR was aimed at the detection of referable DR. Eyes with mild NPDR only will be diagnosed as nonreferable. Our previous study demonstrated that when using the original camera model (Canon CR-2 series), VeriSee DR also had good sensitivity and specificity in detecting any DR which included mild NPDR [14]. In this study, we found that the sensitivity for any DR was good for all three camera models, but the specificity was poorer, which mainly came from the overdiagnosis of mild NPDR (Table 3). One possibility is that trivial artifacts from different cameras might be misinterpreted as small microaneurysms. However, such misinterpretation was limited so that it did not interfere with the diagnosis of referable DR, in which more extensive lesions should exist.

Although the sensitivity for cross-machine external validation was high in this study, there were still 2 images of PDR and 2 severe NPDR were diagnosed as nonreferable DR by VeriSee DR. We think that these 4 cases were worth further investigation. Among these 2 images of PDR, 1 was diagnosed as PDR due to the presence of some laser scars, but no other DR-related lesions were noted. The other one was diagnosed as PDR due to neovascularization of the disc; however, the neovascularization of the disc was not typical for PDR, and only few microaneurysms were noted, which was well recognized by VeriSee DR. For the 2 cases of severe NPDR, one had dot hemorrhage, hard exudate, and intraretinal microvascular abnormality located only at superior temporal quadrant, which were well recognized by VeriSee DR; after reevaluation, the graders rediagnosed this case as BRVO with collateral vessels. The other one was diagnosed as severe NPDR due to the presence of intraretinal microvascular abnormality and hard exudate; after reevaluation, however, the graders rediagnosed it as age-related macular degeneration and old RVO since they found only collateral vessels, drusen, and RPE changes but no microaneurysm or hemorrhage in this case. The original images and heat maps generated by VeriSee DR of these four cases were shown in Figure 1. Finally, although the results of cross-machine external validation revealed high accuracy in diagnosing referable DR for all three different camera machines, it does not mean that VeriSee DR is applicable for all other camera machines that have not been validated. Further evaluation is needed before we apply VeriSee DR in the images taken from other camera machines.

In conclusion, the VeriSee DR automated screening system is applicable to a variety of color fundus cameras (TRC-NW400, TRC-NW8 series, Kowa nonmyd 8, and Kowa nonmyd 8 s) with 100% agreement among the ophthalmologists in gradability and relatively high sensitivity and specificity for the diagnosis of referable DR.

Data Availability

Dataset will be available under request.

Conflicts of Interest

Acer Inc. and National Taiwan University own the intellectual property of VeriSee DR. Y-T Hsieh received speaker's fees from Acer Inc.

Acknowledgments

M-J Tsai and Y-T Hsieh report receipt of grants from Acer Inc. for retinal fundus photography reading.

References

[1] J. W. Yau, S. L. Rogers, R. Kawasaki et al., "Global prevalence and major risk factors of diabetic retinopathy," *Diabetes Care*, vol. 35, no. 3, pp. 556–564, 2012.

[2] C. Sabanayagam, W. Yip, D. S. Ting, G. Tan, and T. Y. Wong, "Ten emerging trends in the epidemiology of diabetic retinopathy," *Ophthalmic Epidemiology*, vol. 23, no. 4, pp. 209–222, 2016.

[3] D. S. Ting, G. C. Cheung, and T. Y. Wong, "Diabetic retinopathy: global prevalence, major risk factors, screening practices and public health challenges: a review," *Clinical & Experimental Ophthalmology*, vol. 44, no. 4, pp. 260–277, 2016.

[4] A. Tufail, C. Rudisill, C. Egan et al., "Automated diabetic retinopathy image assessment software: diagnostic accuracy and cost-effectiveness compared with human graders," *Ophthalmology*, vol. 124, no. 3, pp. 343–351, 2017.

[5] M. D. Abràmoff, J. C. Folk, D. P. Han et al., "Automated analysis of retinal images for detection of referable diabetic retinopathy," *JAMA Ophthalmology*, vol. 131, no. 3, pp. 351–357, 2013.

[6] D. S. W. Ting, L. R. Pasquale, L. Peng et al., "Artificial intelligence and deep learning in ophthalmology," *The British Journal of Ophthalmology.*, vol. 103, no. 2, pp. 167–175, 2019.

[7] M. D. Abramoff, Y. Lou, A. Erginay et al., "Improved automated detection of diabetic retinopathy on a publicly available dataset through integration of deep learning," *Investigative Ophthalmology & Visual Science*, vol. 57, no. 13, pp. 5200–5206, 2016.

[8] V. Gulshan, L. Peng, M. Coram et al., "Development and validation of a deep learning algorithm for detection of diabetic retinopathy in retinal fundus photographs," *JAMA*, vol. 316, no. 22, pp. 2402–2410, 2016.

[9] R. Gargeya and T. Leng, "Automated identification of diabetic retinopathy using deep learning," *Ophthalmology*, vol. 124, no. 7, pp. 962–969, 2017.

[10] D. S. W. Ting, C. Y. Cheung, G. Lim et al., "Development and validation of a deep learning system for diabetic retinopathy and related eye diseases using retinal images from multiethnic populations with diabetes," *JAMA*, vol. 318, no. 22, pp. 2211–2223, 2017.

[11] A. A. van der Heijden, M. D. Abramoff, F. Verbraak, M. V. van Hecke, A. Liem, and G. Nijpels, "Validation of automated screening for referable diabetic retinopathy with the IDx-DR device in the Hoorn diabetes care system," *Acta Ophthalmologica*, vol. 96, no. 1, pp. 63–68, 2018.

[12] F. D. Verbraak, M. D. Abramoff, G. C. F. Bausch et al., "Diagnostic accuracy of a device for the automated detection of diabetic retinopathy in a primary care setting," *Diabetes Care*, vol. 42, no. 4, pp. 651–656, 2019.

[13] D. S. W. Ting, L. Peng, A. V. Varadarajan et al., "Deep learning in ophthalmology: the technical and clinical considerations," *Progress in Retinal and Eye Research*, vol. 72, p. 100759, 2019.

[14] Y. T. Hsieh, L. M. Chuang, Y. D. Jiang et al., "Application of deep learning image assessment software VeriSee™ for diabetic retinopathy screening," *Journal of the Formosan Medical Association*, vol. 120, no. 1, pp. 165–171, 2021.

[15] C. P. Wilkinson, F. L. Ferris 3rd, R. E. Klein et al., "Proposed international clinical diabetic retinopathy and diabetic macular edema disease severity scales," *Ophthalmology*, vol. 110, no. 9, pp. 1677–1682, 2003.

[16] Z. Zhong, L. Zheng, Z. Zheng, S. Li, and Y. Yang, "Camera style adaptation for person re-identification," 2017, http://arxiv.org/abs/1711.10295.

[17] K. B. Nielsen, M. L. Lautrup, J. K. H. Andersen, T. R. Savarimuthu, and J. Grauslund, "Deep learning-based algorithms in screening of diabetic retinopathy: a systematic review of diagnostic performance," *Ophthalmology Retina*, vol. 3, no. 4, pp. 294–304, 2019.

Hindawi
Journal of Diabetes Research
Volume 2022, Article ID 4612554, 8 pages
https://doi.org/10.1155/2022/4612554

Research Article

Application of Improved U-Net Convolutional Neural Network for Automatic Quantification of the Foveal Avascular Zone in Diabetic Macular Ischemia

Yongan Meng,[1] Hailei Lan,[2] Yuqian Hu,[1] Zailiang Chen,[2] Pingbo Ouyang,[1] and Jing Luo[1]

[1]*Department of Ophthalmology, The Second Xiangya Hospital, Central South University, Changsha 410011, China*
[2]*School of Computer Science and Engineering, Central South University, Changsha 410083, China*

Correspondence should be addressed to Jing Luo; luojing001@csu.edu.cn

Received 2 September 2021; Revised 2 October 2021; Accepted 11 February 2022; Published 26 February 2022

Academic Editor: Ali Sharif

Objectives. The foveal avascular zone (FAZ) is a biomarker for quantifying diabetic macular ischemia (DMI), to automate the identification and quantification of the FAZ in DMI, using an improved U-Net convolutional neural network (CNN) and to establish a CNN model based on optical coherence tomography angiography (OCTA) images for the same purpose. *Methods.* The FAZ boundaries on the full-thickness retina of 6×6 mm en face OCTA images of DMI and normal eyes were manually marked. Seventy percent of OCTA images were used as the training set, and ten percent of these images were used as the validation set to train the improved U-Net CNN with two attention modules. Finally, twenty percent of the OCTA images were used as the test set to evaluate the accuracy of this model relative to that of the baseline U-Net model. This model was then applied to the public data set sFAZ to compare its effectiveness with existing models at identifying and quantifying the FAZ area. *Results.* This study included 110 OCTA images. The Dice score of the FAZ area predicted by the proposed method was 0.949, the Jaccard index was 0.912, and the area correlation coefficient was 0.996. The corresponding values for the baseline U-Net were 0.940, 0.898, and 0.995, respectively, and those based on the description data set sFAZ were 0.983, 0.968, and 0.950, respectively, which were better than those previously reported based on this data set. *Conclusions.* The improved U-Net CNN was more accurate at automatically measuring the FAZ area on the OCTA images than the traditional CNN. The present model may measure the DMI index more accurately, thereby assisting in the diagnosis and prognosis of retinal vascular diseases such as diabetic retinopathy.

1. Introduction

Diabetic retinopathy (DR) is a common eye disease that affects the working population and is potentially vision- and life-threatening [1]. Macular perfusion status is important for visual function. Macular ischemia (MI) is a risk factor for DR, which leads to the destruction of the macular capillary structure, affecting treatment and prognosis [2].

The foveal avascular zone (FAZ) is a biomarker for quantifying MI in retinal vascular diseases, such as DR and retinal vein occlusion [3]. Increased size of the FAZ area may be a sign of diabetes onset and progression, providing a screening tool for assessing the progress of macular ischemia (DMI), supporting timely and effective treatment that helps prevent disease progression.

Fluorescein angiography (FA) used to be the original gold standard for FAZ measuring; however, OCTA was found to be a more reliable method in quantifying the FAZ area when compared to FA [4]. In addition, OCTA could be even superior to FA in FAZ measurement due to the fact that it is less affected by macular xanthophyll pigment shadowing by using longer wavelengths in imaging [5]. It is noninvasive, safe, and brief, and associated with excellent repeatability, and accurate determination of the FAZ area [6, 7].

However, OCTA images are detailed, complex, and contain a large volume of information, making comprehensive

interpretation time-consuming and labor-intensive. Artificial intelligence technology based on deep learning can reduce the labor and cost of image acquisition, data mining, and information extraction and improve the efficiency and accuracy of disease screening, diagnosis, and retesting. A convolutional neural network (CNN) with a U-shaped structure is effective for medical image segmentation. Previous studies [8, 9] used traditional CNNs to measure the FAZ area; however, the simple jump connection between the encoder and decoder may cause information loss, and the overall position information of the segmented object in the input image may be neglected. As a result, segmentation artifacts and blurred boundaries become prominent in difficult medical image segmentation tasks, such as the FAZ measurement. The present study is aimed at improving the U-Net CNN and to apply it to the automatic measurement of the FAZ area of DMI to help obtain accurate and clinically meaningful measurements that may improve assessment efficiency.

2. Materials and Methods

This study included patients diagnosed with DMI at the Second Xiangya Hospital of Central South University from April 2020 to April 2021. The exclusion criteria were as follows: eyes with opacity of refractive medium or other fundus diseases such as age-related macular degeneration and retinal vein occlusion. In addition, normal eyes without any fundus diseases were included. This research was approved by the Institutional Medical Ethics Board of the Second Xiangya Hospital of Central South University. All subjects underwent standard ophthalmic examination, and OCTA images were obtained using the RTVue XR Avanti (Optovue, Inc., Fremont, CA) using the AngioVue OCTA system. For OCTA images with macular edema or foveal cysts, manual correction of OCT stratification was performed first. The scanning range was 6×6 mm of the fovea; OCTA images that were clear and had scanning quality score of ≥6/10 were included; images that did not meet the standard were excluded. A total of 110 full-thickness retinal OCTA images were obtained. Two doctors manually marked the outline of FAZ area of the full-thickness retina by using ImageJ software (National Institutes of Health, Bethesda, MD, USA), and two senior doctors reviewed the images. For the divergent images, another retina specialist checked them and made the final decision to remove or include the image (Figure 1).

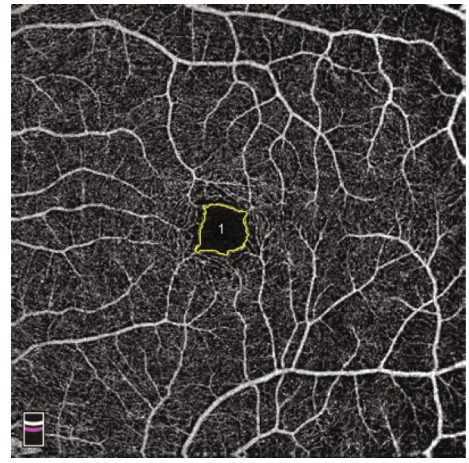

Figure 1: Manual marking of the full-thickness retinal FAZ using ImageJ software.

2.1. CNN Model Construction. In this study, an improved U-Net CNN was used to construct a new model (Figure 2). An attention mechanism was introduced into the jump connection of the traditional U-shaped structure. The baseline model was a CNN with U-Net architecture, and we added two attention modules: a spatial attention block and channel attention block.

The proposed network consisted of an encoder, a spatial attention module, decoder, and channel attention module. The basic convolution module was the basic part of the network, which was composed of a convolution layer, normalization layer, and ReLU activation layers. The encoder compressed the feature maps to obtain feature maps at different scales to extract deeper information. The encoder had four convolution modules, each of which contained two basic convolution modules and a max pooling layer. Its basic convolution module was composed of two convolution layers with a convolution kernel size of 3×3. The space attention block was connected after the encoder. Inspired by CS-Net [10], the basic convolution modules of the three convolution modules in the attention module were composed of a convolution layer with convolution kernel sizes of 1×3, 3×1, and 1×1, respectively. The original feature maps obtained by the encoder were input into these three convolution modules to obtain three feature maps. The first feature map was transposed and reshaped, then the second feature map was reshaped, and then matrix multiplication was applied to fuse the information of these two feature maps. The fusion feature maps were obtained by inputting them into the Softmax layer. Similarly, the third feature map was restored to its original shape after reshaping operation and was added to the original input feature.

After the spatial attention block was the decoder, the decoder reconstructs and restores the compressed feature map, which was composed of four upsampling modules and four channel attention modules. The three basic convolution modules of the channel attention module were composed of a convolution layer with a 3×3 kernel size. Referring to the channel attention module of CA-Net [11], after average pooling and max pooling, the feature maps were passed through the shared fully connected layers, and convolution was performed. Afterward, the elements were element-wise added, and the matrix was multiplied by the input feature map. The input feature map was added to reduce the risk of network overfitting. Finally, the network model was composed of a convolution layer with a 1×1 convolution kernel size and Softmax activation layer to generate binary segmentation results.

The description data set (sFAZ) was introduced for comparison. The data set was collected by the Hong Kong Polytechnic University Eye Clinic from 45 participants,

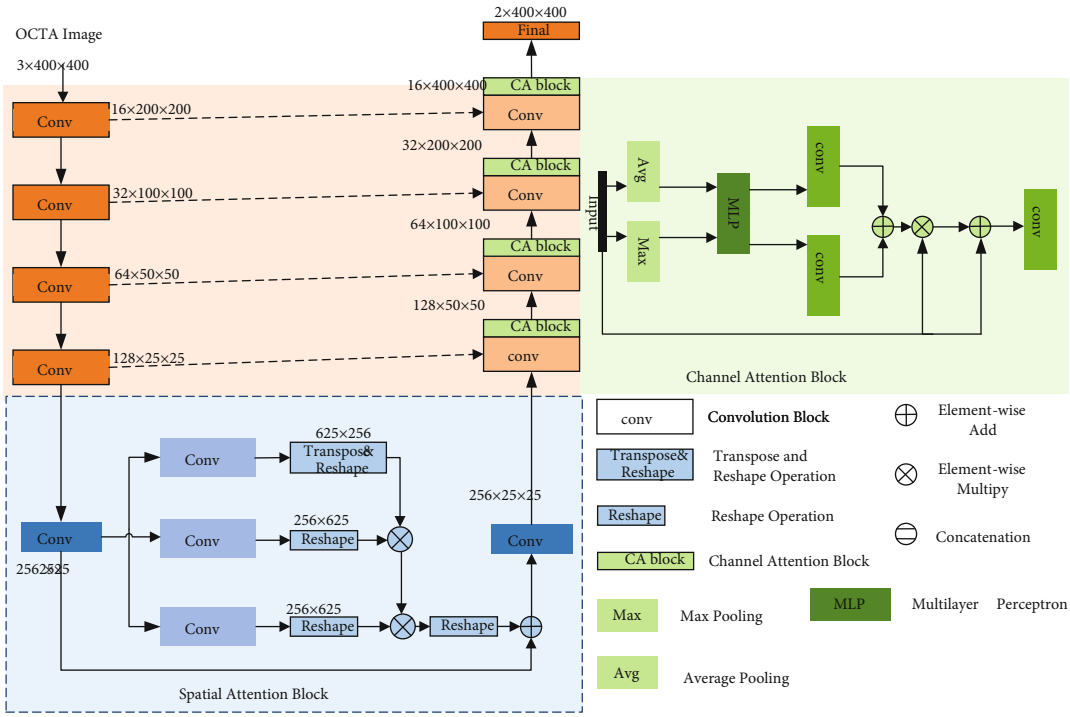

Figure 2: Construction of the convolutional neural network model.

including 22 men and 23 women, aged between 18 and 49 years. The data set contained 45 eyes of the participants with 9 OCTA images per eye and a total of 405 OCTA images.

2.2. Data Processing. Due to the equipment and operating environment conditions, the image quality of the collected data was unstable, which affected network convergence. First, image quality may be improved by adjusting contrast, brightness, and histogram equalization. Second, we randomly divided the dataset into 70%, 10%, and 20% of the images to be used for training, verification, and testing, respectively, and fivefold crossvalidation was performed. For our dataset, we performed data enhancement operations such as rotation. For the sFAZ dataset, the image size was adjusted to 400×400, and data enhancement operations such as cropping and rotation were performed.

The proposed method was implemented using the PyTorch framework. We used Adaptive Moment Estimation (Adam) for the training. The initial learning rate was 0.001, the weight decay was 10^{-8}, the batch size was 2, and the number of iterations was 200. The loss function we used was soft Dice loss, defined as equation (1):

$$\text{Dice loss} = 1 - \frac{|R_p \cap R_g|}{|R_p| + |R_g|}, \tag{1}$$

where R_p and R_g represent the value of FAZ area of algorithm prediction and ground truth, respectively. The algorithm prediction means that after the training of the CNN model is completed, the model will output a predicted value of the FAZ area by inputting the original image. Ground truth refers to the real value of FAZ area that is manually marked on the original image.

The proposed method and the baseline U-Net model [12] were used to process the dataset of our study, and the accuracy of FAZ area prediction was compared between the two methods. The proposed method was applied to the public dataset sFAZ, and the evaluation index was compared with previous studies by Guo et al. [13, 14] and Liang et al. [15].

2.3. Model Evaluation Index. We used three indicators [13, 15, 16] to evaluate the segmentation efficiency of the model for the FAZ area. The first was the Dice score (DSC), defined by equation (2):

$$\text{DSC} = \frac{|R_p \cap R_g|}{|R_p| + |R_g|}. \tag{2}$$

The second index was the Jaccard Index, defined by Equation (3):

$$\text{Jaccard}(R_p, R_g) = \frac{|R_p \cap R_g|}{|R_p| + |R_g| - |R_p \cap R_g|}. \tag{3}$$

The third index was the Pearson correlation coefficient, used to examine the correlation between the FAZ area predicted by the model and the ground truth, as defined in Equation (4):

$$\rho_{R_{p,R_g}} = \frac{\mathrm{cov}\left(R_P, R_g\right)}{\sigma_{R_p R_g}}, \quad (4)$$

where cov is the covariance, and σ is the standard deviation.

3. Results

This study included 110 OCTA images, representing 88 eyes with DMI and 32 normal eyes. The DSC of the FAZ area predicted by the proposed method was 0.948 ± 0.046, the Jaccard index was 0.912 ± 0.069, and the area correlation coefficient was 0.996 ± 004. The DSC based on the baseline U-Net CNN was 0.940 ± 0.044, the Jaccard index was 0.899 ± 0.057, and the area correlation coefficient was 0.995 ± 0.004 (Table 1). In the description data set sFAZ, the DSC of the FAZ area predicted by the proposed method was 0.983 ± 0.005, the Jaccard index was 0.968 ± 0.010, and the area correlation coefficient was 0.950 ± 0.010, which were better than those previously reported in studies using the same dataset (Table 2). Figure 3 shows the visualization results of FAZ segmentation for different degrees of DMI. The green regions of Figures 3(g)–3(l) represent the ground truth, the red regions represent the predicted FAZ area obtained by the baseline U-Net and the improved U-Net model, and the yellow regions represent the overlap between the predicted value and the real value. The larger the yellow area, the higher DSC, Jaccard, and Corr, and the smaller soft Dice loss, suggesting that the present method is more accurate than baseline U-Net for predicting the FAZ area.

Table 1: Processing results of the proposed method and baseline U-Net on our research dataset.

	Dice score	Jaccard index	Area Corr
Baseline (U-Net)	0.940; 0.044	0.899; 0.057	0.995; 0.004
Proposed method	0.948; 0.046	0.912; 0.069	0.996; 0.004

Table 2: Results of the proposed method and other studies on SFAZ dataset.

	Dice score	Jaccard index	Area Corr
2019 Guo et al. [13]	0.976, -	—	0.997, -
2020 Guo et al. [14]	0.920, 0.030	—	—
2021 Liang [15]	0.978, 0.002	0.958, 0.003	0.999, 0.001
Proposed method	0.983, 0.005	0.968, 0.010	0.950, 0.010

4. Discussion

DMI affects vision. MI may help assess disease severity, visual prognosis, and treatment progress [17, 18]; consequently, it has attracted research interest. The FAZ area is an important indicator for evaluating MI. In the present study, the size of the FAZ area was highly positively correlated with the degree of DR. The higher the severity of DR classification (non-DR diabetes, nonproliferative DR, proliferative DR), the larger the FAZ area, and the greater reduction in visual acuity. The longer the onset time, the larger is the FAZ area [2, 19]. Eyes with mild to moderate nonproliferative DR had the smallest FAZ, and eyes with proliferative DR had the largest FAZ [20]. Diabetic eyes have retinal microcirculation disturbances in the macular area, which present before the onset of retinopathy, regardless of whether DR is present, and diabetic eyes show a significant increase in the FAZ area [7]. Therefore, the FAZ enlargement is considered a biomarker of DR progression [21–24]. Fluorescein fundus angiography is a standard method for diagnosing macular edema and MI. However, due to challenges associated with contrast and fluorescein leakage, the nonperfusion area of the capillary is blurred and difficult to quantify; thus, it is suboptimal for quantifying the area of MI, including the FAZ. Previous studies have used OCTA to examine changes in patients with DR, such as enlarged FAZ area, ischemic area, microaneurysms, and neovascularization [25–28]. Quantifying the capillary network of OCTA and objectively identifying the early and subtle microvascular changes in diabetic eyes to optimize the treatment of patients are an important milestone in the clinical application of OCTA.

Progress in the application of artificial intelligence to the measurement of the FAZ area of DR [29–32] has allowed to mark the FAZ area, as the first step in the present study. OCTA images contain a large amount of data, which precludes manual marking due to time and personnel requirements. The training of a CNN model requires a few accurately labeled datasets to realize the rapid positioning and segmentation of the FAZ area, providing a method suitable for use in clinical trials. The CNN greatly accelerates the speed and accuracy of medical image segmentation; thus, many researchers have used this method to measure the FAZ area [33, 34].

However, challenges associated with the use of this method remain. First, many studies on the FAZ area segmentation in OCTA images were performed in healthy subjects [35–37], while the incidence of signal noise and artifacts in OCTA imaging of diabetic patients is higher than that in their counterparts; consequently, most of the FAZ measurements in OCTA images of diabetic eyes have low accuracy [37, 38]. In medical image segmentation tasks, the most commonly used CNN model is based on U-Net [12], which consists of the contraction path of the capture context and symmetric expansion path to achieve precise positioning. The U-shape network simply combines the shallow feature map of the encoder with the deep feature map corresponding to the decoder and inputs it into the next layer. However, the cumulative stack of feature maps creates redundant information, which interferes with the network model learning useful knowledge for segmentation tasks. Guo et al. [13] used a U-Net CNN model to automatically segment and quantify the superficial FAZ area based on OCTA images and compared the automatic segmentation results with the ground truth; the maximum average DSC was 0.976, and the correlation coefficient between the area calculated by the automatic segmentation results and that calculated by the ground truth was 0.997. Liang et al. [15] evaluated two public superficial OCTA image datasets using

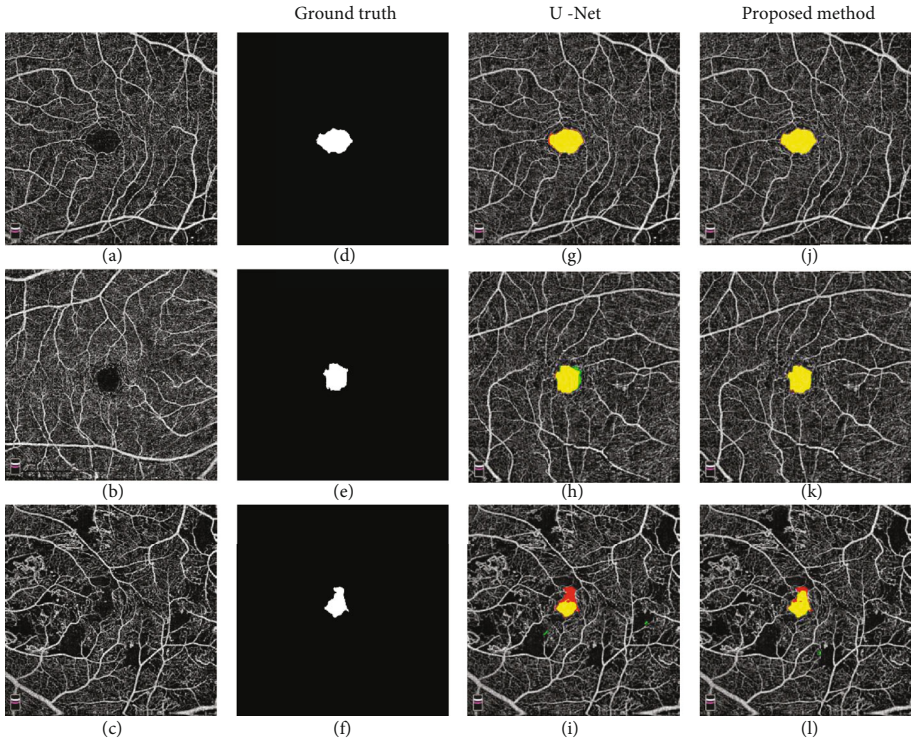

Figure 3: Visualization results for FAZ segmentation. (a)–(c) are the original DR map of different severity. (d)–(f) are manually labeled FAZ area as ground truth. (g)–(i) are the prediction result of traditional U-Net. (j)–(l) are the prediction result of the proposed method. The green, red, and yellow regions represent the ground truth, the predicted area, and the overlap of the two areas, respectively.

the U-Net structure based on image reconstruction, and their DSC values were 0.9263 and 0.9784, respectively. Previous studies have shown that with the progress of network training, the distribution change of data output at each layer of the U-Net network reduced the generalization ability and training speed of the network. Traditional U-Net required development to improve the accuracy of image segmentation and automatic quantification.

For complex feature map information, although the network can provide accurate segmentation results, it is unable to determine a network feature selection strategy. Because of its poor interpretability, the CNN model is called the "black box" [39]. The attention mechanism is designed to imitate human attention, help the network focus on information that contributes greatly to the segmentation task, and visualize attention through the convolution kernel weight map of the module to enhance the interpretability of the network. The attention module has many forms, which can be divided into channel attention, spatial attention, and scale attention according to its characteristics [10]. Channel attention and spatial attention modules were used in the present study. The channel attention module selects feature maps after the fusion of the encoder and decoder, and the spatial attention module extracts position information of the segmented object from the feature map of the connection part of the decoder and encoder. The spatial attention module mainly obtains global information of the feature map through operations such as transformation and reshape and aggregates the information through matrix multiplication, thereby promoting the network to learn the location and background of the segmented objects in the feature map. The spatial attention block we use can learn the weight map of the feature according to the data feedback. It can give low weight to noise and artifacts, but give high weight to the pixels in the FAZ region. After multiplying with the original feature map, it can effectively suppress noise and artifacts. The four channel attention modules compress the connected low-level and high-level information, activate beneficial information, and suppress redundant information by data learning [11]. The segmentation results are refined by extracting the maximum connected region and filling holes. According to the obtained binary segmentation results, the area of FAZ is calculated by the pixel proportion of FAZ and the scale. In the follow-up study, the perimeter of FAZ can be calculated by counting the edge pixel value of FAZ. Using these two parameters, the roundness can be calculated by the formula of roundness, so that the FAZ area can be measured by CNN in more detail.

In this study, the channel attention and spatial attention modules were introduced into the U-Net CNN to automatically quantify the FAZ area of the DR in full-thickness retinal OCTA. The combination of the two modules effectively improved the feature selection ability of the network. In the dataset we collected, the best DSC was 0.981, which was better than that in previous studies based on U-Net [12]. In the public dataset sFAZ, the DSC of the proposed

method was 0.948, which was better than those previously reported by Guo et al. and Liang et al. [13–15].

In the measurement of the FAZ area, some previous studies [24] only detected the superficial retinal capillary plexus (SCP) or deep retinal capillary plexus (DCP) index; however, for the determination of MI, a single-layer index is not accurate. Therefore, we measured the FAZ area of the full-thickness retina, which can more comprehensively reflect the real macular perfusion state. Arya et al. [40] found that measurements on DCP or SCP are susceptible to segmentation errors, while vascular measurements on the full-thickness retina have higher repeatability. Because different OCT instruments have different retinal layering algorithms for the retina assessment, the definitions of the start and end points of the SCP and DCP are different, which precludes the analysis the OCT and OCTA images obtained by different devices in a unified manner [41–44]. The start and end points of the full-thickness retina measurements are essentially the same for different devices. Therefore, Custo et al. [23] believed that full-thickness retinal OCTA images are repeatable and reproducible in the eyes with or without diabetic macular edema and using different devices, and that it is more straightforward and accurate to reproduce them in clinical and ophthalmic reading centers.

Furthermore, the built-in software of the OCTA instrument is more accurate in measuring the FAZ area of normal eyes, but for patients with macular edema in the DR, the OCTA layering deviation may be caused by the edema, which affects the determination of OCTA images by the CNN model. Sorour et al. [45] thought that using the default full retinal projection may lead to the erroneous segmentation duo to the existence of DME, as the DME has little effect of the RPE; so, they customized the lower boundary of the full retina slab according to the RPE to get more accurate results. Reza et al. [9] manually adjusted the automatic stratification of OCT and found that it could effectively reduce the large error caused by the automatic measurement of built-in software. Therefore, in our study, we adopted a strategy of manually adjusting OCT stratification for OCTA images with macular edema or foveal cysts.

This study had several limitations. First, because some DMI patients have concomitant cataracts and/or severe diabetic macular edema, low-quality OCTA images were excluded from this study; the sample size was small, and the grading of different DR degrees was not performed, which limits the learning ability of the CNN model. In future research, increasing the sample size and making a more detailed division may produce more powerful results; second, in addition to DR, MI will appear in many ischemic retinopathies; future studies should account for more diseases and OCTA indicators to improve the automatic quantitative accuracy of a model for MI.

5. Conclusions

The present study has proposed a new CNN model to automatically measure the FAZ area of the DMI, which performed better than did the baseline U-Net model. The present model may improve the diagnosis and prognosis of MI in retinal diseases.

Data Availability

Data are available upon request from authors.

Conflicts of Interest

The authors declare that there is no conflict of interest regarding the publication of this paper.

Acknowledgments

This work was supported by the Fundamental Research Funds for the Central Universities of Central South University (No. 2021zzts0373), the National Natural Science Foundation of China (Nos. 61972419 and 61672542), the Natural Science Foundation of Hunan Province of China (No.2020JJ4120), and the Hunan Provincial Health Commission Scientific Research Project (No. 202207023398).

References

[1] C. Sabanayagam, R. Banu, M. Chee et al., "Incidence and progression of diabetic retinopathy: a systematic review," *The lancet Diabetes & endocrinology*, vol. 7, no. 2, pp. 140–149, 2019.

[2] W. Samara, A. Shahlaee, M. Adam et al., "Quantification of diabetic macular ischemia using optical coherence tomography angiography and its relationship with visual acuity," *Ophthalmology*, vol. 124, no. 2, pp. 235–244, 2017.

[3] J. Werner, F. Böhm, G. Lang, J. Dreyhaupt, G. Lang, and C. Enders, "Comparison of foveal avascular zone between optical coherence tomography angiography and fluorescein angiography in patients with retinal vein occlusion," *PLoS One*, vol. 14, no. 6, article e0217849, 2019.

[4] A. G. Elnahry and D. J. Ramsey, "Automated image alignment for comparing microvascular changes detected by fluorescein angiography and optical coherence tomography angiography in diabetic retinopathy," *Seminars in Ophthalmology*, vol. 36, no. 8, pp. 757–764, 2021.

[5] A. G. Elnahry and D. J. Ramsey, "Optical coherence tomography angiography imaging of the retinal microvasculature is unimpeded by macular xanthophyll pigment," *Clinical & Experimental Ophthalmology*, vol. 48, no. 7, pp. 1012–1014, 2020.

[6] M. Ashraf, P. Nesper, L. Jampol, F. Yu, and A. Fawzi, "Statistical model of optical coherence tomography angiography parameters that correlate with severity of diabetic retinopathy," *Investigative Ophthalmology & Visual Science*, vol. 59, no. 10, pp. 4292–4298, 2018.

[7] N. Takase, M. Nozaki, A. Kato, H. Ozeki, M. Yoshida, and Y. Ogura, "Enlargement of foveal avascular zone in diabetic eyes evaluated by en face optical coherence tomography angiography," *Retina (Philadelphia, Pa)*, vol. 35, no. 11, pp. 2377–2383, 2015.

[8] J. Nunez do Rio, P. Sen, R. Rasheed et al., "Deep learning-based segmentation and quantification of retinal capillary non-perfusion on ultra-wide-field retinal fluorescein angiography," *Journal of Clinical Medicine*, vol. 9, no. 8, p. 2537, 2020.

[9] R. Mirshahi, P. Anvari, H. Riazi-Esfahani, M. Sardarinia, M. Naseripour, and K. Falavarjani, "Foveal avascular zone segmentation in optical coherence tomography angiography images using a deep learning approach," *Scientific Reports*, vol. 11, no. 1, p. 1031, 2021.

[10] L. Mou, Y. Zhao, L. Chen et al., *CS-Net: Channel and Spatial Attention Network for Curvilinear Structure Segmentation*, vol. 11764, Springer International Publishing, 2019.

[11] R. Gu, G. Wang, T. Song et al., "CA-net: comprehensive attention convolutional neural networks for explainable medical image segmentation," *IEEE Transactions on Medical Imaging*, vol. 40, no. 2, pp. 699–711, 2021.

[12] O. Ronneberger, P. Fischer, and T. Brox, *U-Net: Convolutional Networks for Biomedical Image Segmentation*, vol. 9351, Springer International Publishing, 2015.

[13] M. Guo, M. Zhao, A. Cheong, H. Dai, A. Lam, and Y. Zhou, "Automatic quantification of superficial foveal avascular zone in optical coherence tomography angiography implemented with deep learning," *Visual computing for industry, biomedicine, and art*, vol. 2, no. 1, p. 21, 2019.

[14] M. L. Guo, M. Zhao, A. M. Y. Cheong et al., "Can deep learning improve the automatic segmentation of deep foveal avascular zone in optical coherence tomography angiography?," *Biomedical Signal Processing and Control*, vol. 66, p. 102456, 2021.

[15] Z. Liang, J. Zhang, and C. An, "Foveal avascular zone segmentation of Octa images using deep learning approach with unsupervised vessel segmentation," in *ICASSP 2021-2021 IEEE International Conference on Acoustics, Speech and Signal Processing (ICASSP)*, pp. 1200–1204, Toronto, ON, Canada, 2021.

[16] M. Li, Y. Wang, Z. Ji, W. Fan, S. Yuan, and Q. Chen, "Fast and robust fovea detection framework for OCT images based on foveal avascular zone segmentation," *Osa Continuum*, vol. 3, no. 3, pp. 528–541, 2020.

[17] Z. Zhu, Y. Liang, B. Yan et al., "Clinical effect of conbercept on improving diabetic macular ischemia by OCT angiography," *BMC Ophthalmology*, vol. 20, no. 1, p. 382, 2020.

[18] A. Dastiridou, K. Karathanou, P. Riga et al., "OCT angiography study of the macula in patients with diabetic macular edema treated with intravitreal aflibercept," *Ocular Immunology and Inflammation*, vol. 29, pp. 926–931, 2021.

[19] M. Al-Sheikh, H. Akil, M. Pfau, and S. Sadda, "Swept-source OCT angiography imaging of the foveal avascular zone and macular capillary network density in diabetic retinopathy," *Investigative Ophthalmology & Visual Science*, vol. 57, no. 8, pp. 3907–3913, 2016.

[20] G. Lynch, J. Romo, R. Linderman et al., "Within-subject assessment of foveal avascular zone enlargement in different stages of diabetic retinopathy using en face OCT reflectance and OCT angiography," *Biomedical Optics Express*, vol. 9, no. 12, pp. 5982–5996, 2018.

[21] J. Zhang, F. Tang, C. Cheung, X. Chen, and H. Chen, "Different effect of media opacity on automated and manual measurement of foveal avascular zone of optical coherence tomography angiographies," *The British Journal of Ophthalmology*, vol. 105, no. 6, pp. 812–818, 2021.

[22] R. Mastropasqua, L. Toto, A. Mastropasqua et al., "Foveal avascular zone area and parafoveal vessel density measurements in different stages of diabetic retinopathy by optical coherence tomography angiography," *International Journal of Ophthalmology*, vol. 10, no. 10, pp. 1545–1551, 2017.

[23] E. Custo Greig, M. Brigell, F. Cao et al., "Macular and peripapillary optical coherence tomography angiography metrics predict progression in diabetic retinopathy: a sub-analysis of TIME-2b study data," *American Journal of Ophthalmology*, vol. 219, pp. 66–76, 2020.

[24] Z. Sun, F. Tang, R. Wong et al., "OCT angiography metrics predict progression of diabetic retinopathy and development of diabetic macular edema: a prospective study," *Ophthalmology*, vol. 126, no. 12, pp. 1675–1684, 2019.

[25] F. Freiberg, M. Pfau, J. Wons, M. Wirth, M. Becker, and S. Michels, "Optical coherence tomography angiography of the foveal avascular zone in diabetic retinopathy," *Graefe's archive for clinical and experimental ophthalmology = Albrecht von Graefes Archiv fur klinische und experimentelle Ophthalmologie*, vol. 254, no. 6, pp. 1051–1058, 2016.

[26] D. Bhanushali, N. Anegondi, S. Gadde et al., "Linking retinal microvasculature features with severity of diabetic retinopathy using optical coherence tomography angiography," *Investigative Ophthalmology & Visual Science*, vol. 57, no. 9, p. OCT519-525, 2016.

[27] Z. Sun, D. Yang, Z. Tang, D. Ng, and C. Cheung, "Optical coherence tomography angiography in diabetic retinopathy: an updated review," *Eye (London, England)*, vol. 35, no. 1, pp. 149–161, 2021.

[28] Y. Shin, K. Nam, S. Lee et al., "Peripapillary microvasculature in patients with diabetes mellitus: an optical coherence tomography angiography study," *Scientific Reports*, vol. 9, no. 1, p. 15814, 2019.

[29] J. Wang, T. Hormel, Q. You et al., "Robust non-perfusion area detection in three retinal plexuses using convolutional neural network in OCT angiography," *Biomedical Optics Express*, vol. 11, no. 1, pp. 330–345, 2020.

[30] N. Asiri, M. Hussain, F. Al Adel, and N. Alzaidi, "Deep learning based computer-aided diagnosis systems for diabetic retinopathy: a survey," *Artificial Intelligence in Medicine*, vol. 99, article 101701, 2019.

[31] S. Kuwayama, Y. Ayatsuka, D. Yanagisono et al., "Automated detection of macular diseases by optical coherence tomography and artificial intelligence machine learning of optical coherence tomography images," *Journal of Ophthalmology*, vol. 2019, 6319587 pages, 2019.

[32] S. Rêgo, M. Dutra-Medeiros, F. Soares, and M. Monteiro-Soares, "Screening for diabetic retinopathy using an automated diagnostic system based on deep learning: diagnostic accuracy assessment," *Ophthalmologica Journal international d'ophtalmologie International journal of ophthalmology Zeitschrift fur Augenheilkunde*, vol. 244, no. 3, pp. 250–257, 2021.

[33] S. Gayathri, V. Gopi, and P. Palanisamy, "Diabetic retinopathy classification based on multipath CNN and machine learning classifiers," *Physical and engineering sciences in medicine*, vol. 44, no. 3, pp. 639–653, 2021.

[34] A. Galdran, J. Chelbi, R. Kobi et al., "Non-uniform label smoothing for diabetic retinopathy grading from retinal fundus images with deep neural networks," *Translational Vision Science & Technology*, vol. 9, no. 2, p. 34, 2020.

[35] H. Ishii, T. Shoji, Y. Yoshikawa, J. Kanno, H. Ibuki, and K. Shinoda, "Automated measurement of the foveal avascular zone in swept-source optical coherence tomography angiography images," *Translational Vision Science & Technology*, vol. 8, no. 3, p. 28, 2019.

[36] A. Lin, D. Fang, C. Li, C. Cheung, and H. Chen, "Improved automated foveal avascular zone measurement in cirrus

optical coherence tomography angiography using the level sets macro," *Translational Vision Science & Technology*, vol. 9, no. 12, p. 20, 2020.

[37] E. J. Carmona, M. Diaz, J. Novo, and M. Ortega, "Modeling, localization, and segmentation of the foveal avascular zone on retinal OCT-angiography images," *IEEE Access*, vol. 8, pp. 152223–152238, 2020.

[38] M. Díaz, J. Novo, P. Cutrín, F. Gómez-Ulla, M. Penedo, and M. Ortega, "Automatic segmentation of the foveal avascular zone in ophthalmological OCT-A images," *PLoS One*, vol. 14, no. 2, article e0212364, 2019.

[39] S. C. Pang, A. N. Du, M. A. Orgun, Y. Y. Wang, and Z. M. Yu, "Tumor attention networks: better feature selection, better tumor segmentation," *Neural Networks*, vol. 140, pp. 203–222, 2021.

[40] M. Arya, C. Rebhun, A. Alibhai et al., "Parafoveal retinal vessel density assessment by optical coherence tomography angiography in healthy eyes," *Ophthalmic Surgery, Lasers & Imaging Retina*, vol. 49, no. 10, pp. S5–S17, 2018.

[41] A. Kim, Z. Chu, A. Shahidzadeh, R. Wang, C. Puliafito, and A. Kashani, "Quantifying microvascular density and morphology in diabetic retinopathy using spectral-domain optical coherence tomography angiography," *Investigative Ophthalmology & Visual Science*, vol. 57, no. 9, p. OCT362-370, 2016.

[42] S. Agemy, N. Scripsema, C. Shah et al., "Retinal vascular perfusion density mapping using optical coherence tomography angiography in normals and diabetic retinopathy patients," *Retina (Philadelphia, Pa)*, vol. 35, no. 11, pp. 2353–2363, 2015.

[43] M. Lupidi, F. Coscas, C. Cagini et al., "Automated quantitative analysis of retinal microvasculature in normal eyes on optical coherence tomography angiography," *American Journal of Ophthalmology*, vol. 169, pp. 9–23, 2016.

[44] J. Yang, E. Wang, M. Yuan, and Y. Chen, "Three-dimensional choroidal vascularity index in acute central serous chorioretinopathy using swept-source optical coherence tomography," *Graefe's archive for clinical and experimental ophthalmology = Albrecht von Graefes Archiv fur klinische und experimentelle Ophthalmologie*, vol. 258, no. 2, pp. 241–247, 2020.

[45] O. A. Sorour, M. Elsheikh, S. Chen et al., "Mean macular intercapillary area in eyes with diabetic macular oedema after anti-vascular endothelial growth factor therapy and its association with treatment response," *Clinical & Experimental Ophthalmology*, vol. 49, no. 7, pp. 714–723, 2021.

Hindawi
Journal of Diabetes Research
Volume 2022, Article ID 1516668, 9 pages
https://doi.org/10.1155/2022/1516668

Research Article

Investigation of Retinal Microcirculation in Diabetic Patients Using Adaptive Optics Ophthalmoscopy and Optical Coherence Angiography

Florian Baltă,[1,2,3] Irina-Elena Cristescu,[3,4] Andrada-Elena Mirescu,[2,5] George Baltă,[2] Mihail Zemba,[1,6] and Ioana Teodora Tofolean[1,3]

[1]*"Carol Davila" University of Medicine and Pharmacy, 050474 Bucharest, Romania*
[2]*Clinical Emergency Eye Hospital, 030167 Bucharest, Romania*
[3]*"Retina" Clinic, 014142 Bucharest, Romania*
[4]*Manchester Royal Eye Hospital, Manchester University Hospitals NHS Foundation Trust, Manchester, UK*
[5]*Department of Ophthalmology, "Ovidius" University of Medicine, 900470 Constanta, Romania*
[6]*Department of Ophthalmology, "Dr. Carol Davila" Central Military Emergency University Hospital, 010825 Bucharest, Romania*

Correspondence should be addressed to Irina-Elena Cristescu; cristescu.irina@gmail.com

Received 3 September 2021; Revised 21 November 2021; Accepted 3 January 2022; Published 19 January 2022

Academic Editor: Yijun Hu

The current research approaches the retinal microvasculature of healthy volunteers (17 subjects), patients with diabetes mellitus without retinopathy (19 subjects), and of diabetic patients with nonproliferative (17 subjects) and proliferative (21 subjects) diabetic retinopathy, by using adaptive optics ophthalmoscopy and optical coherence ophthalmoscopy angiography. For each imaging technique, several vascular parameters have been calculated in order to achieve a comparative analysis of these imaging biomarkers between the four studied groups. The results suggest that diabetic patients with or without diabetic retinopathy prove signs of retinal arteriole structural alterations, mainly showed by altered values of wall to lumen ratio, calculated for the superior or inferior temporal branch of the central retinal artery, near the optic nerve head, and significant changes of the vascular density in the retinal superficial capillary plexus. Both adaptive optics ophthalmoscopy and optical coherence ophthalmoscopy angiography are providing useful information about the retinal microvasculature from early onset of diabetic disease, having a promising diagnostic and prognostic role in the future.

1. Introduction

Retina is, regarding its metabolism, one of the most active tissues in the human body, due to increased consumption of oxygen and nutrients. Nowadays, there are more and more available data about the pathogenesis of complex retinal diseases [1–3]. Under normal conditions, the ocular system adapts in order to ensure the retinal metabolic demands, thus providing an appropriate visual function.

Several pathologies, such as diabetes mellitus (DM) [2], arterial hypertension, and other cardiovascular disorders [3], target the vessels, determining morphological and functional changes, which can be essentially mirrored by the status of the retinal vessels.

One of the leading causes of vision loss and blindness worldwide is diabetic retinopathy (DR), a microvascular complication of DM [2]. The Early Treatment Diabetic Retinopathy Study (ETDRS) considers the vascular lesions in the retinal layers to be the hallmark of DR [4, 5]. Furthermore, several papers have shown that among the first changes spotted in the retina of diabetic patients are the ones in the vascular calibres [6–8]. Therefore, retinal vessel parameters may become valuable biomarkers for diabetic retinopathy [8].

In order to structurally and functionally assess a microvascular network, both the topology and the geometric abnormalities are to be investigated [9]. The retinal microcirculation has a vascular pattern similar to a fractal, each

part providing similar characteristics with the main structure. A decreased fractal dimension has been shown to be associated with diabetic retinopathy [5, 10]. In order to appreciate the geometry of a vascular network, both the length and the diameters of the vessels are of great interest, in order to calculate different derived parameters.

The current research approaches the retinal microvasculature of healthy volunteers, patients with DM without DR and of diabetic patients with nonproliferative and proliferative diabetic retinopathy, by using adaptive optics ophthalmoscopy (AOO) and optical coherence tomography angiography (OCT-A). These two noninvasive techniques are both powerful and exhibit complementary information regarding the retinal vascular network. On one hand, AOO focuses on the arteriolar structure, while OCT-A delivers high-resolution volumetric angiography images, using motion contrast in seconds. For each imaging technique, several vascular parameters have been calculated in order to achieve a comparative analysis of these imaging biomarkers between the four studied groups.

Adaptive optics ophthalmoscopy is a modern device that uses a cutting-edge technique allowing the visualisation and assessment of the retinal microvasculature, in a noninvasive manner [11]. When using AOO, the retinal arterioles lumen appears to have a bright reflex, while the walls correspond to the darker neighbouring regions. The wall thickness of the blood vessels depends on vessels' size, with large lumens requiring thicker walls. The ratio between the wall thickness and the lumen diameter is known as the wall to lumen ratio (WLR). Among other vascular parameters, WLR has been shown to be significantly correlated with the severity of the diabetic retinopathy [12].

In the recent years, optical coherence tomography angiography has become a valuable tool for diabetic patients, competing with the gold standard fluorescein angiography by allowing the noninvasive quantification of several retinal vascular parameters (vessel density, vascular length density, vessel diameter index, area of the foveal avascular zone, etc.). These quantitative measures may be able to detect changes with the severity and progress of DR.

2. Materials and Methods

2.1. Study Participants. The current research includes seventy-four eyes from seventy-four patients consulted in the Retina Clinic, Bucharest, in 2019 and 2020. According to the ETDRS guidelines [13], the study population was divided into 4 groups: healthy volunteers (17 eyes), subjects diagnosed with diabetes mellitus without retinopathy (19 eyes), diabetic patients with nonproliferative retinopathy (NPDR) (17 eyes), and diabetic patients with proliferative retinopathy (PDR) (21 eyes).

All the participants were adult Caucasians (>18 years old), with small refractive errors (less than 3 spherical diopters; less than 2.5 cylindrical diopters), without significant ocular media opacities or medical history (except for DM and diabetic retinopathy related procedures).

2.2. Subjects' Examination. All participants were conducted a complete ophthalmologic evaluation, namely, medical history, best corrected visual acuity (BCVA), intraocular pressure (IOP), and slit lamp examination of the anterior and posterior segments. In order to better visualise the eye fundus, topical administration of Phenylephrine 10% and Tropicamide 1% was used in patients with relatively small pupillary diameters (<4.5 mm).

rtx1™ adaptive optics retinal camera (Imagine Eyes, Orsay, France) and a swept-source OCT device (DRI OCT Triton, TOPCON Inc., Tokyo, Japan) were both used for microcirculation assessment. Optical biometry (Aladdin, TOPCON Inc., Tokyo, Japan) was used in order to measure the axial length of the included eyes.

2.3. Image Processing. Adaptive optics images were analysed using manufacturer's software (AO detect artery, Imagine Eyes, France) that automatically generates the following vascular parameters for the selected regions of interest: vessel diameter (VD), lumen diameter (LD), mean wall thickness (WT), wall to lumen ratio (WLR), and cross sectional area of the vascular wall (WCSA) (Figure 1).

The OCT instrument software (IMAGEnet® 6, TOPCON Inc.) provided, after automated layer segmentation and projection artefacts exclusion, 3×3 mm *en face* images for the superficial retinal layer (from 2.6 μm below the internal limiting membrane to 15.6 μm below the interface of the inner plexiform layer and inner nuclear layer) (Figure 2).

ImageJ software (Version 1.8; National Institutes of Health, Bethesda, MD, USA) was used in order to calculate the OCT-A related vascular parameters: vascular density along the superficial capillary plexus (SPD), as well as the foveal avascular zone area (FAZ) measured in the superficial capillary plexus (Figure 3). Vascular density is, by definition, the percentage represented by vessels in a selected area [14]. In order to be calculated, the *en face* images were first transformed into 8-bit grey scale pictures, which were further binarised using an automated thresholding algorithm (mean). FAZ was manually sketched and further adjusted for axial length [12].

2.4. Statistical Analysis. IBM SPSS Statistics software (Version 23; Armonk, NY: IBM Corp) was used in order to perform descriptive statistics on the collected data. All the results are expressed as mean ± standard deviation. p values under 0.05 are considered statistically significant.

Shapiro-Wilk's was the test of choice for normality assessment. Groups' characteristics were compared applying the Kruskal Wallis test or one-way ANOVA analysis. Vessels' parameters were compared between the four groups using one-way ANOVA test, followed by Tukey (for data with equal variances) or Games-Howell (for data with unequal variances) post hoc analysis. Moreover, one-way ANCOVA was conducted having age as a covariate, followed by post hoc analysis with a Bonferroni adjustment. A Spearman's rank-order correlation was applied to determine whether there were any correlations between BCVA and the vascular parameters.

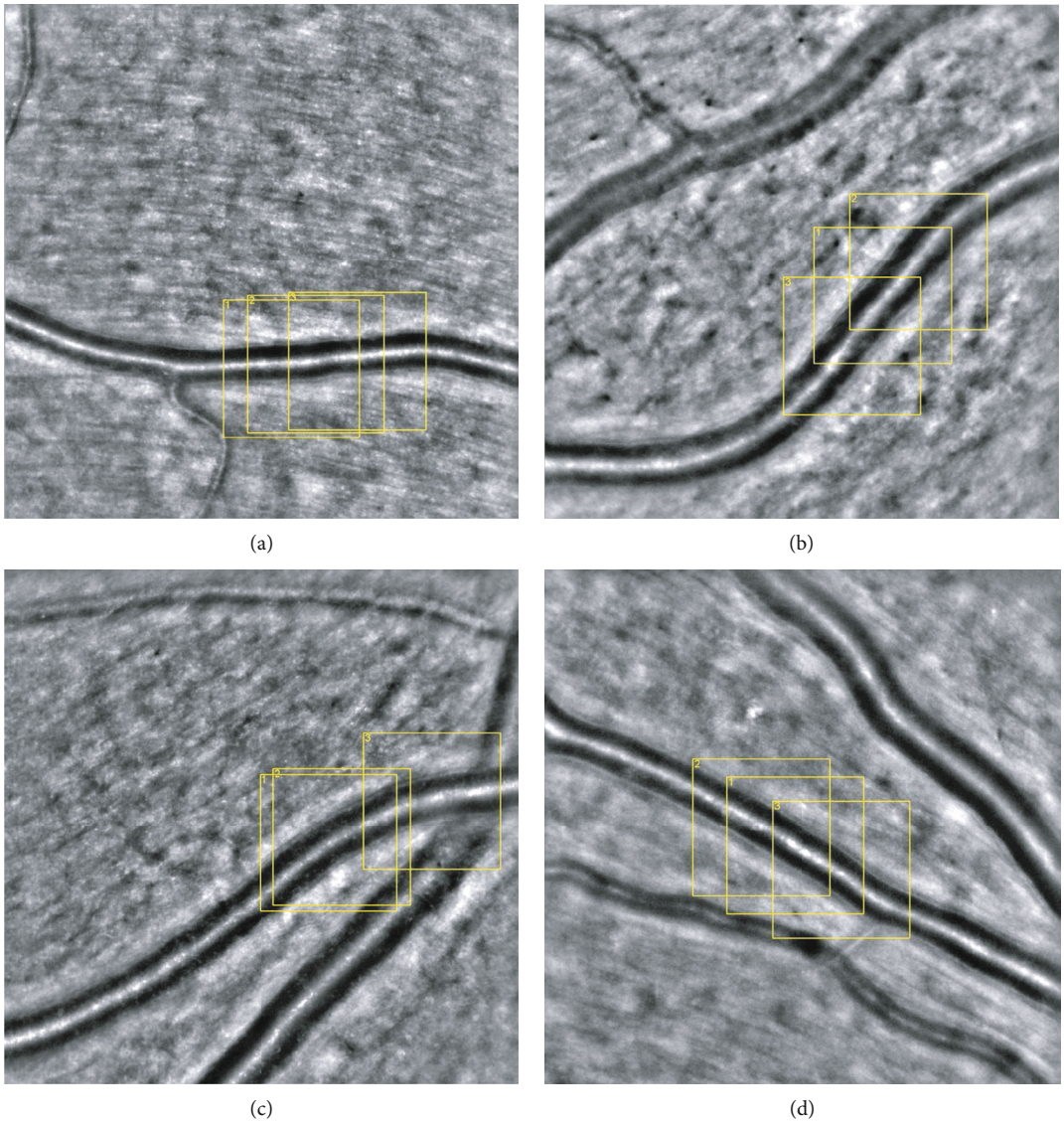

Figure 1: Superior/inferior temporal branch of the central retinal artery—adaptive optics ophthalmoscopy image. (a) Healthy volunteer. (b) Diabetic patient without retinopathy. (c) Diabetic patient with nonproliferative retinopathy. (d) Diabetic patient with proliferative retinopathy. Employing AOdetect software, the mean wall to lumen ratio was calculated from the three selected regions of interest, for each time landmark (100 μm width and height each).

3. Results and Discussion

74 eyes from 57 diabetic patients (36 males and 21 females; 47 subjects with type II DM and 10 subjects with type I DM) and 17 healthy volunteers (8 males and 9 females) were enrolled in the current study (Table 1). 26 diabetic patients are insulin-dependent. The mean age of all the study participants was 52.81 ± 15.13 years, while the mean duration of diabetes mellitus in the three groups with diabetic subjects was 9.73 ± 9.67 years. There were significant differences between the controls and each diabetic group (no DR, NPDR, and PDR groups, respectively) considering the age ($p = 0.018$, 0.009, and 0.016, respectively). Significant differences were also found between the number of patients with diabetic maculopathy in the no DR group and NPDR ($p < 0.001$) and PDR group ($p = 0.009$), respectively. BCVA was significantly lower in the RDP group when compared to the no DR ($p = 0.003$) and control group ($p < 0.001$). The control group had a significant higher BCVA than the NPDR group ($p = 0.002$).

21 out of 38 eyes with diabetic retinopathy have associated maculopathy, 19 eyes underwent panretinal photocoagulation (PRP), 22 patients were injected anti-VEGF molecules, and 4 patients underwent pars plana vitrectomy (PPV), all ophthalmic interventions dating more than 6 months before the inclusion into the current study.

There were no significant differences between the groups concerning the values of VD ($F(3, 37.487) = 1.684$, $p = 0.187$), LD ($F(3, 36.899) = 1.142$, $p = 0.345$), and WCSA ($F(3, 73) = 2.739$, $p = 0.050$). WLR was found to have a significant variation ($F(3, 37.065) = 5.992$, $p = 0.002$) between the groups, according to the one-way Welch ANOVA test.

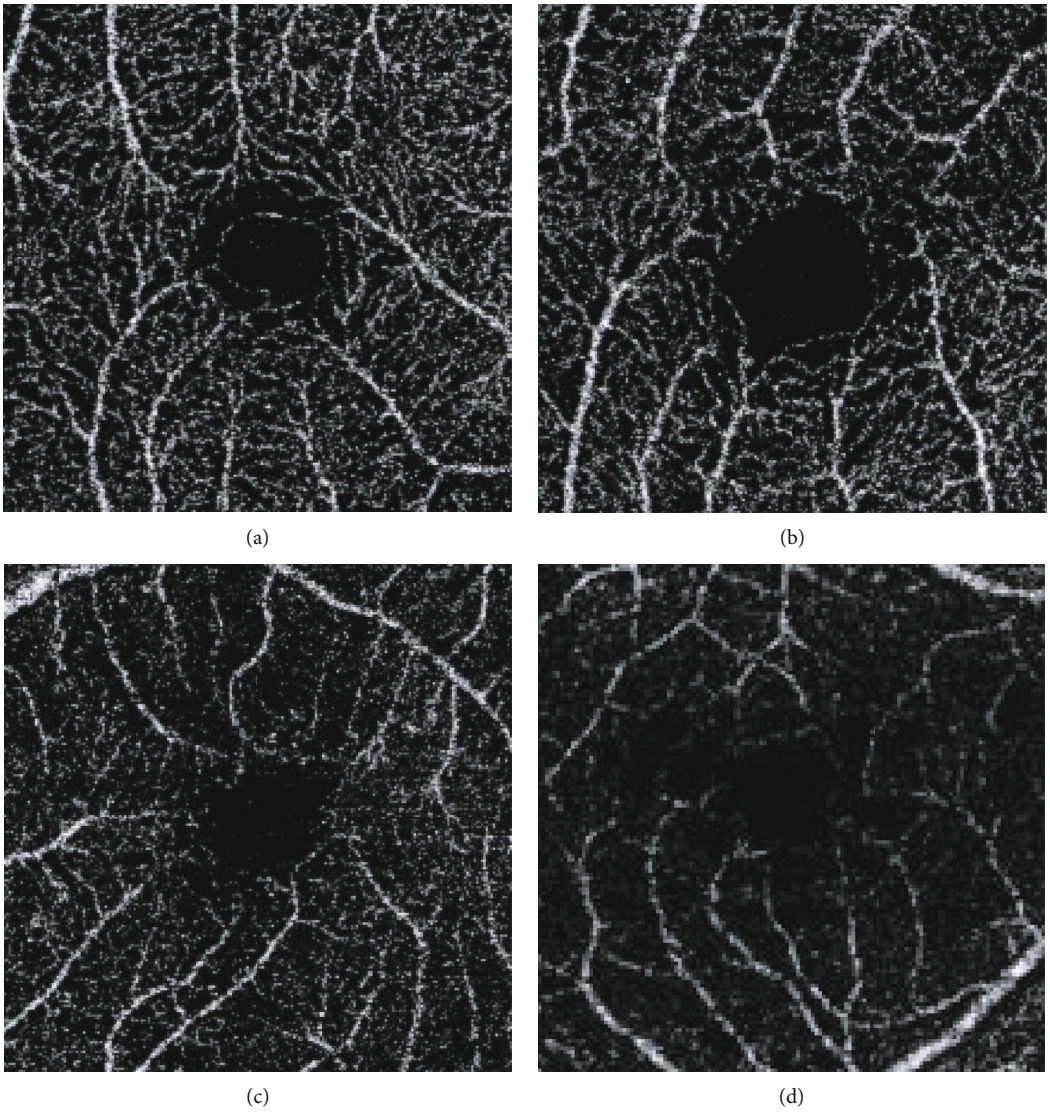

Figure 2: DRI OCT Triton OCT-A 3 × 3 mm *en face* images for the superficial capillary plexus. (a) Healthy volunteer. (b) Diabetic patient without retinopathy. (c) Diabetic patient with nonproliferative retinopathy. (d) Diabetic patient with proliferative retinopathy.

Post hoc Games-Howell analysis showed that in the control group WLR had smaller values (0.24 ± 0.046) compared to the no DR group (0.30 ± 0.073, mean difference = −0.059, 95%CI = −0.113, −0.004; $p = 0.029$) and PDR group (0.34 ± 0.10, mean difference = −0.0959, 95%CI = −0.166, −0.025; $p = 0.005$) values (Tables 2 and 3).

Having age as a covariate, the statistical analysis found no significant differences between the groups concerning the values of VD ($F(3, 69) = 2.029$, $p = 0.118$), LD ($F(3, 69) = 1.837$, $p = 0.148$), and WCSA ($F(3, 69) = 2.156$, $p = 0.101$). WLR was found to have a significant variation ($F(3, 69) = 3.587$, $p = 0.018$) between the groups, according to the ANCOVA analysis. Post hoc analysis showed that in the control group, WLR had smaller values compared to the PDR group values (mean difference = −0.085, 95%CI = −0.161, −0.008; $p = 0.022$) (Table 4). Having examined our vascular parameters between male and female groups, only the "superficial capillary density" has shown statistically significant differences. Running the statistics having the duration of diabetes as a covariate, out of all parameters, significant differences were found for wall-to-lumen ratio only.

With respect to the OCT angiography parameters, the FAZ values ($F(3, 63) = 1.587$, $p = 0.202$) did not vary significantly between the groups. The SPD values decreased with the advance of retinopathy ($F(3, 63) = 202.61$, $p = 0.001$). The control group (34.18 ± 1.40) had higher SPD values than the NPDR (32.27 ± 1.93) (mean difference = 1.909, 95%CI = 0.436, 3.382; $p = 0.006$) and the PDR group (32.31 ± 1.61, mean difference = 1.866, 95%CI = 0.393, 3.339; $p = 0.007$). In addition to this, the PDR group had a significantly lower SPD compared to the no DR group (33.85 ± 1.40, mean difference = 1.537, 95%CI = 0.017, 3.05; $p = 0.046$) (Tables 2 and 3).

Having age as a covariate, FAZ values ($F(3, 58) = 0.545$, $p = 0.653$, $F(3, 59) = 0.763$, $p = 0.519$, $F(3, 59) = 1.026$, $p = 0.388$) still did not vary significantly between the groups, while SPD values exhibited similar changes

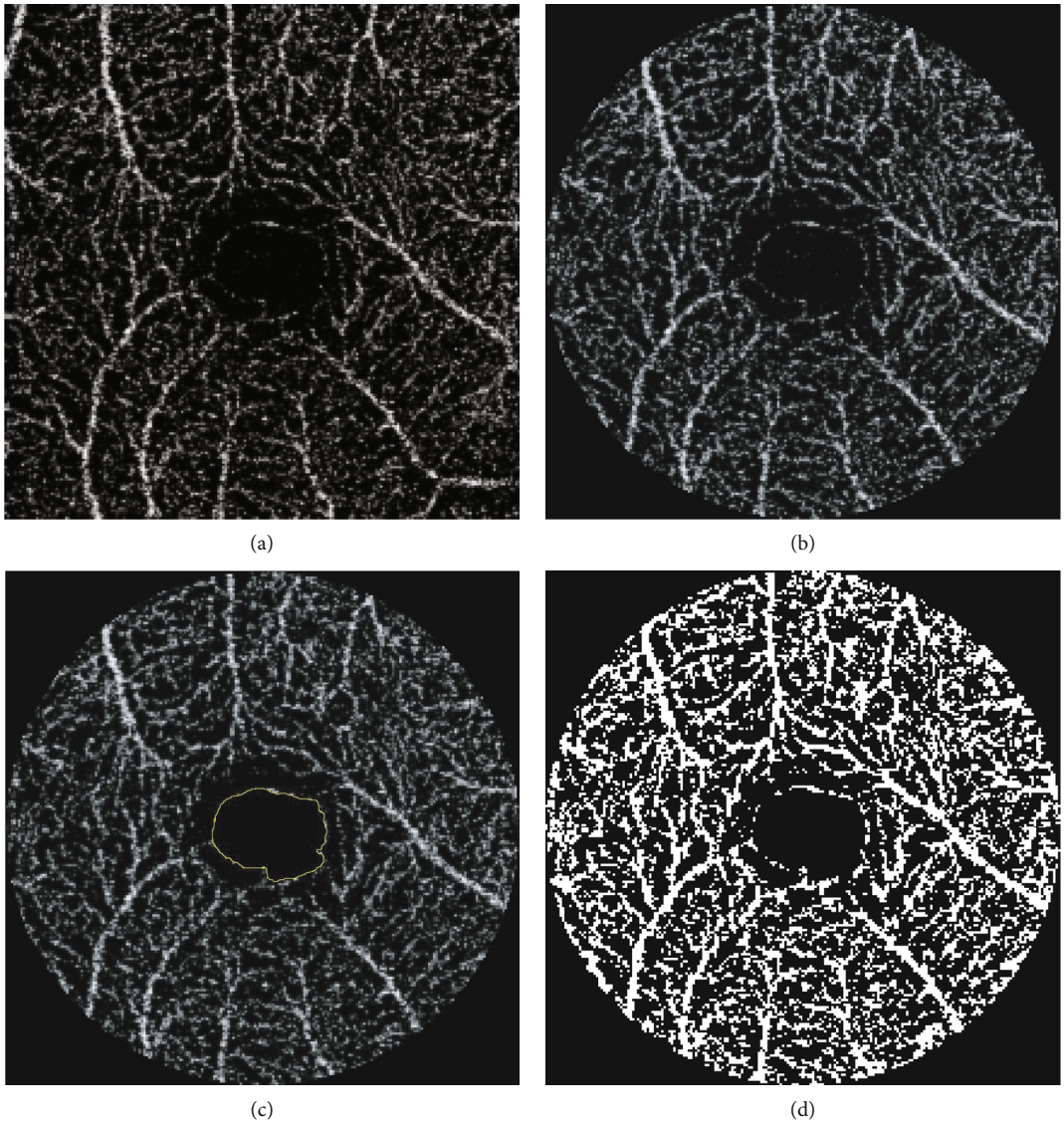

Figure 3: (a) DRI OCT Triton OCT-A 3 × 3 mm *en face* image of the superficial retinal layer in a healthy volunteer. (b) Previous image was cropped to a central circle with 3 mm diameter, using ImageJ software. (c) Manual FAZ area measurement (seen in yellow) in the OCT-A section, using ImageJ software. (d) The *en face* image from (c), transformed into a 8-bit grey scale picture and binarised using an automated thresholding algorithm (mean) from ImageJ software, in order to calculate the vascular density in the superficial capillary plexus.

Table 1: Characteristics of groups included in the study (expressed as mean ± standard deviation or as median, unless otherwise indicated).

	Control	No DR group	NPDR group	PDR group
N	17	19	17	21
Sex (male/female)	8/9	7/12	11/6	18/3
Laterality (right/left)	14/3	8/11	15/2	11/10
Age (years)	44.82 ± 12.85	53.68 ± 20.16	56.24 ± 10.84	55.71 ± 13.06
BCVA (decimal)	1	1	0.8	0.8
Diabetes duration (years)	0	9.18 ± 6.70	13.94 ± 8.97	15.21 ± 10.71
Axial length (mm)	23.87 ± 1.08	23.70 ± 0.88	23.18 ± 0.60	23.47 ± 0.84
Diabetic maculopathy (number of subjects)	0	1	11	9

Legend: BCVA: best corrected visual acuity; DR: diabetic retinopathy; NPDR: nonproliferative diabetic retinopathy; PDR: proliferative diabetic retinopathy.

Table 2: Vascular parameters measured using both adaptive optics ophthalmoscopy and optical coherence ophthalmoscopy angiography in the four study groups (mean ± standard deviation).

Studied parameters	Control	No DR group	NPDR group	PDR group
Vessel diameter (μm)	93.66 ± 14.06	94.30 ± 22.21	111.78 ± 30.21	97.16 ± 26.66
Lumen diameter (μm)	75.70 ± 11.64	73.12 ± 19.52	88.73 ± 30.45	73.85 ± 24.95
Wall thickness (μm)	9.20 ± 1.69	10.55 ± 2.12	11.25 ± 3.00	11.63 ± 2.90
Wall to lumen ratio	0.24 ± 0.046	0.30 ± 0.073	0.29 ± 0.11	0.34 ± 0.10
Wall cross sectional area (μm^2)	2499.05 ± 670.53	2878.81 ± 1143.75	3633.02 ± 1443.40	3194.96 ± 1371.45
Foveal avascular zone (mm^2)	0.326 ± 0.133	0.360 ± 0.258	0.458 ± 0.143	0.402 ± 0.179
Superficial capillary plexus density	34.18 ± 1.40	33.85 ± 1.40	32.27 ± 1.93	32.31 ± 1.61

Legend: DR: diabetic retinopathy; NPDR: nonproliferative diabetic retinopathy; PDR: proliferative diabetic retinopathy.

Table 3: Results of the post hoc analysis between the four groups included in the study.

Studied parameters	Control * no DR group	Control * NPDR group	Control * PDR group	No DR group * NPDR group	No DR group * PDR group	NPDR group * PDR group
Vessel diameter (Games-Howell)	1.00	0.143	0.955	0.143	0.982	0.413
Lumen diameter (Games-Howell)	0.961	0.376	0.990	0.961	0.292	0.381
Wall thickness (Tukey)	0.372	0.90	0.20	0.844	0.530	0.964
Wall to lumen ratio (Games-Howell)	**0.029**	0.462	**0.005**	0.968	0.577	0.483
Wall cross sectional area (Tukey)	0.781	0.0381	0.297	0.248	0.841	0.682
Foveal avascular zone (Tukey)	0.954	0.173	0.630	0.445	0.915	0.824
Superficial capillary density (Tukey)	0.938	**0.006**	**0.007**	**0.038**	**0.046**	1

Legend: DR: diabetic retinopathy; NPDR: nonproliferative diabetic retinopathy; PDR: proliferative diabetic retinopathy.

Table 4: Results of the post hoc analysis between the four groups included in the study controlling for age.

Studied parameters	Control * no DR group	Control * NPDR group	Control * PDR group	No DR group * NPDR group	No DR group * PDR group	NPDR group * PDR group
Vessel diameter	1.000	0.256	1.00	0.215	1.000	0.420
Lumen diameter	1.000	0.575	1.00	0.261	1.000	0.300
Wall thickness	1.000	0.360	0.90	1.000	1.000	1.000
Wall to lumen ratio	0.501	1.000	**0.022**	1.000	1.000	0.120
Wall cross sectional area	1.000	0.111	0.872	1.000	0.445	1.000
Foveal avascular zone	1.000	0.833	1.000	1.000	1.000	1.000
Superficial capillary density	1.000	**0.015**	**0.016**	0.058	0.066	1.000

Legend: DR: diabetic retinopathy; NPDR: nonproliferative diabetic retinopathy; PDR: proliferative diabetic retinopathy.

($F(3, 59) = 5.608$, $p = 0.002$). The control group had higher SPD values than both the PDR group (mean difference = 1.712, 95%CI = 0.010, 3.414; $p = 0.048$) and the NPDR group (mean difference = 1.840, 95%CI = 0.253, 3.427; $p = 0.015$, age as covariate) (Tables 2 and 4).

A Spearman's rank-order correlation was run to assess the relationship between BCVA and AO vascular and OCT-A parameters in diabetic patients. There was a statistically significant, strong negative correlation between the best corrected visual acuity and wall thickness ($r_s(57) = -0.367$,

Table 5: Results of Spearman's rank-order correlation between BCVA and the AO vascular and OCT-A parameters in the diabetic groups.

Spearmen correlation	Vessel diameter	Lumen diameter	Wall thickness	Wall to lumen ratio	Wall cross sectional area	Foveal avascular zone	Superficial capillary density
Coefficient ($r_s(55)$)	0.099	0.183	-0.367	-0.438	-0.052	-0.20	0.223
p value	0.463	0.174	**0.005**	**0.001**	0.701	0.894	0.133

$p = 0.005$) and wall to lumen ratio ($r_s(57) = -0.438$, $p = 0.001$), respectively (Table 5).

Further statistical analysis was focused on both AO and OCT-A parameters, comparing subjects that received anti-VEGF injections/retinal laser treatment/vitrectomy prior to the inclusion in this study with untreated participants. Significant differences were found only for the superficial capillary density parameter only between the diabetic patients that received anti-VEGF injections and those that did not ($p = 0.007$). Wall thickness ($p = 0.011$) and WCSA parameters ($p = 0.043$) varied significantly between the subjects with and without diabetic maculopathy.

4. Conclusions

Retinal circulation should be analyzed from different perspectives. Larger branches (like the superior/inferior branches of the central retinal artery) are easily assessed using AO-related parameters. Retinal microcirculation can be further examined looking at macular capillary plexuses, which are broadly studied with OCT-A and exhibit functional, topographical, and anatomical particularities. A third "window" to the retinal circulation is the analysis of the microvasculature changes in the peripheral retina, which represents an uncovered topic by the current research.

In this control study, focused on subjects without or with different stages of diabetic retinopathy, we assessed the retinal arterioles using the rtx1 adaptive optics retinal camera. By using a principle taken from astronomy, the device allows a detailed noninvasive visualisation of retinal structures at a histological resolution [14]. In addition to this, OCT angiography was performed in order to describe the macular retinal capillaries plexus flow densities and FAZ areas. According to our hypothesis, proportional vascular changes can be tracked in different stages of diabetic retinopathy, slight alterations being present even before any documentable clinical sign.

Our results suggest that diabetic patients with or without diabetic retinopathy prove signs of retinal arterioles and capillaries structural alterations, as shown by the WLR and SPD parameters. The study groups excluded subjects with untreated arterial hypertension or other vascular disorders. Furthermore, any disease-related intervention, such as retinal laser treatments, vitrectomy, or intravitreal drug injections, were performed more than 6 months before the inclusion in the current study, in order to diminish possible interaction.

An increased WLR was found in the diabetic group with no retinopathy and in the group with proliferative retinopathy, when compared to healthy volunteers. This finding is consistent with previous studies that described arteriolar remodeling in subjects with diabetic retinopathy [15–17], as well as in subjects with prediabetes or in diabetic patients without signs of retinopathy [4, 18, 19]. Interestingly, no significant difference was demonstrated between the control and the NPDR group, nor in between the diabetic groups. It is worth mentioning that a consistent number of NPDR and PDR subjects previously benefited of antivascular endothelial growth factor (VEGF) injections for diabetic macular oedema. Anti-VEGF therapy has a vasoconstrictive effect [20] and could have determined the narrowing of retinal vessels. In diabetes, the artery remodeling process is due to smooth muscle cells hypertrophy and fibrosis [21], and it is best mirrored by WLR [22, 23]. The retinal blood vessels are offering direct information on the systemic microcirculation. Thus, retinal structural and functional vascular changes reflect the negative effects of hyperglycemia on the systemic microcirculation. In addition to this, the strong negative correlation in the study groups between the visual acuity and wall thickness and wall to lumen ration, respectively, might reflect how *in vivo* retinal parameters interfere with the visual function. These retinal arteriolar changes highlight underlying structural and functional alterations resulting from pathophysiological mechanisms involved in diabetes [24].

The analysis of the OCT-A parameters demonstrated significant differences in the superficial capillary plexus density between the groups. Two exceptions were recorded: control versus no-DR group and NPDR versus PDR group. It has been previously shown that after 3 months of anti-VEGF intravitreal injections, administered in order to control the diabetic macular oedema, some small vessels disappear on fluorescein angiography [20]. The occluded vessels might remain closed after anti-VEGF discontinuation. This might be the reason why SPD parameter was significantly higher in patients that had no anti-VEGF injections when compared to the group that received this treatment at least 6 months prior to the study.

OCT-A is a useful noninvasive imaging tool in the diagnosis and monitoring of retinal changes in diabetes [25]. Previous studies have identified a decrease in the parafoveal superficial and deep retinal vessel densities, with associated FAZ area increase in diabetic patients with [26, 27] or without retinopathy [28, 29], when compared to normal subjects. These changes suggest abnormal autoregulation of the retinal microcirculation in diabetic patients that can be tracked before the appearance of clinical findings.

We had expected to find consistent significant differences between same groups for both AAO and OCT-A studied vascular parameters, but these were only noticed when

comparing healthy subjects with diabetic patients with proliferative retinopathy. In order to further clarify possible additional correlations, supplementary research is recommended. Larger sample sizes are needed in order to remove any source of bias. Separate analysis should be conducted for every stage of NPDR and PDR in order to draw a comprehensive conclusion. Moreover, several types of artefacts might have influenced the AO ophthalmoscopy and OCT-A analysis.

In conclusion, the present study tried to detect potential differences in the retinal microvasculature parameters for different diabetic retinopathy stages. AO retinal camera and OCT-A were able to detect microvascular changes between healthy subjects and diabetic patients. The results might reflect the superimposed effect of previous anti-VEGF treatment on the actual vascular status in both NPDR and PDR groups. Therefore, AO ophthalmoscopy and OCT-A are complementary techniques that are able to provide useful information about the topological and geometrical features of the retinal microvasculature from early onset of diabetic disease, thus having a promising role in the future. They might be used for routine follow-up, thus providing valuable prognostic information concerning the evolution of diabetic retinopathy.

Data Availability

Raw and derived data supporting the findings of this study are available from the corresponding author [IEC] on request.

Conflicts of Interest

The authors declare that there is no conflict of interest regarding the publication of this paper.

References

[1] V. Coviltir, M. Burcel, A. P. Cherecheanu et al., "Update on myopia risk factors and microenvironmental changes," *Journal of Ophthalmology*, vol. 2019, no. 2019, Article ID 4960852, 2019.

[2] U. V. Shukla and K. Tripathy, "Diabetic retinopathy," in *StatPearls*, StatPearls Publishing, Treasure Island (FL), 2021.

[3] C. Y. L. Cheung, M. K. Ikram, C. Sabanayagam, and T. Y. Wong, "Retinal microvasculature as a model to study the manifestations of hypertension," *Hypertension*, vol. 60, pp. 1094–1103, 2012.

[4] I. E. Cristescu, L. Zagrean, F. Balta, and D. C. Branisteanu, "Retinal microcirculation investigation in type I and II diabetic patients without retinopathy using an adaptive optics retinal camera," *Acta Endocrinologica*, vol. 15, pp. 417–422, 2019.

[5] E. Treatment and D. Retinopathy, "Grading Diabetic Retinopathy from Stereoscopic Color Fundus Photographs–An Extension of the Modified Airlie House Classification: ETDRS Report Number 10," *Ophthalmology*, vol. 98, no. 5, pp. 786–806, 1991.

[6] A. Kifley, J. J. Wang, S. Cugati, T. Y. Wong, and P. Mitchell, "Retinal Vascular Caliber, Diabetes, and Retinopathy," *American Journal of Ophthalmology*, vol. 143, no. 6, pp. 1024–1026, 2007.

[7] T. T. Nguyen, J. J. Wang, A. R. Sharrett et al., "Relationship of retinal vascular caliber with diabetes and Retinopathy," *Diabetes Care*, vol. 31, no. 3, pp. 544–549, 2008.

[8] M. K. Ikram, C. Y. Cheung, M. Lorenzi et al., "Retinal vascular caliber as a biomarker for diabetes microvascular complications," *Diabetes Care*, vol. 36, no. 3, pp. 750–759, 2013.

[9] P. K. Yu, C. Balaratnasingam, S. J. Cringle, I. L. McAllister, J. Provis, and D.-Y. Yu, "Microstructure and network organization of the microvasculature in the human macula," *Investigative Opthalmology & Visual Science*, vol. 51, no. 12, pp. 6735–6743, 2010.

[10] F. Huang, B. Dashtbozorg, J. Zhang et al., "Reliability of using retinal vascular fractal dimension as a biomarker in the diabetic retinopathy detection," *Journal of Ophthalmology*, vol. 2016, 2016.

[11] I. E. Cristescu, R. Ochinciuc, F. Balta, and L. Zagrean, "High-resolution imaging of diabetic retinopathy lesions using an adaptive optics retinal camera," *Romanian Journal of Ophthalmology*, vol. 63, no. 1, pp. 29–34, 2019.

[12] S. A. Burns, A. E. Elsner, K. A. Sapoznik, R. L. Warner, and T. J. Gast, "Adaptive optics imaging of the human retina," *Progress in Retinal and Eye Research*, vol. 68, pp. 1–30, 2019.

[13] D. M. Sampson, P. Gong, D. An et al., "Axial length variation impacts on superficial retinal vessel density and foveal avascular zone area measurements using optical coherence tomography angiography," *Investigative Ophthalmology & Visual Science*, vol. 58, no. 7, pp. 3065–3072, 2017.

[14] R. Ochinciuc, U. Ochinciuc, H. T. Stanca et al., "Photoreceptor assessment in focal laser-treated central serous chorioretinopathy using adaptive optics and fundus autofluorescence," *Medicine*, vol. 99, no. 15, article e19536, 2020.

[15] A. Zaleska-Żmijewska, Z. M. Wawrzyniak, A. Dąbrowska, and J. P. Szaflik, "Adaptive optics (rtx1) high-resolution imaging of photoreceptors and retinal arteries in patients with diabetic retinopathy," *Journal of Diabetes Research*, vol. 2019, 12 pages, 2019.

[16] A. C. Clermont and S. E. Bursell, "Retinal blood flow in diabetes," *Microcirculation*, vol. 14, pp. 49–61, 2007.

[17] M. Inanc, K. Tekin, H. Kiziltoprak, S. Ozalkak, S. Doguizi, and Z. Aycan, "Changes in retinal microcirculation precede the clinical onset of diabetic retinopathy in children with type 1 diabetes mellitus," *American Journal of Ophthalmology*, vol. 207, pp. 37–44, 2019.

[18] A. Zaleska-Żmijewska, P. Piątkiewicz, B. Śmigielska et al., "Retinal photoreceptors and microvascular changes in prediabetes measured with adaptive optics (rtx1™): a case-control study," *Journal of Diabetes Research*, vol. 2017, 9 pages, 2017.

[19] T. A. Gardiner, D. B. Archer, T. M. Curtis, and A. W. Stitt, "Arteriolar involvement in the microvascular lesions of diabetic retinopathy: implications for pathogenesis," *Microcirculation*, vol. 14, no. 1, pp. 25–38, 2007.

[20] S. Bonnin, B. Dupas, C. Lavia et al., "Anti-vascular endothelial growth factor therapy can improve diabetic retinopathy score without change in retinal perfusion," *Retina*, vol. 39, no. 3, pp. 426–434, 2019.

[21] J. Ding, C. Y. Cheung, M. K. Ikram et al., "Early retinal arteriolar changes and peripheral neuropathy in diabetes," *Diabetes Care*, vol. 35, no. 5, pp. 1098–1104, 2012.

[22] D. Rizzoni, C. Agabiti Rosei, C. De Ciuceis, F. Semeraro, M. Rizzoni, and F. Docchio, "New methods to study the microcirculation," *American Journal of Hypertension*, vol. 31, no. 3, pp. 265–273, 2018.

[23] D. Kannenkeril, A. Bosch, J. Harazny et al., "Early vascular parameters in the micro- and macrocirculation in type 2 diabetes," *Cardiovascular Diabetology*, vol. 17, no. 1, p. 128, 2018.

[24] R. Klein, B. E. Klein, S. E. Moss et al., "The relation of retinal vessel caliber to the incidence and progression of diabetic retinopathy: xix: the Wisconsin epidemiologic study of diabetic retinopathy," *Archives of Ophthalmology*, vol. 122, no. 1, pp. 76–83, 2004.

[25] K. Y. Tey, K. Teo, A. C. S. Tan et al., "Optical coherence tomography angiography in diabetic retinopathy: a review of current applications," *Eye and Vision*, vol. 6, no. 1, p. 37, 2019.

[26] J. Khadamy, K. Abri Aghdam, and K. G. Falavarjani, "An update on optical coherence tomography angiography in diabetic retinopathy," *Journal of Ophthalmic & Vision Research*, vol. 13, no. 4, pp. 487–497, 2018.

[27] B. Tan, J. Chua, E. Lin et al., "Quantitative microvascular analysis with wide-field optical coherence tomography angiography in eyes with diabetic retinopathy," *JAMA Network Open*, vol. 3, no. 1, article e1919469, 2020.

[28] G. Dimitrova, E. Chihara, H. Takahashi, H. Amano, and K. Okazaki, "Quantitative retinal optical coherence tomography angiography in patients with diabetes without diabetic retinopathy," *Investigative Ophthalmology & Visual Science*, vol. 58, no. 1, pp. 190–196, 2017.

[29] T. E. de Carlo, A. T. Chin, M. A. Bonini Filho et al., "Detection of microvascular changes in eyes of patients with diabetes but not clinical diabetic retinopathy using optical coherence tomography angiography," *Retina*, vol. 35, no. 11, pp. 2364–2370, 2015.

Hindawi
Journal of Diabetes Research
Volume 2022, Article ID 8435603, 9 pages
https://doi.org/10.1155/2022/8435603

Research Article

Aqueous Level of ANGPTL4 Correlates with the OCTA Metrics of Diabetic Macular Edema in NPDR

Qing Xu, Chaoju Gong, Lei Qiao, Ruifang Feng, Haiyang Liu, Yalu Liu, Sujuan Ji, Yipeng Zhang, Shuang Wu, and Suyan Li

Department of Ophthalmology, The Affiliated Xuzhou Municipal Hospital of Xuzhou Medical University, Xuzhou First People's Hospital, Xuzhou Eye Disease Prevention and Treatment Institute, Xuzhou, 221116 Jiangsu Province, China

Correspondence should be addressed to Suyan Li; lisuyan_med@163.com

Received 30 August 2021; Revised 9 November 2021; Accepted 18 December 2021; Published 19 January 2022

Academic Editor: Lei Liu

Purpose. To investigate the aqueous levels of angiogenic factors in nonproliferative diabetic retinopathy (NPDR) patients with diabetic macular edema (DME) and to ascertain their association with optical coherence tomography angiography (OCTA) metrics. *Methods*. This study enrolled 21 NPDR eyes with DME (NPDR/DME+), 17 NPDR eyes without DME (NPDR/DME-), and 16 diabetic eyes without retinopathy (DWR). Luminex bead-based multiplex array was used to measure the levels of 25 cytokines. OCTA system with a scan area of 3×3 mm was used to measure retinal thickness (RT), retinal volume (RV), superficial vessel density (SVD), deep vessel density (DVD), foveal avascular zone (FAZ) area, perimeter and acircularity index. *Results*. The levels of ANGPTL4 were significantly different among the three groups ($P < 0.05$), in which NPDR/DME+ group had the highest level and NPDR/DME- group had a higher level than the DWR group (all, $P < 0.0167$). OCTA examination showed that, compared with DWR and NPDR/DME- group, RT and RV increased and the whole/parafoveal DVD decreased in NPDR/DME+ group (all, $P < 0.05$). Meanwhile, NPDR/DME- group had lower parafoveal DVD than the DWR group ($P < 0.05$). Correlation analysis showed that the levels of ANGPTL4 were positively correlated with foveal/parafoveal RT and RV and negatively correlated with whole/parafoveal DVD in NPDR patients (all, $P < 0.05$). As the influencing factor of RT, RV, and DVD, every additional 10^3 pg/ml of ANGPTL4 was associated with an increase in foveal and parafoveal RT of 4.299 μm and 3.598 μm, respectively. Every additional 10^6 pg/ml of ANGPTL4 was associated with an increase in foveal and parafoveal RV of 3.371 mm^3 and 17.705 mm^3, respectively. Every additional 10^4 pg/ml of ANGPTL4 was associated with a decrease in whole and parafoveal DVD of 1.705% and 1.799%, respectively. *Conclusions*. The level of ANGPTL4 in aqueous humor of NPDR patients with DME was significantly increased and ANGPTL4 might predict RT, RV, and parafoveal DVD of DME in NPDR patients.

1. Introduction

Diabetic retinopathy (DR) is one of the most destructive microvascular complications of diabetes mellitus. Intraocular neovascularization and diabetic macular edema (DME) are two major clinicopathologic features during the development and progression of DR [1, 2]. The occurrence of neovascularization is closely related to the duration of diabetes mellitus. Patients with recently diagnosed diabetes mellitus have a lower risk of proliferative diabetic retinopathy (PDR) involving neovascularization than those with longer duration [3]. DME is a major cause of visual impairment in DR patients, which can occur at any stage of DR, even at early and mild nonproliferative diabetic retinopathy (NPDR) stage [4]. Therefore, the prevention and early diagnosis of DME in NPDR are extremely important.

The pathogenesis of DME is multifactorial and remains unknown. Recent studies suggest that DME occurrence is induced by the breakdown of the blood-retina barrier (BRB) and the consequent increases in vascular permeability, vascular leakage, and fluid accumulation within the macula, which causes retina thickening, macular malfunction,

and visual impairment [5]. Angiogenesis and inflammation play a critical role in the pathogenesis of DME involving many exudative cytokines [6–9].

As a potent angiogenesis factor, vascular endothelial growth factor (VEGF) can increase vascular permeability in DME pathogenesis [10]. At present, anti-VEGF therapy is a first-line treatment for DME. Studies have shown that VEGF inhibition effectively improved visual acuity and reduced macular thickness [11]. Nevertheless, the responses to anti-VEGF therapy were distinct in different cases. Specially, persistent DME did not improve even after several administrations of anti-VEGF drugs [4, 11]. The above findings reveal that other mechanisms, independent of VEGF, may also contribute to DME.

However, previous studies mainly focused on inflammatory factors in DME, but not angiogenic factors. Furthermore, the conclusions from these studies were only based on the comparison of cytokine levels between DME and nondiabetic control [7, 11, 12], which could not rule out the interference of diabetes and DR severities on cytokine level.

Here, we choose 25 angiogenic factors based on established and hypothesized angiogenesis pathway in DR and DME [13, 14], compared cytokines levels in the aqueous humor of NPDR patients with or without DME, and then investigated the effects of differentially expressed cytokines on optical coherence tomography angiography (OCTA) metrics to explore the potential molecular markers for DME in NPDR patients.

2. Methods

2.1. Study Subjects. This study included 21 eyes of 21 NPDR patients with DME (NPDR/DME+) who received intravitreal injection of anti-VEGF agents in the ophthalmology department of Xuzhou First People's Hospital from July 2017 to December 2018. 33 eyes of 33 senile cataract patients with diabetes mellitus who underwent phacoemulsification at the same time were enrolled, in which 17 eyes of 17 NPDR patients without DME (NPDR/DME-) and 16 eyes of 16 diabetic patients without retinopathy (DWR) were identified by slit-lamp biomicroscopy, fundus photography, and OCTA three days after the operation. DWR group served as controls. The inclusion criteria were as follows: (1) NPDR patients with DME, DME was defined with one or more of the follows: retinal thickening at or within 500 μm of the macular center; hard exudates at or within 500 μm of the macular center, also associated with adjacent retinal thickening; one or more zones of retinal thickening with one optic disc size, at least part of which within the range of one optic disc diameter in the macular center [15]. The diagnosis and classification of NPDR were based on the standards published by the international ophthalmological association [16]. (2) Senile cataract patients with type 2 diabetes mellitus who received phacoemulsification were diagnosed as NPDR without DME or DWR. Exclusion criteria were as follows: (1) proliferative diabetic retinopathy; (2) a history of vitreous hemorrhage, retinal detachment, intraocular surgery (except cataract surgery) or ocular trauma; (3) anti-VEGF or laser therapy previously; (4) complication with uveitis, glaucoma, optic nerve disease, or other eye diseases; (5) low signal strength index (SSI < 50), blink artifacts or motion. This study followed the Declaration of Helsinki and was approved by the Ethics Committee of Xuzhou First People's Hospital (approval number: xyyll [2017] 008). Informed consent was obtained from all patients.

2.2. Ophthalmic Examination. All patients underwent comprehensive ophthalmic examination, including visual acuity, intraocular pressure, slit-lamp biomicroscopy, fundus photography, and OCTA. The images were diagnosed by two independent doctors, and cases with a discrepancy were reviewed by the third doctor with a higher qualification. OCTA (Optovue, Inc., Fremont, CA, USA) was performed using the angio retina mode. For each eye, a 3 × 3 mm area centered on the fovea was scanned. Retinal thickness (RT) and retinal volume (RV) in the foveal and parafoveal area were automatically calculated by the built-in software from internal limiting membrane (ILM) to retinal pigment epithelium (RPE) layer. The fovea was defined as the circle area within the central 1 mm of the macula. Parafovea was defined as an area from the central 1 mm to the central 3 mm ring of the macular [17]. The OCTA images were automatically segmented to superficial capillary plexuses (SCP) and deep capillary plexuses (DCP) using the built-in software segmentation algorithm. The SCP was segmented with an inner boundary at 3 μm beneath the ILM and an outer boundary at 15 μm beneath the inner plexiform layer (IPL). The DCP was segmented with an inner boundary 15 μm beneath the IPL and an outer boundary at 70 μm beneath the IPL [18]. The vessel density values for the SCP and DCP in the whole, foveal, and parafoveal zones were calculated by the Angiovue Analytics built-in software. Vessel density was calculated as the percentage of pixels with flow signal above the preset decorrelation threshold in the defined region. FAZ area, perimeter, acircularity index, and FD-300 vessel density were automatically obtained via the FAZ assessment tool. FAZ surrounded by a continuous vascular closed ring was taken from ILM to outer plexiform layer (OPL). FD-300 was defined as a 300 μm ring around the FAZ [17].

2.3. Sample Collection. Aqueous humor was collected before cataract surgery or intravitreal injection of anti-VEGF agents. After topical anesthesia, 100 μL undiluted aqueous humor was withdrawn aseptically using an insulin syringe with a 30G needle at 1 mm inside the corneal limbus, which was placed in a 0.5 mL sterile Eppendorf tube and then stored at -80°C until measurement.

2.4. Measurement of Cytokines. Twenty-five cytokines, including epidermal growth factor (EGF), hepatocyte growth factor (HGF), heparin-binding EGF-like growth factor (HB-EGF), fibroblast growth factor 1 (FGF-1), FGF-2, FGF-19, FGF-21, FGF-23, granulocyte colony-stimulating factor (G-CSF), bone morphogenetic protein 9 (BMP-9), Endoglin, Endothelin-1, Leptin, Follistatin, α-Fetoprotein, FABP1, interleukin-8 (IL-8), Angiopoietin-2 (ANG-2), angiopoietin-like 3 (ANGPTL3), ANGPTL4, ANGPTL6, placental growth

Table 1: Demographic characteristics of the 3 groups.

Characteristic	DWR ($N = 16$)	NPDR/DME- ($N = 17$)	NPDR/DME+ ($N = 21$)	F/χ^2 value	P value (among the 3 groups)
Age (yrs)	67.94 ± 8.80	64.47 ± 7.19	64.76 ± 11.61	0.675	0.514[a]
Male gender, no. (%)	5 (31.25%)	7 (41.18%)	14 (66.67%)	5.046	0.080[b]
BMI	24.80 ± 3.16	24.19 ± 1.88	25.97 ± 3.27	1.895	0.161[a]
MAP	100.33 ± 7.41	105.02 ± 12.35	101.95 ± 11.07	0.844	0.436[a]
Fasting plasma glucose (mmol/l)	6.72 ± 1.43	7.42 ± 1.91	6.51 ± 1.32	1.667	0.199[a]
HbAlc (%)	7.48 ± 1.25	7.97 ± 1.48	7.56 ± 0.98	0.789	0.460[a]
Duration of diabetes (yrs)	7.88 ± 5.94	11.88 ± 4.96	11.20 ± 9.21	1.485	0.236[a]
NPDR classification				2.354	0.354[b]
Mild (%)	—	5 (29.41%)	4 (19.05%)		
Moderate (%)	—	8 (47.06%)	7 (33.33%)		
Severe (%)	—	4 (23.53%)	10 (47.62%)		

BMI: body mass index; MAP: mean arterial pressure; HbA1c: hemoglobin A1c; —: not analyzed. Values are mean ± standard deviation unless otherwise indicated. [a]One-way analysis of variance with post hoc least significant difference multiple comparison tests. [b]Chi-square test.

Table 2: Comparison of the cytokine levels in the aqueous humor among the 3 groups [M(Q1,Q3)].

Aqueous cytokines	DWR (pg/ml) ($N = 16$)	NPDR/DME- (pg/ml) ($N = 17$)	NPDR/DME+ (pg/ml) ($N = 21$)	χ^2 value	P value
HGF	445.64 (286.17, 583.95)	400.13 (353.31, 688.43)	626.10 (528.81, 805.84)[ab]	9.596	0.008
HB-EGF	1.18 (1.02, 1.62)	1.21 (0.87, 1.48)	1.06 (0.92, 1.27)	1.586	0.453
FGF-2	13.19 (11.17, 18.16)	15.75 (11.66, 19.81)	13.19 (9.33, 15.75)	1.803	0.406
FGF-19	50.29 (33.56, 66.44)	39.42 (32.11, 53.29)	234.78 (35.51, 335.39)[b]	8.362	0.015
Endothelin-1	8.15 (6.24, 13.59)	8.83 (5.97, 10.64)	8.22 (5.78, 10.23)	0.763	0.683
Leptin	68.33 (61.73, 80.97)	64.84 (57.66, 79.31)	88.26 (68.33, 135.53)	5.895	0.052
IL-8	4.64 (3.32, 7.42)	7.16 (3.67, 8.14)	9.97 (6.95, 17.18)[ab]	12.276	0.002
ANG-2	32.28 (26.52, 44.62)	36.52 (25.42, 44.92)	34.58 (25.13, 44.17)	0.014	0.993
ANGPTL4	1529.50 (1078.50, 4347.25)	2726.00 (2025.00, 12519.50)[a]	23778.00 (14490.00, 26311.50)[ab]	31.902	<0.001
PLGF	1.25 (1.02, 1.79)	1.23 (1.07, 3.54)	3.75 (2.74, 6.56)[ab]	20.631	<0.001
VEGF-A	179.14 (132.90, 220.41)	276.25 (159.75, 345.77)	363.93 (242.95, 564.12)[ab]	20.004	<0.001
VEGF-C	38.52 (29.76, 77.98)	45.36 (33.79, 65.16)	47.24 (34.26, 56.01)	0.076	0.963

HGF: hepatocyte growth factor; HB-EGF: heparin-binding EGF-like growth factor; FGF-2: fibroblast growth factor 2; FGF-19: fibroblast growth factor 19; IL-8: interleukin 8; ANG-2: angiopoietin-2; ANGPTL4: angiopoietin-like 4; PLGF: placental growth factor; VEGF-A: vascular endothelial growth factor-A; VEGF-C: vascular endothelial growth factor-C. Cytokine levels (pg/mL) are presented as median with interquartile range. The levels of cytokines in the aqueous humor of the 3 groups were compared by Kruskal-Wallis H test; one-to-one multiple comparisons were performed by Mann–Whitney U test, a: compared with control, [a]$P < 0.0167$, b: compared with NPDR/ME- group, [b]$P < 0.0167$.

factor (PLGF), VEGF-A, VEGF-C, and VEGF-D (angiogenesis/growth factor panels, HAGP1MAG-12K and HLPPMAG-57K; Millipore Corporation, Billerica, MA, USA) were measured with Luminex bead-based multiplex array. All assays were performed strictly according to the manufacturer's guidelines, the detailed procedures of which were described in a previous study [19]. In brief, the assay buffer (25 μL) was added to the background, standard, control, and sample wells. Each standard or control (25 μL) was added into the appropriate wells. Aqueous humor (25 μL) was added into the appropriate wells. Mixed beads (25 μL) were added to each well. Seal, wrap with foil, and incubate with agitation on a plate shaker overnight at 4°C. Gently remove fluid and wash plate 3 times. Next, detection antibody (25 μL) was added, and the plate was incubated for 1 hour at room temperature. Then, streptavidin-Phycoerythrin solution (25 μL) was added to each well, and the plate was incubated for 30 minutes at room temperature. Gently remove well contents and wash plate 3 times. Sheath fluid (100 μL) was added to all wells, and the beads were resuspended on a plate shaker for 5 minutes. Next, the plate was run on the FlexMAP 3D (Luminex) platform with xPONENT software. Median Fluorescent Intensity (MFI) was collected using Milliplex analyst 5.1 software. Standard curve for each cytokine was generated using the standards provided in the kits, and cytokine concentrations were obtained from the standard curves using a 5-parameter curve-fitting algorithm to transform the MFI values into concentrations.

2.5. Statistical Analyses. Statistical analysis was performed with SPSS 19.0. Shapiro-Wilk test was used to assess the

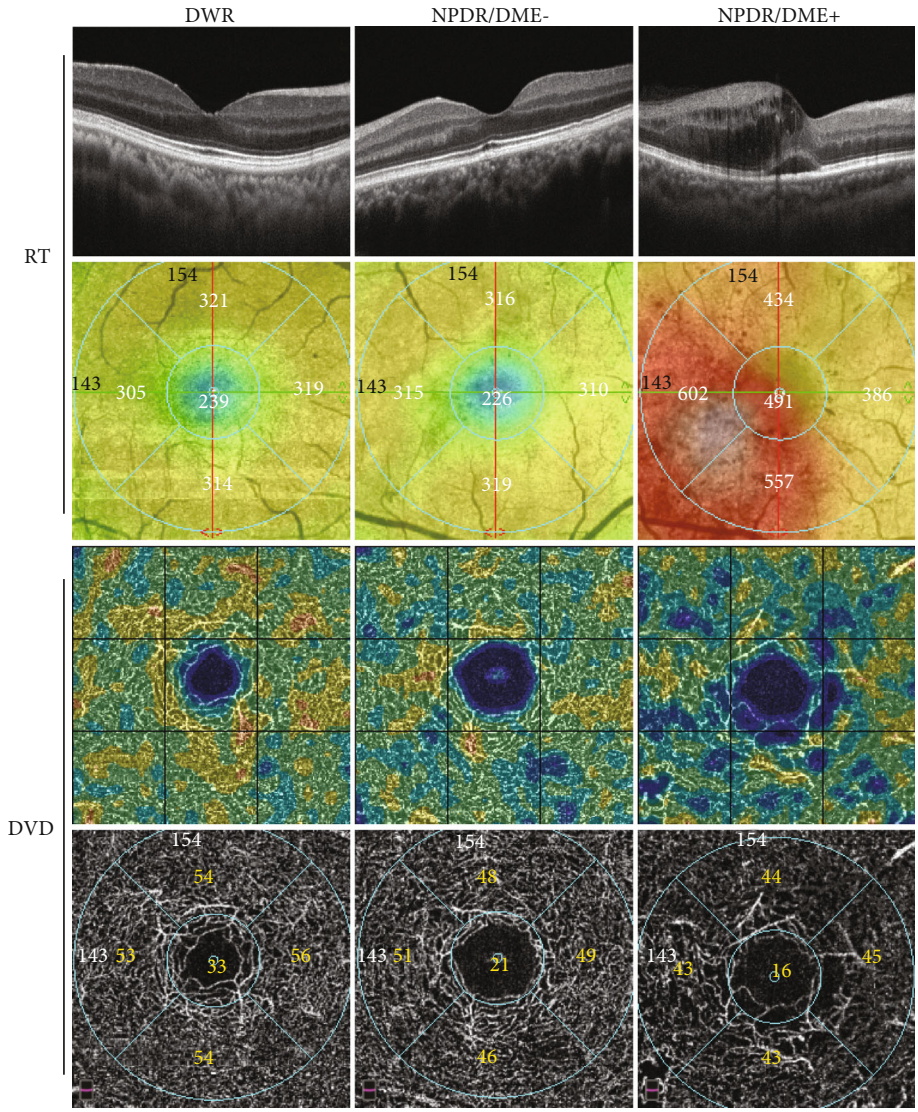

Figure 1: OCTA images of the three groups. Compared with DWR and NPDR/DME- groups, RT was significantly increased and DVD was significantly decreased in NPDR/DME+ groups.

normality of measurement variables. Normally distributed variables were expressed as mean ± standard deviation, whereas skewed distributed variables were expressed as median (Q1, Q3). Categorical variables were summarized as counts and percentage. Comparisons of categorical variables were performed using chi-squared test. One-way analysis of variance with post hoc least significant difference (LSD) multiple comparison tests was performed for normally distributed variables among the three groups. Kruskal-Wallis H test was performed for skewed variables among the three groups. Mann–Whitney U test was performed for skewed variables between two groups, and a $P < 0.0167$ (0.05/3) was considered significant for multiple comparisons. Spearman's rank correlation test was performed to assess the association between cytokine levels and the OCTA metrics. The correlation coefficient was tested by Student's t test and the cytokines with $P < 0.05$ were included for single-factor linear regression analysis, and the cytokines with $P < 0.05$ in the single factor linear regression were further included in the multiple linear regression model. RT (foveal and parafoveal), RV (foveal and parafoveal), and DVD (whole and parafoveal) were used as dependent variables, respectively, ANGPTL4 and VEGF-A were used as independent variables, stepwise multiple linear regression was used to evaluate the cytokines that affect OCTA metrics, and $P < 0.05$ was considered statistically significant.

3. Results

3.1. Demographic Characteristics. There were no significant differences in age, gender composition, body mass index (BMI), mean arterial pressure (MAP), fasting plasma glucose, HbAlc, and the duration of diabetes among the three groups (all, $P > 0.05$). There were no significant differences in severity degree of NPDR between NPDR/DME+ and NPDR/DME- groups ($P > 0.05$) (Table 1).

Table 3: Comparison of the OCTA Metrics among the 3 groups (mean ± SD).

OCTA metrics	DWR ($N = 16$)	NPDR/DME- ($N = 17$)	NPDR/DME+ ($N = 21$)	F value	P value
RT (μm)					
Fovea	240.90 ± 20.57	237.54 ± 22.77	331.76 ± 90.87[ab]	15.617	<0.001
Parafovea	308.59 ± 13.68	313.18 ± 20.56	379.25 ± 76.61[ab]	12.061	<0.001
RV (mm^3)					
Fovea	0.19 ± 0.02	0.19 ± 0.02	0.26 ± 0.07[ab]	15.640	<0.001
Parafovea	1.90 ± 0.09	1.93 ± 0.14	2.26 ± 0.41[ab]	9.838	<0.001
SVD (%)					
Whole	39.37 ± 4.48	40.20 ± 3.63	39.31 ± 5.16	0.211	0.810
Fovea	12.24 ± 5.28	14.25 ± 5.24	15.04 ± 7.04	1.011	0.371
Parafovea	42.35 ± 4.86	42.56 ± 4.11	41.01 ± 5.80	0.535	0.589
DVD (%)					
Whole	49.05 ± 3.38	45.96 ± 4.54	42.35 ± 5.66[ab]	9.260	<0.001
Fovea	27.90 ± 5.24	25.08 ± 6.20	24.79 ± 9.06	0.962	0.389
Parafovea	52.25 ± 3.70	48.64 ± 5.19[a]	44.76 ± 5.94[ab]	9.752	<0.001
FD-300 vessel density (%)	43.57 ± 5.00	44.40 ± 5.19	42.54 ± 5.91	0.561	0.574
FAZ					
Area (mm^2)	0.34 ± 0.08	0.37 ± 0.11	0.42 ± 0.25	1.074	0.349
Perimeter (mm)	2.37 ± 0.31	2.57 ± 0.42	2.82 ± 1.04	1.871	0.164
Acircularity index	1.16 ± 0.05	1.19 ± 0.06	1.23 ± 0.12	2.896	0.064

SD: standard deviation; RT: retinal thickness; RV: retinal volume; SVD: superficial vessel density; DVD: deep vessel densities; FAZ: foveal avascular zone. One-way ANOVA for normal distribution data among the 3 groups followed by post hoc least significant difference analysis between each two groups. a: compared with control; b: compared with NPDR/DME- group, $P < 0.05$ was deemed to be statistically significant.

Table 4: Correlation between cytokine levels in aqueous humor and OCTA metrics in NPDR eyes ($n = 38$).

	Foveal RT		Parafoveal RT		Foveal RV		Parafoveal RV		Whole DVD		Parafoveal DVD	
	r_s	P value	r_s	P value	r_s	P value	r_s	P value	r_s	P value	r_s	P value
HGF	0.250	0.130	0.211	0.203	0.249	0.132	0.127	0.447	-0.087	0.605	-0.144	0.389
FGF19	0.315	0.054	0.332	0.042	0.314	0.055	0.297	0.070	-0.256	0.121	-0.293	0.074
IL-8	0.175	0.293	0.158	0.345	0.172	0.302	0.041	0.807	-0.171	0.304	-0.184	0.268
ANGPTL4	0.569	<0.001	0.555	<0.001	0.566	<0.001	0.519	0.001	-0.352	0.030	-0.421	0.008
PLGF	0.363	0.025	0.352	0.030	0.365	0.024	0.326	0.046	-0.240	0.147	-0.288	0.080
VEGF-A	0.528	0.001	0.437	0.006	0.530	0.001	0.389	0.016	-0.373	0.021	-0.422	0.008

RT: retinal thickness; RV: retinal volume; DVD: deep vessel density. Spearman test, $P < 0.05$ was deemed to be statistically significant.

3.2. Comparison of Cytokine Levels in Aqueous Humor. The levels of ANGPTL4 among the three groups were significantly different from each other ($P < 0.05$). NPDR/DME+ group had the highest level of ANGPTL4 in the three groups, and NPDR/DME- group had a higher ANGPTL4 level than the DWR group (all, $P < 0.0167$). For HGF, IL-8, PLGF, and VEGF-A, NPDR/DME+ group had the highest levels in the three groups (all, $P < 0.0167$), but no significant difference between NPDR/DME- and DWR group was found (all, $P > 0.0167$). In addition, NPDR/DME+ group had a higher level of FGF-19 than the NPDR/DME- group ($P < 0.0167$), but no significant changes were detected in NPDR/DME+ and NPDR/DME- groups, compared with the DWR group (all, $P > 0.0167$). There were no significant differences of HB-EGF, FGF-2, Endothelin-1, Leptin, ANG-2, and VEGF-C among the three groups (all, $P > 0.05$), and the levels of EGF, FGF-1, FGF-21, FGF-23, G-CSF, BMP-9, Endoglin, Follistatin, AFP, FABP1, ANGPTL3, ANGPTL6, and VEGF-D were lower than the minimum detectable levels of the panel (Table 2).

3.3. Comparison of OCTA Metrics. Compared with DWR and NPDR/DME- group, RT and RV in NPDR/DME+ group were significantly increased, and the whole/parafoveal deep vessel densities (DVD) were reduced (Figure 1, Table 3). Besides, NPDR/DME- group had a lower parafoveal DVD than the DWR group (all, $P < 0.05$) (Table 3). There were no significant differences of superficial vessel

Table 5: Target cytokines affecting the OCTA Metrics in NPDR eyes ($n = 38$).

(a)

Cytokines	Foveal RT				Parafoveal RT			
	β	SE	P value	R^2	β	SE	Pvalue	R^2
ANGPTL4	4.299×10^{-3}	0.745×10^{-3}	<0.001	0.480	3.598×10^{-3}	0.572×10^{-3}	<0.001	0.523
VEGF-A	—	—	0.050		—	—	0.658	

(b)

Cytokines	Foveal RV				Parafoveal RV			
	β	SE	P value	R^2	β	SE	P value	R^2
ANGPTL4	3.371×10^{-6}	0.586×10^{-6}	<0.001	0.479	17.705×10^{-6}	3.285×10^{-6}	<0.001	0.447
VEGF-A	—	—	0.050		—	—	0.602	

(c)

Cytokines	Whole DVD				Parafoveal DVD			
	β	SE	P value	R^2	β	SE	P value	R^2
ANGPTL4	-1.705×10^{-4}	0.611×10^{-4}	0.008	0.178	-1.799×10^{-4}	0.665×10^{-4}	0.010	0.169
VEGF-A	—	—	0.148		—	—	0.238	

RT: Retinal thickness; RV: retinal volume; DVD: deep vessel density; —: without data from statistics software, multivariate linear regression models, $P < 0.05$ was deemed to be statistically significant.

density (SVD), foveal DVD, FD-300 vessel density, FAZ area, FAZ perimeter, and acircularity index among the three groups (all, $P > 0.05$) (Table 3).

3.4. Correlation between Cytokine Levels in Aqueous Humor and OCTA Metrics. For all the NPDR patients, correlations between the above differentially expressed cytokines including HGF, FGF19, IL-8, ANGPTL4, PLGF, VEGF-A, and the OCTA metrics including RT, RV, and DVD were analyzed. The levels of ANGPTL4 and VEGF-A were positively correlated with foveal RT ($rs = 0.569$, $P < 0.001$; $rs = 0.528$, $P = 0.001$), parafoveal RT ($rs = 0.555$, $P < 0.001$; $rs = 0.437$, $P = 0.006$), foveal RV ($rs = 0.566$, $P < 0.001$; $rs = 0.530$, $P = 0.001$), parafoveal RV ($rs = 0.519$, $P = 0.001$; $rs = 0.389$, $P = 0.016$), and negatively correlated with whole DVD ($rs = -0.352$, $P = 0.030$; $rs = -0.373$, $P = 0.021$) and parafoveal DVD ($rs = -0.421$, $P = 0.008$; $rs = -0.422$, $P = 0.008$). The level of PLGF was positively correlated with foveal RT ($rs = 0.363$, $P = 0.025$), parafoveal RT ($rs = 0.352$, $P = 0.030$), foveal RV ($rs = 0.365$, $P = 0.024$), and parafoveal RV ($rs = 0.326$, $P = 0.046$) but not with DVD ($P > 0.05$). The level of FGF-19 was positively correlated with parafoveal RT ($rs = 0.332$, $P = 0.042$) but not with foveal RT, RV, and DVD (all, $P > 0.05$). There were no correlations between HGF, IL-8, and RT, RV, and DVD, respectively (all, $P > 0.05$) (Table 4).

3.5. The Effect of Cytokines on OCTA Metrics. VEGF-A and ANGPTL4 with $P < 0.05$ in the single factor linear regression were further included in the multiple linear regression model (Table S1). Multiple regression analysis showed that the level of ANGPTL4 was an influencing factor for RT, RV, and DVD. The regression equations were fitted as follows: foveal RT = $223.422 + 4.299 \times 10^{-3} \times$ ANGPTL4, parafoveal RT = $294.302 + 3.598 \times 10^{-3} \times$ ANGPTL4, foveal RV = $0.176 + 3.371 \times 10^{-6} \times$ ANGPTL4, parafoveal RV = $1.838 + 17.705 \times 10^{-6} \times$ ANGPTL4, whole DVD = $46.587 - 1.705 \times 10^{-4} \times$ ANGPTL4, and parafoveal DVD = $49.265 - 1.799 \times 10^{-4} \times$ ANGPTL4. Every additional 10^3 pg/ml of ANGPTL4 was associated with an increase in foveal and parafoveal RT of 4.299 μm and 3.598 μm, respectively. Every additional 10^6 pg/ml of ANGPTL4 was associated with an increase in foveal and parafoveal RV of 3.371 mm^3 and 17.705 mm^3, respectively. Every additional 10^4 pg/ml of ANGPTL4 was associated with a decrease in whole and parafoveal DVD of 1.705% and 1.799%, respectively. The level of VEGF-A had no effect on RT, RV, and DVD (all, $P \geq 0.05$) (Table 5).

4. Discussion

Our study found that the levels of HGF, FGF-19, IL-8, ANGPTL4, PLGF, and VEGF-A increased in the aqueous humor of NPDR/DME+ patients, compared with NPDR/DME- and DWR patients. Notably, the levels of VEGF-A and ANGPTL4 were correlated with RT, RV, and DVD, in which single factor linear regression showed that both VEGF-A and ANGPTL4 were the influencing factors for RT, RV, and DVD. These findings supported the previous reports that VEGF-A contributed to the pathogenesis of DME [20, 21]. Cytokines with $P < 0.05$ in the single factor regression were further included in the multiple linear regression model. Although the P value for VEGF-A was 0.05, we still considered VEGF-A as an influencing factor for macular edema in NPDR patients. Moreover, in the models with multiple cytokines, VEGF-A had a greater impact on foveal RT and RV than other OCTA metrics.

Our study also found that the three groups were different from each other in the levels of ANGPTL4. Kwon et al. reported that both NPDR and PDR groups with similar severities of DME had higher levels of ANGPTL4 than the cataract controls, and the PDR group had a higher level than the NPDR group [22]. Here, we found that both DME+ and DME- groups with similar severities of NPDR had higher ANGPTL4 levels than the DWR group, and the DME+ group had a higher level than the DME- group. These results suggested that ANGPTL4 was also associated with of DME. Multiple regression analysis revealed that the level of ANGPTL4 in aqueous humor was an influencing factor for RT, RV, and DVD. NPDR patients with high levels of ANGPTL4 in the aqueous humor had higher foveal/parafoveal RT and RV and lower whole/parafoveal DVD than the patients with low levels of ANGPTL4.

As an angiogenesis factor, ANGPTL4 promotes the pathological processes of diverse eye diseases by enhancing angiogenesis, vascular permeability, and inflammation [23, 24]. Aqueous ANGPTL4 was obviously increased in PDR, inducing retinal neovascularization [25, 26]. Lu et al. demonstrated that ANGPTL-4 regulated diabetic retinal inflammation and angiogenesis by, at least partly, activating profilin-1 both in human retinal microvascular endothelial cells and in diabetic rats. Moreover, the activation of the ANGPTL4 was dependent on the overexpression of its upstream regulatory factor, HIF-1α [27]. Using the oxygen-induced retinopathy mouse model for ischemic retinopathy, Xin et al. provided the evidence that hypoxic Müller cells promoted vascular permeability by HIF-1–dependent upregulation of ANGPTL4 [28]. They also observed that inhibition of ANGPTL4 expression reduced the angiogenic potential and vascular permeability of hypoxic retinal Müller cells, which was additive with inhibition of VEGF expression [26]. Further, they identified the ANGPTL4/NRP/RhoA pathway as a therapeutic target for DME [14]. In the present study, multiple regression analysis suggested that ANGPTL4 might be more sensitive for NPDR and DME than VEGF-A, as shown by increased RT, RV, and decreased DVD. Overall, we hypothesized that ANGPTL4 may participate in the pathogenesis of DME through the above pathways, and targeting both ANGPTL4 and VEGF may be essential for effective management of DME.

We evaluated macular perfusion using 3×3 mm scan mode of OCTA which divided retina into foveal and parafoveal area. Compared with DWR and NPDR/DME- group, the whole and parafoveal DVD in NPDR/DME+ group were significantly decreased. The foveal DVD decreased with the severities of the three groups, although there was no statistical significance. Consistently, AttaAllah et al. [29] observed a reduction of parafoveal DVD in NPDR eyes with DME compared with diabetic eyes without DME. Furthermore, Toto et al. investigated the changes of retinal vessel in DME compared with normal controls and found a decrease in foveal and parafoveal DVD, especially in parafoveal area [30]. Similarly, we observed an obvious change of DVD in parafoveal area but not in foveal area, which may attribute to different controls included. Besides, Simonett et al. found that parafoveal DVD was decreased in DWR and NPDR patients compared with nondiabetic controls, while no difference was found in SVD [31, 32], which was consistent with our study. All these evidences suggested that, except for DR, the parafoveal nonperfusion in DCP was also an early indicator for DME. However, a large amount of data will be needed to determine the normal reference range of DVD.

Our study had several limitations. First, PDR patients without DME were usually treated with laser in clinical practice, and their aqueous humor samples could not be collected. For this reason, PDR patients were not included in our study. Further studies including PDR patients with or without DME are needed to explore the role of ANGPTL4 in all types of DR. Second, the stages of DME were not grouped, and thereby, ANGPTL4 involved in early or late stage of DME could not be determined. Considering the small sample size in this study, large sample size and detailed classification of DME will be necessary. Third, our study only analyzed the OCTA images with 3×3 mm scan centered on the fovea, which could not reflect the blood flow of whole retina. Therefore, larger images should be analyzed in the future.

In conclusion, our study showed that microvascular change of NPDR patients with DME initially occurs at DCP with decreased vascular density in parafoveal area. The level of ANGPTL4 in aqueous humor was significantly increased in NPDR patients with DME, and ANGPTL4 was an influencing factor for RT, RV, and DCP, suggesting that ANGPTL4 may predict the progression of DME in NPDR patients.

Data Availability

The data used to support the findings of this study are available from the corresponding author upon request.

Conflicts of Interest

The authors declare that there is no conflict of interest regarding the publication of this paper.

Acknowledgments

This work was supported by Xuzhou science and technology project (social development key project) (grant number KC21153), Xuzhou Medical Innovation (Technical Breakthrough) Team from Xuzhou Health and Planning Committee (grant number XWCX201610), and Key Research and Development Program (Social Development) of Xuzhou (grant number KC20152).

Supplementary Materials

Supplemental Table 1: single factor linear regression between cytokines and OCTA metrics. Single-factor linear regression showed that ANGPTL4 and VEGF-A were the influencing factors of RT, RV, and DVD (all, $P < 0.05$). *(Supplementary Materials)*

References

[1] T. Wang, J. Li, R. Xie et al., "Intraocular tumour necrosis factor ligand related molecule 1 A links disease progression of proliferative diabetic retinopathy after primary vitrectomy," *Clinical*

and Experimental Pharmacology & Physiology, vol. 47, no. 6, pp. 966–976, 2020.

[2] A. Markan, A. Agarwal, A. Arora, K. Bazgain, V. Rana, and V. Gupta, "Novel imaging biomarkers in diabetic retinopathy and diabetic macular edema," *Therapeutic Advances in Ophthalmology*, vol. 12, p. 251584142095051, 2020.

[3] D. P. Hainsworth, I. Bebu, L. P. Aiello et al., "Risk factors for retinopathy in type 1 diabetes: the DCCT/EDIC study," *Diabetes Care*, vol. 42, no. 5, pp. 875–882, 2019.

[4] S. Torres-Costa, M. C. Alves Valente, F. Falcao-Reis, and M. Falcao, "Cytokines and growth factors as predictors of response to medical treatment in diabetic macular edema," *The Journal of Pharmacology and Experimental Therapeutics*, vol. 373, no. 3, pp. 445–452, 2020.

[5] A. Daruich, A. Matet, A. Moulin et al., "Mechanisms of macular edema: beyond the surface," *Progress in Retinal and Eye Research*, vol. 63, pp. 20–68, 2018.

[6] F. Yenihayat, B. Ozkan, M. Kasap et al., "Vitreous IL-8 and VEGF levels in diabetic macular edema with or without subretinal fluid," *International Ophthalmology*, vol. 39, no. 4, pp. 821–828, 2019.

[7] M. Figueras-Roca, A. Sala-Puigdollers, S. Alforja et al., "Aqueous humour cytokine changes with intravitreal dexamethasone implant injection for diabetic macular edema," *Ocular Immunology and Inflammation*, vol. 27, no. 8, pp. 1203–1210, 2019.

[8] Y. R. Chung, Y. H. Kim, S. J. Ha et al., "Role of inflammation in classification of diabetic macular edema by optical coherence tomography," *Journal Diabetes Research*, vol. 2019, article 8164250, 8 pages, 2019.

[9] P. Romero-Aroca, M. Baget-Bernaldiz, A. Pareja-Rios, M. Lopez-Galvez, R. Navarro-Gil, and R. Verges, "Diabetic macular edema pathophysiology: vasogenic versus inflammatory," *Journal Diabetes Research*, vol. 2016, article 2156273, 17 pages, 2016.

[10] B. Sedziak-Marcinek, S. Teper, E. Chelmecka et al., "Diabetic macular edema treatment with bevacizumab does not depend on the retinal nonperfusion presence," *Journal Diabetes Research*, vol. 2021, article 6620122, 15 pages, 2021.

[11] Q. Wei, Z. Wan, Y. Hu, and Q. Peng, "Cytokine and chemokine profile changes in patients after intravitreal conbercept injection for diabetic macular edema," *Drug Design, Development and Therapy*, vol. 13, pp. 4367–4374, 2019.

[12] S. Bandyopadhyay, S. K. Bandyopadhyay, M. Saha, and A. Sinha, "Study of aqueous cytokines in patients with different patterns of diabetic macular edema based on optical coherence tomography," *International Ophthalmology*, vol. 38, no. 1, pp. 241–249, 2018.

[13] G. Wu, B. Liu, Q. Wu et al., "Correlations between different angiogenic and inflammatory factors in vitreous fluid of eyes with proliferative diabetic retinopathy," *Frontiers in Medicine*, vol. 8, article 727407, 2021.

[14] A. Sodhi, T. Ma, D. Menon et al., "Angiopoietin-like 4 binds neuropilins and cooperates with VEGF to induce diabetic macular edema," *The Journal of Clinical Investigation*, vol. 129, no. 11, pp. 4593–4608, 2019.

[15] M. B. Peres, R. T. Kato, V. F. Kniggendorf et al., "Comparison of optical coherence tomography angiography and fluorescein angiography for the identification of retinal vascular changes in eyes with diabetic macular edema," *Ophthalmic Surgery, Lasers & Imaging Retina*, vol. 47, no. 11, pp. 1013–1019, 2016.

[16] C. P. Wilkinson, Ferris FL 3rd, R. E. Klein et al., "Proposed international clinical diabetic retinopathy and diabetic macular edema disease severity scales," *Ophthalmology*, vol. 110, no. 9, pp. 1677–1682, 2003.

[17] M. Inanc, K. Tekin, H. Kiziltoprak, S. Ozalkak, S. Doguizi, and Z. Aycan, "Changes in retinal microcirculation precede the clinical onset of diabetic retinopathy in children with type 1 diabetes mellitus," *American Journal of Ophthalmology*, vol. 207, pp. 37–44, 2019.

[18] K. Ghasemi Falavarjani, N. A. Iafe, J. P. Hubschman, I. Tsui, S. R. Sadda, and D. Sarraf, "Optical coherence tomography angiography analysis of the foveal avascular zone and macular vessel density after anti-VEGF therapy in eyes with diabetic macular edema and retinal vein occlusion," *Investigative Ophthalmology & Visual Science*, vol. 58, no. 1, pp. 30–34, 2017.

[19] F. Zhang, P. Chang, Y. Zhao, and Y. Zhao, "A negative correlation of axial length with aqueous humor concentration of cytokines in patients with congenital cataracts," *Molecular Vision*, vol. 26, pp. 91–96, 2020.

[20] S. W. Lim, E. Bandala-Sanchez, M. Kolic et al., "The influence of intravitreal ranibizumab on inflammation-associated cytokine concentrations in eyes with diabetic macular edema," *Investigative Ophthalmology & Visual Science*, vol. 59, no. 13, pp. 5382–5390, 2018.

[21] S. Y. Yu, D. H. Nam, and D. Y. Lee, "Changes in aqueous concentrations of various cytokines after intravitreal bevacizumab and subtenon triamcinolone injection for diabetic macular edema," *Graefe's Archive for Clinical and Experimental Ophthalmology*, vol. 256, no. 1, pp. 39–47, 2018.

[22] S. H. Kwon, J. P. Shin, I. T. Kim, and D. H. Park, "Aqueous levels of angiopoietin-like 4 and semaphorin 3E correlate with nonperfusion area and macular volume in diabetic retinopathy," *Ophthalmology*, vol. 122, no. 5, pp. 968–975, 2015.

[23] X. Yang, J. Cao, Y. Du, Q. Gong, Y. Cheng, and G. Su, "Angiopoietin-like protein 4 (ANGPTL4) induces retinal pigment epithelial barrier breakdown by activating signal transducer and activator of transcription 3 (STAT3): evidence from ARPE-19 cells under hypoxic condition and diabetic rats," *Medical Science Monitor*, vol. 25, pp. 6742–6754, 2019.

[24] X. Yang, Y. Cheng, and G. Su, "A review of the multifunctionality of angiopoietin-like 4 in eye disease," *Bioscience Reports*, vol. 38, no. 5, 2018.

[25] Q. Lu, W. Zou, B. Chen, C. Zou, M. Zhao, and Z. Zheng, "ANGPTL-4 correlates with vascular endothelial growth factor in patients with proliferative diabetic retinopathy," *Graefe's Archive for Clinical and Experimental Ophthalmology*, vol. 254, no. 7, pp. 1281–1288, 2016.

[26] S. Babapoor-Farrokhran, K. Jee, B. Puchner et al., "Angiopoietin-like 4 is a potent angiogenic factor and a novel therapeutic target for patients with proliferative diabetic retinopathy," *Proceedings of the National Academy of Sciences of the United States of America*, vol. 112, no. 23, pp. E3030–E3039, 2015.

[27] Q. Lu, P. Lu, W. Chen, L. Lu, and Z. Zheng, "ANGPTL-4 induces diabetic retinal inflammation by activating profilin-1," *Experimental Eye Research*, vol. 166, pp. 140–150, 2018.

[28] X. Xin, M. Rodrigues, M. Umapathi et al., "Hypoxic retinal Muller cells promote vascular permeability by HIF-1-dependent up-regulation of angiopoietin-like 4," *Proceedings of the National Academy of Sciences of the United States of America*, vol. 110, no. 36, pp. E3425–E3434, 2013.

[29] H. R. AttaAllah, A. A. M. Mohamed, and M. A. Ali, "Macular vessels density in diabetic retinopathy: quantitative assessment

using optical coherence tomography angiography," *International Ophthalmology*, vol. 39, no. 8, pp. 1845–1859, 2019.

[30] L. Toto, R. D'Aloisio, M. di Nicola et al., "Qualitative and quantitative assessment of vascular changes in diabetic macular edema after dexamethasone implant using optical coherence tomography angiography," *International Journal of Molecular Sciences*, vol. 18, no. 6, p. 1181, 2017.

[31] J. M. Simonett, F. Scarinci, F. Picconi et al., "Early microvascular retinal changes in optical coherence tomography angiography in patients with type 1 diabetes mellitus," *Acta Ophthalmologica*, vol. 95, no. 8, pp. e751–e755, 2017.

[32] J. Khadamy, K. Abri Aghdam, and K. G. Falavarjani, "An update on optical coherence tomography angiography in diabetic retinopathy," *J. Ophthalmic Vis. Res.*, vol. 13, no. 4, pp. 487–497, 2018.

Hindawi
Journal of Diabetes Research
Volume 2022, Article ID 7723706, 9 pages
https://doi.org/10.1155/2022/7723706

Research Article

Fluorescein Leakage and Optical Coherence Tomography Angiography Features of Microaneurysms in Diabetic Retinopathy

Ruoyu Chen,[1,2] Anyi Liang,[1] Jie Yao,[1,3] Zicheng Wang,[1,4] Yesheng Chen,[1,5] Xuenan Zhuang,[1,3] Yunkao Zeng,[1,3] Liang Zhang,[1] and Dan Cao[1,2,5]

[1]*Department of Ophthalmology, Guangdong Provincial People's Hospital, Guangdong Academy of Medical Sciences, Guangzhou 510080, China*
[2]*The Second School of Clinical Medicine, Southern Medical University, Guangzhou 510515, China*
[3]*Shantou University Medical College, Shantou 515041, China*
[4]*School of Medicine, South China University of Technology, Guangzhou 510080, China*
[5]*Guangdong Cardiovascular Institute, Guangzhou 510000, China*

Correspondence should be addressed to Dan Cao; dancao5413@163.com

Received 19 August 2021; Revised 6 November 2021; Accepted 14 December 2021; Published 13 January 2022

Academic Editor: Akira Sugawara

Background and Objective. To correlate optical coherence tomography angiography (OCTA) characteristics of diabetic microaneurysms (MAs) with leakage status on fluorescein angiography (FA). *Patients and Methods.* 167 MAs from 39 diabetic eyes were analyzed using OCTA and FA simultaneously. The characteristics of MAs on OCTA en face, OCT en face, and OCT B-scan with flow overlay were evaluated and correlated with fluorescein leakage status. *Results.* Thirty-six, fifty-two, and seventy-nine MAs showed no, mild, and severe leakage on FA, respectively. Most MAs (61.7%) were centered in the inner nuclear layer. Cystoid spaces were observed adjacent to 60 (35.9%) MAs. MAs with severe leakage had a statistically higher flow proportion compared to MAs with no or mild leakage (both $P < 0.001$). Only 112 MAs (67.1%) were visualized in the OCTA en face images, while 165 MAs (98.8%) could be visualized in the OCT en face images. The location of MAs did not associate significantly with FA leakage status. The presence of nearby cystoid spaces and higher flow proportion by OCT B-scan with flow overlay correlated significantly with FA leakage status. *Conclusion.* The flow proportion of MAs observed on OCT B-scans with flow overlay might be a potential biomarker to identify leaking MAs. A combination of OCT B-scan, OCT en face, and OCTA en face images increased the detection rate of diabetic MAs in a noninvasive way.

1. Introduction

Diabetic retinopathy (DR) is the leading cause of blindness in working age population around the world [1, 2]. MA presents as a small round deep-red dot on fundus color photograph, which is the initial sign appearing in DR patients, as well as the hallmark of clinical diagnosis of DR [3]. Fluorescein angiography (FA) can detect about twice as many MAs as on fundus photograph, which makes it a better tool to discern subtle microvascular abnormalities in DR. Fluorescein leakage from MAs was positively associated with capsular structure disorder and blood-retina barrier breakdown, resulting in vision-threatening focal or diffuse retinal edema [4]. Focal laser therapy guided by FA plays an important role in diabetic macular edema (DME) management, which can accurately close leaking MAs and reduce leakage through the disrupted blood–retinal barrier [5]. However, FA is unsuitable for regular screening of DR because of its potential adverse reactions.

Structural optical coherence tomography (OCT) is a complementary modality that can visualize MAs in a noninvasive way. MAs appear as round or oval well-demarcated intraretinal hyperreflective lesions in OCT B-scan. Optical coherence tomography angiography (OCTA) is another

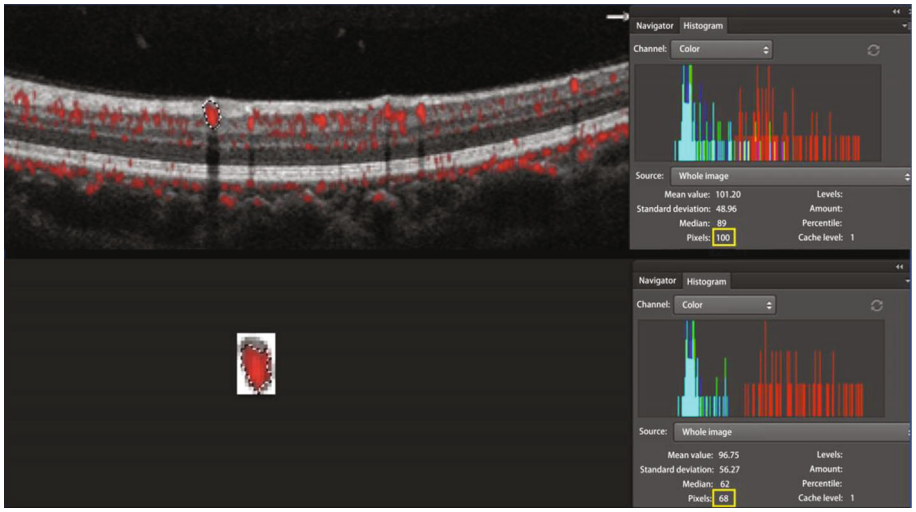

Figure 1: The measurement of flow proportion. MA area and flow area were measured using a Photoshop program. Every MA area in OCT B-scan with flow overlay was dragged using the Photoshop dragging tool and a tablet pen. The histogram of every dragged image was examined and the pixel value of each dragged area was obtained. After that, the selected MA area was cropped out using the Photoshop cropping tool and was pasted to a new image. The flow area in the new MA image was also dragged using the Photoshop dragging tool, and the pixel value of each dragged area was calculated in the histogram panel. Flow proportion was defined as the ratio of flow area divided by MA area. The flow proportion of the MA selected in the figure was 68% (68 pixels/100 pixels).

noninvasive imaging technique that provides three-dimensional images of the retinal and choroidal microvasculature. Recently, OCTA has displayed its effectiveness in monitoring DR progression and provided more details of microvascular alterations than FA [6–8]. Now the review software implemented in OCTA enables us to observe individual structural OCT B-scans with flow overlay. AngioAnalytics software built in AngioVue OCTA system, which provides fine histologic visualization of both the retinal microstructure and the blood flow at the same time. However, one of the major disadvantages of OCTA is its inability to visualize the leakage.

To our knowledge, there is no prior study correlating the MAs on OCTA en face images, OCT en face images, OCT B-scan with flow overlay, and FA images. The purpose of this study was to find out whether certain characteristics of MAs on OCTA en face images, and OCT B-scan with flow overlay could reflect the leakage status of MAs on FA images.

2. Methods

2.1. Subjects. In this retrospective, cross-sectional observational study, thirty-nine patients with type 2 diabetes mellitus (T2DM) and complicated with nonproliferative diabetic retinopathy (NPDR) were included. The diagnosis of T2DM was established according to the diagnostic criteria of American Diabetes Association [9]. Informed consent was obtained from each study participant before examination. Diagnosis and classification of DR were confirmed according to the international clinical diabetic retinopathy and diabetic macular edema disease severity scales [10].

All enrolled subjects were evaluated and underwent successively OCTA and FA imaging at the Ophthalmology Department, Guangdong Provincial People's Hospital, Guangzhou between June 1, 2019 and December 30, 2019. One eye of each patient was randomly selected if both eyes were eligible. The OCTA and FA imaging were evaluated by two masked retina specialists (DC and LZ) independently, and in case of disagreement, there was open adjudication until a consensus was established. The case series were performed according to the Declaration of Helsinki and was approved by the Research Ethics Committee of Guangdong Provincial People's Hospital (registration number: GDREC2018380H (R2)). Eyes with MAs with good-quality FA and OCTA images available were included.

The exclusion criteria were as follows: (1) patients with other retinal vascular diseases; (2) patients with history of intraocular surgeries including antivascular endothelial growth factor (VEGF) treatment, etc.; (3) patients treated with direct photocoagulation of the MAs, or focal/grid photocoagulation, and/or panretinal photocoagulation within 6 months; and (4) patients with ocular conditions that affect imaging of OCTA (scan quality < 6, e.g. advanced cataract).

2.2. Image Acquisition. All participants were tested for best corrected visual acuity (BCVA), intraocular pressure (IOP), and refractive error (measured with autorefractometry). Slit-lamp and fundus examinations using direct and/or indirect ophthalmoscope were performed. ETDRS 35 degree 7-standard fields color retinal photographs (Topcon TRC; Topcon, Tokyo, Japan) were obtained from each participant.

Fifty-five-degree FA images were obtained using Heidelberg Retinal Angiography 2 (Spectralis HRA2; Heidelberg Engineering, Heidelberg, Germany). MAs were detected as hyperfluorescent dots in the early phase of FA imaging, and leakage was graded as no, mild, or severe by comparing the FA images of the MAs in the early phase with those in the late phase, as described by Wang and colleagues [11].

OCTA examinations were conducted at the same day after pupil dilation and before the FA acquisition by using

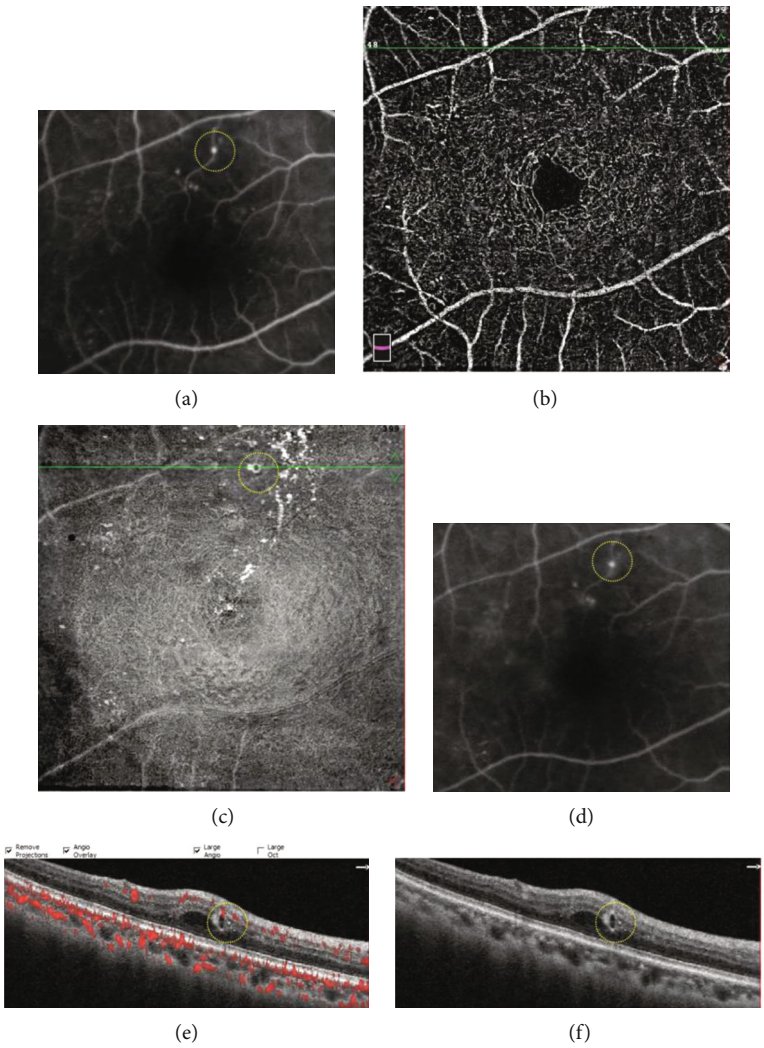

Figure 2: A typical diabetic microaneurysm with no leakage seen by FA (yellow circle (a), early phase of FA (d), late phase of FA). The microaneurysm was not visualized in OCTA en face image (b). On OCT en face image, the microaneurysm appeared as luminescent ring-shaped morphology (c). The microaneurysm was recognized as an oval well-demarcated lesion on OCT B-scan (f), and the lumen was devoid of flow signal on OCT B-scan with flow overlay (e).

AngioVue OCTA system (RTVue-XR Avanti; Optovue, Fremont, CA, USA). We chose the macular HD 6 mm × 6 mm program, which uses an 840 nm light source and provides 70,000 A scans/second. Superficial vascular complex (SVC) and deep vascular complex (DVC) were automatically generated by the built-in software. SVC is defined as a slab extending from internal limiting membrane (ILM) to 10 μm above inner plexiform layer (IPL). DVC is a slab extending from 10 μm above IPL to 10 μm below outer plexiform layer (OPL).

The built-in AngioAnalytics software (version 2017.1.0.151) was adopted which included important advance in three-dimensional projection artifact removal (3D PAR). With 3D PAR, projection artifacts are minimized pixel-by-pixel throughout the entire OCTA volume, facilitating clearer visualization of vascular structures in en face images and in B-scans at all depths. MAs were classified according to three types of shape: nodular type, comma-like type, and absent type. MAs that were visible as nodular findings on OCTA en face images were defined as the nodular type. MAs presented as coil-shaped, comma-shaped, semilunar, crescent, or earlobe-like shape were all defined as the comma-like type. MAs that could not be not be confirmed on OCTA en face images were defined as the absent type [12].

The 6 mm × 6 mm AngioRetina scan could provide 400 OCT B-scans spanning 15 μm apart as well as OCT B-scans with flow overlay. The flow information can be visualized in the cross-sectional B-scans, allowing us to analyze retinal microstructure together with perfused retinal vasculature.

Flow proportion was defined as the ratio of flow area divided by MA area. MA area and flow area were measured using Photoshop (AdobeSystems, San Jose, CA, USA). Every MA area in the OCT B-scan image with flow overlay was dragged using the Photoshop dragging tool (Figure 1), and a color histogram of each dragged image was examined. The pixel value of each dragged area in the individual frames was calculated and defined as the total area of each MA. After that, the selected MA area was cropped out using the

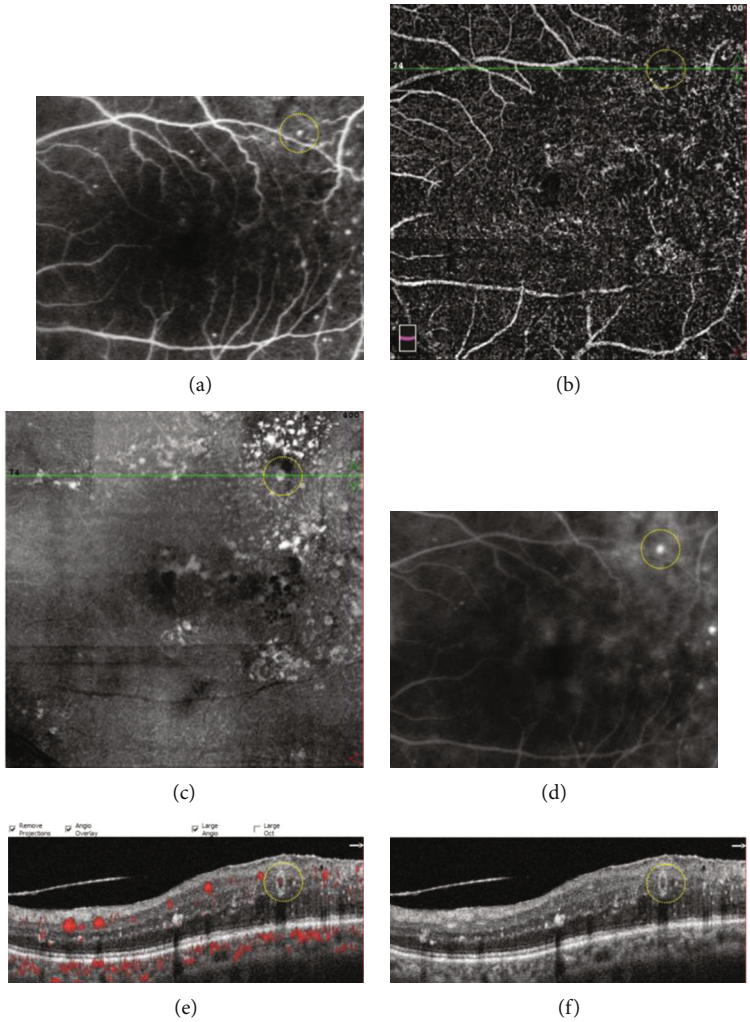

Figure 3: A typical diabetic microaneurysm with mild leakage on FA (yellow circle (a), early phase of FA (d), late phase of FA). The microaneurysm was visualized as comma-like type in OCTA en face image (yellow circle (b)). On OCT en face image, the microaneurysm appeared as a luminescent spot (yellow circle (c)). The microaneurysm was recognized an oval well-demarcated lesion on OCT B-scan (yellow circle (f)), and the flow proportion of the microaneurysm was 24.8% on OCT B-scan with flow overlay (yellow circle (e)).

Photoshop cropping tool and was pasted to a new image. The flow area in the new MA image was also dragged using the Photoshop dragging tool, and the pixel value of each dragged area was calculated in the color histogram panel and defined as the area of flow.

To compare the MAs seen on FA to those seen on OCT en face/OCTA en face/OCT B-scan, we superimposed the FA macular vascular landmarks onto the vascular landmarks of the OCTA SVC and vascular landmarks on the near infrared images. In addition, we observed cystoid spaces surrounding the MAs on the OCT B-scan images, and we determined whether surrounding cystoid spaces was present or absent. We also analyzed the distributions of MAs by defining which layer the center of each MA went through (Figures 2–4).

2.3. Statistical Analysis. Statistical analysis was performed with SPSS software package version 19.0 (SPSS. Inc., Chicago, IL, USA). The Wilcoxon signed rank test was used to compare the morphology of the MAs in the OCTA en face images, FA findings, distribution of MAs (OCT B-scan), flow proportion of MAs, and presence of nearby cystoid spaces around the MAs. For all the tests, $P < 0.05$ was considered statistically significant.

3. Results

3.1. Baseline Data. A total of 39 eyes from 39 DR patients were included in the study, comprising of 10 eyes with mild NPDR (25.6%), 16 eyes with moderate NPDR (41.1%), and 13 eyes with severe NPDR (33.3%). Gender distribution, mean age, and BCVA of patients were listed in Table 1. The mean age, the mean duration of T2DM, and the mean glycosylated hemoglobin (HbA1c) of enrolled subjects was 58.3 ± 7.2 years, 8.6 ± 4.3 years, and 8.9 ± 2.6%, respectively.

3.2. Fluorescein Angiography. A total of 167 MAs in 39 diabetic eyes were evaluated by FA and OCTA imaging

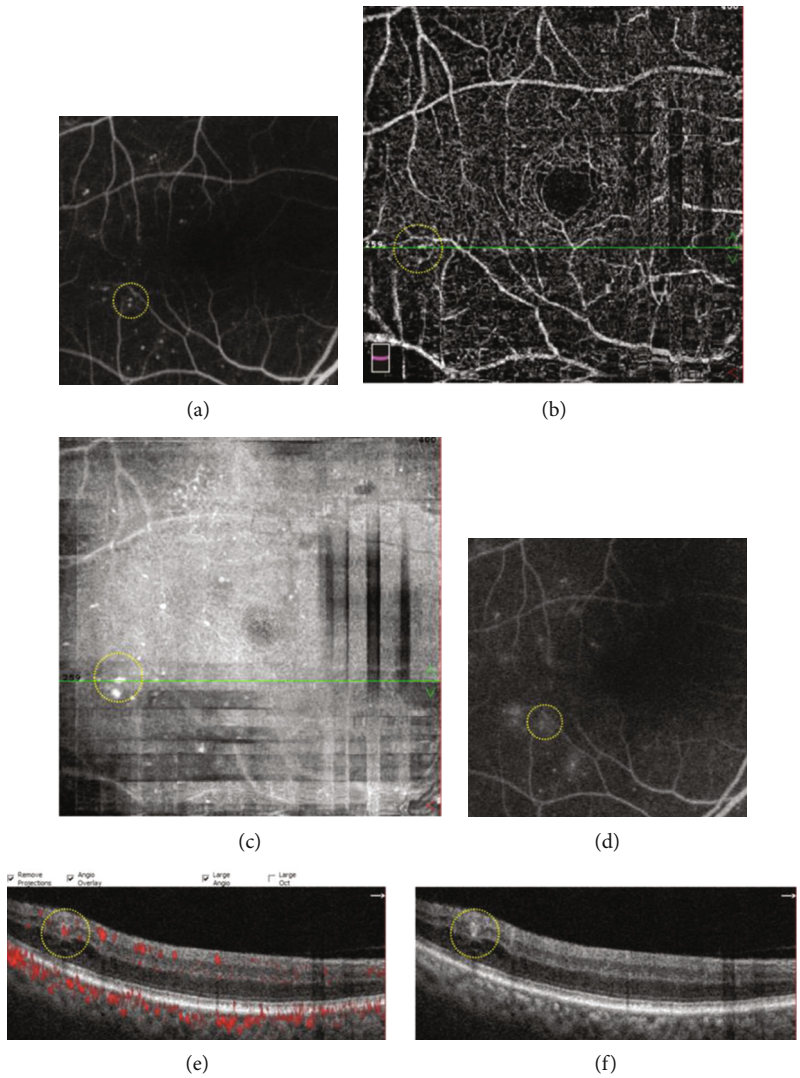

Figure 4: A typical diabetic microaneurysm with severe leakage on FA (yellow circle (a), early phase of FA (d), late phase of FA). The microaneurysm was visualized as nodular type in OCTA en face image (yellow circle (b)). On OCT en face image, the microaneurysm appeared as a luminescent spot (yellow circle (c)). The microaneurysm was recognized a thin-walled oval lesion on OCT B-scan with a retinal cyst nearby (yellow circle (f)), and the flow proportion of the microaneurysm was 57.8% on OCT B-scan with flow overlay (yellow circle (e)).

Table 1: Demographics of patients.

Eyes/patients	39/39
Male/female	20/19
Age, years	58.3 ± 7.2
BCVA (ETDRS letters)	75.3 ± 3.1
Duration of diabetes, years	8.6 ± 4.3
HbA1c, mean ± SD (%)	8.9 ± 2.6
DR stage, *N* eyes (%)	
Mild NPDR	10 (25.6%)
Moderate NPDR	16 (41.1%)
Severe NPDR	13 (33.3%)

DR: diabetic retinopathy; *n*: number.

simultaneously. Seventy-nine out of 167 MAs showed severe leakage (47.4%), followed by 52 MAs with mild leakage (31.1%). The number of MAs with no leakage on FA was 36 (21.5%).

3.3. Distribution of Diabetic MAs. The center of diabetic MAs was observed mostly in inner nuclear layer (103/167, 61.7%), followed by inner plexiform layer (35/167, 20.9%), retinal nerve fiber layer/ganglion cell layer (16/167, 9.6%), outer plexiform layer (11/167, 6.6%), and outer nuclear layer (2/167, 1.2%) (Figure 5). The distribution of MAs was not significantly correlated with FA leakage status ($P = 0.774$).

3.4. Adjacent Cystoid Spaces of MAs by OCT B-Scan. Cystoid spaces were observed adjacent to 60 MAs (35.9%). Adjacent cystoid spaces on OCT B-scan were associated with increasing FA leakage status ($P < 0.001$). In the severe leakage

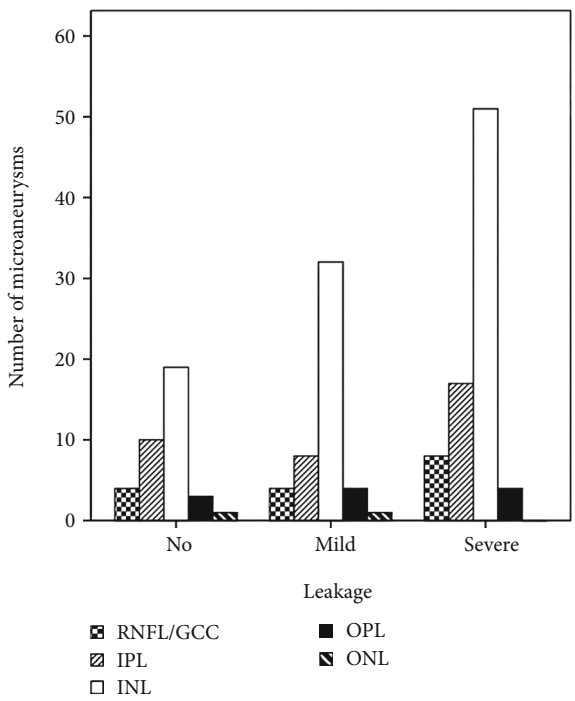

Figure 5: Distribution of the center of diabetic microaneurysms ($N = 167$) by retinal layers. RNFL: retinal nerve fiber layer; GCC: ganglion cell layer; IPL: inner plexiform layer; INL: inner nuclear layer; OPL: outer plexiform layer; ONL: outer nuclear layer.

group, 55.7% MAs had nearby cystoid spaces, while only 5.6% MAs with no leakage had nearby cysts (Figure 6).

3.5. Flow Proportion of Diabetic MAs. MA area and flow area of each MA were measured using Photoshop, and the flow proportion was recorded. MAs with severe leakage had a significantly higher flow proportion compared to MAs with no or mild leakage (both $P < 0.001$) (Table 2, Figure 7).

3.6. Visualization of Diabetic MAs Using Different Imaging Modalities. Of the 167 diabetic MAs, only 112 MAs (67.1%) were visualized in the OCTA en face images, while 165 MAs (98.8%) could be visualized in the OCT en face images. OCT en face images had a 100% detection rate of MAs with no leakage and mild leakage in FA. However, only 22.2% of MAs with no leakage and 67.3% of MAs with mild leakage could be seen in the OCTA en face images. With regard to the MAs with severe leakage, OCTA en face images could detect 87.3% of them and OCT en face images could detect 97.5% of them (Table 3).

3.7. Type of MA Visualized by OCTA En Face Image. Altogether there were 81 nodular type (48.5%), 31 comma-like type (18.6%), and 55 absent type (32.9%) MAs in the 167 angiographically visible MAs. The type of MAs visualized by OCTA en face images was significantly correlated with FA leakage status ($P < 0.001$). MAs with no leakage showed more absent type on OCTA en face than MAs with mild or severe leakage (Figure 8).

4. Discussion

This study outlined particular characteristics of diabetic MAs on OCTA en face and OCT B-scan with flow overlay, with the aim of correlating these features of MAs on noninvasive examinations to the leakage status of MAs on FA images. Our results demonstrated that only 67.1% MAs visualized on FA were detected by OCTA, while 98.8% MAs were seen in OCT en face images. MAs with severe leakage are easier to be recognized in OCTA en face images compared to those with no leakage (87.3% versus 22.2%). Besides, most MAs centered in DVC (INL>IPL>RNFL/GCC>OPL) and the location of MAs did not seem to affect their leakage status. However, increasing FA leakage of MAs was associated with adjacent cystoid spaces and higher flow proportion in the OCT B-scan with flow overlay.

Diabetes is characterized by vessel basement membrane thickening and selective degeneration with pericyte loss, which leads to asymmetric dilatations of the capillary wall where it is weakened. The loss of supporting pericytes and localized increase in hydrostatic pressure subsequently caused the formation of MAs. Histological studies showed that the MAs ranged in morphology from thin-walled, cellular forms to dense, acellular, hyalinized forms. Lumen contents of microaneurysms may be comprised of polymorphonuclear cells, red blood cells, fibrotic cells, thrombi, or lipid aggregates. And most of MAs were observed in the inner layers of the retina although, less frequently, they could be found in the outer plexiform layer [13–15].

Our results demonstrated that adjacent cystoid spaces were associated with increased leakage of MAs on FA images, which is in accordance with previous studies that the leakage of MAs is the contributing factor to extracellular fluids aggregation and diabetic macular edema [16]. Thus, monitoring the extent of leakage of MAs may be advantageous to macular edema treatment. In the clinical setting, FA can provide good capillary images showing leakage of MAs. Focal laser photocoagulation targeting leaking diabetic MAs with FA guidance can increase accuracy and hit rate of laser. Moreover, FA can be used to evaluate the closure of MAs and monitor the progression of DME [5]. However, FFA is invasive, time-consuming, and with the potential side effect that is not suitable in certain conditions, such as pregnancy and kidney failure. Thus, it could not be applied to every patient in daily practices.

Ito et al. [17] evaluated the characteristics of diabetic MAs seen on color fundus photography, FA, and spectral domain OCT (SD-OCT). They found that focal fluorescein leakage from MAs was associated positively with the absence of a capsular structure, hyperreflective spots in the lumen, and nearby cystoid spaces. Horii et al. [18] characterized MAs in DR depicted by SD-OCT and categorized the MAs into 3 types (complete ring sign, incomplete ring sign, and no structure) according to the status of the capsule structure, and they showed that MAs with the ring sign were positively correlated with nearby cystoid spaces and protrusion into the cystoid spaces.

A previous study had assessed the internal reflectivity of MAs on SD-OCT B-scan and compared them with MA

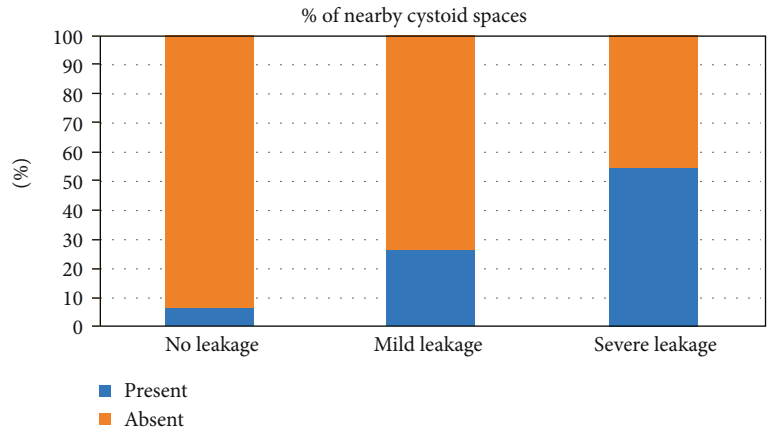

Figure 6: Percentages of presence of nearby cystoid spaces around diabetic microaneurysms in different fluorescein leakage groups.

Table 2: Flow proportion of diabetic microaneurysms by OCT B-scan with flow overlay.

Leakage status	*N*	Median	Range
No leakage	36	10.1%	0-53.2%
Mild leakage	52	35.0%	20.2%-86.1%
Severe leakage	79	71.1%	30.3%-95.6%
P value		<0.001	

OCT: optical coherence tomography; *N*: number.

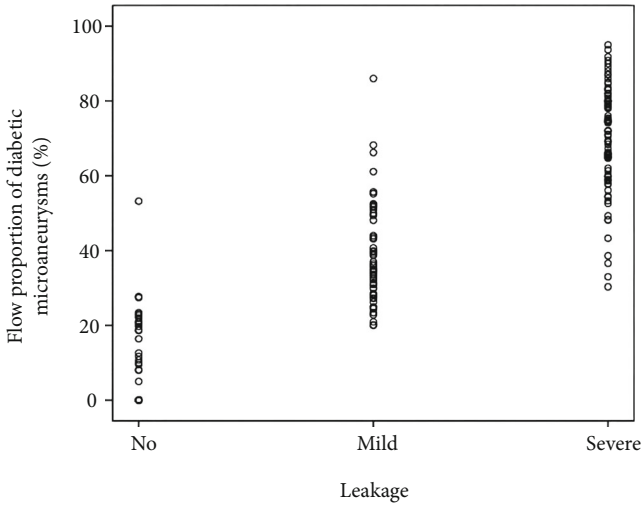

Figure 7: Scatter plot of flow proportion of diabetic microaneurysms in different fluorescein leakage groups.

visualization on the OCTA images. The authors found that MAs with internal hyporeflectivity on SD-OCT B-scan had a significantly lower detection rate on OCTA (66.7%) compared to MAs with internal hyperreflectivity (88.9%) or moderate reflectivity (88.9%) [19]. They further investigated the progression of diabetic MAs according to the SD-OCT and OCTA characteristics and found that the presence of flow, the visibility, and the deep location were strongly associated with the development of extracellular fluid at 12 months [20]. However, the internal reflectivity of MAs on OCT B-scan is not a true reflection of blood flow proportion of MAs.

Recently, OCTA has become more available and popular. Because of its rapidness and noninvasiveness, OCTA can provide much of the information given by FA. However, OCTA cannot visualize the leakage. Now, the OCTA with AngioVue provides 3D PAR, facilitating clearer visualization of vascular structures in en face images and in B-scans at all depth. The OCT B-scan with flow overlay generated by AngioVue device offers a new aspect for us to investigate the flow signal and microstructure of MAs at the same time. Our study defined flow proportion as the ratio of flow area divided by MA area in OCT B-scan images with the help of Photoshop, and the results indicated that high flow proportion of MAs on segmentation OCT B-scan with flow overlay correlated well with increasing leakage of MAs on FA. Therefore, OCT B-scan with flow overlay could be a clinically useful tool to predict the leakage status of diabetic MAs and to monitor the turnover of MAs. If we combine the flow proportion of MAs and the structure findings on OCT B-scan together, for example nearby cystoid spaces in a diabetic eye with macular edema, we might be able to monitor its treatment response. Our study has provided a new prospective to observe flow signal changes inside the MAs, so that we can evaluate the turnover of MAs more objectively.

Couturier et al. [21] analyzed the clinical features of 20 eyes of 14 patients with DR and concluded that FA is more sensitive than OCTA in detecting MAs. They found that only 62% of microaneurysms visualized on FA were detected by OCTA, which is quite similar to the detection rate of MAs on OCTA en face images in our study (112/167, 67.1%). Therefore, OCTA en face image alone is not sensitive enough to observe MAs. MAs observed on OCTA en face images had a broad range of morphologies, including focal bulging, saccular, fusiform, mixed saccular/fusiform, pedunculated, and irregular form [22]. Sometimes it is difficult to differentiate MAs from the capillary background on OCTA en face images, and only MAs with a certain amount of flow signal can be detected on OCTA en face images. The above

Table 3: FA leakage status and OCTA/OCT en face visualization of diabetic MAs.

FA leakage status	Number of MAs, *N*	OCTA en face visualization, *N* (%)	OCT en face visualization, *N* (%)
No leakage	36	8 (22.2%)	36 (100%)
Mild leakage	52	35 (67.3%)	52 (100%)
Severe leakage	79	69 (87.3%)	77 (97.5%)

FA: fluorescein angiography; OCTA: optical coherence tomography angiography; OCT: optical coherence tomography; MA: microaneurysm; *N*: number.

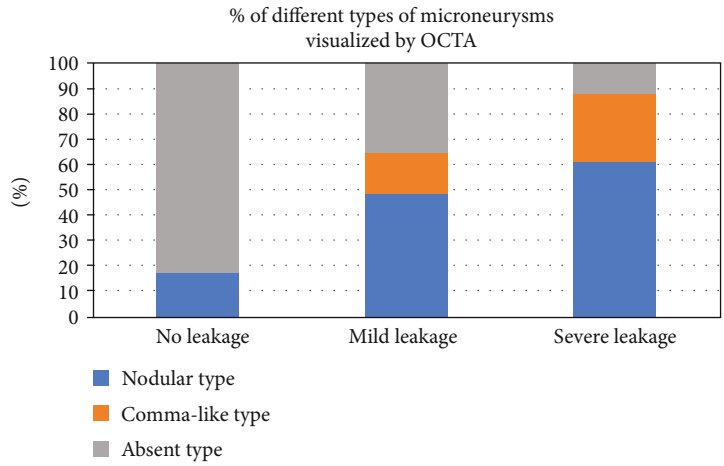

Figure 8: Percentages of different types of microaneurysms visualized by OCTA in different fluorescein leakage groups. OCTA: optical coherence tomography angiography.

reasons accounted for the relatively low detection rate of MAs on OCTA.

On OCT enface images, MAs appeared as luminescent ring-shaped morphologies or spots. Our results showed that nearly all the MAs could be located in the corresponding area where angiographically visible MAs lied in. Therefore, if we combine OCT B-scan, OCT en face, and OCTA en face images together, the detection rate of MAs can be raised to about 98.8% in our study.

Our study has some limitations. Firstly, our results showed that flow proportion of MAs might be a possible biomarker to identify leaking MAs, but this is a preliminary result based on small simple size. Larger studies are needed to learn more about this relationship between flow proportion and leakage status of MAs. Secondly, it was a cross-sectional study. The leakage status or flow proportion of MAs was not followed up continuously. This situation deserves special attention in future studies. Thirdly, although potential source of error has been minimized in calculating flow proportion, MA area and flow area were manually selected, so the accuracy of these two components might be lost to some degree. Potential automatic analysis software may help to solve this problem and improve accuracy of flow proportion in the future.

In conclusion, OCT B-scan with flow overlay might be a good alternative to assess leakage of MAs in diabetic eyes. The presence of adjacent cystoid spaces around MAs on OCT B-scan correlated positively with leakage status seen on FA. A combination of OCT B-scan with flow overlay, OCT en face, and OCTA en face imaging appears to be a superior method for detecting MAs when only using OCTA imaging.

Data Availability

The data used to support the findings of this study are available if needed.

Conflicts of Interest

The authors declare that there is no conflict of interest regarding the publication of this paper.

Authors' Contributions

Ruoyu Chen and Anyi Liang contributed equally to this work.

Acknowledgments

This study was supported by the Guangzhou Science and Technology Program (Grant Number: 201904010092) and Bethune Merck Diabetes Research Foundation (Grant Number: 2018-133).

References

[1] D. S. Ting, G. C. Cheung, and T. Y. Wong, "Diabetic retinopathy: global prevalence, major risk factors, screening practices and public health challenges: a review," *Clinical & Experimental Ophthalmology*, vol. 44, no. 4, pp. 260–277, 2016.

[2] J. E. Shaw, R. A. Sicree, and P. Z. Zimmet, "Global estimates of the prevalence of diabetes for 2010 and 2030," *Diabetes Research and Clinical Practice*, vol. 87, no. 1, pp. 4–14, 2010.

[3] E. M. Kohner and P. Henkind, "Correlation of fluorescein angiogram and retinal digest in diabetic retinopathy," *American Journal of Ophthalmology*, vol. 69, no. 3, pp. 403–414, 1970.

[4] S. Nunes, I. Pires, A. Rosa, L. Duarte, R. Bernardes, and J.&. Cunha-Vaz, "Microaneurysm turnover is a biomarker for diabetic retinopathy progression to clinically significant macular edema: findings for type 2 diabetics with nonproliferative retinopathy," *Ophthalmologica*, vol. 223, no. 5, pp. 292–297, 2009.

[5] G. S. Tan, N. Cheung, R. Simó, G. C. Cheung, and T. Y. Wong, "Diabetic macular oedema," *The Lancet Diabetes and Endocrinology*, vol. 5, no. 2, pp. 143–155, 2017.

[6] A. H. Kashani, C. L. Chen, J. K. Gahm et al., "Optical coherence tomography angiography: a comprehensive review of current methods and clinical applications," *Progress in Retinal and Eye Research*, vol. 60, pp. 66–100, 2017.

[7] A. Koustenis Jr., A. Harris, J. Gross, I. Januleviciene, A. Shah, and B. Siesky, "Optical coherence tomography angiography: an overview of the technology and an assessment of applications for clinical research," *The British Journal of Ophthalmology*, vol. 101, no. 1, pp. 16–20, 2017.

[8] D. S. W. Ting, G. S. W. Tan, R. Agrawal et al., "Optical coherence tomographic angiography in type 2 diabetes and diabetic retinopathy," *JAMA Ophthalmology*, vol. 135, no. 4, pp. 306–312, 2017.

[9] "Diagnosis and classification of diabetes mellitus," *Diabetes Care*, vol. 37, Supplement 1, pp. S81–S90, 2014.

[10] C. P. Wilkinson, F. L. Ferris 3rd, R. E. Klein et al., "Proposed international clinical diabetic retinopathy and diabetic macular edema disease severity scales," *Ophthalmology*, vol. 110, no. 9, pp. 1677–1682, 2003.

[11] H. Wang, J. Chhablani, W. R. Freeman et al., "Characterization of diabetic microaneurysms by simultaneous fluorescein angiography and spectral-domain optical coherence tomography," *American Journal of Ophthalmology*, vol. 153, no. 5, pp. 861–867.e1, 2012.

[12] M. Hamada, K. Ohkoshi, K. Inagaki, N. Ebihara, and A. Murakami, "Visualization of microaneurysms using optical coherence tomography angiography: comparison of OCTA en face, OCT B-scan, OCT en face, FA, and IA images," *Japanese Journal of Ophthalmology*, vol. 62, no. 2, pp. 168–175, 2018.

[13] A. W. Stitt, T. A. Gardiner, and D. B. Archer, "Histological and ultrastructural investigation of retinal microaneurysm development in diabetic patients," *The British Journal of Ophthalmology*, vol. 79, no. 4, pp. 362–367, 1995.

[14] M. López-Luppo, V. Nacher, D. Ramos et al., "Blood vessel basement membrane alterations in human retinal microaneurysms during aging," *Investigative Ophthalmology & Visual Science*, vol. 58, no. 2, pp. 1116–1131, 2017.

[15] E. Beltramo and M. Porta, "Pericyte loss in diabetic retinopathy: mechanisms and consequences," *Current Medicinal Chemistry*, vol. 20, no. 26, pp. 3218–3225, 2013.

[16] P. Romero-Aroca, M. Baget-Bernaldiz, A. Pareja-Rios et al., "Diabetic macular edema pathophysiology: vasogenic versus inflammatory," *Journal of Diabetes Research*, vol. 2016, Article ID 2156273, 17 pages, 2016.

[17] H. Ito, T. Horii, K. Nishijima et al., "Association between fluorescein leakage and optical coherence tomographic characteristics of microaneurysms in diabetic retinopathy," *Retina*, vol. 33, no. 4, pp. 732–739, 2013.

[18] T. Horii, T. Murakami, K. Nishijima, A. Sakamoto, M. Ota, and N. Yoshimura, "Optical coherence tomographic characteristics of microaneurysms in diabetic retinopathy," *American Journal of Ophthalmology*, vol. 150, no. 6, pp. 840–848.e1, 2010.

[19] M. Parravano, D. de Geronimo, F. Scarinci et al., "Diabetic microaneurysms internal reflectivity on spectral-domain optical coherence tomography and optical coherence tomography angiography detection," *American Journal of Ophthalmology*, vol. 179, p. 90, 2017.

[20] M. Parravano, D. de Geronimo, F. Scarinci et al., "Progression of Diabetic Microaneurysms According to the Internal Reflectivity on Structural Optical Coherence Tomography and Visibility on Optical Coherence Tomography Angiography," *American Journal of Ophthalmology*, vol. 198, pp. 8–16, 2019.

[21] A. Couturier, V. Mané, S. Bonnin et al., "Capillary plexus anomalies in diabetic retinopathy on optical coherence tomography angiography," *Retina*, vol. 35, no. 11, pp. 2384–2391, 2015.

[22] V. Schreur, A. Domanian, B. Liefers et al., "Morphological and topographical appearance of microaneurysms on optical coherence tomography angiography," *British Journal of Ophthalmology*, vol. 103, 2019.

Hindawi
Journal of Diabetes Research
Volume 2022, Article ID 2552186, 10 pages
https://doi.org/10.1155/2022/2552186

Research Article

Serum Antithyroglobulin Antibody Levels Are Associated with Diabetic Retinopathy among Euthyroid Type 2 Diabetes Patients: A Hospital-Based, Retrospective Study

Xiaotong Gao,[1] **Xichang Wang**,[1] **Yifan Zhong**,[2] **Lei Liu**,[2] **Weiping Teng**,[1] **and Zhongyan Shan**[1]

[1]*Department of Endocrinology and Metabolism and the Institute of Endocrinology, The NHC Key Laboratory of Diagnosis and Treatment of Thyroid Diseases, The First Hospital of China Medical University, Shenyang 110001, China*
[2]*Department of Ophthalmology, The First Hospital of China Medical University, Shenyang 110001, China*

Correspondence should be addressed to Lei Liu; liuleijiao@163.com and Zhongyan Shan; cmushanzhongyan@163.com

Received 29 July 2021; Revised 10 December 2021; Accepted 13 December 2021; Published 6 January 2022

Academic Editor: Eusebio Chiefari

Background. Previous studies have revealed that the variation of thyroid indicators may be associated with the risk of diabetic retinopathy (DR) among euthyroid type 2 diabetes (T2D) patients. But the specific conclusions are currently inconsistent. *Methods*. This is a hospital-based retrospective survey. We recruited 1,145 euthyroid T2D patients and checked the thyroid function and fundus photographs. The modified Airlie House classification system was used to categorize the stages of DR. The association between thyroid indicators and different stages of DR was analyzed. *Results*. We divided free triiodothyronine (FT3) into tertiles and found that the prevalence of mild nonproliferative DR (NPDR) was significantly higher in T2, compared with T1 (32.0% vs. 25.2%, $p < 0.05$). When FT3 was within the level of T2, FT3 could be an independent risk factor for mild NPDR (OR 1.426, 95% CI (1.031, 1.971), $p < 0.05$). In addition, the prevalence of severe NPDR and proliferative DR (PDR) was significantly higher in thyroglobulin antibody (TgAb) positive group (8.8% vs. 4.1%, $p < 0.05$) and vice versa (33.3% vs. 18.4%, $p < 0.05$). TgAb positivity was also an independent risk factor for severe NPDR and PDR (OR 2.212, 95% CI (1.244, 3.934), $p < 0.05$). *Conclusions*. We hardly observed a significant change in DR risk with the elevation or reduction of serum TSH or thyroid hormone within the reference interval. Although the slightly elevated FT3 may be associated to mild NPDR, the extensibility of this result remains to be seen. For T2D patients with euthyroid function, there may be a significant correlation between serum TgAb positivity and severe NPDR and PDR.

1. Introduction

Thyroid dysfunction and diabetes are the two most common endocrine diseases in clinical practice. A recent national cross-sectional study has revealed that in mainland China the weighted prevalence of thyroid dysfunction and diabetes have reached up to 15.33% and 12.88%, respectively [1, 2], and a huge amount of evidence have demonstrated the potential association between them [3]. Type 2 diabetes (T2D) is currently the most common type of diabetes, accounting up to 95% of overall diabetes [4]. Several previous studies have demonstrated a significantly higher prevalence of thyroid dysfunction among T2D patients and vice versa [5–11]. Subclinical hypothyroidism (SCH) is recognized as the most common type of thyroid dysfunction [1], and there are currently the most studies on SCH in the relevant investigations on thyroid dysfunction and diabetic complications. Han et al. have meta-analyzed ten studies and found that there was a 2.32-fold increasing risk for SCH, among patients with T2D [12]. Based on the same meta-analysis, the prevalence risks of diabetic nephropathy (DN), diabetic retinopathy (DR), peripheral arterial disease, and neuropathy were also positively associated with SCH [12]. In addition, several studies have found that although

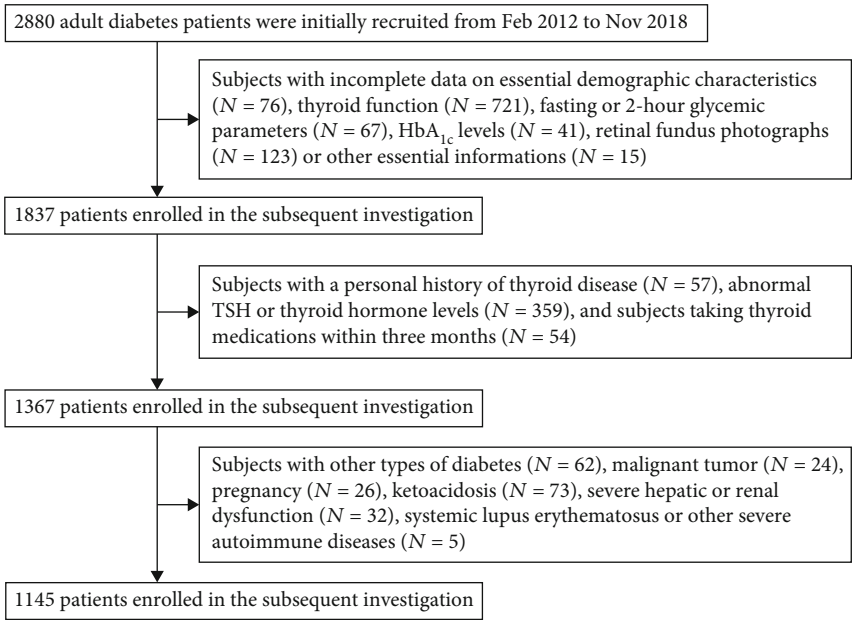

Figure 1: The screening process of the participants.

the prevalence of hyperthyroidism in T2D patients is far lower than hypothyroidism, it is generally higher than in the normoglycemic population [9, 13, 14].

As for the prevalence risk of T2D and its complications among euthyroid subjects, there are currently few but inconsistent conclusions. Since the variation of thyroid function within the normal range may also be associated with poor glycemic control in T2D patients [15, 16], there must be a potential association between thyroid indicators and T2D complications in euthyroid subjects. However, the evidence is currently scarce, and there are a few discrepancies in the relevant conclusions [17–19]. Therefore, we need to carry out more studies to analyze whether various thyroid indicators are associated with T2D complications among euthyroid subjects.

As the leading cause of moderate to severe blindness in working aged adults, as well as the most common and specific microvascular complication, DR has received more and more extensive attention in recent years [20, 21]. Optimal control of hyperglycemia, hypertension, and dyslipidemia remains the foundation for reduction of DR development and progression [20]. However, in light of the higher prevalence of thyroid dysfunction among T2D patients, it is necessary to explore the potential impact of thyroid indicators on the prevalence and development of DR. There is currently insufficient evidence in this field, especially for euthyroid subjects. In this hospital-based retrospective survey, we conducted an association analysis for euthyroid T2D patients, in order to supplement and innovate the relevant previous conclusions.

2. Materials and Methods

2.1. Study Participants. The present study was approved by the Medical Ethics Committee of the First Affiliated Hospital of China Medical University. The protocol of this hospital-based retrospective study has been previously described in another article [22]. Briefly speaking, we recruited 2,880 diabetic patients aged ≥ 18 years between February 2012 and November 2018. The diagnostic criteria for diabetes were derived from the 2019 American Diabetes Association (ADA) guidelines [4]. If the patient met one of the four following items, diabetes could be diagnosed: fasting plasma glucose (FPG) ≥ 7.0 mmol/L, glycosylated hemoglobin (HbA_{1c}) $\geq 6.5\%$, 2-hour plasma glucose (2h − PG) $\geq$ 11.1 mmol/L, with classic symptoms plus random plasma glucose ≥ 11.1 mmol/L. In addition, patients who reported a personal history of diabetes were also recognized as diabetes patients. All patients signed an informed consent form and then completed the questionnaire survey. Information about demographics, personal history of diseases, and medications was all covered by the questionnaire.

The screening process of the study population is shown in Figure 1. We first excluded patients with incomplete essential information, and then patients with a personal history of thyroid disease, abnormal TSH or thyroid hormone levels (FT3 or FT4), and those who had taken thyroid drugs within 3 months were also excluded. To avoid the impact of nonthyroid disease syndrome (NTIS) or pregnancy on thyroid function, patients with malignancy, ketoacidosis, severe hepatic or renal failure, other forms of diabetes, or severe autoimmune diseases, as well as pregnant women were also excluded. Finally, 1,145 euthyroid T2D patients were involved in the final analysis.

2.2. Clinical and Laboratory Measurement. As previously described [22], weight and height were measured by trained nurses, and body mass index (BMI, kg/m^2) was calculated as weight divided by the square of the height. Systolic BP (SBP), diastolic BP (DBP), and heart rate (HR) were measured three times with standard mercury sphygmomanometers, and the average was regarded as the final value. After

an overnight fasting (≥8 hours), venous blood samples were taken and immediately transferred to the Endocrinology Laboratory of China Medical University for further measurements.

The following fasting biochemical parameters could be queried in the Hospital Information System (HIS), which mainly include high-density lipoprotein (HDL, mmol/L), low-density lipoprotein (LDL, mmol/L), triglyceride (TG, mmol/L), total cholesterol (TC, mmol/L), FPG (mmol/L), fasting insulin (FINS, mU/L), fasting C peptide (FCP, pmol/L), and HbA_{1c} (%). In addition, all the participants went through a 2-hour 75 g oral glucose tolerance test (2h-OGTT). We also recorded the results of 2h-PG, 2h-INS, and 2h-CP after taking the glucose. The specific testing instruments of the above indicators were the same as the previous study [22]. What is more, serum TSH, FT3, FT4, thyroid peroxidase antibody (TPOAb), and TgAb were tested with supersensitive chemiluminescence immunoassay (ARCHITECT system i2000SR, Abbott, Chicago, US). The five thyroid parameters of each patient were also queried by trained nurses from the HIS.

2.3. Diagnostic Criteria of Thyroid Dysfunction and Dyslipidemia. As defined by the manufacturer, the reference interval of serum TSH, FT3, FT4, TPOAb, and TgAb was 0.35-4.94 mU/L, 2.43-6.01 pmol/L, 9.01-19.05 pmol/L, ≤5.61 IU/mL, and ≤4.11 IU/mL, respectively. Euthyroid was defined as normal TSH plus normal free thyroid hormone (FT3 and FT4) levels, with or without positive TPOAb or TgAb. The diagnostic criteria for dyslipidemia and hyperuricemia were also defined by the kit. If the subject met all the following four items and was not taking lipid-lowering drugs, it could be considered as normal lipidemia; otherwise, dyslipidemia was diagnosed: HDL ≥ 0.91 mmol/L, LDL ≤ 3.64 mmol/L, TG ≤ 1.7 mmol/L, and TC ≤ 5.72 mmol/L. The upper limit of the reference value of uric acid is 428 μmol/L. If the level of serum uric acid was higher than the above value or the participant was currently taking hypouricemic drugs, then hyperuricemia would be diagnosed.

2.4. Assessment and Stratification of DR. A nonmydriatic fundus camera (CR6-45NM; Canon, Tokyo, Japan) was used to evaluate the presence and severity of DR. Two-field fundus examination focusing on the fovea and optic disk was applied by trained ophthalmologists to evaluate the location and extent of lesions. The specific protocol of fundus examination has been previously introduced [22]. According to the Early Treatment for Diabetic Retinopathy Study (ETDRS), the modified Airlie House classification system was referred to evaluate the severity of DR [23], which grouped DR into nonproliferative DR (NPDR) and proliferative DR (PDR). NPDR was further divided into mild, moderate, and severe NPDR.

2.5. Statistical Analysis. The above data were input into the Statistical Package for the Social Sciences version 25 (SPSS Inc., Chicago, IL, USA). All p values obtained were based on two-tailed tests, with significance level set at 0.05. In the descriptive analysis, continuous variables were described as means and standard deviations (SD), and dichotomous variables were described as numbers and corresponding percentages. Single-sample t-test and chi-square test were, respectively, used to compare the differences in continuous and dichotomous variables, both between the two groups with or without DR, as well as between the groups with different levels of thyroid function. Multivariate logistic regression was used to analyze the influence of different thyroid parameters on the prevalence DR.

In order to explore whether different concentrations of serum thyroid indicators are related to the risk of different stages of DR, we divided the thyroid indicators, i.e., TSH, FT3, and FT4, into three tertiles (T1-T3) according to the principle of equalizing the number of people in each group. T2 and T3 were assessed to explore the variation of DR risk with the elevation of the three indicators, compared with T1. In addition, subjects were also divided into two groups according to the values of TPOAb and TgAb (i.e., positive group and negative group).

3. Results

3.1. General Characteristics of the Patients. As shown in Table 1, the patients were grouped into two groups by the present of DR. The present study included 719 T2D patients without DR and 426 DR patients. Anthropometric, demographic, and biochemical information were listed and compared between patients with and without DR.

We found that T2D patients with DR were significantly older than those without DR ($p < 0.01$). Compared with T2D patients without DR, DR patients had a significantly lower BMI ($p = 0.04$). What is more, the HR and SBP values were both significantly higher in the DR group ($p < 0.01$). However, the difference in the prevalence of hypertension between DR and non-DR patients was not significant.

As for the comparison of serum biochemical indicators (Table 1), we found that the level of plasma HbA_{1c} was significantly higher in the DR group ($p = 0.04$). However, the remaining plasma glycemic indicators did not show significancy between the two groups, whether it was a fasting or a 2-hour indicator. Moreover, regarding the difference in the homeostasis model assessment of insulin resistance (HOMA-IR), DR patients had a slightly but insignificantly higher degree of insulin resistance.

3.2. The Changing Patterns of Thyroid Indicators with Different Stages of DR. Due to the extremely low prevalence of PDR (17/1,145), to ensure the reliability of the results of the investigation, patients with severe NPDR or PDR in this study were combined into one group. According to the presentation and severity of retinopathy, the subjects were divided into four groups, and the serum thyroid index levels between the groups were compared.

As shown in Table 2, except for the positive rate of serum TgAb, there was no statistical difference in the remaining four thyroid indicators among subjects in different groups. We found that the positive rate of serum TgAb had a significantly increasing trend (p for trend <0.05), with the continuous aggravation of ocular lesions. Moreover,

Table 1: General characteristics of participants stratified by the presence of DR.

Number (*N*, %)	Total 1,145	Non-DR 719	DR 426	*p* value
Sex (female, %)	494 (43.1%)	305 (42.4%)	189 (44.4%)	0.52
Age (years)	56.30 ± 13.32	55.45 ± 14.11	57.73 ± 11.74	<0.01
T2D duration (>10 years, %)	726 (63.4%)	443 (61.6%)	283 (66.4%)	0.10
Smoking (*N*, %)	1,017 (88.8%)	635 (88.3%)	382 (89.7%)	0.48
Drinking (*N*, %)	1004 (87.7%)	628 (87.3%)	376 (88.3%)	0.64
BMI (kg/m^2)	25.62 ± 3.78	25.75 ± 3.94	25.40 ± 3.50	0.04
HR (per min)	81.34 ± 11.19	80.78 ± 10.82	82.30 ± 11.74	<0.01
SBP (mmHg)	135.15 ± 20.28	133.77 ± 19.25	137.49 ± 21.74	<0.01
DBP (mmHg)	82.50 ± 11.88	82.08 ± 11.75	83.19 ± 12.09	0.06
Hypertension (*N*, %)	579 (50.6%)	348 (48.4%)	231 (54.2%)	0.06
Hyperuricemia (*N*, %)	113 (9.9%)	39 (9.2%)	74 (10.3%)	0.53
Dyslipidemia (*N*, %)	604 (52.8%)	373 (51.9%)	231 (54.2%)	0.44
HbA_{1c} (%)	8.64 ± 2.43	8.54 ± 2.37	8.80 ± 2.52	0.04
FPG (mmol/L)	9.25 ± 3.89	9.24 ± 3.47	9.26 ± 4.12	0.92
2h-PG (mmol/L)	17.47 ± 5.89	17.24 ± 5.18	17.61 ± 6.27	0.14
FINS (mU/L)	14.55 ± 49.88	14.25 ± 51.14	15.06 ± 47.73	0.73
2h-INS (mU/L)	32.57 ± 28.04	31.77 ± 25.10	33.91 ± 32.41	0.18
FCP (pmol/L)	651.81 ± 531.62	649.36 ± 514.26	655.96 ± 560.28	0.81
2h-CP (pmol/L)	1727.33 ± 1201.89	1732.11 ± 1223.63	1792.37 ± 1165.27	0.19
HOMA-IR	6.05 ± 20.38	5.67 ± 15.48	6.70 ± 26.70	0.43

T2D: type 2 diabetes; DR: diabetic retinopathy; BMI: body mass index; HR: heart rate; SBP: systolic blood pressure; DBP: diastolic blood pressure; HbA_{1c}: glycosylated hemoglobin; FPG: fasting plasma glucose; FINS: fasting insulin; FCP: fasting C peptide; HOMA-IR: homeostasis model assessment of insulin resistance. The diagnosing criteria of hypertension were SBP ≥ 140 mmHg or DBP ≥ 90 mmHg or current administration of antihypertensive drugs. Smoking and drinking were defined as a personal history of smoking/drinking or current smoking/drinking, regardless of the frequency. Dyslipidemia and hyperuricemia were defined by the reference interval provided by the kit, and subjects currently taking lipid-lowering or hypouricemic drugs were also regarded as dyslipidemia or hyperuricemia patients. HOMA-IR was calculated as follows: HOMA − IR = FPG × FINS/22.5.

Table 2: Thyroid indicators corresponding to different severities of DR.

	Non-DR	Mild NPDR	Moderate NPDR	Severe NPDR or PDR
Number	719	325	44	57
TSH (mU/L)	1.92 ± 0.99	1.99 ± 1.08	1.99 ± 1.14	1.83 ± 0.88
FT4 (pmol/L)	13.58 ± 1.72	13.72 ± 1.78	13.57 ± 1.70	13.57 ± 1.79
FT3 (pmol/L)	4.10 ± 0.61	4.11 ± 0.62	4.06 ± 0.59	4.10 ± 0.74
pTPOAb (*N*, %)	94 (13.1%)	48 (14.8%)	5 (11.4%)	6 (10.5%)
pTgAb (*N*, %)[b]	132 (18.4%)	56 (17.2%)	10 (22.7%)	19 (33.3%)[a]

TSH: thyroid-stimulating hormone; FT4: free thyroxine; FT3: free triiodothyronine; pTPOAb: positive thyroid peroxidase antibody; pTgAb: positive thyroglobulin antibody; DR: diabetic retinopathy; NPDR: nonproliferative diabetic retinopathy; PDR: proliferative diabetic retinopathy. Data are expressed as mean ± SD or number and proportion. The superscript a indicates that the value in the corresponding group is significantly higher than the non-DR group ($p < 0.05$). The superscript b indicates that the variation of the thyroid indicator shows a significantly upward trend.

compared with patients without DR, patients with severe NPDR or PDR had a significantly higher positive rate of TgAb (33.3% vs. 18.4%, $p < 0.05$).

3.3. The Changing Patterns of DR Prevalence with Thyroid Indicators. Serum TSH, FT4, and FT3 were all divided into tertiles, and the DR prevalence corresponding to different tertiles was calculated; at the same time, DR prevalence was also calculated according to the presentation of positive serum thyroid antibodies. The subgroups with the lowest levels of hormones or negative antibodies were regarded as the reference.

As shown in the (a) and (b) in Figure 2, we found that the prevalence of different stages of DR or overall DR was not significantly higher or lower, with the increase of TSH or FT4. The prevalence of DR corresponding to different

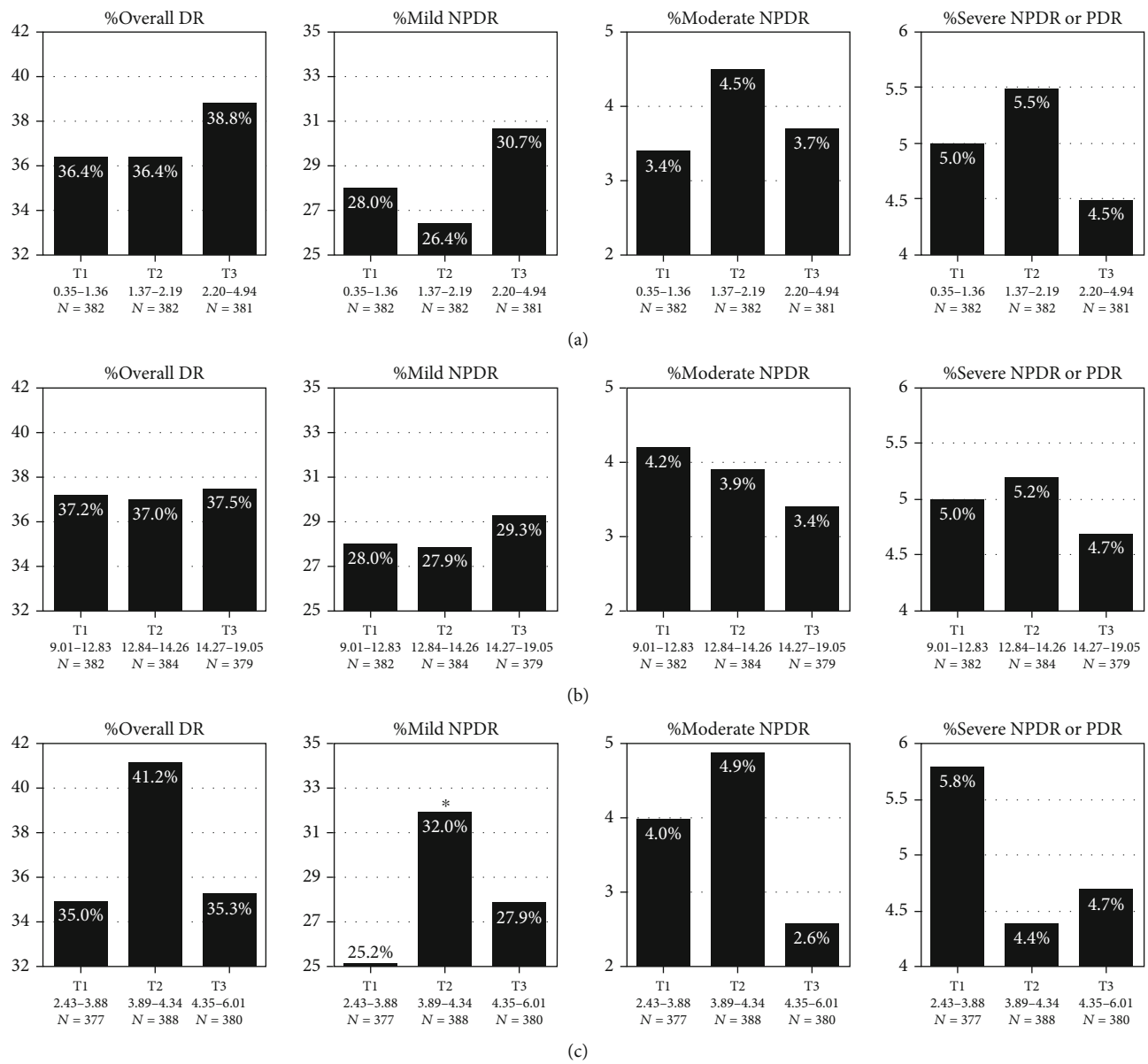

Figure 2: The variation of different stages of DR prevalence with serum TSH (a), FT4 (b), and FT3 (c). DR: diabetic retinopathy; NPDR: nonproliferative diabetic retinopathy; PDR: proliferative diabetic retinopathy; TSH: thyroid-stimulating hormone; FT4: free thyroxine; FT3: free triiodothyronine. The stratification of the thyroid indicators is stated in the figure, and the unit of TSH, FT4, and FT3 should be mU/L, pmol/L, and pmol/L, respectively. The * indicates that the corresponding prevalence was significantly higher than the control group (T1) ($p < 0.05$).

levels of TSH or FT4 was relatively comparable. In addition, the overall DR prevalence corresponding to different levels of FT3 was also similar. However, the prevalence of mild NPDR in the second tertile (T2) of FT3 was significantly higher (32.0% vs. 25.2%, $p < 0.05$), suggesting that the prevalence of mild NPDR was significantly higher in T2D patients with slightly elevated FT3 within reference interval (3.89-4.34 pmol/L).

Regarding the prevalence of DR under different thyroid autoantibody titers, we found that the DR prevalence did not significantly increase or decrease for T2D patients with positive TPOAb (Figure 3(a)). On the other side, the prevalence of severe NPDR or PDR was significantly higher in TgAb-positive patients (8.8% vs. 4.1%, $p < 0.05$) (Figure 3(b)), while the prevalence of other stages of DR did not show significancy.

3.4. Regression Analysis between Thyroid Function and DR Risks. In order to further confirm the association between the thyroid indicators and different grades of DR risk, univariable and multivariable regression analyses were applied to explore the abovementioned differences in DR prevalence (Table 3). The grouping of thyroid indicators was similar to the above description, and then, the groups with the lowest tertile and the antibody-negative groups were set as the reference.

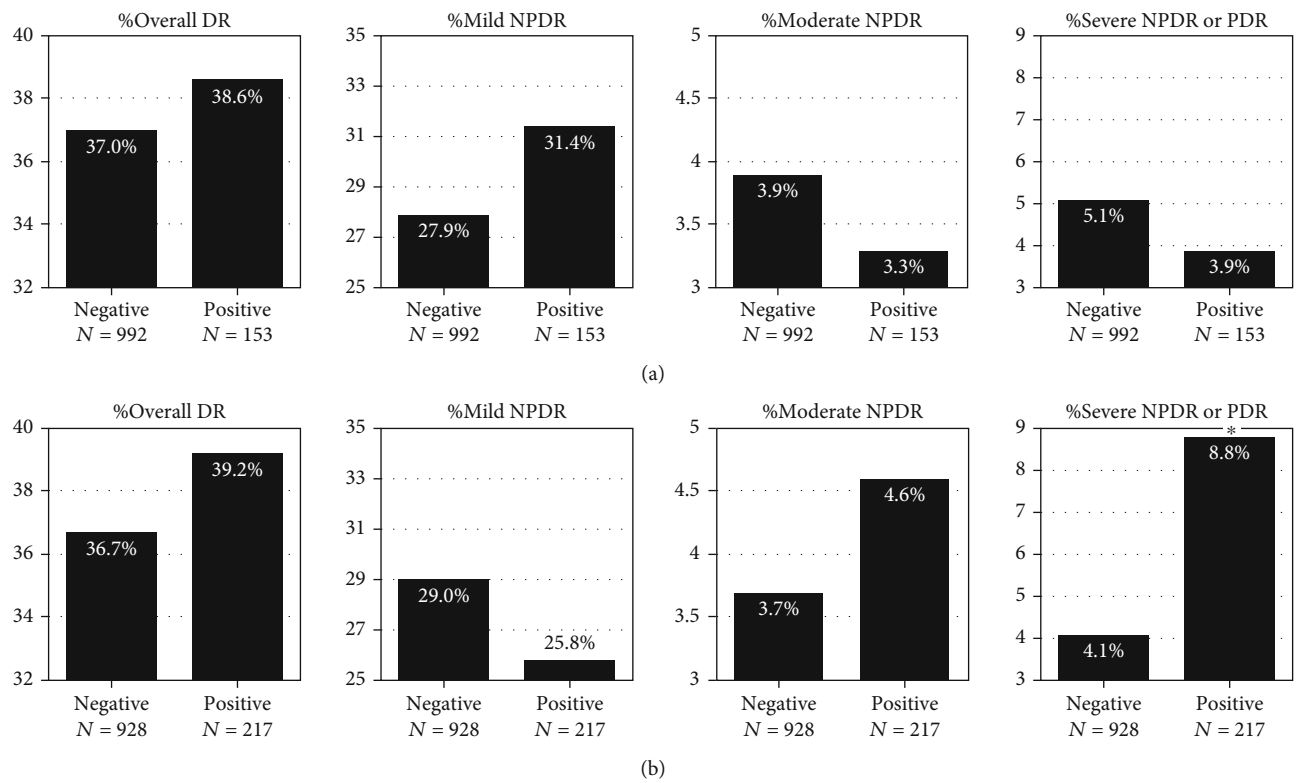

Figure 3: The variation of different stages of DR prevalence with serum TPOAb (a) and TgAb (b). DR: diabetic retinopathy; NPDR: nonproliferative diabetic retinopathy; PDR: proliferative diabetic retinopathy; TPOAb: thyroid peroxidase antibody; TgAb: thyroglobulin antibody. The * indicates that the corresponding prevalence in the positive group was significantly higher than the negative group ($p < 0.05$).

As shown in Table 3, the T2 of FT3 correlated with the risk of mild NPDR (OR 1.426 (1.031, 1.971), $p < 0.05$). What is more, TgAb positivity was also significantly associated with the risk of severe NPDR or PDR (OR 2.212 (1.244, 3.934), $p < 0.05$). The above correlations were both significant in both model 1 and model 2. However, our results were unable to deduce the significant relationships between the variations in TSH or FT4 within the reference range or the TPOAb positivity and the risk of DR. In addition, we also explored whether the risk of each stage of DR and overall DR would change significantly with the linear changes of TSH, FT4, and FT3. However, with per SD-increase in the abovementioned three indicators, there was no significant variation in the risk of DR.

4. Discussion

In this hospital-based retrospective survey, 1,145 T2D patients with normal thyroid function were included. We found that a slight increase in FT3 (3.89-4.34 pmol/L) within the reference range may be significantly associated with the risk of mild NPDR. Patients with a slightly higher FT3 within the specific range had a significantly higher prevalence of mild NPDR. It should be emphasized that although the mild increase in serum FT3 is significantly correlated with mild NPDR, this conclusion does not have much significance in clinical practice. More research is needed to explore the potential association between FT3 levels beyond the reference interval and different stages of DR. In addition, we found that the prevalence of severe NPDR or PDR in TgAb-positive patients was also significantly higher and vice versa. TgAb positivity may also be an independent risk factor for severe DR in euthyroid T2D patients.

The anthropometric and biochemical information were compared in patients with or without DR. We found that compared with non-DR patients, T2D patients with DR are significantly older and have significantly lower levels of BMI, and there are also slight differences in the prevalence of hypertension between the two groups, especially in the significantly higher SBP in DR patients. Compared with patients without DR, patients with DR had a slightly increased prevalence of dyslipidemia and hyperuricemia. In addition, similar to our inherent knowledge that T2D patients with complications generally have worse control of blood glucose than noncomplicated patients, the DR group showed a higher HbA_{1c}, and fasting and 2-hour plasma indicators, as well as insulin resistance level also showed insignificant but slight worsen trend.

As mentioned above, several previous studies have been conducted on DR risk and thyroid function, especially SCH, but the conclusion is not clear yet. Similar to the conclusions of several individual studies [24–27], Han et al. have meta-analyzed ten Chinese studies and found that T2D patients with SCH were more likely to be accompanied with DR, and the risk could be increased by 42% [12]. However, a recent Indian study found that not only DR but other

Table 3: Associations between thyroid indicators and various stages of DR risk.

		Overall DR	Mild NPDR	Moderate NPDR	Severe NPDR or PDR
TSH	T1 (ref)	1	1	1	1
	T2 (model 1)	1.000 (0.745, 1.343)	0.924 (0.672, 1.271)	1.322 (0.633, 2.761)	1.111 (0.588, 2.102)
	T2 (model 2)	0.990 (0.734, 1.333)	0.917 (0.665, 1.264)	1.274 (0.607, 2.674)	1.133 (0.596, 2.152)
	T3 (model 1)	1.110 (0.828, 1.489)	1.139 (0.834, 1.556)	1.083 (0.502, 2.335)	0.892 (0.456, 1.744)
	T3 (model 2)	1.062 (0.789, 1.431)	1.116 (0.814, 1.529)	0.954 (0.437, 2.081)	0.851 (0.431, 1.680)
	Per SD increase (model 1)	1.055 (0.938, 1.187)	1.081 (0.954, 1.225)	1.049 (0.783, 1.404)	0.893 (0.679, 1.174)
	Per SD increase (model 2)	1.043 (0.926, 1.175)	1.072 (0.945, 1.216)	1.017 (0.757, 1.367)	0.891 (0.675, 1.176)
FT4	T1 (ref)	1	1	1	1
	T2 (model 1)	0.992 (0.740, 1.330)	0.993 (0.724, 1.361)	0.930 (0.453, 1.909)	1.050 (0.551, 2.000)
	T2 (model 2)	1.035 (0.768, 1.395)	1.030 (0.748, 1.418)	0.973 (0.471, 2.010)	1.073 (0.562, 2.050)
	T3 (model 1)	1.013 (0.755, 1.358)	1.064 (0.777, 1.458)	0.813 (0.385, 1.713)	0.953 (0.492, 1.845)
	T3 (model 2)	0.983 (0.728, 1.328)	1.069 (0.776, 1.471)	0.808 (0.379, 1.726)	0.826 (0.421, 1.620)
	Per SD increase (model 1)	1.035 (0.967, 1.109)	1.047 (0.973, 1.127)	0.985 (0.827, 1.172)	0.983 (0.843, 1.147)
	Per SD increase (model 2)	1.028 (0.959, 1.102)	1.042 (0.968, 1.122)	0.984 (0.826, 1.173)	0.968 (0.831, 1.128)
FT3	T1 (ref)	1	1	1	1
	T2 (model 1)	1.302 (0.972, 1.745)	1.394 (1.017, 1.912)[c]	1.243 (0.622, 2.483)	0.739 (0.386, 1.416)
	T2 (model 2)	1.349 (0.997, 1.824)	1.426 (1.031, 1.971)[c]	1.146 (0.566, 2.320)	0.840 (0.431, 1.637)
	T3 (model 1)	1.011 (0.750, 1.363)	1.148 (0.831, 1.586)	0.652 (0.289, 1.471)	0.802 (0.423, 1.521)
	T3 (model 2)	1.031 (0.757, 1.405)	1.179 (0.844, 1.647)	0.588 (0.254, 1.363)	0.846 (0.434, 1.646)
	Per SD increase (model 1)	1.016 (0.837, 1.235)	1.051 (0.853, 1.295)	0.876 (0.538, 1.425)	0.973 (0.632, 1.499)
	Per SD increase (model 2)	1.016 (0.829, 1.246)	1.061 (0.853, 1.318)	0.744 (0.445, 1.244)	1.047 (0.673, 1.628)
TPOAb	Negative	1	1	1	1
	Positive (model 1)	1.069 (0.753, 1.517)	1.180 (0.816, 1.706)	0.826 (0.320, 2.128)	0.753 (0.318, 1.786)
	Positive (model 2)	1.085 (0.761, 1.547)	1.191 (0.822, 1.726)	0.859 (0.332, 2.226)	0.749 (0.314, 1.785)
TgAb	Negative	1	1	1	1
	Positive (model 1)	1.108 (0.818, 1.502)	0.852 (0.609, 1.192)	1.270 (0.618, 2.613)	2.247 (1.269, 3.981)[c]
	Positive (model 2)	1.112 (0.818, 1.511)	0.849 (0.606, 1.190)	1.343 (0.649, 2.780)	2.212 (1.244, 3.934)[c]

Model 1: crude; Model 2: adjusted for age, sex, BMI, SBP, and HbA_{1c}. The superscript c indicates that the p value of corresponding OR is less than 0.05.

T2D complications such as nephropathy, neuropathy, or cardiovascular disease were not significantly related with any forms of thyroid dysfunction [28]. What is more, several studies also concluded that supranormal or high-normal TSH level was not related with DR, while the risk of nephropathy showed significance [29–31].

Therefore, currently, we have insufficient evidence to support an explicit relationship between thyroid dysfunction (especially SCH) and DR. Compared with the above studies, there are fewer studies on thyroid function and DR risk among euthyroid T2D subjects. In a similar hospital-based retrospective study [32], Zou et al. revealed that the prevalence of DR decreased significantly with the increase of serum FT3 level among euthyroid subjects, and the level of FT3 also decreased significantly with the severity of DR. However, the level of TSH or FT4 or the positivity of TPOAb showed no significant trends. Different from the above findings, Kong et al. found that the DR prevalence showed a significantly decreasing trend across the tertiles of FT4, plus a significantly increasing trend across the tertiles of TSH. However, the level of FT3 hardly showed any significance regarding DR or PDR [33]. We speculate that the scales of the previous studies were small, so sampling bias might lead to the inconsistency of the conclusions. In addition, the kits used in various studies are different, so the inconsistent reference intervals for TSH, FT3, or FT4 might also contribute to inconsistent conclusions. Finally, the relevant studies so far are based on hospital-based retrospective populations, so untreated or undiagnosed T2D patients were ignored. It remains to be further explored that whether these evidence truly revealed the association between thyroid indicators and DR risk among euthyroid T2D patients.

Compared with the previous findings, the results of the present research are somewhat different. The prevalence of overall or each stage of DR showed no significant difference across the tertiles of TSH or FT4. However, the prevalence of mild NPDR in the T2 of FT3 was significantly higher than in the T1 of FT3. The following regression analysis further confirmed the above difference in prevalence. We found that when serum FT3 was in the range of T2 (3.89-4.34 mmol/L), the risk of mild NPDR was significantly associated with it. However, when FT3 continues to rise to the level of T3, the above association has no

statistical significance. Unlike the previous negative correlation, we consider that the slight increase in FT3 within the reference range may be positively correlated with the risk of mild NPDR. Although previous meta-analysis found that SCH might be related to the risk of DR, there are currently very few relevant studies carried out in euthyroid T2D patients. Based on the evidence from previous studies, we cannot conclude whether changes in thyroid hormones within the reference range will affect the risk of DR in euthyroid patients with T2D. Our study proposed for the first time a significant association between mildly elevated FT3 and mild DR in euthyroid T2D patients, which is a good supplement to the existing evidence.

Because of the common cooccurrence of autoimmune diseases [34], there have been a number of relevant studies on thyroid autoimmune and DR in T1D patients [35], but we could hardly find any explicit findings on T2D patients. In this study, we found a significant positive correlation between TgAb positivity and the risk of severe NPDR or PDR among euthyroid T2D patients. This is the first ever explicit conclusion about the relationship between thyroid autoimmunity and T2D-DR. Therefore, more future evidence is required to confirm such a correlation between thyroid autoimmune and the complications of T2D. A variety of inflammatory cytokines in serum have been confirmed to be closely related to the occurrence and development of T2D-DR [36–38]. At the same time, a large number of studies also showed that a variety of circulating cytokines involving in the occurrence and development of thyroid autoimmunity [39–41]. We speculate that the above two groups of pathological processes might overlap or promote each other, which induces a higher TgAb titer in patients with severe DR and vice versa. In view of the fact that there are few basic investigations in the related fields at present, more research is needed for in-depth exploration in the future. Although the manifestations of autoimmune thyroid disease (AITD) are generally ignored in practice, it has a certain impact on long-term thyroid function. Given that severe DR patients have a significantly higher TgAb positive rate, it is necessary to discuss in more depth whether it is essential to screen for serum thyroid autoantibodies in T2D patients with severe DR.

This study has some limitations. Firstly, this is a retrospective survey, so we cannot know the causal relationship between thyroid function and DR. Secondly, the current treatment rate of diabetes in mainland China is less than half [2]. Therefore, whether this hospital-based survey reflects the actual association between thyroid function and DR risk in general T2D patients remains unknown.

5. Conclusions

In summary, we hardly found that the risks of various stages of DR showed a significant upward or downward trend with serum TSH or thyroid hormone within the reference interval. Although mildly elevated FT3 may be associated with an increased risk of mild NPDR, the extensibility of this finding remains to be explored. In addition, there is a significant positive correlation between TgAb positivity and severe DR. The positive rate of TgAb in severe NPDR and PDR patients is much higher than that in non-DR T2D patients and vice versa. Further prospective studies are needed to get enough evidence on the association between the thyroid autoantibodies and the presence or development of severe DR.

Data Availability

The database of the study is available on request to Prof. Lei Liu (email address: liuleijiao@163.com).

Conflicts of Interest

The authors declare that there is no conflict of interest regarding the publication of this paper.

Authors' Contributions

Xiaotong Gao and Xichang Wang contributed equally to this work.

Acknowledgments

This study was funded by the Key Laboratory Project of Thyroid Diseases, National Health Commission (Grant No. 2019PT330001).

References

[1] Y. Li, D. Teng, J. Ba et al., "Efficacy and safety of long-term universal salt iodization on thyroid disorders: epidemiological evidence from 31 provinces of mainland China," *Thyroid*, vol. 30, no. 4, pp. 568–579, 2020.

[2] Y. Li, D. Teng, X. Shi et al., "Prevalence of diabetes recorded in mainland China using 2018 diagnostic criteria from the American Diabetes Association: national cross sectional study," *BMJ*, vol. 369, article m997, 2020.

[3] B. Biondi, G. J. Kahaly, and R. P. Robertson, "Thyroid dysfunction and diabetes mellitus: two closely associated disorders," *Endocrine Reviews*, vol. 40, no. 3, pp. 789–824, 2019.

[4] W. T. Cefalu, E. G. Berg, M. Saraco, M. P. Petersen, S. Uelmen, and S. Robinson, "2. Classification and diagnosis of diabetes: standards of medical care in diabetes-2019," *Diabetes Care*, vol. 42, Supplement 1, pp. S13–S28, 2019.

[5] R. H. Chen, H. Y. Chen, K. M. Man et al., "Thyroid diseases increased the risk of type 2 diabetes mellitus: a nation-wide cohort study," *Medicine (Baltimore)*, vol. 98, no. 20, article e15631, 2019.

[6] S. A. Chubb, W. A. Davis, Z. Inman, and T. M. Davis, "Prevalence and progression of subclinical hypothyroidism in women with type 2 diabetes: the Fremantle Diabetes Study," *Clinical Endocrinology*, vol. 62, no. 4, pp. 480–486, 2005.

[7] M. F. Celani, M. E. Bonati, and N. Stucci, "Prevalence of abnormal thyrotropin concentrations measured by a sensitive assay in patients with type 2 diabetes mellitus," *Diabetes Research*, vol. 27, no. 1, pp. 15–25, 1994.

[8] P. Perros, R. J. McCrimmon, G. Shaw, and B. M. Frier, "Frequency of thyroid dysfunction in diabetic patients: value of annual screening," *Diabetic Medicine*, vol. 12, no. 7, pp. 622–627, 1995.

[9] M. Al-Geffari, N. A. Ahmad, A. H. Al-Sharqawi, A. M. Youssef, D. Alnaqeb, and K. Al-Rubeaan, "Risk factors for thyroid dysfunction among type 2 diabetic patients in a highly diabetes mellitus prevalent society," *International Journal of Endocrinology*, vol. 2013, Article ID 417920, 2013.

[10] J. J. Diez and P. Iglesias, "An analysis of the relative risk for hypothyroidism in patients with type 2 diabetes," *Diabetic Medicine*, vol. 29, no. 12, pp. 1510–1514, 2012.

[11] F. Song, C. Bao, M. Deng et al., "The prevalence and determinants of hypothyroidism in hospitalized patients with type 2 diabetes mellitus," *Endocrine*, vol. 55, no. 1, pp. 179–185, 2017.

[12] C. Han, X. He, X. Xia et al., "Subclinical hypothyroidism and type 2 diabetes: a systematic review and meta-analysis," *PLoS One*, vol. 10, no. 8, article e0135233, 2015.

[13] Y. Zhu, F. Xu, J. Shen et al., "Prevalence of thyroid dysfunction in older Chinese patients with type 2 diabetes-a multicenter cross-sectional observational study across China," *PLoS One*, vol. 14, no. 5, article e0216151, 2019.

[14] J. J. Diez and P. Iglesias, "Subclinical hyperthyroidism in patients with type 2 diabetes," *Endocrine*, vol. 42, no. 1, pp. 157–163, 2012.

[15] T. Zhang, J. Shi, Y. Peng et al., "Sex-influenced association between free triiodothyronine levels and poor glycemic control in euthyroid patients with type 2 diabetes mellitus," *Journal of Diabetes and its Complications*, vol. 34, no. 11, article 107701, 2020.

[16] X. Zhang, J. Sun, W. Han et al., "The type 2 deiodinase Thr92Ala polymorphism is associated with worse glycemic control in patients with type 2 diabetes mellitus: a systematic review and meta-analysis," *Journal Diabetes Research*, vol. 2016, article 5928726, 2016.

[17] J. B. Zhou, H. B. Li, X. R. Zhu, H. L. Song, Y. Y. Zhao, and J. K. Yang, "Subclinical hypothyroidism and the risk of chronic kidney disease in T2D subjects: a case-control and dose-response analysis," *Medicine (Baltimore)*, vol. 96, no. 15, article e6519, 2017.

[18] L. Wang, T. Chen, J. Yu, H. Yuan, X. Deng, and Z. Zhao, "Clinical associations of thyroid hormone levels with the risk of atherosclerosis in euthyroid type 2 diabetic patients in Central China," *International Journal of Endocrinology*, vol. 2020, Article ID 2172781, 2020.

[19] Y. Chen, W. Zhang, N. Wang et al., "Thyroid parameters and kidney disorder in type 2 diabetes: results from the METAL study," *Journal Diabetes Research*, vol. 2020, article 4798947, 2020.

[20] N. Cheung, P. Mitchell, and T. Y. Wong, "Diabetic retinopathy," *Lancet*, vol. 376, no. 9735, pp. 124–136, 2010.

[21] M. S. Parmar, "Evaluation and care of patients with diabetic retinopathy," *The New England Journal of Medicine*, vol. 383, no. 5, article e31, 2020.

[22] L. Yao, Y. Zhong, L. He et al., "Serum CA125 level is associated with diabetic retinopathy in Chinese patients with type 2 diabetes," *Diabetes, Metabolic Syndrome and Obesity*, vol. 13, pp. 1803–1812, 2020.

[23] ETDRSR Group, "Grading diabetic retinopathy from stereoscopic color fundus photographs-an extension of the modified Airlie House classification," *Ophthalmology*, vol. 98, no. 5, pp. 786–806, 1991.

[24] J. K. Yang, W. Liu, J. Shi, and Y. B. Li, "An association between subclinical hypothyroidism and sight-threatening diabetic retinopathy in type 2 diabetic patients," *Diabetes Care*, vol. 33, no. 5, pp. 1018–1020, 2010.

[25] G. R. Yang, J. K. Yang, L. Zhang, Y. H. An, and J. K. Lu, "Association between subclinical hypothyroidism and proliferative diabetic retinopathy in type 2 diabetic patients: a case-control study," *The Tohoku Journal of Experimental Medicine*, vol. 222, no. 4, pp. 303–310, 2010.

[26] B. Y. Kim, C. H. Kim, C. H. Jung, J. O. Mok, K. I. Suh, and S. K. Kang, "Association between subclinical hypothyroidism and severe diabetic retinopathy in Korean patients with type 2 diabetes," *Endocrine Journal*, vol. 58, no. 12, pp. 1065–1070, 2011.

[27] N. Reddy, T. V. S. Pradeep, S. Tirupati, V. Sarathi, and D. Kumar, "Thyroid dysfunction and its association with microvascular complications in patients with type 2 diabetes mellitus in South India," *Diabetes and Metabolic Syndrome: Clinical Research and Reviews*, vol. 14, no. 4, pp. 615–617, 2020.

[28] V. Mehalingam, J. Sahoo, Z. Bobby, and K. V. Vinod, "Thyroid dysfunction in patients with type 2 diabetes mellitus and its association with diabetic complications," *Journal of Family Medicine and Primary Care*, vol. 9, no. 8, pp. 4277–4281, 2020.

[29] J. N. Ramis, C. F. Artigas, M. A. Santiago, F. J. Manes, R. S. Canonge, and L. M. Comas, "Is there a relationship between TSH levels and diabetic retinopathy in the Caucasian population?," *Diabetes Research and Clinical Practice*, vol. 97, no. 3, pp. e45–e47, 2012.

[30] Q. Qi, Q. M. Zhang, C. J. Li et al., "Association of thyroid-stimulating hormone levels with microvascular complications in type 2 diabetes patients," *Medical Science Monitor*, vol. 23, pp. 2715–2720, 2017.

[31] H. S. Chen, T. E. Wu, T. S. Jap et al., "Subclinical hypothyroidism is a risk factor for nephropathy and cardiovascular diseases in type 2 diabetic patients," *Diabetic Medicine*, vol. 24, no. 12, pp. 1336–1344, 2007.

[32] J. Zou, Z. Li, F. Tian et al., "Association between normal thyroid hormones and diabetic retinopathy in patients with type 2 diabetes," *BioMed Research International*, vol. 2020, Article ID 8161797, 2020.

[33] X. Kong, J. Wang, G. Gao et al., "Association between free thyroxine levels and diabetic retinopathy in euthyroid patients with type 2 diabetes mellitus," *Endocrine Research*, vol. 45, no. 2, pp. 111–118, 2020.

[34] V. K. Kawai, M. Shi, Q. Feng et al., "Pleiotropy in the genetic predisposition to rheumatoid arthritis: a phenome-wide association study and inverse variance-weighted meta-analysis," *Arthritis & Rheumatology*, vol. 72, no. 9, pp. 1483–1492, 2020.

[35] A. Rogowicz-Frontczak, B. Falkowski, A. Grzelka-Wozniak, A. Uruska, A. Araszkiewicz, and D. Zozulinska-Ziolkiewicz, "Does autoimmune hypothyroidism increase the risk of neurovascular complications in type 1 diabetes?," *Journal of Endocrinological Investigation*, vol. 43, no. 6, pp. 833–839, 2020.

[36] M. Nalini, B. V. Raghavulu, A. Annapurna, P. Avinash, and V. Chandi, "Correlation of various serum biomarkers with the severity of diabetic retinopathy," *Diabetes and Metabolic Syndrome: Clinical Research and Reviews*, vol. 11, Supplement 1, pp. S451–S454, 2017.

[37] I. Chatziralli, T. N. Sergentanis, R. Crosby-Nwaobi et al., "Model for risk-based screening of diabetic retinopathy in people with newly-diagnosed type 2 diabetes mellitus," *Investigative Ophthalmology & Visual Science*, vol. 58, no. 6, p. BIO99, 2017.

[38] L. B. Lamine, A. Turki, G. Al-Khateeb et al., "Elevation in circulating soluble CD40 ligand concentrations in type 2 diabetic retinopathy and association with its severity," *Experimental and Clinical Endocrinology & Diabetes*, vol. 128, no. 5, pp. 319–324, 2020.

[39] D. Arpaci, S. Karakas Celik, M. Can et al., "Increased serum levels of IL-28 and IL-29 and the protective effect of IL28B rs8099917 polymorphism in patients with Hashimoto's thyroiditis," *Immunological Investigations*, vol. 45, no. 7, pp. 668–678, 2016.

[40] L. Sieminska, C. Wojciechowska, B. Kos-Kudla et al., "Serum concentrations of leptin, adiponectin, and interleukin-6 in postmenopausal women with Hashimoto's thyroiditis," *Endokrynologia Polska*, vol. 61, no. 1, pp. 112–116, 2010.

[41] Q. Guo, Y. Wu, Y. Hou et al., "Cytokine secretion and pyroptosis of thyroid follicular cells mediated by enhanced NLRP3, NLRP1, NLRC4, and AIM2 inflammasomes are associated with autoimmune thyroiditis," *Frontiers in Immunology*, vol. 9, p. 1197, 2018.

Hindawi
Journal of Diabetes Research
Volume 2021, Article ID 2751695, 9 pages
https://doi.org/10.1155/2021/2751695

Research Article

Data Homogeneity Effect in Deep Learning-Based Prediction of Type 1 Diabetic Retinopathy

Jui-En Lo,[1,2] Eugene Yu-Chuan Kang,[3,4,5] Yun-Nung Chen,[2] Yi-Ting Hsieh,[6] Nan-Kai Wang,[7] Ta-Ching Chen,[6,8] Kuan-Jen Chen,[3,4] Wei-Chi Wu,[3,4] Yih-Shiou Hwang,[3,4,9,10] Fu-Sung Lo,[4,11] and Chi-Chun Lai[3,4,12]

[1]*School of Medicine, National Taiwan University College of Medicine, Taipei 106, Taiwan*
[2]*Department of Computer Science and Information Engineering National Taiwan University, Taipei 106, Taiwan*
[3]*Department of Ophthalmology, Chang Gung Memorial Hospital, Linkou Medical Center, Taoyuan 333, Taiwan*
[4]*College of Medicine, Chang Gung University, Taoyuan 333, Taiwan*
[5]*Graduate Institute of Clinical Medical Sciences, Chang Gung University, Taoyuan 333, Taiwan*
[6]*Department of Ophthalmology, National Taiwan University Hospital, Taipei 100, Taiwan*
[7]*Department of Ophthalmology, Edward S. Harkness Eye Institute, Columbia University, New York, New York 10032, USA*
[8]*Graduate Institute of Clinical Medicine, College of Medicine, National Taiwan University, Taipei 106, Taiwan*
[9]*Department of Ophthalmology, Chang Gung Memorial Hospital, Xiamen 361028, China*
[10]*Department of Ophthalmology, Jen-Ai Hospital Dali Branch, Taichung 400, Taiwan*
[11]*Division of Pediatric Endocrinology and Genetics, Chang Gung Memorial Hospital, Linkou Medical Center, Taoyuan 333, Taiwan*
[12]*Department of Ophthalmology, Chang Gung Memorial Hospital, Keelung 204, Taiwan*

Correspondence should be addressed to Fu-Sung Lo; lofusu@cgmh.org.tw and Chi-Chun Lai; chichun.lai@gmail.com

Jui-En Lo and Eugene Yu-Chuan Kang contributed equally to this work.

Received 1 September 2021; Revised 27 October 2021; Accepted 25 November 2021; Published 28 December 2021

Academic Editor: Tao Li

This study is aimed at evaluating a deep transfer learning-based model for identifying diabetic retinopathy (DR) that was trained using a dataset with high variability and predominant type 2 diabetes (T2D) and comparing model performance with that in patients with type 1 diabetes (T1D). The Kaggle dataset, which is a publicly available dataset, was divided into training and testing Kaggle datasets. In the comparison dataset, we collected retinal fundus images of T1D patients at Chang Gung Memorial Hospital in Taiwan from 2013 to 2020, and the images were divided into training and testing T1D datasets. The model was developed using 4 different convolutional neural networks (Inception-V3, DenseNet-121, VGG1, and Xception). The model performance in predicting DR was evaluated using testing images from each dataset, and area under the curve (AUC), sensitivity, and specificity were calculated. The model trained using the Kaggle dataset had an average (range) AUC of 0.74 (0.03) and 0.87 (0.01) in the testing Kaggle and T1D datasets, respectively. The model trained using the T1D dataset had an AUC of 0.88 (0.03), which decreased to 0.57 (0.02) in the testing Kaggle dataset. Heatmaps showed that the model focused on retinal hemorrhage, vessels, and exudation to predict DR. In wrong prediction images, artifacts and low-image quality affected model performance. The model developed with the high variability and T2D predominant dataset could be applied to T1D patients. Dataset homogeneity could affect the performance, trainability, and generalization of the model.

1. Introduction

Diabetic retinopathy (DR) is a severe vascular complication that may lead to blindness in patients with type 1 diabetes (T1D) [1]. As early detection and intervention can delay disease progression, patients are encouraged to undergo eye examination 3–5 years after the onset of disease and an annual DR screening thereafter [2, 3]. Despite the benefits of early treatment, approximately 60% of patients receive regular DR screening [2]. Reported reasons for nonadherence to recommended annual screening include cost, lack of access to eye care, and no perceived need [4]. Therefore, automated detection may fill these resource gaps and even improve patient outcomes by providing timely detection.

In an era of advancing technology in artificial intelligence, numerous studies have proven the effectiveness of applying deep convolutional networks for detecting DR [5–7]. However, wide variability exists in the approaches to prediction problems across different studies [8]. Understanding the factors that influence the reliability and robustness of the algorithm is important for clinical deployment and may help ensure consistency in performance under various conditions. A previous study reviewed the potential factors [9]; however, whether different etiologies of diabetes or variability of training images affect the algorithm's performance has yet to be investigated.

Diabetes patients can be classified into two major categories based on different etiologies: T1D, which is caused by insulin deficiency and is also known as insulin-dependent diabetes, and type 2 diabetes (T2D), which is caused by insulin resistance and is also known as insulin-independent diabetes mellitus. T2D accounts for most cases of diabetes. In the US population, >90% of patients with diabetes have T2D, whereas T1D accounts for only 5% [10]. T1D predominantly affects the European population [11], and its prevalence in the Asian population is even lower; for example, T1D is present in <1% of the diabetic population in Taiwan [12]. Although T1D presents as the minority in the diabetic population, patients with T1D are more likely to develop DR and have more severe visual outcomes than patients with T2D [1, 2, 13, 14]. A study reported that youth with T1D also develop DR faster than those with T2D [15]. When evaluating the cause of vision impairment in diabetes, DR accounts for 86% of poor visual acuity in T1D and only 33% in T2D [14]. As machine learning has been widely used for the automatic detection of DR, most images are obtained from the dataset predominantly containing the images of T2D patients. Furthermore, the investigation of the performance of models in identifying DR in the specific T1D population is limited.

To assess whether different etiologies of diabetes (i.e., T1D and T2D) affect the performance and robustness of deep learning models, we conducted this study using deep learning models trained using two datasets: one from open-access datasets with high image variability from T2D patients predominantly and the other one consisting of images obtained only from T1D patients followed at a single medical center. As our dataset is small compared with the recommended size [9], the deep transfer learning method is preferably used, which allows for low training cost and the use of a smaller training dataset by reusing a pretrained network to solve a different task [16]. The performance and heatmaps of deep learning models trained with the two datasets were then compared.

2. Materials and Methods

2.1. Datasets. An open-access dataset was subsampled from one of the Kaggle datasets, namely, Train.001, which is a publicly available dataset provided by EyePACS [17], which contained a group of patients with a mean age of around 55.4 years and a standard deviation of 11.3 years [5]. The other dataset of retinal fundus images was retrospectively acquired from T1D patients at a 3700-bed medical center, Chang Gung Memorial Hospital, Linkou Medical Center, Taiwan, between 2013 and 2020. All T1D patients were from the Chang Gung Juvenile Diabetes Eye Study [18, 19] and diagnosed based on the World Health Organization diagnosis criteria [20]. The T1D dataset consisted of patients with a mean age of 25.7 years and a standard deviation of 5.8 years. In the T1D dataset, two types of color fundus cameras were used (Topcon Medical Systems, Oakland, NJ, USA; Kowa, Tokyo, Japan, and Digital Non-Mydriatic Retinal Camera, Canon, Tokyo, Japan). Image resolution in both datasets ranged from 1,000 × 1,500 to 2,500 × 3,500 pixels. This study was approved by the Institutional Review Board of Chang Gung Memorial Hospital (no. 201900477B0) and adhered to the tenets of the Declaration of Helsinki.

2.2. Classification of DR. Retinal fundus images from T1D patients were graded by two trained retinal ophthalmologists (EYK and NKW) according to the International Clinical Diabetic Retinopathy Disease Severity Scale. Images with artifacts, shadows, or poor quality that could not be classified were excluded. Retinal ophthalmologists were unaware of clinical information, such as demographics, laboratory data, and prior treatment. On the other hand, DR classification in the Kaggle dataset was defined according to the labels provided with the dataset. In this study, DR was defined as the diagnosis of DR at any stage [21].

2.3. Data Preprocessing and Division. All input images from both datasets were cropped and resized using OpenCV-python to a 320-pixel wide square that tightly contained the circular fundus region. Monochromatic fundus photography and images not having both the optic disc and macular region were filtered out (Figure 1). For each dataset, images were randomly divided into two sets: two-thirds in the training set to develop the model and one-third in the testing set to evaluate model performance (Figure 2). Then, the training set was further divided into two subsets: two-thirds of the training set for optimizing the weights of the network and one-third as the validation set to select hyperparameters for the model. As images from the T1D dataset may come from the same patients, to avoid data leakage, images from same patients were placed in the same sets. After division, the images were randomly shuffled in their own dataset to reduce overfitting and variance before training and were then further batch

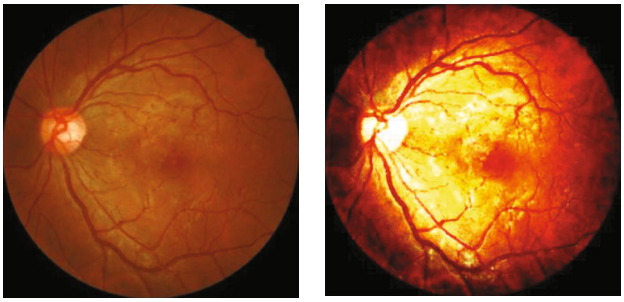

(a) (b)

Figure 1: Fundus image after (a) cropping and (b) normalization.

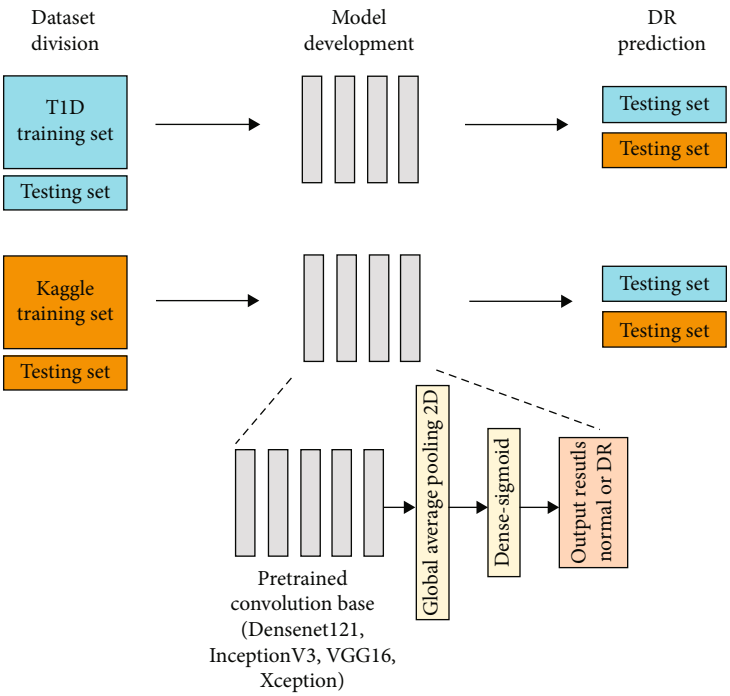

Figure 2: Schematic of the development and evaluation of models. Two groups of models were trained using the T1D and Kaggle training sets, and they were tested with both the T1D and Kaggle testing sets.

Table 1: Summary of the prediction performance of different transfer learning models in predicting diabetic retinopathy.

	Trained on Kaggle training set						Trained on T1D training set					
	Tested on T1D testing set			Tested on Kaggle testing set			Tested on T1D testing set			Tested on Kaggle testing set		
	AUC	SEN	SPE	AUC	SEN	SPE	AUC	SEN	SPE	AUC	SEN	SPE
DenseNet-121	0.86	0.77	0.79	0.74	0.67	0.71	0.91	0.81	0.86	0.55	0.55	0.54
InceptionV3	0.86	0.74	0.79	0.74	0.62	0.74	0.87	0.73	0.86	0.59	0.56	0.59
VGG16	0.88	0.78	0.82	0.77	0.66	0.75	0.84	0.67	0.84	0.54	0.59	0.49
Xception	0.86	0.74	0.82	0.71	0.60	0.72	0.88	0.74	0.90	0.59	0.61	0.52

T1D: type 1 diabetes; AUC: area under the curve; SEN: sensitivity; SPE: specificity.

normalized by subtracting the average and dividing by the standard deviation calculated from the training dataset using ImageDataGenerator of Keras API. Real-time data augmentation was applied by randomly rotating, shifting, and shearing the images during the model training based on previously published methods [22].

2.4. Architecture and Evaluation of the Model. The deep transfer learning model consisted of a pretrained convolutional neural network (CNN), followed by a global average pooling layer and a dense layer to output prediction results (Figure 2). The weights from the pretrained model were trainable and were used to extract image features, and predictions

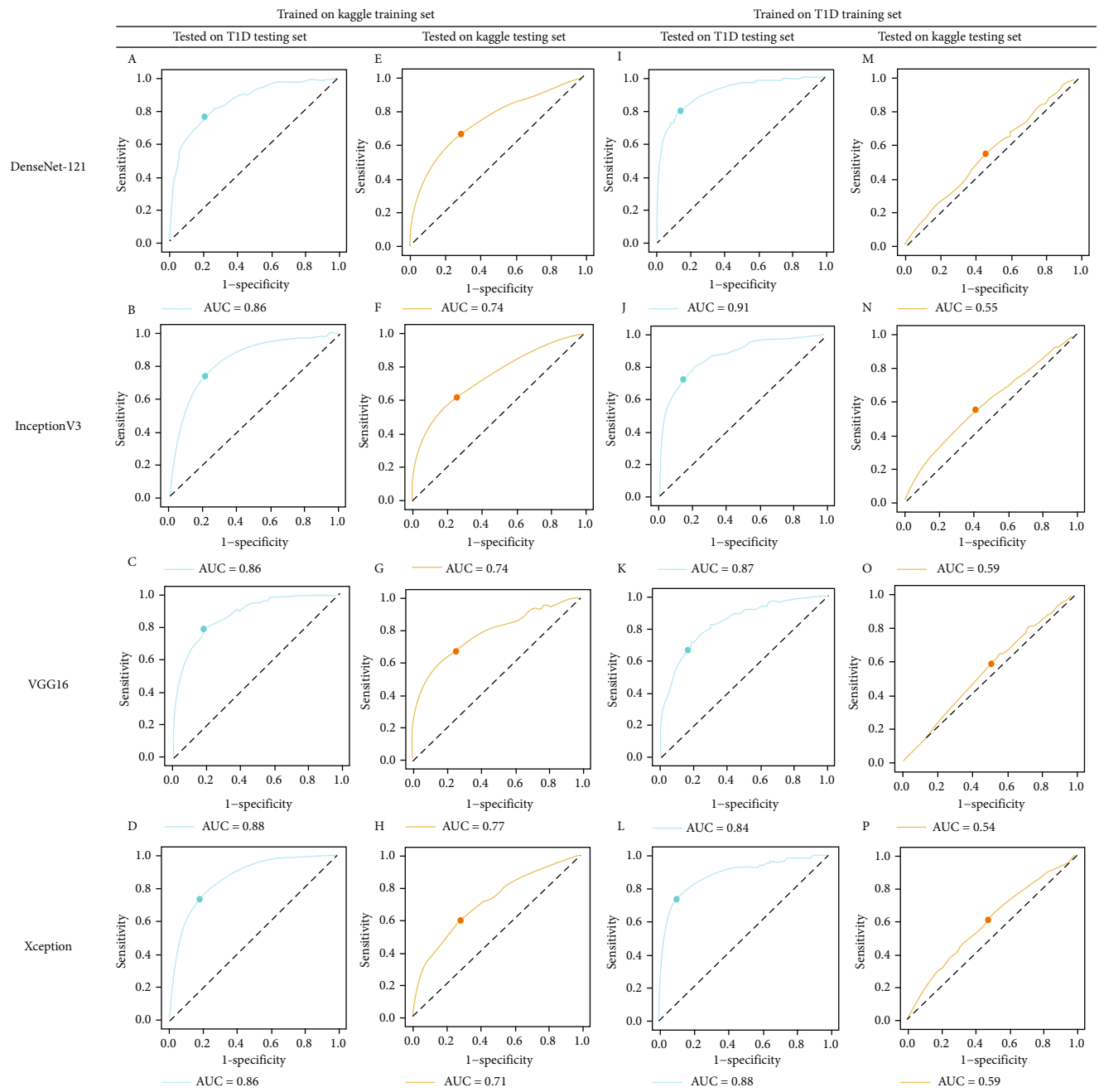

Figure 3: Receiver operating characteristic (ROC) curves of different transfer learning models in predicting diabetic retinopathy. The ROC curve of models that were tested with the type 1 diabetes (T1D) testing set was plotted in blue, whereas those tested with the Kaggle testing set were plotted in orange. The point on the ROC curve was the selected threshold. (e)–(h) There was a significant decrease in AUC when models previously trained with the T1D training set were tested with the Kaggle dataset. (i)–(l) The models that were previously trained with the Kaggle training set have a more robust performance when tested with the T1D testing set.

were then made using the final classifier. Class imbalance was addressed by estimating reweighting loss. Early stopping after 8–12 epochs of no improvement was applied to avoid overfitting, and the learning curves of both the training and validation sets were plotted to detect underfitting or overfitting. Binary cross entropy was used as the loss function, and stochastic gradient descent [23] or the Adam optimizer [24] was used with a learning rate of 1e-3 to 1e-4. Hyperparameters were optimized using random search. The development and analysis of the models were implemented using Keras 2.4.3 and Tensorflow 2.4.1 on Google colaboratory [25], whereas a part of image preprocessing and gradient-weighted class activation (Grad-CAM) visualization were run in Jupyter Notebook [26]. Two groups of models trained using the T1D and Kaggle training sets were tested in both the T1D and Kaggle testing sets (Figure 2).

In our model, CNNs including Inception-V3 [27], DenseNet-121 [28], VGG16 [29], and Xception [30] were

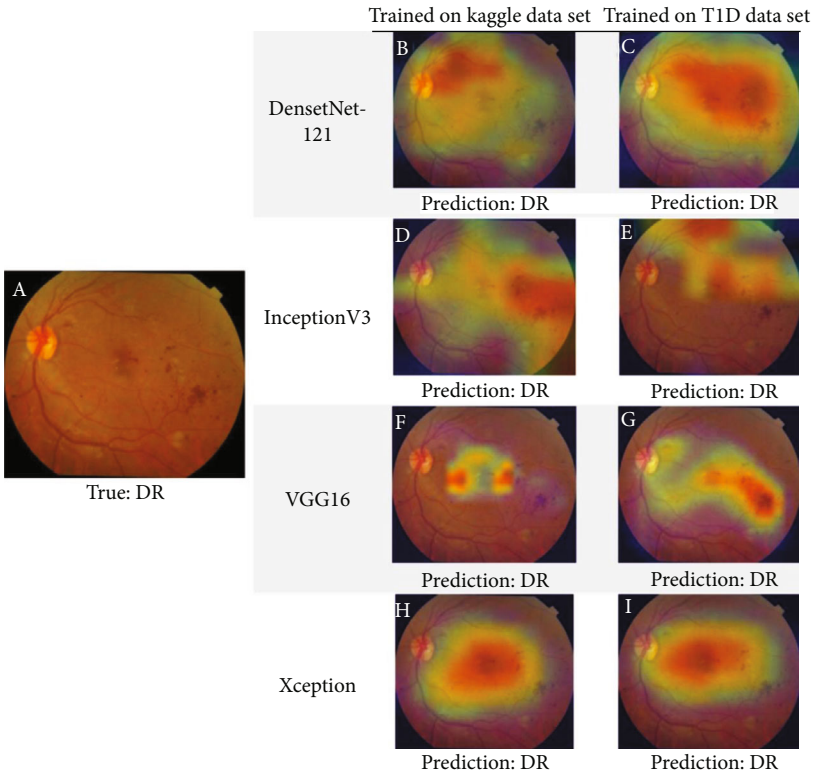

Figure 4: The images demonstrate the original (a) and superimposed Grad-CAM activation maps ((b)–(i)) of the selected diabetic retinopathy (DR) color fundus image. All models gave a true-positive prediction. There were some similarities in activation maps even in different transfer learning models trained with different datasets.

selected for model training because of their high performance in ImageNet Large Scale Visual Recognition Challenge and wide implementation in other medical image classifications [9]. All networks were pretrained on ImageNet [31]. Performance of the model with each CNN was evaluated.

2.5. Visualization Method. To observe how the models led to the prediction, the final convolutional layer of each model was extracted to obtain the activation map using the Grad-CAM visualization method [32], which highlighted the regions that provided an important contribution to the prediction. The activation map was then superimposed on the original image for interpretation.

2.6. Statistical Analysis. Receiver operating characteristic (ROC) curves were plotted using Matplotlib 3.2.2. Area under the ROC curve (AUC), sensitivity, and specificity were calculated to compare the performance of different models trained with both datasets using Python 3.7.1 and Sklearn 0.22.2. Optimal threshold of ROCs was chosen by maximizing the geometric mean of sensitivity and specificity. The descriptive results in this study are expressed as numbers and percentages for discrete variables.

3. Results

3.1. Image Characteristics. In the Kaggle dataset, 8,408 images were subsampled from the original dataset, with 6,150 (73%) images classified as normal and 2,258 (27%) images as DR. In the T1D dataset, 7,064 images from 475 patients with T1D were collected. Of these, 873 (13%) images from 79 (17%) patients were classified as DR.

3.2. Model Performance. Model performance is shown in Table 1. When the models were trained using the Kaggle imaging dataset, the overall AUC reached a mean (range) of 0.74 (0.03) in the Kaggle testing set, with VGG16 providing the best performance (AUC = 0.77). AUCs increased to a mean (range) of 0.87 (0.01) when the models trained with the Kaggle training set were tested using the T1D testing set. On the other hand, the transfer learning models achieved a mean (range) AUC of 0.88 (0.03) when trained and tested using the T1D imaging dataset, with DenseNet-121 providing the best performance (AUC = 0.91) and VGG16 the worst (AUC = 0.84). However, when models that were previously trained using the T1D training set were tested using the Kaggle dataset, AUCs significantly decreased to a mean (range) of 0.57 (0.02). The corresponding ROC curves are illustrated in Figure 3.

3.3. Class Activation Maps. The results of activation maps from different transfer learning models of both DR and normal cases are presented in Figures 4 and 5. Aside from highlighting the clinically observable retinal abnormalities, which were the traditional characteristic findings of DR, including microaneurysms, hemorrhages, and exudates (Figures 4(c), 4(d), and 4(g)), other regions including the macula (Figures 4(h), 4(i), 5(d), 5(h), 5(f), and 5(i)), optic disc

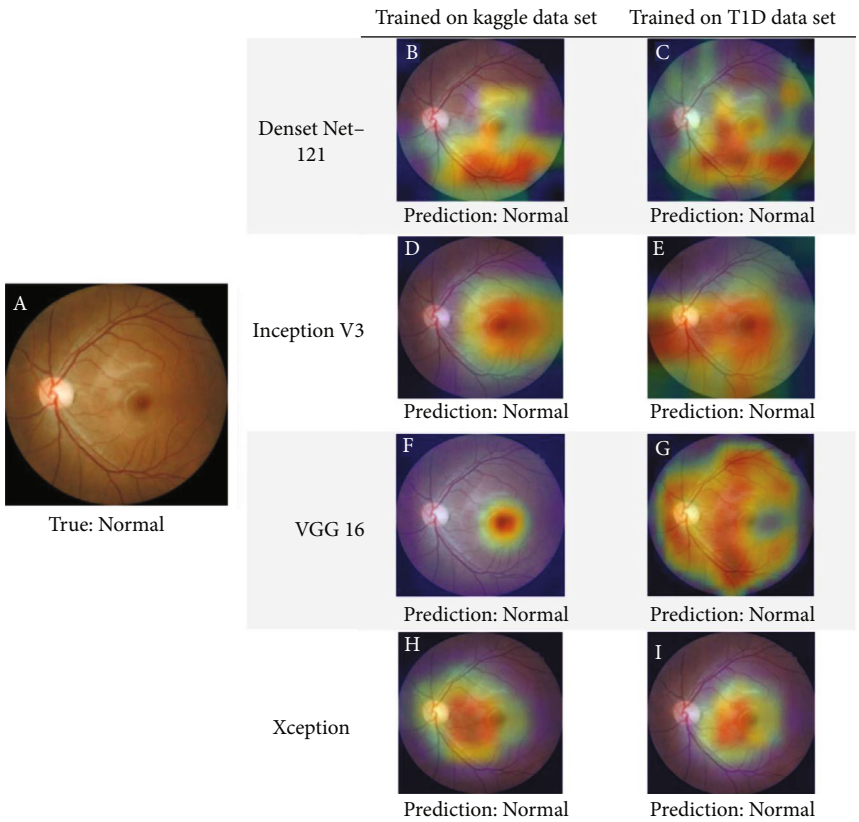

Figure 5: The images present the original (a) and superimposed Grad-CAM activation maps ((b)–(i)) of the selected normal color fundus image. All models gave a true-negative prediction. There was a high variation in the activation map when given a normal fundus image. Some models focus on the optic disc ((e) and (g)), whereas others highlight the retinal vessels ((b), (c), and (g)), or macular region ((d), (h), (f), and (i)).

(Figures 5(e) and 5(g)), and retinal vessels (Figures 5(b), 5(c), and 5(g)) were also occasionally highlighted. Greater similarities were observed in activation maps among transfer learning models trained using the DR fundus image (Figure 4) rather than the normal fundus image (Figure 5).

4. Discussion

4.1. Main Findings of the Present Study. In our study, we trained models using the open-access Kaggle dataset, which has high image variability and theoretically predominant T2D patients, and the T1D dataset from the single medical center. We found that the model trained using the Kaggle dataset had an average AUC of 0.74 when testing using the same dataset, but this increased to 0.87 when testing using the T1D dataset. By contrast, the model trained using the T1D dataset had high accuracy (up to AUC of 0.91) in T1D patients, but it decreased (lowest AUC of 0.54) with the Kaggle dataset. Heatmaps demonstrated weighted features of retinal microaneurysm, hemorrhage, exudation, and vessels. Dataset homogeneity dataset may affect the trainability and generalization of the model.

4.2. Importance of External Validation and Standardization of Hyperparameters. Previous studies proposed numerous models that achieved high performance in diagnosing DR, even when trained with only a small dataset containing thousands of images [16]. The performance of our results yielded comparable results with the previous study (AUCs ranged from 0.65 to 0.86) when using a similar data size from the Kaggle dataset [33]. However, a large DR screening validation study found that most algorithms had significant performance differences and even obtained concerning results when evaluated through external validation, even though these algorithms were already in active use in real-world clinical settings [34]. In our study, models trained using the T1D dataset also exhibited acceptable performance (AUCs between 0.84 and 0.91) when internally validated, but their performance significantly decreased when evaluated using the external dataset. These results highlight the need for rigorous training and testing of models by using datasets containing a similar distribution of target population to avoid the huge discrepancy between expected and real performance. In addition, to produce a stable and reproducible prediction outcome, considerably more hyperparameters should be standardized. Although a previous study had already investigated the large number of possible factors that influence the performance of deep learning model [9], we anticipate that many more elements still need to be determined. For instance, the etiology of DM, age range, and comorbid eye diseases were shown to be possible influencing factors in our study.

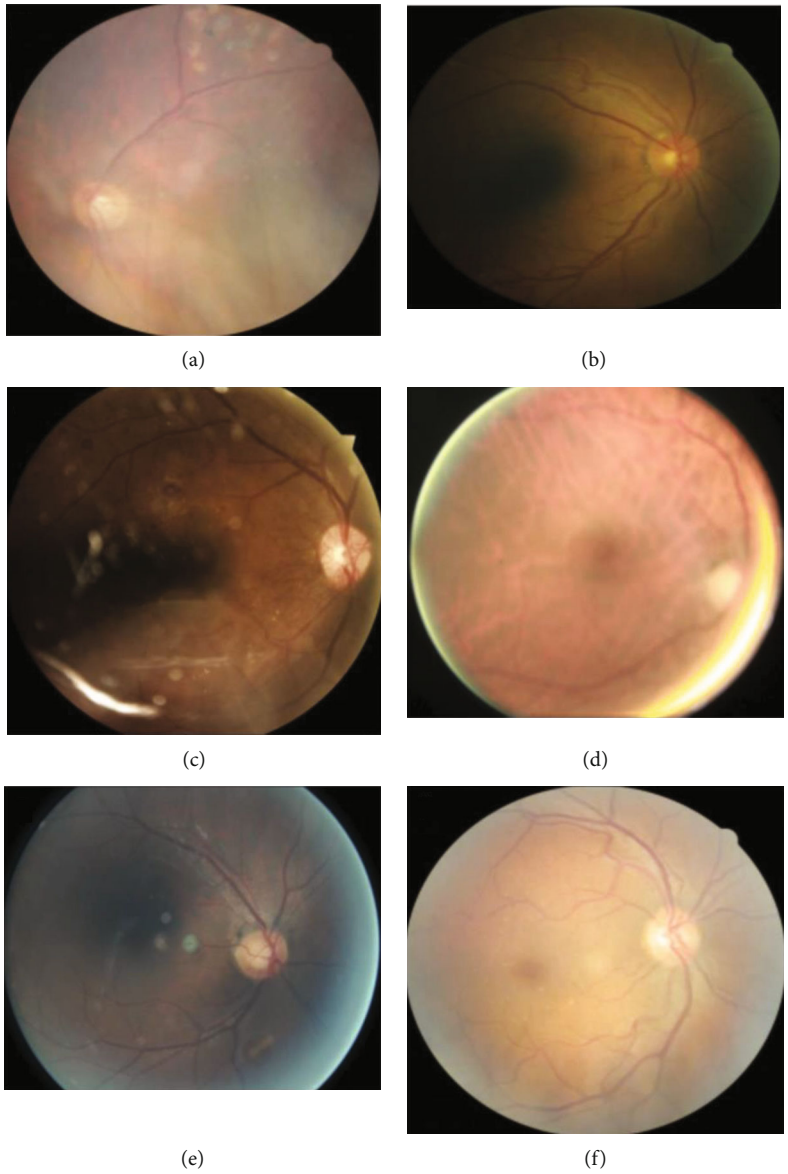

Figure 6: Images in the Kaggle dataset with wrong prediction. (a) False-negative in an image with foggy view and retinal laser scar. (b) False-negative in an image with poor illumination. (c) False-negative in an image with reflective spots and shadows. (d) False-positive in an image with overexposure and halo. (e) False-positive in an image with underexposure and halo. (f) False-positive in an image with exudates caused by age-related macular degeneration.

4.3. Different Performance Levels in Different Datasets. The models trained using the T1D dataset had poor performance when tested using the Kaggle dataset, whereas those trained using the Kaggle dataset showed better performance when tested using the T1D dataset. There are several possible explanations for the differences in the generalization of models trained using different datasets despite the use of the same method, similar dataset size, and imbalance ratio. When reviewing the wrong prediction images, we found that the images had similar problems affecting model prediction (Figure 6). Images from the T1D dataset were evaluated by retinal ophthalmologists, and images with poor quality or those that could not be graded were excluded. As the T1D dataset contained images of patients over multiple visits, the number of unique patients with T1D may be less than that in the Kaggle dataset, resulting in homogeneous data and thus rendering the T1D database much easier to predict for models trained using either of the databases. By contrast, images from the Kaggle dataset may not be cleaned and may contain more noise and artifacts, including out-of-focus, overexposure, or underexposure images, than images from the T1D dataset. Furthermore, the Kaggle dataset could be collected from a more diverse population with older age and higher age variation, thus, having more heterogeneous characteristics, whereas T1D patients had similar demographics and younger age. Therefore, patients in the Kaggle dataset may have other ocular diseases related to aging or other comorbidities such as cataract and age-related macular degeneration. Retinal features of ocular diseases other than DR, such as retinal exudates in age-related macular

degeneration, may affect model prediction. In addition, cataracts may affect image quality. These findings have been reported in our previous studies [35, 36]. As the T1D dataset contained images of patients over multiple visits, the characteristic variation in T1D may be less than that in the Kaggle dataset, also resulting in homogeneous data. Therefore, a homogeneous dataset may have resulted in higher trainability and lower generalization of models and vice versa in a more heterogenous dataset. Therefore, heterogeneity of the testing population also influences the performance of prediction models.

4.4. Highlighted Regions by Grad-CAM. Typical characteristic findings of DR, such as retinal microaneurysms, hemorrhages, exudates, and neovascularization, were among the most common highlighted regions by Grad-CAM in our study, consistent with a previous report [37]. In addition, nontraditional regions including the macula and optic disc were occasionally highlighted. As DR may also present with diabetic macular edema and neovascularization of the disc, abnormal features in these regions may also be extracted. Although neurodegeneration precedes vascular lesion in DR [38], whether deep learning models can detect abnormalities before the appearance of clinically observable lesions requires further investigation.

4.5. Limitations. This study has several limitations. First, we only assessed how training using only the T1D dataset affects detection performance; these results may not apply to other etiologies, such as the inherited form, maturity onset diabetes of the young, or other secondary causes. Second, our T1D data were collected from a single medical center and from a single ethnicity, making the dataset relatively small with less heterogeneity. Third, DR was identified using macula-centered retinal fundus images in the T1D dataset, instead of images obtained through 7-field retinal fundus photography, as suggested by the Early Treatment Diabetic Retinopathy Study [39]. In addition, we did not justify further DR grading, which may help with the determination of treatment-required DR, because the detection of early DR in the T1D population could provide more information in patient care and education [18]. Finally, our models were developed with a limited combination of hyperparameters, and we did not conduct a combined model training on both datasets. A different implementation may thus provide different results.

5. Conclusion

Our study investigated a deep learning-based DR prediction model using two datasets. Our results showed that dataset homogeneity can have a significant effect on the trainability and generalization of the model. This implied that deep learning models should be trained with data similar to the target population and updated according to the landscape of DM to ensure a robust prediction and outcome. As the prevalence of diabetes continues to rise [2], along with an alarming increase in the frequency of T2D among youth [40], the epidemiology of diabetes will continue to change. In addition, activation maps produced inferred that in addition to characteristic findings of DR, the macula and optic disc may also contribute to the detection of abnormalities in fundus imaging.

Data Availability

The T1D dataset is not publicly available due to the data security policy of Chang Gung Memorial Hospital and is available upon reasonable request.

Disclosure

The funding group had no role in study conduction and result interpretation.

Conflicts of Interest

The authors declare that there is no conflict of interest regarding the publication of this paper.

Authors' Contributions

Jui-En Lo and Eugene Yu-Chuan Kang contributed equally to this work.

Acknowledgments

The study was supported by the Chang Gung Memorial Hospital, Taiwan (CMRPG3K0481 and CMRPG3L0251).

References

[1] D. S. Fong, L. Aiello, T. W. Gardner et al., "Retinopathy in diabetes," *Diabetes Care*, vol. 27, Supplement 1, pp. S84–S87, 2004.

[2] C. J. Flaxel, R. A. Adelman, S. T. Bailey et al., "Diabetic retinopathy preferred practice pattern®," *Ophthalmology*, vol. 127, pp. 66–145, 2020.

[3] American Diabetes Association, "Standards of medical care in diabetes," *Diabetes Care*, vol. 27, Supplement 1, pp. S15–S35, 2004.

[4] C.-F. Chou, C. E. Sherrod, X. Zhang et al., "Barriers to eye care among people aged 40 years and older with diagnosed diabetes, 2006-2010," *Diabetes Care*, vol. 37, pp. 180–188, 2014.

[5] V. Gulshan, L. Peng, M. Coram et al., "Development and validation of a deep learning algorithm for detection of diabetic retinopathy in retinal fundus photographs," *JAMA*, vol. 316, pp. 2402–2410, 2016.

[6] D. S. W. Ting, C. Y. Cheung, G. Lim et al., "Development and validation of a deep learning system for diabetic retinopathy and related eye diseases using retinal images from multiethnic populations with diabetes," *JAMA*, vol. 318, pp. 2211–2223, 2017.

[7] D. S. W. Ting, L. R. Pasquale, L. Peng et al., "Artificial intelligence and deep learning in ophthalmology," *The British Journal of Ophthalmology*, vol. 103, no. 2, pp. 167–175, 2019.

[8] M. M. Islam, H. C. Yang, T. N. Poly, W. S. Jian, and Y. C. Jack Li, "Deep learning algorithms for detection of diabetic retinopathy in retinal fundus photographs: a systematic review and

meta-analysis," *Computer Methods and Programs in Biomedicine*, vol. 191, p. 105320, 2020.

[9] M. Y. T. Yip, G. Lim, Z. W. Lim et al., "Technical and imaging factors influencing performance of deep learning systems for diabetic retinopathy," *NPJ Digital Medicine*, vol. 3, no. 1, p. 40, 2020.

[10] American Diabetes Association, "Diagnosis and classification of diabetes mellitus," *Diabetes Care*, vol. 33, Supplement_1, pp. S62–S69, 2010.

[11] S. Sivaprasad, B. Gupta, R. Crosby-Nwaobi, and J. Evans, "Prevalence of diabetic retinopathy in various ethnic groups: a worldwide perspective," *Survey of Ophthalmology*, vol. 57, pp. 347–370, 2012.

[12] Y.-D. Jiang, C.-H. Chang, T.-Y. Tai, J.-F. Chen, and L.-M. Chuang, "Incidence and prevalence rates of diabetes mellitus in Taiwan: analysis of the 2000–2009 Nationwide Health Insurance database," *Journal of the Formosan Medical Association*, vol. 111, pp. 599–604, 2012.

[13] M. C. Eppens, M. E. Craig, J. Cusumano et al., "Prevalence of diabetes complications in adolescents with type 2 compared with type 1 diabetes," *Diabetes Care*, vol. 29, pp. 1300–1306, 2006.

[14] R. Klein, B. E. Klein, and S. E. Moss, "Visual impairment in diabetes," *Ophthalmology*, vol. 91, no. 1, pp. 1–9, 1984.

[15] S. Y. Wang, C. A. Andrews, W. H. Herman, T. W. Gardner, and J. D. Stein, "Incidence and risk factors for developing diabetic retinopathy among youths with type 1 or type 2 diabetes throughout the United States," *Ophthalmology*, vol. 124, pp. 424–430, 2017.

[16] M. T. Hagos and S. Kant, "Transfer learning based detection of diabetic retinopathy from small dataset," 2019, http://arxiv.org/abs/190507203.

[17] Kaggle, "Diabetic Retinopathy Detection," 2015, July 2012 https://www.kaggle.com/c/diabetic-retinopathy-detection.

[18] E. Y. Kang, F. S. Lo, J. P. Wang et al., "Nomogram for prediction of non-proliferative diabetic retinopathy in juvenile-onset type 1 diabetes: a cohort study in an Asian population," *Scientific Reports*, vol. 8, p. 12164, 2018.

[19] N. K. Wang, C. C. Lai, J. P. Wang et al., "Risk factors associated with the development of retinopathy 10 yr after the diagnosis of juvenile-onset type 1 diabetes in Taiwan: a cohort study from the CGJDES," *Pediatric Diabetes*, vol. 17, pp. 407–416, 2016.

[20] K. G. Alberti and P. Z. Zimmet, "Definition, diagnosis and classification of diabetes mellitus and its complications. Part 1: diagnosis and classification of diabetes mellitus provisional report of a WHO consultation," *Diabetic Medicine*, vol. 15, pp. 539–553, 1998.

[21] C. P. Wilkinson, F. L. Ferris 3rd, R. E. Klein et al., "Proposed international clinical diabetic retinopathy and diabetic macular edema disease severity scales," *Ophthalmology*, vol. 110, pp. 1677–1682, 2003.

[22] F. Chollet, "Building powerful image classification models using very little data," *The Keras Blog*, 2016, July 2021 https://blog.keras.io/building-powerful-image-classification-models-using-very-little-data.html.

[23] S. Ruder, "An overview of gradient descent optimization algorithms," 2016, http://arxiv.org/abs/160904747.

[24] D. P. Kingma and J. Ba, "Adam: a method for stochastic optimization," 2014, http://arxiv.org/abs/14126980.

[25] T. Carneiro, R. V. M. D. NóBrega, T. Nepomuceno, G. Bian, V. H. C. D. Albuquerque, and P. P. R. Filho, "Performance analysis of Google Colaboratory as a tool for accelerating deep learning applications," *IEEE Access*, vol. 6, pp. 61677–61685, 2018.

[26] T. Kluyver, B. Ragan-Kelley, F. Pérez et al., *Jupyter Notebooks*, A Publishing Format for Reproducible Computational Workflows, 2016.

[27] C. Szegedy, V. Vanhoucke, S. Ioffe, J. Shlens, and Z. B. Wojna, "Rethinking the Inception Architecture for Computer Vision," in *Proceedings of the IEEE conference on computer vision and pattern recognition*, pp. 2818–2826, 2016.

[28] G. Huang, Z. Liu, L. V. D. Maaten, and K. Q. Weinberger, "Densely connected convolutional networks," in *2017 IEEE Conference on Computer Vision and Pattern Recognition (CVPR)*, pp. 2261–2269, 2017.

[29] K. Simonyan and A. Zisserman, "Very deep convolutional networks for large-scale image recognition," 2014, http://arxiv.org/abs/14091556.

[30] F. Chollet, "Xception: deep learning with depthwise separable convolutions," in *2017 IEEE Conference on Computer Vision and Pattern Recognition (CVPR)*, pp. 1800–1807, 2017.

[31] O. Russakovsky, J. Deng, H. Su et al., "ImageNet large scale visual recognition challenge," *International Journal of Computer Vision*, vol. 115, no. 3, pp. 211–252, 2015.

[32] R. R. Selvaraju, M. Cogswell, A. Das, R. Vedantam, D. Parikh, and D. Batra, "Grad-cam: visual explanations from deep networks via gradient-based localization," 2019, http://arxiv.org/abs/1610.02391.

[33] P. Burlina, W. Paul, P. Mathew, N. Joshi, K. D. Pacheco, and N. M. Bressler, "Low-shot deep learning of diabetic retinopathy with potential applications to address artificial intelligence bias in retinal diagnostics and rare ophthalmic diseases," *JAMA ophthalmology*, vol. 138, no. 10, pp. 1070–1077, 2020.

[34] A. Y. Lee, R. T. Yanagihara, C. S. Lee et al., "Multicenter, head-to-head, real-world validation study of seven automated artificial intelligence diabetic retinopathy screening systems," *Diabetes Care*, vol. 44, pp. 1168–1175, 2021.

[35] E. Y. Kang, L. Yeung, Y. L. Lee et al., "A multimodal imaging-based deep learning model for detecting treatment-requiring retinal vascular diseases: model development and validation study," *JMIR Medical Informatics*, vol. 9, no. 5, p. e28868, 2021.

[36] Y. T. Hsieh, L. M. Chuang, Y. D. Jiang et al., "Application of deep learning image assessment software VeriSee™ for diabetic retinopathy screening," *Journal of the Formosan Medical Association*, vol. 120, pp. 165–171, 2021.

[37] S. Keel, J. Wu, P. Y. Lee, J. Scheetz, and M. He, "Visualizing deep learning models for the detection of referable diabetic retinopathy and glaucoma," *JAMA ophthalmology*, vol. 137, no. 3, pp. 288–292, 2019.

[38] S. F. Abcouwer and T. W. Gardner, "Diabetic retinopathy: loss of neuroretinal adaptation to the diabetic metabolic environment," *Annals of the New York Academy of Sciences*, vol. 1311, pp. 174–190, 2014.

[39] G. H. Bresnick, D. B. Mukamel, J. C. Dickinson, and D. R. Cole, "A screening approach to the surveillance of patients with diabetes for the presence of vision-threatening retinopathy," *Ophthalmology*, vol. 107, pp. 19–24, 2000.

[40] J. N. Wei, F. C. Sung, C. C. Lin, R. S. Lin, C. C. Chiang, and L. M. Chuang, "National surveillance for type 2 diabetes mellitus in Taiwanese children," *JAMA*, vol. 290, no. 10, pp. 1345–1350, 2003.

Hindawi
Journal of Diabetes Research
Volume 2021, Article ID 3033219, 9 pages
https://doi.org/10.1155/2021/3033219

Research Article

Choroidal Vascularity Index as a Biomarker for Visual Response to Antivascular Endothelial Growth Factor Treatment in Diabetic Macular Edema

Ningxin Dou, Shanshan Yu, Ching-Kit Tsui, Boyu Yang, Jianqiang Lin, Xi Lu, Yue Xu, Benjuan Wu, Jinfeng Zhao, and Xiaoling Liang

State Key Laboratory of Ophthalmology, Zhongshan Ophthalmic Center, Sun Yat-sen University, Guangzhou 510060, China

Correspondence should be addressed to Xiaoling Liang; liangxlsums@qq.com

Received 10 July 2021; Accepted 6 November 2021; Published 26 November 2021

Academic Editor: Lei Liu

Purpose. To investigate the choroidal vascularity index (CVI) as a prognostic factor for the visual efficacy of antivascular endothelial growth factor (VEGF) treatment in diabetic macular edema (DME). *Methods*. We retrospectively reviewed 92 DME eyes receiving anti-VEGF treatment, which were stratified as responders (≥5 letters gained) and nonresponders (<5 letters gained or lost). Baseline systematic features and optical coherence tomography features, including the CVI, adjusted ellipsoid zone (EZ) reflectivity, subretinal fluid (SRF), and disorganization of the retinal inner layers (DRIL), were evaluated between the two groups. *Results*. The baseline CVI was significantly lower in nonresponders than in responders (0.66 ± 0.05, 0.69 ± 0.05, and 0.72 ± 0.05, $p = 0.014$). After adjusting for other factors, the baseline CVI, DRIL, SRF, and adjusted EZ reflectivity were significantly associated with visual outcomes (CVI: odds ratio (OR) = 0.17, $p = 0.006$; adjusted EZ reflectivity: OR = 0.56, $p = 0.007$; DRIL: OR = 6.71, $p = 0.001$; and SRF: OR = 0.29, $p = 0.008$). *Conclusion*. DME patients with a higher CVI, higher adjusted EZ reflectivity, the presence of SRF, and the absence of DRIL at baseline were more likely to gain >5 letters in visual acuity after anti-VEGF treatment. CVI may serve as a novel biomarker for visual response to anti-VEGF treatment in DME.

1. Introduction

Diabetic macular edema (DME) is a leading cause of visual impairment in patients with diabetes [1]. Intravitreal vascular endothelial growth factor (VEGF) inhibitors have achieved favorable functional and structural outcomes in patients with DME. In the RIDE and RISE study, 33.6%–45.7% of patients with DME had a best-corrected visual acuity (BCVA) gain of more than three lines after 2 years of anti-VEGF treatment. A considerable proportion of patients (19.7%–39.2%) responded poorly to treatment [2]. Moreover, repeated injections are often required to maintain the treatment efficacy for DME [3]. To assist therapeutic selection for individual patients with DME, identification of prognostic factors for visual response before anti-VEGF treatment is critically important.

Spectral-domain optical coherence tomography (SD-OCT), which provides a noninvasive retinal image, is undoubtedly a potential tool for this purpose. Previous studies have reported a series of OCT retinal morphological features associated with the visual prognosis of anti-VEGF treatment in DME, such as disorganization of the retinal inner layers (DRIL), disruption of the ellipsoid zone (EZ) and external limiting membrane (ELM), subretinal fluid (SRF), epiretinal membrane (ERM), and hyperreflective foci (HRFs) [4–8]. However, most studies have focused on retinal features in OCT, neglecting the prognostic value of choroidal features.

The choroidal vasculature provides oxygen and nutrients to the outer retina and supports highly metabolically active photoreceptors, particularly in the foveal region. Damage to the choroidal vasculature may cause severe functional damage to the retina and impair visual recovery. Choroidal abnormalities are considerable in DME pathology [9, 10]. Recognizing choroidal features may provide a more comprehensive picture of the prognostic factors for anti-VEGF

treatment in DME. Enhanced depth imaging OCT (EDI-OCT) shows a more detailed and deepened choroidal vasculature image. Based on the EDI image, the newly developed marker of the choroidal vascularity index (CVI) provides information on the relative change between the stromal and luminal vascular components and is more robust than the subfoveal choroidal thickness (SFCT) [11]. The CVI shows a good correlation with the severity of diabetic retinopathy (DR) and decreases significantly in DME, which may be a sensitive marker of choroidal vascular change in DME [12, 13]. However, the association between the CVI and visual outcomes of anti-VEGF treatment in DME remains unclear.

In this study, we aimed to investigate the correlation between the CVI and visual prognosis of anti-VEGF treatment in DME. We performed multiple factor analysis to integrate the CVI and other candidate choroidal and retinal features to identify biomarkers that may provide more accurate prognostic information for anti-VEGF treatment in DME.

2. Materials and Methods

All research and measurements adhered to the tenets of the Declaration of Helsinki after the study protocol were approved by the Ethics Committee of Zhongshan Ophthalmic Center, Sun Yat-sen University. All participants provided written informed consent before enrollment in the study.

We conducted a retrospective case-control study. The recruited patients received three or more monthly intravitreal anti-VEGF drug injections (ranibizumab or conbercept) for the treatment of DME at Zhongshan Ophthalmic Center, Sun Yat-sen University, from February 2019 to July 2020. The patients had at least 4 months of follow-up. Patients who fulfilled the following criteria were included in the study: (1) age ≥ 18 years; (2) type 1 or 2 diabetes mellitus; and (3) center-involved DME treated with anti-VEGF drugs, with a study eye baseline BCVA lower than 0.63 (20/32). For patients who received bilateral injections, both eyes were included. The exclusion criteria were as follows: (1) other concomitant ocular diseases that compromise VA or cause macular edema (refractive errors of more than ±6 diopters, glaucoma, uveitis, or retinal vein occlusion); (2) previous vitreoretinal surgery or cataract surgery within 3 months; (3) previous intravitreal anti-VEGF drug injections or dexamethasone implants at any time; and (4) low-quality OCT image in which firm identification of retinal and choroidal features is not feasible. Mild lens opacity is acceptable if there is no impact on OCT image quality.

Baseline ocular and systemic data were recorded at the first visit, including demographic data, duration of diabetes, history of hypertension, and type of retinopathy (nonproliferative or proliferative stage). For the first three loading doses administered at monthly intervals, a doctor reviewed the patients 1 month after each injection. After that, a repeat course of injections was given depending on the ophthalmologist's judgment at the follow-up visit, taking a 3 + PRN regimen described in the previous study as reference [14]. Examination of BCVA using ETDRS visual acuity charts, comprehensive ophthalmologic examination with a slit-lamp microscope, intraocular pressure (IOP) measurement, and OCT scanning was performed at the baseline and every follow-up visit. BCVA after treatment was recorded 1 month after the last injection during the follow-up period, which was the last follow-up. Patients were categorized according to their BCVA evolution from baseline and were stratified into two treatment response groups: responders (≥5 ETDRS letters gained) and nonresponders (<5 ETDRS letters gained or lost) [5].

2.1. Optical Coherence Tomography Analysis. OCT scans were obtained using SD-OCT (Heidelberg Spectralis, Heidelberg, Germany). Vertical and horizontal line scans dissecting the fovea were acquired using the 30-degree EDI mode. One hundred images were overlaid to create high-resolution images.

A series of qualitative and quantitative morphological features were evaluated in the baseline OCT images as shown in Figure 1, including features describing the choroid, as follows: (1) CVI and (2) SFCT. Additionally, the following features describing the retina were considered: (1) adjusted EZ reflectivity, (2) adjusted ELM reflectivity, (3) DRIL, (4) disruption of the EZ, (5) disruption of the ELM, (6) presence of SRF, (7) presence of cystoid abnormalities, (8) presence of an ERM, and (9) HRF quantity.

The listed features were evaluated on horizontal and vertical scans passing through the fovea. All image analyses were performed using ImageJ, a software program in the public domain.

The CVI was calculated using the protocol described by Sonoda et al. [15]. The subfoveal choroidal area of 1.5 mm wide, centered on the fovea, was selected as the total choroidal area (TCA). The luminal choroidal area (LCA) was obtained after Niblack's auto local binarization was applied to the OCT image. The CVI was calculated as the ratio of the LCA to TCA. The SFCT was measured as the distance between Bruch's membrane and the choroid-scleral interface just beneath the fovea.

Morphological features describing the retina were measured within the central 1 mm area in both vertical and horizontal scans. The OCT images were exported without adjustment to the preset contrast or brightness in the OCT software. The extent of EZ and ELM disruption was measured as the transverse length with loss of the hyperreflective signal that characterizes the EZ and ELM, respectively. The reflectivity is represented by the gray value. EZ, ELM, and RPE were outlined in the 1 mm zone, in which the average reflectivity was measured. Adjusted EZ and ELM reflectivity was calculated as raw data relative to the average reflectivity of the RPE. The results of the measurements on vertical and horizontal sectional images were averaged. DRIL was defined as the inability to distinguish boundaries between any two of the ganglion cell/inner plexiform layer complex, inner nuclear layer, and outer plexiform layer in >50% of the foveal 1 mm zone [4]. The presence of DRIL, SRF, cystoid abnormalities, and epiretinal membranes on either vertical or horizontal sectional images was recorded.

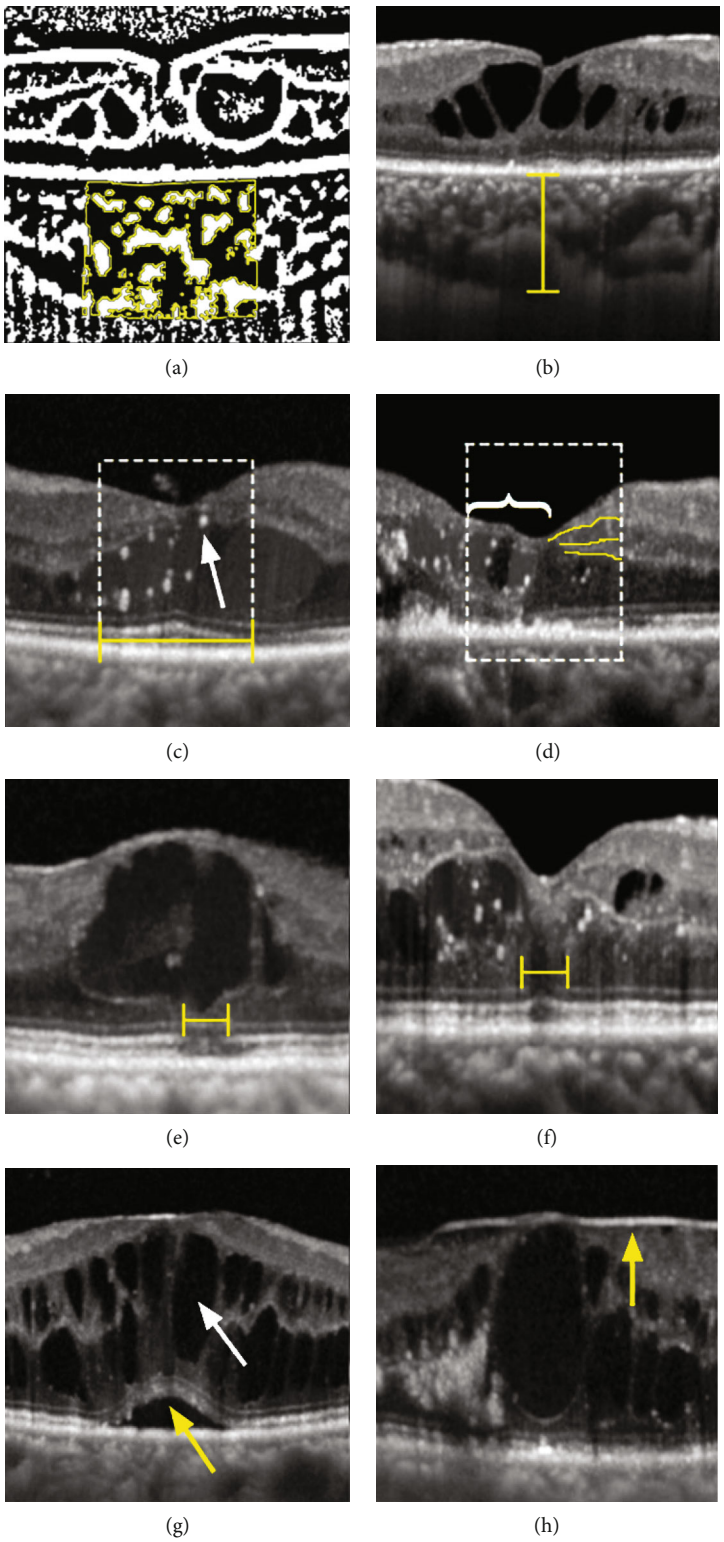

Figure 1: The morphological features evaluated in optical coherence tomography: (a) choroidal vascularity index (CVI); (b) subfoveal choroidal thickness (SFCT); (c) adjusted ellipsoid zone and external limiting membrane reflectivity; hyperreflective foci (HRF) (white arrow); (d) disorganization of the retinal inner layers (DRIL); (e) disruption of the ellipsoid zone; (f) disruption of the external limiting membrane; (g) the presence of subretinal fluid (SRF) (yellow arrow) and cystoid abnormalities (white arrow); (h) presence of an epiretinal membrane.

2.2. Statistics. To adjust for correlation between the two study eyes within the same patient, a generalized estimating equation (GEE) was used to compare the baseline ocular features between the responder and nonresponder groups. Odds ratios (ORs) with confidence intervals (95% CIs) were generated from the GEE-corrected binary logistic regression.

All tests were two-sided, and the significance level was set at 0.05. Statistical analyses were performed using IBM SPSS Statistics 20.

3. Results

A total of 97 eyes from 72 patients were included in the study. After excluding five DME eyes with low-quality OCT images, 92 DME eyes from 67 patients were included in the analysis. In the total 67 patients, the mean age was 57.9 ± 10.1 years. 41 patients (61.2%) were male. 38 patients (56.7%) had hypertension. 27 patients (40.3%) had histories of diabetes more than 10 years.

According to BCVA changes from baseline to 1 month after the last injection, 50 eyes (54.3%) were considered responders, whereas 42 eyes (45.7%) were considered nonresponders. The mean number of anti-VEGF injections during the follow-up period was 3.5 (range: 3–6). The mean duration of follow-up was 5.1 months (range: 4–8). Baseline ocular characteristics based on visual treatment responses are shown in Table 1. There were no significant differences in baseline ocular characteristics between the responders and nonresponders.

3.1. Baseline Optical Coherence Tomography Morphological Features between Responders and Nonresponders. The comparisons of the baseline OCT structural characteristics are shown in Table 2. The baseline CVI was significantly different between the two groups. Responders exhibited significantly higher CVI than nonresponders at baseline (0.69 ± 0.06 vs. 0.66 ± 0.05, $p = 0.014$, Figure 2(a)). This suggests that the baseline CVI may be related to the visual prognosis of DME anti-VEGF treatment. Compared with the nonresponder group, the baseline LCA and TCA of the responders were larger; however, the differences were not significant. However, as measured by the percentage of the difference in the mean value of the responder group, the degree of difference in LCA between the two groups was greater than that of TCA (13% vs. 9%). This indicated that the higher baseline CVI in responders may be more affected by the difference in LCA. There was no statistically significant difference in the SFCT between the two groups.

Analysis of the retinal characteristics of the OCT showed that the baseline adjusted EZ reflectivity in the responder group was significantly higher than that in the nonresponder group (0.73 ± 0.09 vs. 0.65 ± 0.15, $p = 0.006$, Figure 2(b)). Notably, there was no statistical difference in the range of EZ interruption between the two groups, and the standard deviation of the results was large, reflecting large individual differences. In the baseline OCT, the proportion of DRIL in the nonresponders was significantly higher than that in responders (47.6% vs. 16.0%, $p = 0.001$, Figure 2(c)), suggesting that DRIL may be related to the poor response after DME treatment. The proportion of SRF in the responders was significantly greater than that in nonresponders (52.0% vs. 38.1%, $p = 0.038$, Figure 2(d)), suggesting that baseline SRF may be a protective factor for visual improvement after anti-VEGF treatment. No relationship was found between the treatment response and the adjusted ELM reflectivity, disruption of the EZ or ELM, cystoid abnormalities, ERM, or HRF quantity.

In conclusion, compared with the nonresponders, the responder group had a high mean baseline CVI and adjusted EZ reflectivity, a high proportion of SRF, and a low proportion of DRIL.

3.2. Multifactor Regression Analysis for Detecting the Prognostic Factors of the Response to the Anti-VEGF Treatment. Several OCT characteristics, including the CVI that showed significant differences between the two groups, were found through the above analysis. A GEE-corrected binary logistic regression was performed to further identify the independent prognostic factors for the visual response after anti-VEGF treatment, including age, baseline BCVA, stage of retinopathy, the CVI, adjusted EZ reflectivity, the presence of DRIL, and the presence of SRF. The results are shown in Table 3. The higher CVI at baseline seems to be a protective factor for BCVA gain from anti-VEGF treatment, with an OR of 0.17 ($p = 0.006$) for nonresponders versus responders. Alternatively, for every 0.1 increase in the baseline CVI, the risk of being nonresponders after anti-VEGF treatment was reduced by 83%. The higher adjusted EZ reflectivity and presence of SRF at baseline were also protective for the visual response to anti-VEGF treatment. Similarly, for every 0.1 increase in baseline EZ relative light reflectance, the risk of poor response after anti-VEGF treatment was reduced by 44% (OR = 0.56, $p = 0.007$). The risk of poor response after anti-VEGF treatment in DME patients with SRF at baseline OCT was 29% of patients without SRF (OR = 0.29, $p = 0.008$). The presence of DRIL at baseline was a risk factor for poor visual response to treatment, with ORs of 6.71 ($p = 0.001$).

Before treatment, DME patients with high CVI and adjusted EZ reflectivity, SRF, and no DRIL were likely to gain visual acuity improvement of 5 letters or more.

4. Discussion

In this study, we identified CVI as a novel biomarker, along with DRIL, SRF, and adjusted EZ reflectivity, which may predict the visual response to anti-VEGF treatment. A higher CVI, the absence of DRIL, the presence of SRF, and higher adjusted EZ reflectivity at baseline indicated that the individual was more likely to be a responder and gain more than five letters in BCVA after anti-VEGF treatment.

In recent years, SFCT has been commonly used to evaluate the choroid in DR or DME. However, SFCT is an unstable factor affected by various systemic and ocular factors, such as age, axial length, IOP, or systolic blood pressure, which was reflected in the inconsistent results of SFCT in DR or DME in different studies. SFCT has been reported to be reduced, unchanged, and even increased in DR [16,

Table 1: Baseline ocular characteristic comparison between responders and nonresponders by a generalized estimating equation model with adjusting for correlation between two eyes within the same patient ($N = 92$ eyes).

	Responders ($n = 50$)	Nonresponders ($n = 42$)	p
OCT quality index	36.6 ± 4.6	36.1 ± 3.8	0.509
Number of injections	3.4 ± 0.8	3.7 ± 0.9	0.094
PDR (%)	28 (56.0)	26 (61.9)	0.300
BCVA	36.4 ± 16.2	41.4 ± 15.1	0.137

OCT: optical coherence tomography; PDR: proliferative diabetic retinopathy; BCVA: best-corrected visual acuity.

Table 2: Baseline optical coherence tomography morphological feature comparison between responders and nonresponders by a generalized estimating equation model with adjusting for correlation between two eyes within the same patient ($N = 92$ eyes).

	Responders ($n = 50$)	Nonresponders ($n = 42$)	p
LCA (mm^2)	0.39 ± 0.12	0.34 ± 0.11	0.059
TCA (mm^2)	0.56 ± 0.15	0.51 ± 0.15	0.168
SFCT (μm)	365.85 ± 92.77	334.61 ± 92.00	0.145
CVI	0.69 ± 0.06	0.66 ± 0.05	0.014
Reflectivity of EZ	140.9 ± 25.3	129.0 ± 34.2	0.030
Reflectivity of ELM	94.2 ± 21.7	91.4 ± 28.7	0.538
Reflectivity of RPE	193.0 ± 18.2	197.5 ± 14.8	0.243
Adjusted reflectivity of EZ	0.73 ± 0.09	0.65 ± 0.15	0.006
Adjusted reflectivity of ELM	0.49 ± 0.10	0.46 ± 0.13	0.335
Disruption of the EZ (μm)	91.22 ± 164.44	160.40 ± 234.30	0.168
Disruption of the ELM (μm)	71.50 ± 170.60	105.88 ± 181.78	0.421
DRIL, n (%)	8 (16.0)	20 (47.6)	0.001
SRF, n (%)	26 (52.0)	16 (38.1)	0.038
Cystoid abnormalities, n (%)	39 (78.0)	33 (78.6)	0.987
Epiretinal membrane, n (%)	16 (32.0)	13 (31.0)	0.640
HRF	10.98 ± 9.03	10.70 ± 8.82	0.563

LCA: luminal choroidal area; TCA: total choroidal area; SFCT: subfoveal choroidal thickness; CVI: choroidal vascularity index; EZ: ellipsoid zone; ELM: external limiting membrane; RPE: retinal pigment epithelium; DRIL: disorganization of the retinal inner layers; SRF: subretinal fluid; HRF: hyperreflective foci.

17]. The relationship between baseline SFCT and the treatment response of VEGF in DME has been variable in previous studies. Rayess et al. found that a greater baseline SFCT was associated with a better anatomic and functional response [18], whereas Campos et al. showed that SFCT did not predict the DME outcome [19]. In this study, the SFCT exhibited a large degree of variation and was not significantly different between responders and nonresponders. Compared with SFCT, the CVI showed less variability under the above-mentioned physiological factors, indicating that it is a relatively stable choroidal index. Unlike SFCT, which works as a crude parameter, the CVI discriminates between the luminal and stromal areas, providing more detailed information about changes in the choroidal vessels. In our study, we found that the CVI in any group showed low variability, and the baseline CVI was significantly lower in nonresponders than in responders.

Changes in the CVI in DR have been reported in several recent studies. Gupta et al. reported that the CVI was significantly decreased in eyes with DME and DR compared to controls [12]. A decrease in the CVI was observed in patients with diabetes even in the absence of DR, and a further decrease occurred along with the severity of DR [13]. These results suggest that the CVI is a relatively early and sensitive biomarker of diabetic fundus changes that may predict DR development. In the current study, we reported the CVI as a possible novel biomarker for the functional efficacy of anti-VEGF treatment in DME for the first time. Considering that the severity of DR is associated with the CVI, we included the CVI, the severity of DR, and other possibly related baseline factors in the multivariate analysis; a high baseline CVI remained significantly related to a greater possibility of being a functional responder after treatment, which confirmed the predictive value of the CVI independent of factors including the severity of DR.

The choroid is important in the metabolic exchange of the outer layers of the retina, particularly the photoreceptors, which are critical for visual function. Histopathologic studies revealed variable choroidal vascular changes secondary to diabetes mellitus, such as vascular dropout, areas of vascular

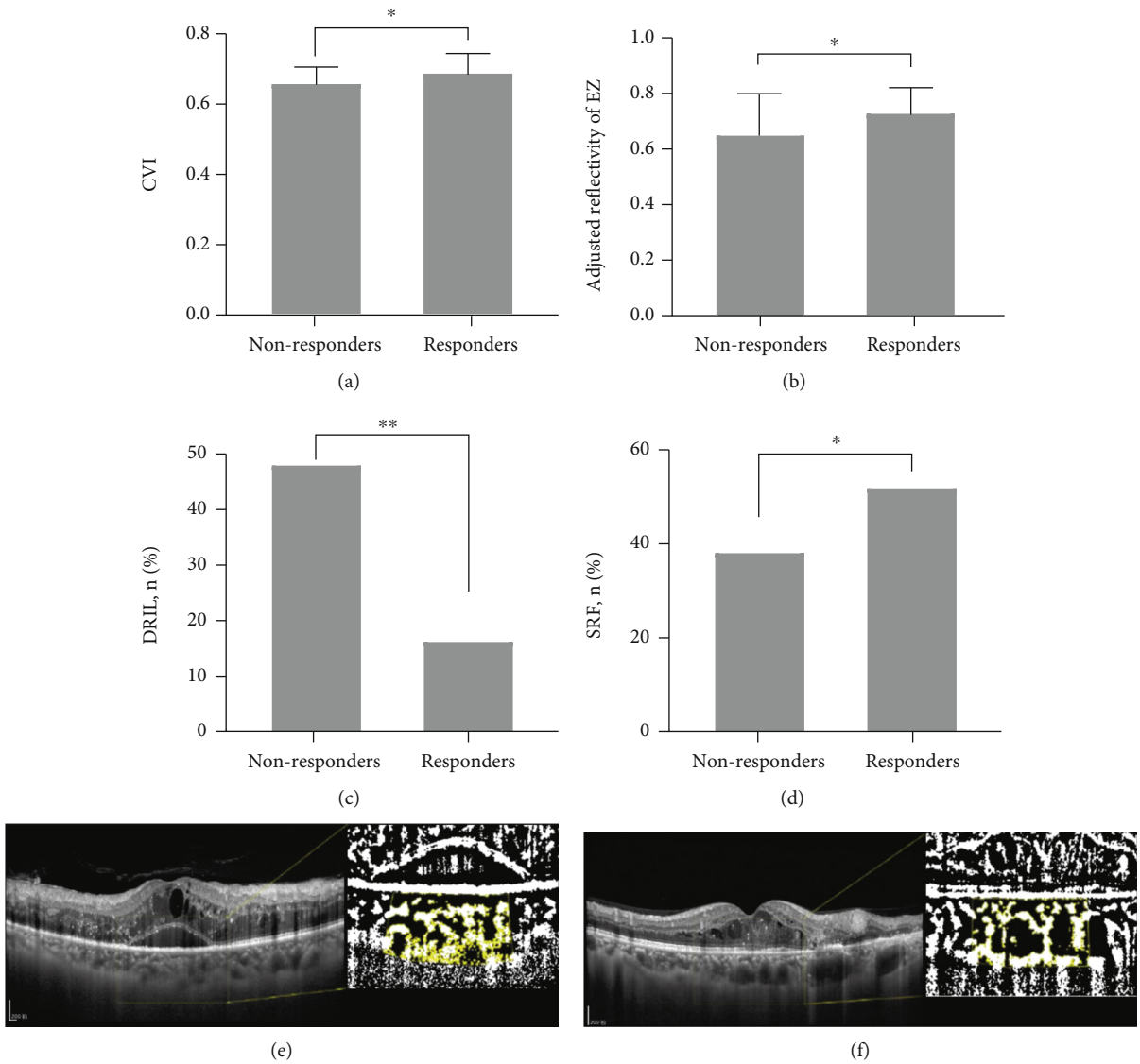

Figure 2: Baseline optical coherence tomography (OCT) morphological features between responders and nonresponders. Baseline choroidal vascularity index (CVI) (a). Adjusted ellipsoid zone (EZ) reflectivity (b). Proportion of disorganization of the retinal inner layers (DRIL) (c). Subretinal fluid (SRF) (d) in responders and nonresponders. The left eye of a 50-year-old man had a baseline CVI of 62%. Her baseline BCVA was 20/100. After three injections of VEGF inhibitors, the visual acuity decreased to 20/160. The treated eyes were categorized as nonresponders (e). The right eye of a 44-year-old man had a baseline CVI of 69%. Her baseline BCVA was 20/63. After three injections of VEGF inhibitors, the visual intensity increased to 20/40. The treated eyes were categorized as responders (f).

nonperfusion, and choroidal neovascularization [9]. The exact role of choroidal abnormalities in the pathology of DME and its impact on the response to anti-VEGF treatment remain unclear. Some early histopathologic and functional studies can provide insight into this subject. Studies from postmortem subjects demonstrated that diabetic choroids had a more than fourfold greater focal choriocapillaris degeneration area than nondiabetic choroids [20]. In addition to the choriocapillaris, large and medium choroidal vessels are also involved. Focal vascular loss in Sattler's layer, vascular stump, and narrowing in Haller's layer have been observed more frequently in patients with DR than those in controls [21]. Structural damage in the three layers of choroid vessels may affect choroidal blood flow. Laser Doppler flowmetry and OCT angiography measurements revealed that patients with diabetes, particularly those with DME, exhibited significantly decreased choriocapillaris blood flow in the foveal region [22, 23].

Choroidal vasculature impairment and associated decreased choriocapillaris blood flow can aggravate hypoxia of the outer retina, which increases the expression of VEGF and promotes the formation of macular edema [10]. Damage to the choriocapillaris and larger choroidal vessels involved in diabetes, as described above, may cause a decrease in the CVI. Choroidal blood flow, which partly reflects the choroidal vascular perfusion state, may also involve changes in the CVI. It is hypothesized that DME eyes with a low CVI at baseline may already have relatively

Table 3: Multifactor regression analysis for detecting the prognostic factors of the response to the antivascular endothelial growth factor (VEGF) treatment by a generalized estimating equation model with adjusting for correlation between two eyes within the same patient ($N = 92$ eyes).

	OR (95% CI)	p
Age	1.01 (0.97, 1.07)	0.658
BCVA	1.00 (0.97, 1.04)	0.840
Stage of DR	1.04 (0.41, 2.63)	0.942
CVI	0.17 (0.05, 0.61)	0.006
Adjusted reflectivity of EZ	0.56 (0.36, 0.86)	0.007
DRIL	6.71 (2.26, 19.89)	0.001
SRF	0.29 (0.12, 0.73)	0.008

OR: odds ratio; CI: confidence interval; BCVA: best-corrected visual acuity; CVI: choroidal vascularity index; EZ: ellipsoid zone; DRIL: disorganization of the retinal inner layers; SRF: subretinal fluid.

severe structural damage of choroidal vessels, which cannot be reconstructed during anti-VEGF treatment. This group of patients may also present a relatively obvious decrease in the choroidal blood flow at baseline, which may hinder the absorption of edema liquid. These two aspects of choroidal vascular changes may result in the individual eye with a low CVI being likely to be a nonresponder to anti-VEGF treatment. According to the hypothesis above, the change in the luminal area possibly played a major role in the difference in the CVI between the two groups, which was consistent with our results that the difference in LCA was greater than that of TCA between the two groups. Further studies are necessary to reveal the detailed pathophysiological mechanisms behind the change in the CVI and its relation to the response to anti-VEGF treatment.

DRIL on OCT was considered to indicate structural damage in the transmission pathway of visual signals from photoreceptors to retinal ganglion cells, which was correlated with a visual response to anti-VEGF treatment in eyes with DME [4]. Our results support the findings of previous studies that DRIL is a valuable predictive biomarker, with a risk for poor visual outcomes that is almost seven times higher than that in patients without DRIL.

According to our results, SRF appears to be a protective factor. The effects of SRF on treatment outcomes following anti-VEGF treatment have not been fully clarified. Our result is consistent with some of the previous studies that baseline SRF is related to a greater visual or structural improvement of anti-VEGF treatment [8, 24]. A possible reason is that compared to diffuse retinal thickening or cystoid macular edema, the internal structure of the neuroretina is less disturbed in SRF, which may result in less mechanical damage to retinal nerve cells. Some studies provide opposite conclusions. Seo et al. reported that SRD was correlated with poorer visual outcomes, and disruption of photoreceptor integrity occurred more frequently in SRD. Considering that the analysis was performed in a relatively small number of patients (16 patients in the SRD group) and simultaneous presence of diffuse retinal thickening or cystoid macular edema was also classified as SRD in this study, the conclusions need further demonstration [25].

In contrast to previous studies, we did not find significant associations between the extent of EZ or ELM disruption and the functional response to anti-VEGF treatment. This is partly because, in many cases of DME eyes, the EZ and ELM gradually lose hyperreflectivity in an inhomogeneous manner. Disruption of the EZ and ELM did not occur as a definite area. It is challenging to measure the extent of disruption precisely. From this consideration, the reflectivity of the whole area of the EZ and ELM in the central 1 mm zone may be a more representative marker for quantitative evaluation. Guyon et al. reported that EZ reflectivity was lower in resolved DME than that in diabetic eyes without DME and nondiabetic control eyes [26]. A larger proportion of EZ with reflectivity recovering to the normal level after 1 week can predict better BCVA treatment response at 1 month [27].

In our study, considering that the opacity of refracting media, such as cataract or vitreous conditions and differences in the ingredients of edema, affected the transmission of light, which altered the reflectivity of retinal layers on the light path, the adjusted reflectivity of EZ and ELM was used by calculating the ratio of the reflectivity of RPE on the same optical axis. In our study, the adjusted reflectivity of EZ at baseline was significantly lower in nonresponders than in responders. The EZ on OCT was supposed to represent a cellular compartment full of mitochondria in photoreceptors in histology. EZ reflectivity is closely correlated with the cone density [28]. Decreased reflectivity of EZ may be related to the loss of mitochondria, leading to dysfunction of photoreceptors or the direct loss of photoreceptors at baseline, resulting in a poor visual response. After adjusting in the multivariate analysis, the higher adjusted reflectivity of EZ was associated with a lower risk of being a visual nonresponder, which indicated that the adjusted reflectivity of EZ may also be a prognostic factor for anti-VEGF treatment in DME.

The limitations of this study include its retrospective design and relatively small sample size. BCVA after treatment was evaluated 1 month after the last injection. The number of injections differed among patients, ranging from three to six. Prospective studies with longer follow-up periods are needed to confirm these findings. Besides OCT exhibiting the structural features of the retina and choroid, functional examinations, such as OCTA, and intraocular inflammatory factors are also related to the efficiency of treatment [29]. An integrated prediction model should be developed to optimize patient care in the context of DME. In conclusion, this study demonstrated the CVI as a possible novel biomarker of visual response to anti-VEGF treatment. DRIL, SRF, and the adjusted reflectivity of EZ were also confirmed to be useful markers strongly associated with anti-VEGF treatment efficiency.

5. Conclusion

DME patients with a higher CVI, the absence of DRIL, the presence of SRF, and higher adjusted EZ reflectivity at baseline were more likely to gain more than five letters in BCVA

after anti-VEGF treatment. The CVI is possibly a novel prognostic factor for anti-VEGF treatment.

Data Availability

The data used to support the findings of this study are available from the corresponding author upon request.

Conflicts of Interest

The authors declare that they have no conflicts of interest.

Authors' Contributions

Ningxin Dou and Shanshan Yu contributed equally to this work.

References

[1] R. Lee, T. Y. Wong, and C. Sabanayagam, "Epidemiology of diabetic retinopathy, diabetic macular edema and related vision loss," *Eye and Vis*, vol. 2, no. 1, p. 17, 2015.

[2] D. S. Boyer, Q. D. Nguyen, D. M. Brown, K. Basu, and J. S. Ehrlich, "Outcomes with As-Needed Ranibizumab after Initial Monthly Therapy: Long-Term Outcomes of the Phase III RIDE and RISE Trials," *Ophthalmology*, vol. 122, no. 12, pp. 2504–2513, 2015.

[3] S. B. Bressler, A. R. Glassman, T. Almukhtar et al., "Five-year outcomes of ranibizumab with prompt or deferred laser versus laser or triamcinolone plus deferred ranibizumab for diabetic macular edema," *American Journal of Ophthalmology*, vol. 164, pp. 57–68, 2016.

[4] J. K. Sun, S. H. Radwan, A. Z. Soliman et al., "Neural retinal disorganization as a robust marker of visual acuity in current and resolved diabetic macular edema," *Diabetes*, vol. 64, no. 7, pp. 2560–2570, 2015.

[5] A. R. Santos, M. Â. Costa, C. Schwartz et al., "Optical coherence tomography baseline predictors for initial best-corrected visual acuity response to intravitreal anti-vascular endothelial growth factor treatment in eyes with diabetic macular EDEMA," *Retina*, vol. 38, no. 6, pp. 1110–1119, 2018.

[6] The Sunderland Eye Infirmary study group, Y. Wong, D. H. W. Steel et al., "Vitreoretinal interface abnormalities in patients treatedwith ranibizumab for diabetic macular oedema," *Graefe's Archive for Clinical and Experimental Ophthalmology*, vol. 255, no. 4, pp. 733–742, 2017.

[7] T. Yoshitake, T. Murakami, K. Suzuma, Y. Dodo, M. Fujimoto, and A. Tsujikawa, "Hyperreflective foci in the outer retinal layers as a predictor of the functional efficacy of ranibizumab for diabetic macular edema," *Scientific Reports*, vol. 10, no. 1, p. 873, 2020.

[8] S. B. Bressler, I. Odia, M. G. Maguire et al., "Factors associated with visual acuity and central subfield thickness changes when treating diabetic macular edema with anti-vascular endothelial growth factor Therapy," *JAMA Ophthalmology*, vol. 137, no. 4, pp. 382–389, 2019.

[9] D. Melancia, A. Vicente, J. P. Cunha, L. Abegão Pinto, and J. Ferreira, "Diabetic choroidopathy: a review of the current literature," *Graefe's Archive for Clinical and Experimental Ophthalmology*, vol. 254, no. 8, pp. 1453–1461, 2016.

[10] P. A. Campochiaro, "Molecular pathogenesis of retinal and choroidal vascular diseases," *Progress in Retinal and Eye Research*, vol. 49, pp. 67–81, 2015.

[11] C. Iovino, M. Pellegrini, F. Bernabei et al., "Choroidal vascularity index: an in-depth analysis of this novel optical coherence tomography parameter," *Journal of Clinical Medicine*, vol. 9, no. 2, p. 595, 2020.

[12] C. Gupta, R. Tan, C. Mishra et al., "Choroidal structural analysis in eyes with diabetic retinopathy and diabetic macular edema-a novel OCT based imaging biomarker," *PLoS One*, vol. 13, no. 12, article e0207435, 2018.

[13] M. Kim, M. J. Ha, S. Y. Choi, and Y. H. Park, "Choroidal vascularity index in type-2 diabetes analyzed by swept-source optical coherence tomography," *Scientific Reports*, vol. 8, no. 1, p. 70, 2018.

[14] P. Mitchell, F. Bandello, U. Schmidt-Erfurth et al., "The RESTORE study: ranibizumab monotherapy or combined with laser versus laser monotherapy for diabetic macular edema," *Ophthalmology*, vol. 118, no. 4, pp. 615–625, 2011.

[15] S. Sonoda, T. Sakamoto, T. Yamashita et al., "Luminal and stromal areas of choroid determined by binarization method of optical coherence tomographic images," *American Journal of Ophthalmology*, vol. 159, no. 6, article e1, pp. 1123–1131.e1, 2015.

[16] I. Laíns, K. E. Talcott, A. R. Santos et al., "Choroidal thickness in diabetic retinopathy assessed with swept-source optical coherence tomography," *Retina*, vol. 38, no. 1, pp. 173–182, 2018.

[17] J. T. Kim, D. H. Lee, S. G. Joe, J. G. Kim, and Y. H. Yoon, "Changes in choroidal thickness in relation to the severity of retinopathy and macular edema in type 2 diabetic patients," *Investigative Ophthalmology & Visual Science*, vol. 54, no. 5, pp. 3378–3384, 2013.

[18] N. Rayess, E. Rahimy, G. S. Ying et al., "Baseline choroidal thickness as a predictor for response to anti-vascular endothelial growth factor therapy in diabetic macular edema," *American Journal of Ophthalmology*, vol. 159, no. 1, pp. 85–91.e3, 2015.

[19] A. Campos, E. J. Campos, A. do Carmo, and R. Silva, "Response to: choroidal thickness changes stratified by outcome in real-world treatment of diabetic macular edema," *Graefe's Archive for Clinical and Experimental Ophthalmology*, vol. 257, no. 1, pp. 243-244, 2019.

[20] J. Cao, S. McLeod, C. A. Merges, and G. A. Lutty, "Choriocapillaris degeneration and related pathologic changes in human diabetic eyes," *Archives of Ophthalmology*, vol. 116, no. 5, pp. 589–597, 1998.

[21] T. Murakami, A. Uji, K. Suzuma et al., "In vivo choroidal vascular lesions in diabetes on swept-source optical coherence tomography," *PLoS One*, vol. 11, no. 8, article e0160317, 2016.

[22] T. Nagaoka, N. Kitaya, R. Sugawara et al., "Alteration of choroidal circulation in the foveal region in patients with type 2 diabetes," *The British Journal of Ophthalmology*, vol. 88, no. 8, pp. 1060–1063, 2004.

[23] L. Li, S. Almansoob, P. Zhang, Y. D. Zhou, Y. Tan, and L. Gao, "Quantitative analysis of retinal and choroid capillary ischaemia using optical coherence tomography angiography in type 2 diabetes," *Acta Ophthalmologica*, vol. 97, no. 3, pp. 240–246, 2019.

[24] J. F. Korobelnik, C. Lu, T. A. Katz et al., "Effect of baseline subretinal fluid on treatment outcomes in VIVID-DME and

VISTA-DME studies," *Ophthalmology Retina*, vol. 3, no. 8, pp. 663–669, 2019.

[25] K. H. Seo, S. Y. Yu, M. Kim, and H. W. Kwak, "Visual and morphologic outcomes of intravitreal ranibizumab for diabetic macular edema based on optical coherence tomography patterns," *Retina*, vol. 36, no. 3, pp. 588–595, 2016.

[26] B. Guyon, E. Elphege, M. Flores, A. S. Gauthier, B. Delbosc, and M. Saleh, "Retinal reflectivity measurement for cone impairment estimation and visual assessment after diabetic macular edema resolution (RECOVER-DME)," *Investigative Ophthalmology & Visual Science*, vol. 58, no. 14, pp. 6241–6247, 2017.

[27] A. R. Santos, D. Alves, T. Santos, J. Figueira, R. Silva, and J. G. Cunha-Vaz, "Measurements of retinal fluid by optical coherence tomography leakage in diabetic macular EDEMA," *Retina*, vol. 39, no. 1, pp. 52–60, 2019.

[28] M. Flores, G. Debellemanière, A. Bully et al., "Reflectivity of the outer retina on spectral-domain optical coherence tomography as a predictor of photoreceptor cone density," *American Journal of Ophthalmology*, vol. 160, no. 3, pp. 588–595.e2, 2015.

[29] J. Lee, B. G. Moon, A. R. Cho, and Y. H. Yoon, "Optical Coherence Tomography Angiography of DME and Its Association with Anti- VEGF Treatment Response," *Ophthalmology*, vol. 123, no. 11, pp. 2368–2375, 2016.

Hindawi
Journal of Diabetes Research
Volume 2021, Article ID 9765119, 12 pages
https://doi.org/10.1155/2021/9765119

Research Article

An *In Vitro* Model of Diabetic Retinal Vascular Endothelial Dysfunction and Neuroretinal Degeneration

Qiyun Wang,[1,2] Xinyuan Zhang,[1,2] Kaiyue Wang,[1] Ling Zhu,[3] Bingjie Qiu,[1,2] Xiaosi Chen,[1,2] Xiao Lin,[1] and Yao Nie[1,2]

[1]*Beijing Institute of Ophthalmology, Tongren Eye Center, Beijing Tongren Hospital, Capital Medical Univeristy, Beijing, China*
[2]*Beijing Retinal and Choroidal Vascular Diseases Study Group, China*
[3]*Save Sight Institute, Department of Ophthalmology, Faculty of Medicine and Health, The University of Sydney, Sydney, Australia*

Correspondence should be addressed to Xinyuan Zhang; mmzxy2010@163.com

Received 19 August 2021; Accepted 9 October 2021; Published 10 November 2021

Academic Editor: Honghua Yu

Background. Diabetic retinopathy (DR) is a leading cause of blindness in working-age populations. Proper *in vitro* DR models are crucial for exploring pathophysiology and identifying novel therapeutic targets. This study establishes a rational *in vitro* diabetic retinal neuronal-endothelial dysfunction model and a comprehensive downstream validation system. *Methods*. Human retinal vascular endothelial cells (HRMECs) and retinal ganglion cells (RGCs) were treated with different glucose concentrations with mannitol as matched osmotic controls. Cell proliferation and viability were evaluated by the Cell Counting Kit-8. Cell migration was measured using a transwell migration assay. Cell sprouting was assessed by a tube formation assay. The VEGF expression was assessed by ELISA. RGCs were labeled by neurons and RGC markers TUJ1 and BRN3A for quantitative and morphological analysis. Apoptosis was detected using PI/Hoechst staining and TUNEL assay and quantified by ImageJ. *Results*. Cell proliferation and migration in HRMECs were significantly higher in the 25 mM glucose-treated group ($p < 0.001$) but lower in the 50 mM and 100 mM groups ($p < 0.001$). The permeability and the apoptotic index in HRMECs were statistically higher in the 25 mM, 50 mM, and 100 mM groups ($p < 0.05$). The tube formation assay found that all the parameters were significantly higher in the 25 mM and 50 mM groups ($p < 0.001$) concomitant with the elevated VEGFA expression in HRMECs ($p = 0.016$). Cell viability was significantly lower in the 50 mM, 100 mM, and 150 mM groups in RGCs ($p_{50\text{mM}} = 0.013$, $p_{100\text{mM}} = 0.019$, and $p_{150\text{mM}} = 0.002$). Apoptosis was significantly elevated, but the proportion of RGCs with neurite extension was significantly lower in the 50 mM, 100 mM, and 150 mM groups ($p_{50\text{mM}} < 0.001$, $p_{100mM} < 0.001$, and $p_{150\text{mM}} < 0.001$). *Conclusions*. We have optimized glucose concentrations to model diabetic retinal endothelial (25-50 mM) or neuronal (50-100 mM) dysfunction *in vitro*, which have a wide range of downstream applications.

1. Introduction

Diabetic retinopathy (DR) is a leading cause of blindness in the working-age population in both developed and developing countries [1]. DR is the most important neurovascular ocular complications of diabetes mellitus. Identifying new biomarkers for diagnosis and therapeutic targets would greatly benefit patients with DR to prevent vision loss [2].

In vitro models of DR have a crucial role in understanding the pathophysiology of the disease and identifying new therapeutic strategies. The effects of high glucose on retinal cell homeostasis and the identification of potentially protective molecules provide deeper insight from *in vitro* studies. We have previously shown that apoptosis of neurons and dysfunctions of the retinal blood barrier are the early and key features of DR. Furthermore, neuronal vascular unit dysfunction was identified as the key pathogenesis of DR [1]. Ganglion cells have been recognized as the earliest damaged retinal neurons under hyperglycemia, proved by our previous studies [3].

There is no universally accepted glucose concentration for *in vitro* studies to simulate human DR. The *in vitro* model of diabetes is currently and commercially established by treating cells with 5.5 mM to 25 mM concentrations of

glucose [4–6] and in endothelial cells only. Furthermore, the *in vitro* glucose concentration is not entirely equivalent to the physiological condition of human beings. The monoglucose concentrations are not optimal for simulation of the blood glucose levels in patients with hyperglycemia, especially for DR. Under the external environment, different cell types have different tolerance to high glucose. Nevertheless, the proper concentrations and the effect of the glucose concentration and osmotic pressure on the biological behavior of HRMEC and neurons have not been fully elucidated [7].

In this study, we investigate the influence of the glucose concentrations gradient on the biological characteristics of HRMEC and RGCs [8]. As the osmotic pressure could be a coeffector in a hyperglycemia pathological condition, we also set up serial control groups of gradient increased osmotic pressure to exclude this effect in human endothelial cells.

2. Materials and Methods

2.1. Cell Culture of Human Retinal Microvascular Endothelial and Retinal Ganglion Cells. Primary HRMECs and RGCs were purchased from Shanghai Xuanya Biotechnology Co., Ltd (Shanghai, China). Dulbecco's modified Eagle's medium (DMEM) powder and fetal bovine serum (FBS) were bought from Gibco Life Technologies (New York, NY, USA). HRMECs were cultured in a 5.5 mM glucose DMEM medium containing 10% FBS in a humidified atmosphere containing 5%CO_2/95% air at 37°C. Cells passaged for 4 and 8 times were eased for further experiments.

2.2. Experimental Grouping. Cells were divided in two groups: the control group, which was cultured in DMEM medium supplemented with 5.5 mM glucose, and the high-glucose group, cultured in DMEM medium supplemented with G25, G50, G100, and G150 (D-glucose concentrations 25, 50, 100, and 150 mmol/L, respectively). The maximum glucose concentration for RGCs is 150 mmol/L. Mannitol was added to the 5.5 mM group to adjust the osmotic pressure to correspond with the same osmotic pressure of G25, G50, G100, and G150, thus forming M25, M50, M100, and M150 (mannitol concentrations 19.5, 44.5, 94.5, and 133.5 mmol/l, respectively). Each experiment was repeated three times.

2.3. Evaluation of the Cutoff and Extreme Value of High Glucose in HRMECs and RGCs. A pilot study was designed to evaluate the cutoff and acute value of high glucose for HRMECs and RGCs. A series glucose concentration was set up as follows: 5.5 mM, 10 mM, 15 mM, 25 mM, 35 mM, 50 mM, 75 mM, and 100 mM. Cell proliferative capacity of HRMECs and cell viability of RGCs were assessed via CCK-8 assay before they were treated with different glucose concentrations as previously described [9]. Briefly, cells were seeded in 96-well culture plates (1×10^4cells/well). After 24 h, the cells were mixed with the control or experimental medium and cultured for an additional 24, 48, and 72 h (each treatment group has five repeat wells). At each time point, 10 μl CCK-8 reagent (Dojindo Molecular Technologies, Inc., Kumamoto, Japan) was added to each well and incubated for another 2 h at 37°C. The OD value of each well was detected at the wavelength of 450 nm with a microplate reader (SpectraMax 250; GE Healthcare Life Sciences, Chalfont, UK).

2.4. The Endothelial Cell Transwell Migration and Invasion Assay. To investigate the migratory response of endothelial cells to hyperglycemia, HRMECs were incubated in a serum-free-conditioned medium at 37°C with a humidified atmosphere for 24 h before the suspension. 100 μl of serum-free medium (containing 2×10^4 cells) was added to the upper chambers of a transwell plate with the pore of 8 μm (24 wells, Corning, NY, USA), while the lower chambers were added with 600 μl of complete medium with 20% FBS. After incubation for 24 h, 48 h, and 72 h, migrated cells attached to the other side of the insert were fixed with 90% ethanol followed stained with 0.1% crystal violet. Five randomly field (×200) photographs were taken under an inverted microscope (Carl Zeiss, Jena, Germany), and the average number of cells was counted. The experiment was repeated three times.

2.5. Detection and Percentage of Apoptotic Cells. Apoptotic cells were detected using a dUTP Nick-End Labeling (TUNEL) kit (#11684795910, Roche, Mannheim, Germany) and PI/Hoechst staining method. TUNEL assay is designed to identify extensive DNA degradation during the late stages of apoptosis *in situ* in the apoptotic cells. Briefly, the cells grown on coverslips were fixed with 4% paraformaldehyde for 1 h at RT. The cells were incubated with permeabilization solution (0.1% Triton X-100 in 0.1% sodium citrate, freshly prepared) for 2 min on ice after washing with PBS. The cells were then incubated with the TUNEL reaction mixture in a humidified chamber in the dark at 37°C for 1 h. After counterstaining with DAPI (1 μg/ml), stained sections were examined by a fluorescence microscope (Carl Zeiss, Jena, Germany). TUNEL-positive nuclei were stained green, and all other nuclei were stained blue.

For PI/Hoechst staining, cells were seeded in 24-well culture plates (2×10^4 cells/well). After each time point of 24 h, 48 h, and 72 h, PI (#M5109, Abmole Bioscience, USA) and Hoechst (#M5113, Abmole Bioscience, USA) were added into each well, and the cells were incubated in the dark for 15 min followed by PBS (5 minutes each) washing for two times. For quantitative analysis, nine fields were randomly photographed under a 200-fold inverted microscope (Carl Zeiss, Jena, Germany) [10]. Apoptosis index was calculated as the number of positive cells (TUNEL or PI-positive nuclei/the number of DAPI or Hoechst-stained cells).

2.6. Cell Permeability Assay. To evaluate the effects of hyperglycemia on endothelial cell proliferative ability, cell permeability was tested using the BSA-FITC kit [11, 12]. HRMECs were seeded in the upper Transwell-COL membrane insert (24 wells, Corning Incorporated, NY, USA). After reaching 90% confluence, the HRMECs were starved for 12 h in serum-free medium and subsequently replaced with control or experimental medium for 24 h. After 24 h, a tracer solution of FITC-labeled BSA (250 μg/ml; Sigma-Aldrich,

Germany) was added to the upper insert, and 500 μl medium without FITC-BSA was added to the lower insert. After incubation for 2 hours, the collected media were measured using a fluorophotometer (Tecan, Switzerland) at an emission/excitation wavelength of 495/520 nm.

2.7. Tube Formation Assay. To evaluate the angiogenic capability under hyperglycemia, 50 μl Matrigel (#356234, BD Biosciences, Oxford, UK) was added to each well of a 96-well plate and incubated for 45 min at 37°C in a humidified atmosphere with 5% CO_2 as previously described [13, 14]. Until Matrigel was polymerized, 5×10^4 cells in 100 μl DMEM were seeded in each well. Capillary-like tubes were formed within 9 hours and recorded with a video camera (Carl Zeiss, Jena, Germany). Images of tube morphology were obtained at ×100 magnification and quantified by the ImageJ software (NIH Image, Bethesda, MD) [13, 14].

2.8. Detection of VEGFA Protein Concentration. To investigate the pathological mechanisms under hyperglycemia, the supernatant of the different groups was harvested and centrifuged at 4°C for 10 min at 3000 × g to remove the cell debris, and then it was stored at -80°C for ELISA. After dilution, the concentration of VEGFA in cell supernatants was quantitatively detected using the Human VEGFA ELISA kit (RayBiotech Systems, USA) following the manufacturer's instruction. Data was quantified in comparison to VEGF standards.

2.9. Immunochemistry. RGCs were harvested and seeded in a 24-well culture plate (3×10^4 cells/well). After incubation for 24 h, 48 h, and 72 h, cells were fixed with 4% paraformaldehyde at RT for 30 min according to previously described methods [15–17]. After washing with Hank's Balanced Salt Solution (HBSS basic 1x, Gibco Company, USA), cells were permeabilized in 0.3% Triton (Sigma-Aldrich, Germany) in HBSS for 15 min at RT. The cells were then blocked with a blocking buffer containing 1% bovine serum albumin (BSA) and 5% goat serum in HBSS for 60 minutes after washing with HBSS. After incubation with the primary antibodies, rabbit anti-beta III tubulin (1 : 1000,Cat#ab18207,Abcam,Cambridge, MA), which was specific for neurofilament heavy chains [18], and mouse anti-Brn3a (1 : 25, Cat#sc-8429, Santa, USA), which was specific expression in RGCs nucleus [17, 19] for overnight at 4°C, the cells were washed three times and incubated with secondary antibodies (goat anti-mouse and goat anti-rabbit) (1 : 500, Cat #ab150077, Cat #ab150116, Abcam, Cambridge, MA) at RT for 2 hours with light-shielded and counterstained with DAPI. Five fields were randomly photographed under a 200-fold inverted microscope (Carl Zeiss, Jena, Germany). The number of cells which had neurite lengths equal to or greater than three times the cell body diameter was calculated by ImageJ.

2.10. Statistical Analysis. Statistical analysis was performed using the SPSS software version 20.0 (SPSS, Inc., Chicago, IL, USA). Data distribution was assessed by the One-Sample Kolmogorov-Smirnov test. Data were expressed as means ± SD or median (interquartile range). Variance (ANOVA) analysis for continuous variables and chi-square test for noncontinuous variables were applied. The Bonferroni correction was used for multiple-comparison correction. A p value less than 0.05 is considered significant.

If the above analysis confirmed any significant difference, a comparison between two groups was then conducted by independent Student's t-test for continuous variables and post hoc test to compare the difference between groups for noncontinuous variables. p values < 0.05 was considered statistically significant.

3. Results

3.1. 25 mM and 50 mM May Be Taken as the Cutoff Value of Hyperglycemia for Retinal Vascular Endothelial Cells. Significant difference was found in the optical density (OD) value in the different glucose concentration groups at 24 h, 48 h, and 72 h by the CCK-8 assay ($F_{24h} = 41.789$, $p < 0.001$; $F_{48h} = 181.054$, $p < 0.001$; and $F_{72h} = 51.189$, $p < 0.001$). There was significant difference in the OD value in the groups of 25 mM, 50 mM, and 100 mM compared to the 5.5 mM group ($p < 0.01$), but no difference was found in the 10 mM and 15 mM groups compared to the 5.5 mM control group ($p > 0.05$). The glucose concentration of 25 mM can be regarded as the cutoff value of DR. When the glucose concentration is greater than 50 mM (50 mM, 75 mM, and 100 mM), the proliferation capacity of HREMC was obviously inhibited.

We further investigate the CCK-8 assay and AI in the groups of 5.5 mM, 25 mM, 50 mM, and 100 mM to explore the extreme value of *in vitro* model of DR. We found that the proliferative capacity in the 50 mM is significantly lower compared to the 5.5 mM group (24 h: 0.91 ± 0.03 vs. 0.96 ± 0.45, $p < 0.001$; 48 h: 1.27 ± 0.05 vs. 1.36 ± 0.05, $p < 0.001$; and 72 h: 1.48 ± 0.06 vs. 1.58 ± 0.03, $p = 0.001$); furthermore, cell proliferation capacity was obviously inhibited in the 100 mM group (24 h: 0.87 ± 0.02 vs. 0.96 ± 0.45, $p < 0.001$; 48 h: 1.18 ± 0.02 vs. 1.36 ± 0.05, $p < 0.001$; and 72 h: 1.23 ± 0.01 vs. 1.58 ± 0.03, $p < 0.001$), which was not suitable for further study (Figure 1). In the TUNEL assay, the AI is significantly increased in the 25 mM glucose-treated group compared with the 5.5 mM group (19.89% ± 5.82% vs. 8.87% ± 3.09%, $p = 0.024$), and the increasing linear trend was found. In summary, the cell permeability, migration ability and AI of HRMEC showed an increasing trend, from 25 mM to 50 mM, while capacities were inhibited when glucose concentration increased further. 50 mM may be equal to the acute clinical value of diabetes and the extreme limit value in an *in vitro* study.

3.2. Cells Treated with 25 mM Have Higher Proliferative Capacity Compared to those Treated with 5.5 mM. The CCK-8 assay showed significant difference in OD values of each group after 24 h of culture ($F = 25.567$, $p < 0.001$). Compared to the control group, the OD in the G25 group was significantly higher (1.01 ± 0.05 vs. 0.96 ± 0.45 (control), $p < 0.001$), while it was significantly lower in the G50 and G100 groups (0.91 ± 0.03 vs. 0.96 ± 0.45, $p_{G50} < 0.001$; 0.87 ± 0.02 vs. 0.96 ± 0.45, $p_{G100} < 0.001$, respectively); in

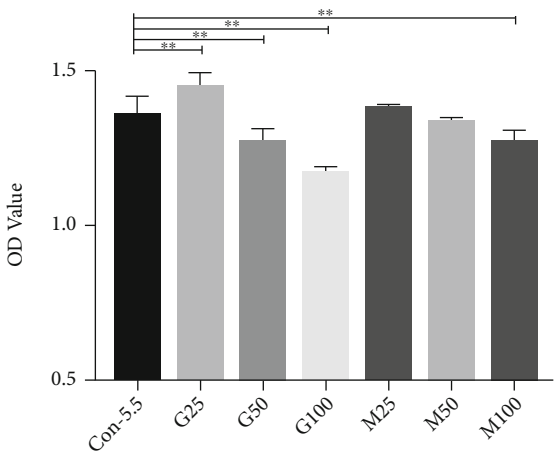

Figure 1: Cell proliferative ability of HRMECs using the CCK-8 assay. At 48 h after culturing, compared to the control group, increased cell proliferation at 48 was found in the G25 group, while the OD value was significantly lower in the G50 and G100 groups. No significant difference was observed between the hypertonic group and the control group. Con-5.5, G25-G100: concentration of glucose (5.5, 25, 50, and 100 mmol/l, respectively); M25-M100: concentration of M-mannitol (19.5, 44.5, and 94.5 mmol/l, respectively). CCK-8: Cell Counting Kit-8 assay. HRMEC: human retinal endothelial cell. OD value: optical density value. $^{*}p < 0.05$; $^{**}p < 0.01$.

addition, no significant difference was observed between the hypertonic group and the control group.

Similar results were observed after 48 h of culturing ($F = 79.037$, $p < 0.001$). Compared to the control group, the OD in the G25 group was significantly higher (1.45 ± 0.04 vs. 1.36 ± 0.05, $p < 0.001$), while it was significantly lower in the G50 and G100 groups (1.27 ± 0.05 vs. 1.36 ± 0.05, $p < 0.001$; 1.18 ± 0.02 vs. 1.36 ± 0.05, $p < 0.001$, respectively). In addition, the M100 group was lower than the control group, and the difference was statistically significant (1.18 ± 0.02 vs. 1.36 ± 0.05, $p < 0.001$, respectively) (Figure 1).

After 72 h culturing, the overall difference of OD value between the groups was statistically significant ($F = 61.144$, $p < 0.001$). Compared to the control group, the OD in the G25 group was significantly higher (1.65 ± 0.12 vs. 1.58 ± 0.03, $p = 0.006$), while it was significantly lower in the G50 and G100 groups (1.48 ± 0.06 vs. 1.58 ± 0.03, $p < 0.001$; 1.23 ± 0.01 vs. 1.58 ± 0.03, $p < 0.001$, respectively). Compared with the control group, the M50 and M100 groups in the hypertonic group were significantly reduced (1.41 ± 0.02 vs. 1.58 ± 0.03, $p < 0.001$; 1.39 ± 0.07 vs. 1.58 ± 0.03, $p < 0.001$, respectively) (Figure 1). The results indicated that the better time point for studying HRMECs under higher glucose is at 48 h after culturing.

3.3. HRMECs Treated with 25 mM or 50 mM Have Higher Migration Capacity Compared to Those Treated with 5.5 mM (Transwell). Significant difference of the migration cells was found between the different glucose concentration groups at 48 h by transwell assay ($F = 4.412$, $p = 0.008$). The migration ability in HRMECs using transwell assay revealed that there was a significantly increased number of migration cells in the 25 mM (238 ± 29 vs. 200 ± 42, $p = 0.026$), 50 mM (230 ± 16 vs. 200 ± 42, $p = 0.021$), and 100 mM groups (228 ± 18 vs. 200 ± 42, $p = 0.031$) in comparison with the control 5.5 mM group at 48 h (Figure 2).

After 24, 48, and 72 h, the cell migration rate of the control group was $35.84\% \pm 8.19\%$, $49.00\% \pm 11.43\%$, and $59.31\% \pm 13.29\%$, respectively. Compared to the control group, at 24 h of culture, higher cell migration rate was observed in the G25 and G50 groups ($45.79\% \pm 5.28\%$ vs. $35.84\% \pm 8.19\%$, $p < 0.001$; $46.13 \pm 5.53\%$ vs. $35.84\% \pm 8.19\%$, $p < 0.001$), while it was lower in the G100 and M100 groups ($25.54\% \pm 3.38\%$ vs. $35.84\% \pm 8.19\%$, $p < 0.001$; $20.39\% \pm 7.62\%$ vs. $35.84\% \pm 8.19\%$, $p < 0.001$). A similar effect was observed at 48 and 72 h post culture (all $p < 0.05$).

3.4. Apoptosis Indexes in Cells Treated with 25 mM or 50 mM Compared to Those Treated with 5.5 mM in HRMEC. PI/Hoechst staining and ImageJ were used to quantify the live and dead cells. We found that the apoptosis indexes of 5.5 mM groups, G25, G50, G100, M25, M50, and M100 groups were $7.71\% \pm 0.80\%$, $10.67\% \pm 2.06\%$, $11.06\% \pm 0.47\%$, $5.04\% \pm 0.40\%$, $8.07\% \pm 0.60\%$, $8.93\% \pm 0.56\%$, and $5.98\% \pm 0.33\%$, respectively, and the overall difference between the two groups was statistically significant ($F = 51.101$, $p < 0.001$) after 24 h of cell culturing. The apoptosis indexes of the G25 and G50 groups were significantly higher compared to the control group ($10.67\% \pm 2.06\%$ vs. $7.71\% \pm 0.80\%$, $p < 0.001$; $11.06\% \pm 0.47\%$ vs. $7.71\% \pm 0.80\%$, $p < 0.001$).

At 48 h, the cell apoptosis indexes of 5.5 mM groups, G25, G50, G100, M25, M50, and M100 groups were $11.16\% \pm 0.84\%$, $20.84\% \pm 0.44\%$, $18.50\% \pm 0.88\%$, $11.19\% \pm 0.60\%$, $11.87\% \pm 0.40\%$, $15.55\% \pm 0.81\%$, and $14.15\% \pm 0.43\%$, respectively. The overall difference between the groups was statistically significant ($F = 297.784$, $p < 0.001$). The apoptosis indexes of G25, G50, and M50 groups were significantly higher compared to the control group, and the difference was statistically significant ($20.84\% \pm 0.44\%$ vs. $11.16\% \pm 0.84\%$, $p < 0.001$; $18.50\% \pm 0.88\%$ vs. $11.16\% \pm 0.84\%$, $p < 0.001$; and $15.55\% \pm 0.81\%$ vs. $11.16\% \pm 0.84\%$, $p < 0.001$).

At 72 h, the AI of 5.5 mM, G25, G50, G100, M25, M50, and M100 groups was $16.06\% \pm 0.42\%$, $27.02\% \pm 0.96$, $25.56\% \pm 0.96\%$, $20.15\% \pm 0.64\%$, $17.97\% \pm 1.17\%$, $20.86\% \pm 0.68\%$, and $21.72\% \pm 0.81\%$, respectively. The overall difference between the groups was statistically significant ($F = 194.267$, $p < 0.001$). The apoptosis indexes of the G25, G50, M25, M50, and M100 groups were significantly higher than that in the control group, and the difference was statistically significant ($p < 0.001$).

The TUNEL analysis further confirmed the PI/Hoechst result. The AI of the HRMECs in the 25 mM, 50 mM, and 100 mM is significantly higher than that in the control group ($p_{25\text{mM}} = 0.024$, $p_{50\text{mM}} = 0.001$, and $p_{100\text{mM}} < 0.001$) at 48 h (Figure 3).

3.5. HRMEC Treated with Hyperglycemia Groups Poses Higher Permeability Compared to Those Treated with 5.5 mM. After 24 h of cell culturing, the cell permeability of

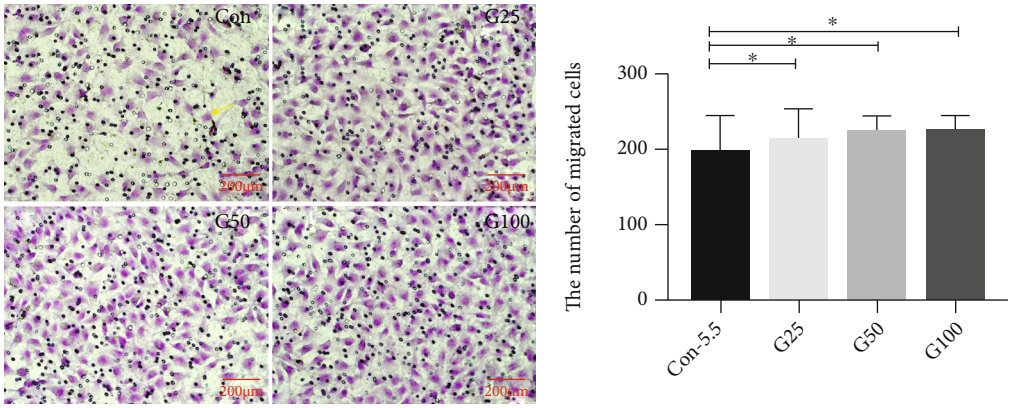

(a) (b)

Figure 2: Cell migration ability detected by Transwell assay. (a) Representative images of migrated HRMECs treated with 5.5 mM, 25 mM, 50 mM, and 100 mM glucose, respectively, at 48 h. HRMEC cells were stained with 0.1% crystal violet (yellow, arrows). (b) The number of migrated HRMEC was significant higher in the 25 mM (238 ± 29 vs. 200 ± 42, $p = 0.026$), 50 mM (230 ± 16 vs. 200 ± 42, $p = 0.021$), and 100 mM (228 ± 18 vs. 200 ± 42, $p = 0.031$) groups in comparison with the 5.5 mM groups. Scale bar: 200 μm (a). HRMEC: human retinal vascular endothelial cells; Con: control group (5.5 mmol/l); G25: 25 mmol/l; G50: 50 mmol/l; G100: 100 mmol/l. $^{*}p < 0.05$.

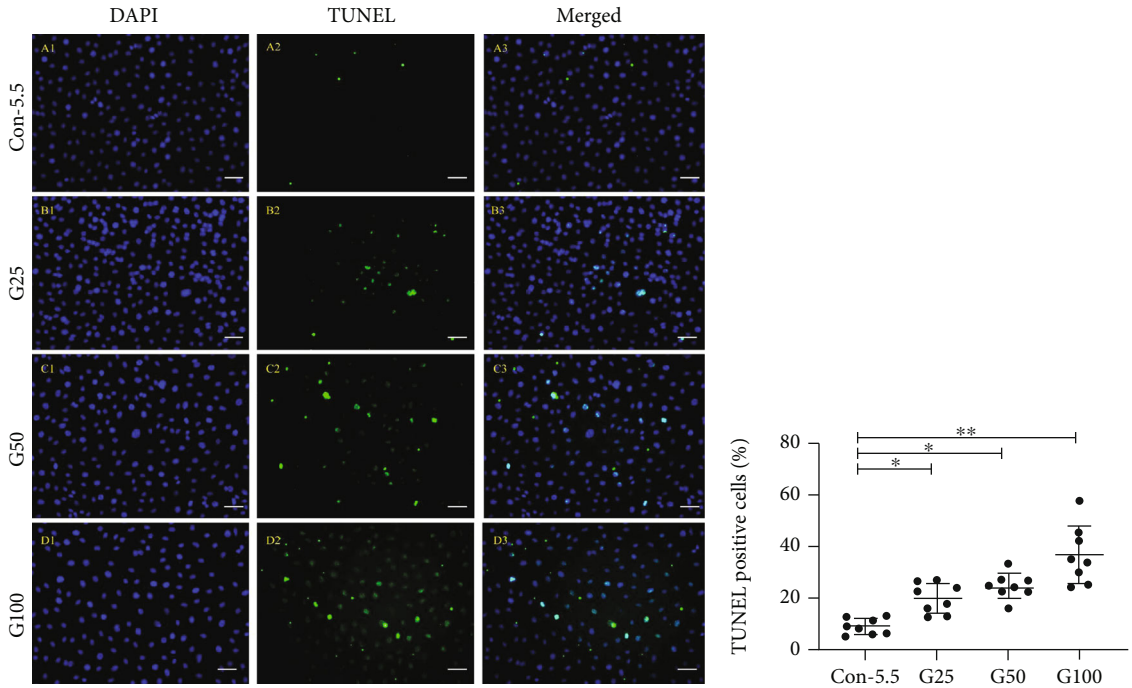

Figure 3: Representative fluorescence images and quantification of TUNEL-positive HRMECs. TUNEL staining (green, A2-D2), DAPI staining (blue, A1-D1), and merged image of HRMECs with different treatments. Merged images are presented as A3-D3. Con-5.5, G25-G100: concentration of glucose (5.5, 25, 50, and 100 mmol/l, respectively). HRMECs: human retinal microvascular endothelial cells. Scale bar: 200 μm. $^{*}p < 0.05$; $^{**}p < 0.01$.

5.5 mM, G25, G50, G100, M25, M50, and M100 groups was 8.12% ± 0.56%, 8.42% ± 0.23%, 8.82% ± 0.26%, 8.83% ± 0.25%, 8.39% ± 0.24%, 8.47% ± 0.25%, and 8.52% ± 0.27%, respectively. Cell permeability slightly increased with the increase of glucose concentration. In addition, no significant effect on cell permeability was observed in the mannitol-control groups.

3.6. The Angiogenic Ability of HRMEC Is Higher in the 25 mM and 50 mM Groups Compared to the 5.5 mM Group. Angiogenesis was evaluated by a Matrigel-based tube formation assay and protein expression analysis of VEGFA in different groups. The number of tubes at 9 hours increased with the concentration of glucose (5.5 mM: 23.5 ± 9.87, 25 mM: 34.33 ± 1.51; and 50 mM: 40 ± 5.02), respectively ($F = 10.124$, $p = 0.002$), showing a statistical significance among the groups. The number of branch points was also significantly increased in the higher glucose groups (5.5 mM: 9 ± 3.16, 25 mM: 21.67 ± 0.52, and 50 mM: 26.67 ± 1.97, respectively, $F = 105.613$, $p < 0.001$). The area of

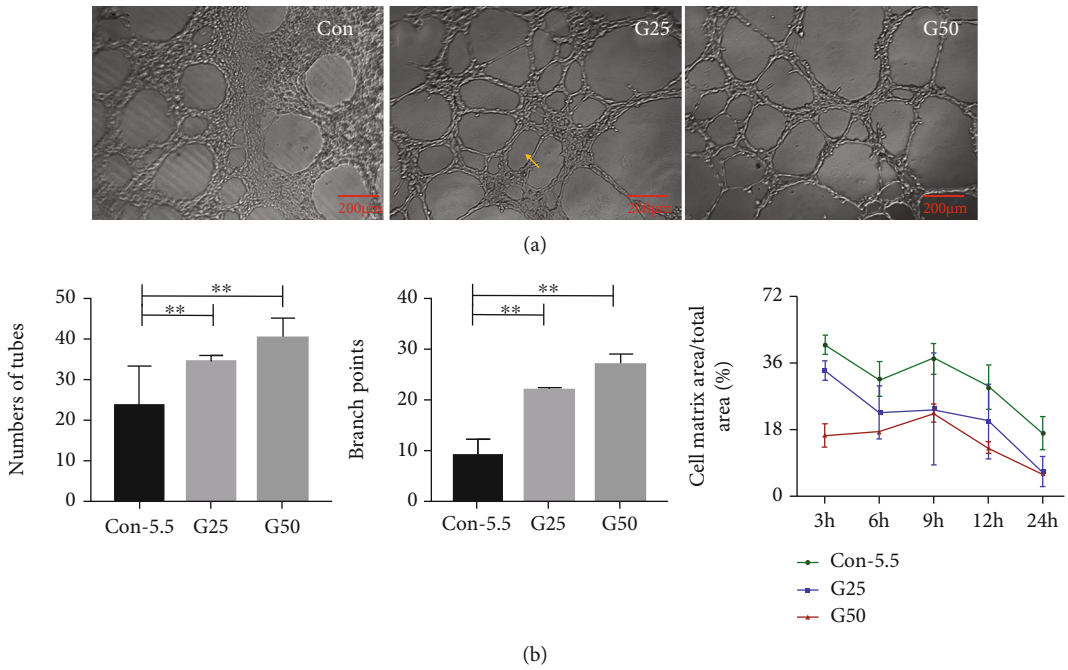

Figure 4: A Matrigel-based tube formation assay to assess the vasogenic activity of HRMEC. G25/G50 showed a stimulatory effect on angiogenic tube formation in the Matrigel assay. (a) HREMCs were cultured on Matrigel, and the cumulative numbers of circle-like structures (yellow arrow) and branch points were measured after 9 h. (b) The vasculogenic capacity was quantified in cells treated with different groups. Con-5.5, G25, and G50: concentration of glucose (5.5, 25, and 50 mmol/l, respectively). Tube formation assay was examined under an inverted fluorescence microscope with a ×10 objective. HRMEC: human retinal vascular endothelial cells. Scale bar: 200 μm (a). $^{*}p < 0.05$; $^{**}p < 0.01$.

the extracellular (tube metrics area) in the G25 and G50 groups were significantly less than that in the 5.5 mM group ($p_{G25} = 0.013$, $p_{G50} = 0.024$) (Figure 4).

ELISA was used to detect VEGFA secretion from HRMECs into the medium. The results showed that the amount of VEGFA secreted increased with increasing glucose concentrations ($F = 9.000$, $p = 0.016$).

3.7. The Biological Behavior of RGCs under Hyperglycemia Condition. The cell variability of RGCs was detected by the CCK-8 assay. The OD value between the 5.5 mM, G25, G50, G100, G150, M25, M50, M100, and M150 groups was statistically significant ($F = 8.041$, $p < 0.001$) at 48 h. The OD value was significantly higher in the 25 mM (1.871 ± 0.218 vs. 1.718 ± 0.100, $p = 0.023$), while it was lower in the 50 mM (1.607 ± 0.128 vs. 1.718 ± 0.100, $p = 0.013$), 100 mM (1.562 ± 0.215 vs. 1.718 ± 0.100, $p = 0.019$), and 150 mM (1.535 ± 0.185 vs. 1.718 ± 0.100, $p = 0.002$) in comparison with the control 5.5 mM at 48 h. Compared with the control group, the M25, M50, and M100 groups were not significantly reduced ($p_{M25} = 0.240$, $p_{M50} = 0.416$, and $p_{M100} = 0.163$) at 48 h. The same declined trend of OD value was also found at 24 h and 72 h (Figure 5).

RGCs are the earliest affected retinal neurons in the retina. The long axons of RGCs play an important role in transmitting visual information along with photoreceptors, horizontal cells, amacrine cells, and bipolar cells, from the retina to the brain [20, 21]. To further evaluate the effects of hyperglycemia, the axons, which are the sole retinal neuron projections, connect the RGC cell body and brain. It is defined as the longest neurite extending from the RGC cell body [22]. RGCs were labeled by neurons and RGC-specific markers TUJ1 and BRN3A, respectively, followed by the ImageJ quantitative analysis. The proportion of RGCs with neurite extensions in the 5.5 mM, G25, G50, G100, G150, M25, M50, M100, and M150 groups was statistically significant ($F = 49.655$, $p < 0.001$) at 48 h. Immunofluorescence staining revealed that the proportion of RGCs with neurite extensions was significantly lower in the 25 mM (33 ± 13 vs. 49 ± 5, $p = 0.007$), 50 mM (21 ± 7 vs. 49 ± 5, $p < 0.001$), 100 mM (20 ± 7 vs. 49 ± 5, $p < 0.001$), and 150 mM (17 ± 6 vs. 49 ± 5, $p < 0.001$) groups in comparison with that in the control group (5.5 mM) at 48 h. Compared with the control group, the M25, M50, M100, and M150 groups in the hypertonic group were not significantly different ($p_{M25} = 0.691$, $p_{M50} = 0.297$, $p_{M100} = 0.716$, and $p_{M150} = 0.356$) (Table 1). Apoptosis in RGCs was detected and quantified by the PI/Hoechst fluorescent staining and TUNEL assay, followed by the ImageJ analysis. AI was found statistical significance in the different glucose concentration groups at 24 h, 48 h, and 72 h detected by the PI/Hoechst staining ($F_{24h} = 27.648$, $p = 0.001$; $F_{48h} = 11.863$, $p < 0.001$; and $F_{72h} = 9.880$, $p < 0.001$). Compared to the control group, the AI of the G50, G100, and G150 groups was significantly higher after 24 h of cell culturing ($p_{G50} = 0.015$, $p_{G100} = 0.003$, and $p_{G150} = 0.001$). AI in the G25, G100, and G150 groups was significantly higher than that in the control group at 48 h ($p_{G25} = 0.006$, $p_{G100} = 0.006$, and $p_{G150} = 0.002$). The AI of

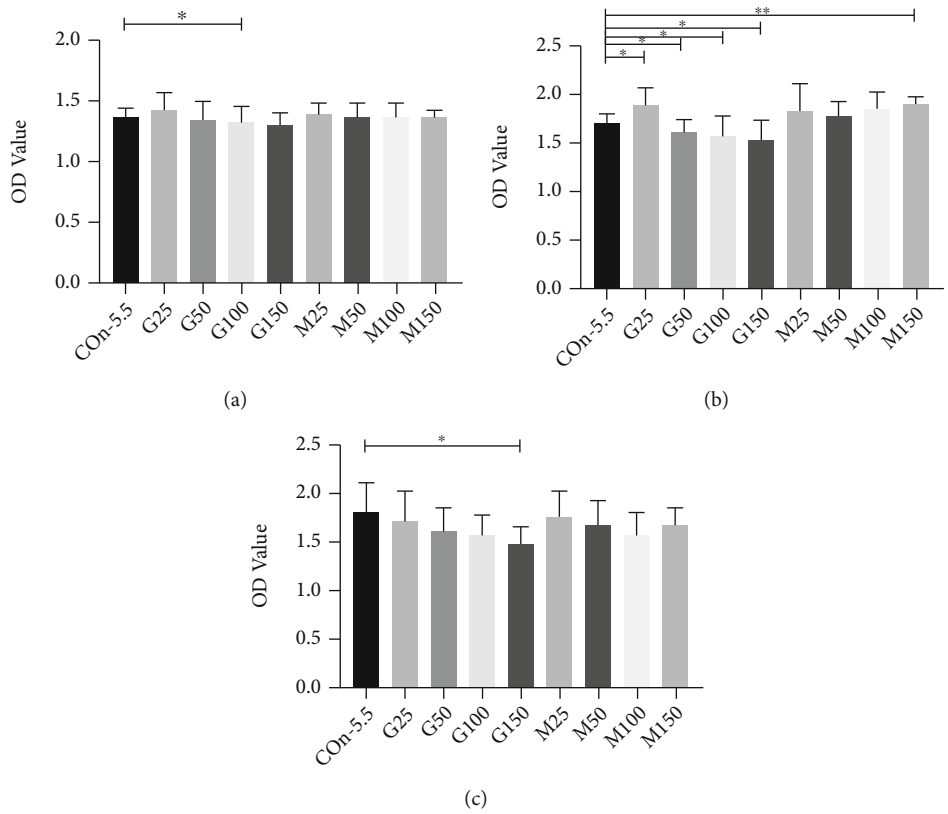

Figure 5: Cell viability of RCGs by the CCK-8 assay. Compared to the control group, the OD value was significantly lower in the G50, G100, and G150 at 48 h. (a–c) Cell proliferation ability in RGCs treated with different groups at 24, 48, and 72 h. Con-5.5, G25-G150: concentration of glucose (5.5, 25, 50, 100, and 150 mmol/l, respectively); M25-M150: concentration of M-mannitol (19.5, 44.5, 94.5, and 133.5 mmol/l, respectively). $^{*}p < 0.05$; $^{**}p < 0.01$. RGCs: retinal ganglion cells CCK-8: Cell Counting Kit-8 assay OD value: optical density value.

Table 1: Neurite extensions in RGCs detected by immunofluorescence staining at 48 h.

Groups	The proportion of RGCs with neurite extensions (%)	p value
Con	49 ± 5	—
G25	33 ± 13	*0.007*[a] *
G50	21 ± 7	*<0.001*[a] *
G100	20 ± 7	*<0.001*[a] *
G150	17 ± 6	*<0.001*[a] *
M25	51 (42-55)	0.691[b]
M50	43 ± 15	0.297[b]
M100	50 ± 13	0.716[a]
M150	46 ± 9	0.356[a]

*Statistically significant: $^{*}p < 0.05$. According to the type of data and the data distribution, [a]independent-sample t-test and the [b]Mann-Whitney U test were applied. Con-5.5, G25-G150: concentration of glucose (5.5, 25, 50, 100, and 150 mmol/l, respectively); M25-M150: concentration of M-mannitol (19.5, 44.5, 94.5, and 133.5 mmol/l, respectively). RGCs: retinal ganglion cells.

the G50, G100, and G150 groups was significantly higher than that of the control group at 72 h ($p_{G50} = 0.003$, $p_{G100} = 0.016$, and $p_{G150} = 0.001$). In addition, the AI of hypertonic groups was not significantly higher than that in the 5.5 mM group at 24 h, 48 h, and 72 h (all $p > 0.05$) (Table 2).

TUNEL assay further confirmed the above results. The AI of the RGCs in the 50 mM, 100 mM, and 150 mM is significantly higher than that in the control group ($p_{50mM} < 0.001$, $p_{100mM} < 0.001$, and $p_{150mM} < 0.001$) at 48 h (Table 3).

4. Discussion

In this study, we have optimized glucose concentrations to model diabetic retinal endothelial (25-50 mM) or neuronal (50-150 mM) dysfunction *in vitro*, which have a wide range of downstream applications.

In vitro studies have been colloquially named "test-tube" experiments, providing a convenient, time- or cost-consuming, specific, and more detailed analysis which cannot be done within the whole organism. The advantages of *in vitro* study are simplicity [22–24], species specificity [25], convenience and automation [26]. *In vitro* studies are essential to explore the pathophysiology of retinal damage by hyperglycemia [27, 28]. Immortalized cell lines and primary isolated retinal endothelial and ganglion cells are currently the most widely used *in vitro* models for exploring the pathogenesis of DR, a neuronal vascular disorder [8].

Table 2: Apoptotic index in RGCs at 24 h, 48 h, and 72 h.

Groups	24 h Apoptotic index	p value	48 h Apoptotic index	p value	72 h Apoptotic index	p value
Con	0.042 (0.028-0.047)	—	0.013 ± 0.007		0.091 ± 0.031	—
G25	0.069 (0.031-0.112)	0.171[b]	0.024 ± 0.007	0.006[a]	0.132 ± 0.083	0.182[a]
G50	0.108 (0.071-0.144)	0.015[b]	0.018 ± 0.009	0.284[a]	0.225 ± 0.095	*0.003*[a] *
G100	0.120 (0.061-0.256)	0.003[b]	0.025 ± 0.008	0.006[a]	0.181 ± 0.088	*0.016*[a] *
G150	0.148 (0.079-0.184)	0.001[b]	0.055 ± 0.027	0.002[a]	0.291 ± 0.124	*0.001*[a] *
M25	0.049 (0.025-0.082)	0.691[b]	0.016 ± 0.003	0.329[a]	0.089 ± 0.024	0.893[a]
M50	0.036 (0.024-0.059)	0.691[b]	0.017 ± 0.004	0.221[a]	0.089 ± 0.030	0.856[a]
M100	0.050 (0.030-0.065)	0.354[b]	0.019 ± 0.004	0.054[a]	0.097 ± 0.040	0.733[a]
M150	0.056 (0.030-0.082)	0.270[b]	0.016 ± 0.008	0.455[a]	0.093 ± 0.031	0.918[a]

*Statistically significant: * $p < 0.05$. According to the type of data and the data distribution, [a]independent-sample t-test and the [b]Mann-Whitney U test were applied. Con-5.5, G25-G150: concentration of glucose (5.5, 25, 50, 100, and 150 mmol/l, respectively); M25-M150: concentration of M-mannitol (19.5, 44.5, 94.5, and 133.5 mmol/l, respectively).

Table 3: TUNEL-positive cells in RGCs using TUNEL staining at 48 h.

Groups	TUNEL-positive cells (%)	p value
Con	14.97 ± 7.48	—
G25	27.31 ± 2.41	0.364
G50	44.88 ± 7.31	*<0.001* *
G100	52.20 ± 2.86	*<0.001* *
G150	84.37 ± 2.43	*0.001* *

* p value: the difference of the high-glucose groups (25 mM, 50 mM, 100 mM, and 150 mM) and the control group (5.5 mM) was analyzed with one-way analysis of variance.

Currently, the commercially available *in vitro* model of DR in different cell types is 5.5 mM (as the normal control) and 25 mM (as the higher glucose) for HRMEC and 35 mM for RGCs, respectively [29–31]. However, there is no evidence to prove that 25 mM or 30 mM-35 mM glucose *in vitro* model is simulation to the physiological conditions (hyperglycemia) of the human body, and 25 mM should not be considered the upper limit of *in vitro* research. In this study, we found that concentrations of 25 mM to 50 mM glucose could induce the proliferation of HRMEC, promote cell migration capacity, and improve angiogenic ability (tube formation), promoting cell apoptosis (from 25 mM to 100 mM). All of the above results indicate that 25 mM is a cutoff value, and 25-50 mM is the proper concentration to stimulate diabetic microvasculopathy. This concentration range also can be used to study retinal neovascularization in proliferative retinopathy. Furthermore, under the hyperglycemia pathological condition, the AI of HRMEC was significantly increased, indicating that a high concentration of glucose may increase the oxidative stress within the cell, activating the signal transduction pathway, promoting cell apoptosis. Leal et al. [32] found that the number of apoptotic cells significantly increased after HRMEC was treated with 30 mM glucose, consistent with our result.

On the other hand, the concentration of 50 mM to 150 mM glucose exhibits inhibition on the cell variability of RGCs at 24 h, 48 h, and 72 h. Immunofluorescence staining revealed that the proportion of RGCs with neurite extensions was significantly lower in the 50 mM, 100 mM, and 150 mM groups than that in the control group (5.5 mM) at 48 h. The TUNEL assay also found that AI is significantly higher in the 50 mM, 100 mM, and 150 mM groups, indicating 50 mM may be taken as the cutoff value for *in vitro* study of neuronal degeneration under hyperglycemia, and 50 mM-100 mM may be the proper concentration to stimulate diabetic microvasculopathy.

In the present study, we found that glucose concentration was positively correlated with the cell permeability of HRMEC. This may due to the decreased expression levels of cell tight junction proteins [33]. Extremely high glucose concentrations (100 mM) can significantly inhibit cell proliferation. However, we cannot ignore the effect of osmotic pressure on cell biological behavior at this concentration. These results suggest that the extremely high glucose concentrations may not be suitable for *in vitro* testing. By contrast, considering the behavior of the HRMEC under different glucose concentrations, 25 mM-50 mM may be of the appropriate range and can be further applied in further *in vitro* study such as drug interventions for DR.

HRMEC has an important role in the maintenance of the normal function of RBB in human. Its pathological changes are the basis of diabetic microvasculopathy [34]. Our study investigated the gradient of glucose concentration and osmotic pressure on the biological behavior of HRMEC *in vitro*. The results have provided new insight into this area.

Previous studies have found a significantly lower cell proliferation rate in cells treated with a glucose concentration of 25 mM compared to cells treated with 5.5 mM [32, 35]. However, Sun et al. found that 25 mM glucose concentration promoted cell proliferation, migration, and apoptosis, consistent with our findings [36]. In our study, we have shown that increased osmotic pressure does not affect the biological behavior of HRMEC, which was consistent with

previous studies that osmotic pressure did not affect cell viability at all, but some studies concluded that osmotic pressure of 25 mM had a negligible effect on the biological behavior of HRMEC [37–39].

The best concentration of D-glucose to use in human cell cultures to mimic the diabetic condition is yet to be set up. Furthermore, the concentration of D-glucose concentration will vary accordingly based on different cell lines. In the current study, we investigated for the first time the effects of the concentration gradient of glucose and osmotic pressure on the biological behavior of HRMEC, providing the rational concentration of D-glucose to mimic the DR condition. We found that 25 mM (the cutoff value) to 50 mM (the extreme value) is a suitable high glucose concentration.

To further analyze the effects and mechanisms of high sugar on HREMC biological behavior, we carried out a tube formation assay, a fast, quantifiable method to detect the angiogenic activity of HRMEC [40]. The advantages of this assay are that it is relatively easy to set up, requires a short culture period, is quantifiable, and is amenable to high-throughput analysis. HRMECs treated with 25 mM or 50 mM glucose have a larger angiogenic capacity than those treated with 5.5 mM glucose. This result suggested a potential biological basis of abnormal neovascularization in DR patients. We also found that the quantification results of the tube formation assay are concomitant with the elevated protein expression of VEGFA. This finding suggested that VEGFA may be the key regulator for the high glucose-induced angiogenesis process and established the rationality of 25 mM-50 mM glucose concentration for the *in vitro* hyperglycemia model.

In this study, we found that the cell variability of RGCs is significantly lower in the 50 mM to 150 mM and the linear declined trend was evidence from 5.5 mM to 150 mM, which is consistent with previous studies [41]. RGCs were further labeled with neurons and RGC-specific markers TUJ1 and BRN3A, respectively, followed by the ImageJ quantitative analysis [42]. Immunofluorescence staining revealed that the proportion of RGCs with neurite extensions was significantly lower in the 50 mM ($p < 0.05$), 100 mM ($p < 0.05$), and 150 mM ($p < 0.05$) groups in comparison with that in the control group (5.5 mM) at 48 h. the AI is significantly higher in the 50 mM ($p < 0.001$), 100 mM ($p < 0.001$), and 150 mM ($p < 0.001$) groups compared to the control 5.5 mM at 48 h. The results indicate that 50 mM-100 mM may be used as the hyperglycemia *in vitro* model, and 50 mM and 150 mM may be taken as the cutoff and extreme value.

In this study, we set the hyperosmotic control group by artificially changing the osmotic pressure in the cell culture medium: Mannitol was added to the 5.5 mM group to adjust the osmotic pressure to correspond with the same osmotic pressure of G25, G50, G100, and G150, thus forming M25, M50, M100, and M150 (mannitol concentrations 19.5, 44.5, 94.5, and 133.5 mmol/l, respectively). The osmosis pressure of the control group (Con-5.5) was about 320 mOsm. According to the permeable pressure calculation formula, it can be obtained that the remaining groups of osmosis pressure were approximately 340 mOsm (G25/M25), 365 mOsm (G50/M50), 415 mOsm (G100/M100), and 465 mOsm (G150/M150). In our study, we have shown that increased osmotic pressure does not affect the biological behavior of RGCs from 25 mM to 50 mM.

Our previous studies have shown that neurodegeneration is an earlier pathological change in the retina than microvasculopathy. It is interesting to study further the interactions between retinal endothelium cells and neurons. This study provides a basis for the next step in exploring how gene transfection can rescue vascular disease and early neuropathy. As the Müller glia are also involved in DR and are a component in the neuronal vascular unit, further studies warrant setting up more complicated *in vitro* models to stimulate the retinal neural vascular unit.

We used the healthy HRMECs and RGCs for establishing the *in vitro* model of DR. As the endothelial and neuronal cells in advanced DR stages may react differently to the 25-50 mM or 50-100 mM of glucose, respectively, this *in vitro* model may more applicable to stimulate the early stage of DR or even the preclinical stage of DR. This *in vitro* model also represents a valid tool useful for pathological investigation, drug screenings, and gene therapy of DR.

US-FDA approved Voretigene neparvovec-rzyl (Luxturna) gene therapy in 2017 to rescue the apoptotic photoreceptors in Leber's congenital amaurosis [43, 44]. This led to the bright prospects of gene therapy on multigene eye diseases, including DR. Currently, 12 serotypes of adeno-associated virus have been applied as gene vectors. It is necessary to test the cell-specific serotype *in vitro*, especially in pathological conditions (high glucose) first [45]. Therefore, the establishment of proper hyperglycemia *in vitro* model is essential for further study of DR.

Due to the complexity of the internal environment and the diversity of the microenvironment, the application of animal models for investigating diabetic retinopathy faces great limitations and challenges. Therefore, the *in vitro* study could provide insight for studying the pathogenesis, progression, and even drug intervention of retinal diseases.

In conclusion, glucose of 25 mM to 50 mM is the appropriate range and 100 mM extreme value of hyperglycemia for HRMEC *in vitro*; 50 mM and 150 mM are the proper range for RGCs. The impact of osmotic in higher glucose can be omitted. High glucose-induced VEGF is the key pathogenic factor of angiogenesis in endothelial cells.

Abbreviations

AI: Apoptosis index
BRB: Blood retinal barrier
BSA: Bovine serum albumin
CCK-8: Cell Counting Kit-8
DMEM: Dulbecco's modified Eagle's medium
DR: Diabetic retinopathy
ELISA: Enzyme-linked immunosorbent assay
FITC: Fluorescein Isothiocyanate
FBS: Fetal bovine serum
HBSS: Hank's balanced salt solution
HRMEC: Human retinal microvascular endothelial cell
OD: Optical density
PBS: Permeabilization solution

PI: Propidium iodide
RMEC: Retinal microvascular endothelial cell
RGCs: Retinal ganglion cells
TUJ1: Antineuronal class III β-tubulin
VEGFA: Vascular endothelial growth factor-A.

Data Availability

All data generated or analyzed during this study are included in this published article.

Disclosure

All authors make sure that all data and materials as well as software application or custom code support, their published claims and comply with field standards.

Conflicts of Interest

All authors in this work have no financial and personal relationships with other people or organizations that could inappropriately influence (bias) the work.

Authors' Contributions

All authors have contributed to manuscript writing. All authors read and approved the final manuscript. The corresponding author managed all communication between the journal and all coauthors, before and after publication. The disclosures, declarations, and transparency on data statements from all authors are included in the manuscript as appropriate. We have provided transparency on reuse of material and mention of any unpublished material (for example manuscripts in press) included in the manuscript in a cover letter to the editor.

Acknowledgments

This work was supported by the National Natural Science Foundation of China (grants 81570850, 81170859, and 82070988) and the Ministry of Science and Technology Foundation of China (grant 2016YFC1305604).

Supplementary Materials

Supplemental Figure 1: cell migration ability detected by scratch assay. Compared to the control group, at 24 h of culture, higher cell migration rate was observed in the G25 and G50 groups, while lower in the G100 and M100 groups. Similar effect was observed at 48 ($p < 0.05$) and 72 h ($p < 0.01$). (A1-A7) The images of the scratches at 0 h, 24 h (A8-A14), 48 h (A15-A21), and 72 h (A22-A28). (B1-B3) Cell migration rate in cells treated with different groups at 24, 48, and 72 h. Con-5.5, G25-G100: concentration of glucose (5.5, 25, 50, and 100 mmol/l, respectively); M25-M100: concentration of M-mannitol (19.5, 44.5, and 94.5 mmol/l, respectively). Scratch assay was examined under an inverted fluorescence microscope with a ×4 objective. Scale bar: 200 μm (A). $^{*}p < 0.05$; $^{**}p < 0.01$. Supplemental Figure 2: representative composite images showing morphological changes of selected HREMCs detected with dual staining of Hoechst33342/PI. Green arrows: (1) viable cells with normal nuclei and (2) cells with apoptotic nuclei which was labeled by Hoechst33342. White arrows: (1) dead cells with normal nuclei and (2) dead cells with apoptotic nuclei which was labeled by PI. Yellow arrows: dead cells with apoptotic nuclei which were labeled by PI and Hoechst33342. Con-5.5, G25-G100: concentration of glucose (5.5, 25, 50, and 100 mmol/l, respectively); M25-M100: concentration of M-mannitol (19.5, 44.5, and 94.5 mmol/l, respectively). Cells were imaged by fluorescence microscope (magnification ×100). AI: apoptosis index: the number of PI-positive cells/the number of Hoechst-stained cells. HRMEC: human retinal vascular endothelial cells. PI: propidium iodide. Scale bar: 200 μm (A). $^{*}p < 0.05$; $^{**}p < 0.01$. Supplemental Figure 3: HRMEC permeability evaluated by the FITC-labeled BSA method in different groups. After 24 h of cell culture, cell permeability slightly increased with the increase of glucose concentration. No significant effect on cell permeability was observed in the mannitol-control groups. Con-5.5, G25-G100: concentration of glucose (5.5, 25, 50, and 100 mmol/l, respectively); M25-M100: concentration of M-mannitol (19.5, 44.5, and 94.5 mmol/l, respectively). $^{*}p < 0.05$; $^{**}p < 0.01$. Supplemental Figure 4: the protein expression analysis of VEGFA in different groups using ELISA. Compared to the control group, increased VEGF expression at 24, 48, and 72 h was found in the G25 group. (A–C) VEGFA expression in HRMECs treated with different groups at 24, 48, and 72 h. Con-5.5, G25, and G50: concentration of glucose (5.5, 25, and 50 mmol/l, respectively). VEGFA: vascular endothelial growth factor-A. ELISA: enzyme-linked immunosorbent assay. $^{*}p < 0.05$; $^{**}p < 0.01$. Supplemental Figure 5: representative immunofluorescence images of RGCs in different groups at 48 h. RGCs were positively stained with TUJ1 (green, A1-A9, yellow arrows), DAPI (blue, B1-B9, white arrows), and Brn3a (red, C1-C9, green arrows) which are neuronal-specific, nucleus, and RGC-specific markers, respectively. Merged images were presented as D1-D9. Con-5.5, G25-G150: concentration of glucose (5.5, 25, 50, 100, and 150 mmol/l, respectively); M25-M150: concentration of M-mannitol (19.5, 44.5, 94.5, and 133.5 mmol/l, respectively). RGCs: retinal ganglion cells. Scale bar: 200 μm (A). $^{*}p < 0.05$; $^{**}p < 0.01$. Supplemental Figure 6: apoptotic index of RGCs in different groups detected and quantified by the PI/Hoechst33342 fluorescence staining. RGCs were cultured and stained by the PI/Hoechst33342 fluorescence staining at 24 h (A1-A9), 48 h (A10-A18), and 72 h (A19-A27). (B1-B3) AI in cells treated with different groups at 24, 48, and 72 h. Quantification of apoptotic RGCs at 24 h (B1), 48 h (B2), and 72 h (B3) by the ImageJ analysis. Compared to the control group, the AI of the G50, G100, and G150 groups was significantly higher after 24 h of cell culturing ($p < 0.05$). At 48 h, the AI in the G50, G100, and G150 groups was significantly higher compared to that in the control group ($p < 0.05$). At 72 h, the AI of the G50, G100, and G150 groups was significantly higher than that of the control group ($p < 0.05$). Green arrow indicates (1) viable cells with normal nuclei and (2) cells with apoptotic nuclei which was labeled by Hoechst33342. Yellow arrow

indicates (1) dead cells with normal nuclei and (2) dead cells with apoptotic nuclei which was labeled by PI. White arrow indicates dead cells with apoptotic nuclei which was labeled by PI and Hoechst33342. Con-5.5, G25-G150: concentration of glucose (5.5, 25, 50, 100, and 150 mmol/l, respectively); M25-M150: concentration of M-mannitol (19.5, 44.5, 94.5, and 133.5 mmol/l, respectively). RGCs: retinal ganglion cells, AI: apoptosis index: the number of PI-positive cells/the number of Hoechst-stained cells. Cells were imaged by fluorescence microscope (magnification ×100). Scale bar: 200 μm (A). $^{*}p < 0.05$; $^{**}p < 0.01$. Supplemental Figure 7: representative immunofluorescence images and quantification of TUNEL-positive cells. TUNEL staining (green, A2-E2), DAPI staining (blue, A1-E1), and merged image of RGCs with different treatments. Merged images were presented as A3-E3. Con-5.5, G25-G150: concentration of glucose (5.5, 25, 50, 100, and 150 mmol/l, respectively). Scale bar: 200 μm (A). $^{*}p < 0.05$; $^{**}p < 0.01$. *(Supplementary Materials)*

References

[1] J. Cai and M. Boulton, "The pathogenesis of diabetic retinopathy: old concepts and new questions," *Eye (Lond)*, vol. 16, no. 3, pp. 242–260, 2002.

[2] R. Simó, J. M. Sundstrom, and D. A. Antonetti, "Ocular anti-VEGF therapy for diabetic retinopathy: the role of VEGF in the pathogenesis of diabetic retinopathy," *Diabetes Care*, vol. 37, no. 4, pp. 893–899, 2014.

[3] X. Zhang, S. Bao, B. D. Hambly, and M. C. Gillies, "Vascular endothelial growth factor-A: a multifunctional molecular player in diabetic retinopathy," *The International Journal of Biochemistry & Cell Biology*, vol. 41, no. 12, pp. 2368–2371, 2009.

[4] E. A. Stewart, S. Saker, and W. M. Amoaku, "Dexamethasone reverses the effects of high glucose on human retinal endothelial cell permeability and proliferation _in vitro_," *Experimental Eye Research*, vol. 151, pp. 75–81, 2016.

[5] Y. Shi, C. Chen, Y. Xu, Y. Liu, H. Zhang, and Y. Liu, "LncRNA FENDRR promotes high-glucose-induced proliferation and angiogenesis of human retinal endothelial cells," *Bioscience, Biotechnology, and Biochemistry*, vol. 83, no. 5, pp. 869–875, 2019.

[6] H. Shi, T. W. Carion, Y. Jiang, J. J. Steinle, and E. A. Berger, "VIP protects human retinal microvascular endothelial cells against high glucose-induced increases in TNF-α and enhances RvD1," *Prostaglandins & Other Lipid Mediators*, vol. 123, pp. 28–32, 2016.

[7] N. Wang, Y. Fan, and P. Ni, "High glucose effect on the role of CD146 in human proximal tubular epithelial cells in vitro," *Journal of Nephrology*, vol. 21, no. 6, pp. 931–940, 2008.

[8] X. Zhang, D. Lai, S. Bao, B. D. Hambly, and M. C. Gillies, "Triamcinolone acetonide inhibits p38MAPK activation and neuronal apoptosis in early diabetic retinopathy," *Current Molecular Medicine*, vol. 13, no. 6, pp. 946–958, 2013.

[9] L.-T. Liu, L. Liang, W. Wang et al., "Isolariciresinol-9'-O-α-L-arabinofuranoside protects against hydrogen peroxide-induced apoptosis of human umbilical vein endothelial cells via a PI3K/Akt/Bad-dependent pathway," *Molecular Medicine Reports*, vol. 17, 2018.

[10] W. Liu, X. Zhang, C. Song et al., "Expression and characterization of a soluble VEGF receptor 2 protein," *Cell & Bioscience*, vol. 4, no. 1, 2014.

[11] Y. Zhou, J. Yuan, C. Qi, X. Shao, S. Mou, and Z. Ni, "Calcium dobesilate may alleviate diabetes-induced endothelial dysfunction and inflammation," *Molecular Medicine Reports*, vol. 16, no. 6, pp. 8635–8642, 2017.

[12] J. Liu, G. Miao, B. Wang et al., "_Chlamydia pneumoniae_ infection promotes monocyte transendothelial migration by increasing vascular endothelial cell permeability _via_ the tyrosine phosphorylation of VE-cadherin," *Biochemical and Biophysical Research Communications*, vol. 497, no. 2, pp. 742–748, 2018.

[13] P. Che, J. Liu, Z. Shan et al., "miR-125a-5p impairs endothelial cell angiogenesis in aging mice via RTEF-1 downregulation," *Aging Cell*, vol. 13, no. 5, pp. 926–934, 2014.

[14] S.-i. Miura, Y. Matsuo, and K. Saku, "Transactivation of KDR/Flk-1 by the B2 receptor induces tube formation in human coronary endothelial cells," *Hypertension*, vol. 41, no. 5, pp. 1118–1123, 2003.

[15] L. A. Mesentier-Louro, C. Zaverucha-do-Valle, A. J. da Silva-Junior et al., "Distribution of mesenchymal stem cells and effects on neuronal survival and axon regeneration after optic nerve crush and cell therapy," *PLoS One*, vol. 9, no. 10 article e110722, 2014.

[16] K. Kashiwagi, Y. Iizuka, Y. Tanaka, M. Araie, Y. Suzuki, and S. Tsukahara, "Molecular and cellular reactions of retinal ganglion cells and retinal glial cells under centrifugal force loading," *Investigative Ophthalmology & Visual Science*, vol. 45, no. 10, pp. 3778–3786, 2004.

[17] J. Wu, H. K. Mak, and Y. K. Chan, "An _in vitro_ pressure model towards studying the response of primary retinal ganglion cells to elevated hydrostatic pressures," *Scientific Reports*, vol. 9, no. 1, 2019.

[18] G. R. Musada, G. Dvoriantchikova, C. Myer, D. Ivanov, S. K. Bhattacharya, and A. S. Hackam, "The effect of extrinsic Wnt/β-catenin signaling in Muller glia on retinal ganglion cell neurite growth," *Developmental Neurobiology*, vol. 80, no. 3-4, pp. 98–110, 2020.

[19] K. Omodaka, T. Kurimoto, and O. Nakamura, "Artemin augments survival and axon regeneration in axotomized retinal ganglion cells," *Journal of Neuroscience Research*, vol. 92, no. 12, pp. 1637–1646, 2014.

[20] D.-Y. Yu, S. J. Cringle, C. Balaratnasingam, W. H. Morgan, P. K. Yu, and E.-N. Su, "Retinal ganglion cells: energetics, compartmentation, axonal transport, cytoskeletons and vulnerability," *Progress in Retinal & Eye Research*, vol. 36, pp. 217–246, 2013.

[21] E. Kaplan and E. Benardete, "Chapter 2 The dynamics of primate retinal ganglion cells," *Progress in Brain Research*, vol. 134, 2001.

[22] B. Alberts, *Molecular Biology of the Cell*, Garland Science, New York, 2008.

[23] V. Paulette and V. Pierre, *Discovering Life, Manufacturing Life: How the Experimental Method Shaped Life Sciences*, Springer, Berlin, 2010.

[24] J. Nairn and N. C. Price, *Exploring Proteins: a Student's Guide to Experimental Skills and Methods*, Oxford University Press, America, 2009.

[25] A. Bertero, J. Augustyniak, L. Buzanska, and F. Caloni, "Species-specific models in toxicology: in vitro epithelial barriers," *Environmental Toxicology and Pharmacology*, vol. 70, p. 103203, 2019.

[26] N. Quignot, J. Hamon, and F. Bois, *Extrapolating in vitro results to predict human toxicity*, Springer, New York, 2014.

[27] N. G. Hattangady and M. S. Rajadhyaksha, "A brief review of in vitro models of diabetic neuropathy," *International Journal of Diabetes in Developing Countries*, vol. 29, no. 4, pp. 143–149, 2009.

[28] A. Matteucci, M. Varano, C. Mallozzi et al., "Primary retinal cultures as a tool for modeling diabetic retinopathy: an overview," *Biomed Research International*, vol. 2015, Article ID 364924, 16 pages, 2015.

[29] A. Zambrano, E. Jara, and P. Murgas, "Cytokine stimulation promotes increased glucose uptake via translocation at the plasma membrane of GLUT1 in HEK293 cells," *Journal of Cellular Biochemistry*, vol. 110, no. 6, pp. 1471–1480, 2010.

[30] Y. Song, Y. Du, W. Zou, Y. Luo, X. Zhang, and J. Fu, "Involvement of impaired autophagy and mitophagy in Neuro-2a cell damage under hypoxic and/or high-glucose conditions," *Scientific Reports*, vol. 8, 2018.

[31] Y. Wang, Y. Zhou, L. Xiao, S. Zheng, N. Yan, and D. Chen, "E2f1 mediates high glucose-induced neuronal death in cultured mouse retinal explants," *Cell cycle*, vol. 16, no. 19, pp. 1824–1834, 2017.

[32] E. C. Leal, C. A. Aveleira, Á. F. Castilho et al., "High glucose and oxidative/nitrosative stress conditions induce apoptosis in retinal endothelial cells by a caspase-independent pathway," *Experimental Eye Research*, vol. 88, no. 5, pp. 983–991, 2009.

[33] S. Roy, J. X. Jiang, A.-F. Li, and D. Kim, "Connexin channel and its role in diabetic retinopathy," *Progress in Retinal and Eye Research*, vol. 61, pp. 35–59, 2017.

[34] A. P. Adamis, J. W. Miller, M.-T. Bernal et al., "Increased vascular endothelial growth factor levels in the vitreous of eyes with proliferative diabetic retinopathy," *American Journal of Ophthalmology*, vol. 118, no. 4, pp. 445–450, 1994.

[35] Y. Qiao, C. L. Fan, and M. K. Tang, "Astragaloside IV protects rat retinal capillary endothelial cells against high glucose-induced oxidative injury," *Drug Design, Development and Therapy*, vol. Volume 11, pp. 3567–3577, 2017.

[36] J. Sun, Y. Xu, and H. Deng, "Intermittent high glucose exacerbates the aberrant production of adiponectin and resistin through mitochondrial superoxide overproduction in adipocytes," *Journal of Molecular Endocrinology*, vol. 44, no. 3, pp. 179–185, 2010.

[37] J.-H. Wu, Y.-H. Wang, W. Wang et al., "MiR-18b suppresses high-glucose-induced proliferation in HRECs by targeting IGF-1/IGF1R signaling pathways," *International Journal of Biochemistry & Cell Biology*, vol. 73, pp. 41–52, 2016.

[38] Y. Zeng, Z. Cui, J. Liu, J. Chen, and S. Tang, "MicroRNA-29b-3p promotes human retinal microvascular endothelial cell apoptosis via blocking SIRT1 in diabetic retinopathy," *Frontiers in Physiology*, vol. 10, 2020.

[39] F. Qiu, H. Tong, Y. Wang, J. Tao, H. Wang, and L. Chen, "Inhibition of miR-21-5p suppresses high glucose-induced proliferation and angiogenesis of human retinal microvascular endothelial cells by the regulation of AKT and ERK pathways via maspin," *Bioscience, Biotechnology, and Biochemistry*, vol. 82, no. 8, pp. 1366–1376, 2018.

[40] Z. Zhao, X. Ma, J. Ma, X. Sun, F. Li, and J. Lv, "Naringin enhances endothelial progenitor cell (EPC) proliferation and tube formation capacity through the CXCL12/CXCR4/PI3-K/Akt signaling pathway," *Chemico-Biological Interactions*, vol. 286, pp. 45–51, 2018.

[41] H.-Y. Chen, Y.-J. Ho, H.-C. Chou et al., "The role of transforming growth factor-beta in retinal ganglion cells with hyperglycemia and oxidative stress," *International Journal of Molecular Sciences*, vol. 21, no. 18, p. 6482, 2020.

[42] A. Ebneter, "Protection of retinal ganglion cells and the optic nerve during short-term hyperglycemia in experimental glaucoma," *Archives of ophthalmology*, vol. 129, no. 10, pp. 1337–1344, 2011.

[43] J. J. Darrow, "Luxturna: FDA documents reveal the value of a costly gene therapy," *Drug Discov Today*, vol. 24, no. 4, pp. 949–954, 2019.

[44] M. Stopa, "Gene therapy prospects in ophthalmology," *Klin Oczna*, vol. 104, no. 3-4, pp. 289–292, 2002.

[45] R. Li, Y. Qu, Y. Liu, A. F. Noor, and J. Tran, "Characteristics and advantages of adeno-associated virus vector-mediated gene therapy for neurodegenerative diseases," *Neural Regeneration Research*, vol. 14, no. 6, pp. 931–938, 2019.

Hindawi
Journal of Diabetes Research
Volume 2021, Article ID 8746114, 11 pages
https://doi.org/10.1155/2021/8746114

Review Article

Reverse Cholesterol Transport Pathway and Cholesterol Efflux in Diabetic Retinopathy

Xinyuan Zhang,[1,2] **Kaiyue Wang**,[1] **Ling Zhu**,[3] **and Qiyun Wang**[1,2]

[1]*Beijing Institute of Ophthalmology, Department of Ophthalmology, Beijing Tongren Hospital, Capital Medical University, China*
[2]*Beijing Retinal and Choroidal Vascular Study Group, China*
[3]*Save Sight Institute, University of Sydney, Australia*

Correspondence should be addressed to Xinyuan Zhang; mmzxy2010@163.com

Received 19 August 2021; Revised 16 September 2021; Accepted 1 October 2021; Published 26 October 2021

Academic Editor: Honghua Yu

Cholesterol esters, synthesized from cholesterol with long-chain fatty acids, are essential components of plasma lipoproteins and cell membranes that participate in various metabolic processes in the body. Cholesterol can be excreted through the cholesterol reverse transport (RCT) pathway when excessive cholesterol is produced in the extrahepatic cells, which is regulated by the *liver X receptor* (*LXR*) and its downstream regulators *ATP-binding cassette subfamily A member 1* (*ABCA1*) and *ATP-binding cassette subfamily G member 1* (*ABCG1*) genes. Abnormal cholesterol metabolism is closely associated with the development of diabetic retinopathy (DR). However, the precise underlying mechanism of the RCT pathway in the pathogenesis of DR is still not fully understood. This review focused on cholesterol metabolism, with a particular emphasis on the RCT pathway and its correlation with the development of DR. Particular attention has been paid to the key regulators of the RCT pathway: *LXR*, *ABCA1*, and *ABCG1* genes and their potential therapeutic targets in the management of DR.

1. Introduction

The association between abnormal lipid metabolism and microvascular complications of diabetes has received considerable attention recently. The imbalance of the reverse transport (RCT) pathway of cholesterol under high glucose pathological conditions is a new focus of research becoming a hot topic. This review summarizes the recent progress on cholesterol metabolism abnormalities, particularly emphasizing the association of the RCT pathway in the pathogenesis of diabetic retinopathy (DR). This novel research direction may lead to an insight into discovering biomarkers and molecular targets for tailored therapies. The key regulators of the RCT pathway will expect to be a frontline in the prevention and treatment of DR.

2. Cholesterol: Biosynthesis and Regulation

2.1. Synthesis and Transportation. Cholesterol is the most common and abundant molecule in the body, comprising approximately 30% of all mammalian cell membranes [1]. In addition to supporting the structure of cells, cholesterol is the precursor of synthetic bile acids, vitamin D, and steroid hormones [2]. Cholesterol further exhibits essential physiological roles in cell transport, signal transduction, and nerve conduction [3, 4]. Exogenous cholesterol is mainly derived from dietary sources, as well as from internal endogenous biosynthetic pathways. The liver and intestinal mucosa are the main organs for cholesterol synthesis, in addition to the brain.

Metabolism of cholesterol includes two main pathways: endogenous synthesis and exogenous absorption. Almost all mammalian cells can synthesize cholesterol, and the most active site of synthesis is the liver. Acetyl-CoA is used in cells to synthesize cholesterol de novo through a multistep enzymatic reaction. Acetyl-CoA reductase is the key enzyme that catalyzes mevalonate production from Acetyl-CoA. Endogenous cholesterol synthesized in hepatocytes is mainly transported by low-density lipoprotein (LDL) to the peripheral tissues in the form of LDL cholesterol (LDL-C). LDL-C found in the blood is recognized by the LDL receptor and transported into the cells [5]. The second pathway involves

the exogenous cholesterol pathway: the small intestine directly obtains exogenous cholesterol from dietary sources, which mainly occurs in the upper and middle parts of the small intestine. Niemann-Pick C1-Like protein (a polytopic transmembrane protein of 1332 amino acids) mediates cholesterol absorption and is highly specific and inhibits plant sterol uptake [6].

2.2. Conversion and Efflux. The metabolic pathway of cholesterol includes conversion and efflux. Cholesterol synthesized in the liver is transported to peripheral tissues through circulation to meet the body's regular metabolic needs. Cholesterol is not entirely oxidized and decomposed into CO_2 and H_2O in mammalian cells. Cholesterol is subsequently converted to other compounds containing a cyclopentane polyhydrophenanthrene nucleus *via* enzyme catalysis (oxidation and reduction reactions). Under normal circumstances, excessive cholesterol is excreted from cells and transported to the liver through circulation and is metabolized in hepatocytes and finally excreted through bile and feces. Such a process is called reverse cholesterol transport (RCT).

Cholesterol efflux from cells has been proved to be an early step of RCT. The RCT pathway plays a vital role in maintaining the kinetic balance of cholesterol metabolism and is regulated by several genes and proteins. Liver X receptor (LXR) and ATP-binding cassette transporters A1 (ABCA1) and G1 (ABCG1) have been identified as the key regulators in atherosclerosis [7]. It has been reported that serum capacity to induce ABCA1- and SR-BI-mediated cholesterol efflux is impaired in diabetic patients with incipient or overt nephropathy. Such impairment may contribute to the accelerated development of atherosclerosis in these patients, suggesting that the capacity of serum to induce cellular cholesterol efflux is an independent predictor of atherosclerosis and diabetic nephropathy [8].

2.3. Liver X Receptors (LXRs) and Metabolism of Cholesterol

2.3.1. Classification and Distribution of LXR. LXR, a ligand-activated nuclear transcription factor, is a member of the nuclear receptor superfamily and is involved in regulating cholesterol metabolism. LXR is a receptor for cholesterol metabolism and lipid biosynthesis. As an insulin sensitizer, LXR has been found to upregulate glucose transporter type 4 (GLUT4) expression. Furthermore, LXR agonist promotes glucose uptake in adipocyte, suggesting that activation of LXR could alter the expression of genes in liver and adipose tissue, limiting glucose output and improving peripheral glucose uptake [9]. In addition, LXR participates in water-electrolyte balance and immune response, regulating the physiological functions of a variety of apolipoproteins (apos) [10], thereby maintaining cholesterol homeostasis [10].Two subtypes of LXR in humans have been identified: LXRα (NR1H3) and LXRβ (NR1H2). LXRα is mainly expressed in the macrophages from the liver, kidney, adrenal gland, and small intestine, while LXRβ is almost expressed in all of the tissues throughout the body [11]. LXRα and LXRβ share over 75% amino acid sequence identity and are important regulators in the cholesterol and lipid metabolism process. Balasubramanian et al. found that LXRα has a significant role in regulating the expression of GLUT4 in adipocytes and potential targets in treating diabetes [12]. LXRα(-/-), LXRβ(-/-), and LXRα/β(-/-) mice developed acellular capillaries and endothelial progenitor cell dysfunction similar to the streptozotocin-injected DBA/2J mice fed a high-fat Western diet, but activation of LXR with a synthetic ligand reversed those pathological changes [13].

LXR combines with their binding partner retinoid X receptor (RXR) in the nucleus to form an LXR/RXR heterodimer. Upon LXR agonist binding, the LXR/RXR heterodimer releases a corepressor that possesses transcription factor activity and is bound to the target gene-specific gene starter sequence. Such transcription plays a major role in regulating the absorption, storage, excretion, and metabolism of cholesterol [14, 15] (Figure 1).

Endogenous agonists of LRX are mainly derivatives of cholesterol, including hydroxysterols 24(S),25-epoxycholesterol, 22(R)–hydroxycholesterol, and 24(S)-hydroxycholesterol. Exogenous agonists are mainly synthesized, such as T0901317 and GW3965. The majority of these exogenous agonists are nonselective.

2.3.2. Target Genes of LXR associated with Cholesterol Metabolism. Activation of LXR initiates the transcription of multiple genes, participates in the RCT pathway, maintains lipid metabolism balance, and promotes cholesterol outflow. The direct target genes of LXR which have been identified include *ABCA1* [16], *ABCD2*, *ATP-binding cassette subfamily G member 1* (*ABCG1*) [17], *SREBP-1c* [18], *FAS* [19], *CETP*, *LPL*, *CYP7a* [20], *apoE* [21], and *GLUT4* [22]. The main downstream regulators are *ABCA1*, *ABCG1*, *SREBP-1c*, *apoE* genes, and phospholipid transporter [23]. ATP-binding cassette transporters (ABC transporters) are a type of one-way transmembrane transporter, which uses ATP as an energy source. ABC transporters mediate the transmembrane transport of several different substrates, such as amino acids, lipids, ions, and sugars. The target genes of LXR mainly include the four ABC transporters, namely, *ABCA1*, *ABCG1*, *ABCG5*, and *ABCG8* [23, 24], all of which are involved in cholesterol transport. Binding of ligand to LXR results in the upregulation of ABCA1 and ABCG1 in cells [25–27].

ABCA1 contains an asymmetric transmembrane domain and is composed of a dimer containing six transmembrane segments. ABCA1 is widely expressed on a variety of cell membranes and binds to apolipoproteins during RCT and participates in HDL formation. ABCA1 promotes the redistribution of cholesterol and sphingomyelin and assists free cholesterol flow to lean apolipoproteins, which are esterified into mature HDL particles [28]. ABCG1 is a semitransporter that mainly transfers intracellular cholesterol to extracellular mature HDL, thereby reducing intracellular cholesterol concentration [29, 30]. ABCG1 mediates intracellular cholesterol transfer to extracellular mature HDL which is the main pathway for cholesterol efflux from endothelial cells, concomitant with a higher level of ABCG1 than ABCA1, which is activated by LXR [31]. In addition, ABCG1 plays a significant role in mediating cholesterol efflux and HDL

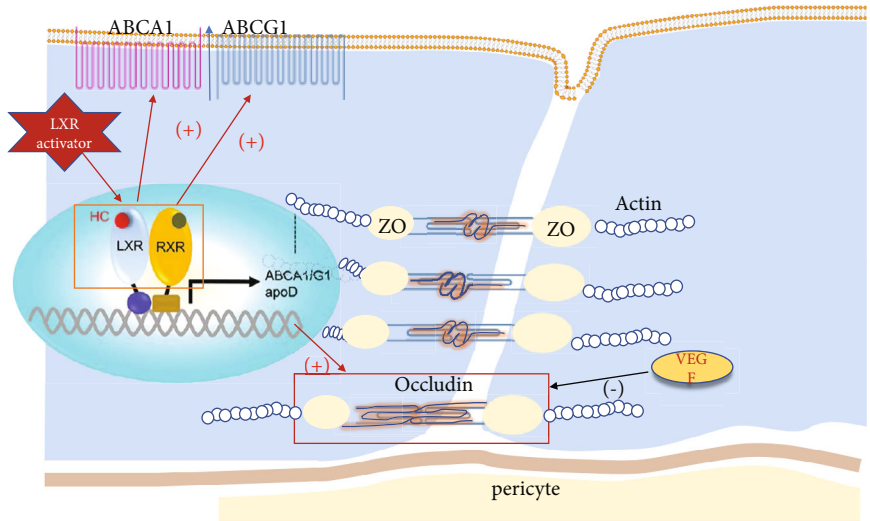

Figure 1: Liver X receptor perturbations of lipid metabolism in diabetic retinopathy. Under normal physiological conditions, transcriptional activity of LXRs is increased in response to elevated cellular levels of cholesterol. A high glucose environment attenuates activation of LXR, inducing the downregulations of transporters ABCA1 and ABCG1 on the cell membrane. Consequence of cellular cholesterol accumulation causes oxidative stress and inflammation in vascular endothelial cells. Furthermore, the increased expression level of VEGF downregulates tight junction proteins ZO-1 and occludin, leading to blood-retinal breakdown. LXR agonists can eventually reverse this pathological process. LXR: liver X receptor; RXR: retinoid X receptor; ABCA1: ATP-binding cassette subfamily A member 1; ABCG1: ATP-binding cassette subfamily G member 1; apo: apolipoprotein; ZO-1: zonula occludens-1.

transport, preventing cellular lipid accumulation in endothelial cells [32, 33]. HDL combines free cholesterol excreted from cells (mainly macrophages and endothelial cells) and promotes its transport to the liver under the action of cholesterol ester transfer protein (CETP). This causes the formation of bile acids and their excretion or the production of hormones by cholesterol in tissues. LXR mediates HDL return to the liver via directly acting on CETP [34]. Furthermore, HDL involves in the RCT pathway through lipid exchange with other apolipoproteins.

Immunochemistry confirms that both ABCA1 and ABCG1 are localized to the ganglion cell layer, outer plexiform layer, and RPE in the retina from primates, suggesting that RCT is an HDL-based intraretinal lipid transport. ABCA1 seems to localize more intensively to the apical side of the RPE, while ABCG1 localizes to the basal side. ABCA1 or ABCG1 is 1.4- or 2.5-folds greater in the human retina than in the liver [35]. Moreover, ABCA1, localized on both sides of the retinal epithelial cells, is modulated by LXR *in vitro* [36, 37]. However, it remains to be confirmed that the inducer LXR and the impaired ABCA1 and/or ABCG1 contribute to lipid efflux and subsequently lead to DR.

2.3.3. LXR and Apolipoprotein Profiles. Blood lipids, including triglycerides, cholesterol, and lipids (phospholipids, glycolipids, and steroids), are insoluble in water and are mainly transported in the form of lipoproteins. Lipoproteins are mainly classified into chylomicrons (CM), very low-density lipoprotein (VLDL), low-density lipoprotein (LDL), and high-density lipoprotein (HDL) particles. The main function of HDL is to participate in the reverse transport of cholesterol. The protein part of the plasma lipoproteins is called apolipoprotein, which is divided into the following five types and several subclasses: apolipoprotein A (apoA1, apoA2, apoA4, and apoA5), apoB (apoB48 and apoB100), apoC (apoC-I, apoC-II, apoC-III, and apoC-IV), apoD, apoE, apoF, apoH, apoL, apoM, and apolipoprotein (a).

Different lipoproteins contain different apolipoproteins that carry lipids and stabilize the lipoprotein structure. Also, certain apolipoproteins possess key enzyme activities that regulate lipoprotein metabolism and participate in lipoprotein receptor recognition. LXR is considered the key regulatory target of lipid metabolism and can directly or indirectly regulate *apo* mRNA expression, protein synthesis and secretion, and apolipoprotein-mediated cholesterol outflow [38, 39]. Following LXR activation by an agonist, cholesterol efflux is promoted through the RCT pathway and is taken up by apoA-I and apoE to form new HDL molecules, which enter the visceral liver for further transformation and/or decomposition [40].

apoA-I is mainly secreted by the liver and small intestine and is the main structural protein and responsible for the major functions of HDL. apoA-I, a 28 kDa single-chain polypeptide consisting of 243 amino acid residues, possess antioxidant, anti-inflammatory, and antiatherosclerotic activity [41]. apoA-I participates in intracellular cholesterol efflux with ABCA1 [42] to transport blood cholesterol to the liver [43]. apoA4 is a major protein component of lymph chylomicrons, VLDL, and HDL. Both apoA-I and apoA4, essential for lipoprotein metabolism to maintain plasma lipid levels, are modulators of vascular disease [44].

apoA1 can be upregulated by LXR dependent or independent of ABCA1. Endogenous ABC1 gene expression and apolipoprotein A1-mediated cholesterol efflux are upregulated via both receptor ligands, indicating that activation of the LXR-RXR heterodimer by ligands contributes to

the ABCA1 pathway therapeutic modulation [9]. The LXR agonist GW3965 has also been shown to increase apoA1 expression independent of ABCA1; apoA1 participates in brain-blood barrier regulation and serves to integrate peripheral and CAN lipid metabolism [25].

apoB is a major component protein of LDL, very low-density lipoprotein (VLDL), intermediate-density lipoprotein (IDL), chylomicrons, and LDL. apoB plays a significant role in lipoprotein transport. Plasma levels of apoB and LDL were increased by IDOL (the E3 ubiquitin ligase) which was induced by a synthetic LXR agonist in a nonhuman primate model [45]. Intracellular trafficking of the apical apolipoprotein B was also downregulated by LXR agonists to lower the risk of cardiovascular disorders and T2DM in an *in vitro* model [46].

Liver secreted apoE in lipid metabolism after entering circulation. apoE is also mainly synthesized in the astrocytes in the brain. apoE has three major allies: *apoE-ε2* (cys112, cys158), *apoE-ε3* (cys112, arg158), and *apo-ε4* (arg112, arg158). *apoE-ε2* has both increased and decreased risk for atherosclerosis [47]. *apoE-ε3* has been thought to be the "neutral" *apoE* genotype; *apo-ε4* was reported to be involved in the pathogenesis of atherosclerosis [47] and Alzheimer's diseases [48]. LXR directly regulates *apoE* gene expression in macrophages to control its expression [38]. apoE plays an antiatherosclerotic effect by cooperating with specific apolipoproteins, maybe *via* maintaining the stability of ABCA1. apoE4 is an independent risk factor for Alzheimer's disease [49].

apoD in the formation of HDL is positively regulated by LXR *via* reverse transport of cholesterol by promoting cholesterol esterification. apoM is mainly synthesized by the liver and kidneys to regulate the formation of pre-β-HDL *via* reverse cholesterol transport [50]. apoM also modulates the expression of inflammatory factors and adhesion molecules [49].

Although apoC-II and apoC-III have been implicated in cardiovascular diseases and DM, few literatures reported their link to the RCT pathway. It is interesting to investigate the correlations between other apo members and LXR in future studies.

2.3.4. LXR and Cholesterol Transport under Normal Physiological Conditions. LXR activation promotes cholesterol efflux in cells. In the presence of excess intracellular cholesterol, cholesterol oxidation derivatives activate the LXR/RXR heterodimer, initiate the target gene transcription, increase the protein expression of ABCA1 and ABCG1 on the cell membrane, and promote the excretion of cholesterol from the cell. In addition, LXR indirectly inhibits cholesterol synthesis and small intestine absorption *via* activating the transcriptional expression of its downstream genes. Cholesterol is synthesized in hepatocytes using Acetyl-CoA. This process is inversely regulated by the RCT pathway *via* inhibiting the expression of the key enzyme squalene synthase [51]. Following LXR activation, *ABCA1*, *ABCG5*, and *ABCG8* are upregulated to reduce cholesterol absorption in the small intestine. In addition, LXR activation also promotes liver cholesterol conversion and efflux to maintain the whole-body cholesterol level because the liver is the main organ to be used for cholesterol excretion. Cholesterol is converted into bile acids and excreted in the liver using cholesterol 7α hydroxylase (CY7PA). Activated LXR upregulates the expression levels of ABCG5 and ABCG8 and promotes the secretion and/or excretion of hepatobiliary cholesterol.

3. Cholesterol Metabolism in the Retina

Cholesterol metabolism in the retina includes uptake from the systemic circulation, self-synthesis, and clearance. However, the underlying mechanism is not fully understood. The blood-retinal barrier and blood-brain barrier are the unique structures that represent a functional interface between the bloodstream and neuronal vascular microenvironment, respectively. Cholesterol derived from the brain and retina is mainly found in the form of nonesterified cholesterol, suggesting that the retina may maintain cholesterol metabolism balance in a similar way to that of the brain. Current research indicates that the cholesterol in the brain all relies on its own synthesis and that cholesterol is not obtained from systemic circulation [52]. Previous studies have rarely examined cholesterol metabolism in the retina, and very little is known regarding the balance of cholesterol metabolism in the neuroretina. Cholesterol is found to be synthesized in the retina using radioactive cholesterol precursors and immunohistochemically labelled cholesterol synthesis rate-limiting enzyme HMGCR in rats [53]. Specific compounds were shown to inhibit the last step of cholesterol synthesis which leads to degradation of 7-dehydrocholesterol, suggesting that a large amount of cholesterol precursors is accumulated in the retina [54]. Furthermore, reduction of the cholesterol levels is found to be accompanied by progressive retinal degeneration, suggesting that the retinal tissue requires cholesterol metabolism balance *via* endogenous cholesterol synthesis in order to maintain the normal structure and function of the retina.However, a controversial finding is also reported, showing that cholesterol synthesis does not occur in the retina by itself but from the systemic circulation. Cholesterol enters the retinal neuroepithelial layer through the RPE layer. Fluorescently labelled cholesterol was detected in the RPE layer, and a small amount of fluorescence is presented in the neural retina following injection of fluorescently labelled low-density lipoproteins in the rhesus monkeys [55]. The strong signal of fluorescently labelled LDL is detected in the RPE layer of the retina and then is found to be gradually spread in the entire retina [56]. Only a small amount of fluorescent label is detected in the HDL cholesterol group. Such finding further illustrates that RPE and neural retinas could rapidly take up cholesterol from the systemic circulation, suggesting that LDL may be an important transporter that uptakes systemic cholesterol to the retina.

4. Correlation between Cholesterol Metabolism, Diabetes, and Diabetic Retinopathy

Elevated serum LDL-C and reduced HDL-C levels are high-risk factors for cardiovascular disease, whereas it has also been shown that excessive cholesterol concentration leads to hypercholesterolemia. Dyslipidemia with microvascular complications has been intensively investigated [57]. However, the

associations between traditional lipid markers and DR remain controversial. The full understanding and recognition of the importance of lipid-lowering treatment are considered important for the tertiary prevention of diabetes microvascular complications [58, 59].

The mechanism of dyslipidemia promotion may be at several certain levels. The retinal-specific lipid metabolism contributes to low-grade inflammation resulting in diabetic BRB breakdown [60]. Furthermore, the number of bone marrow-derived (BMD) circulating angiogenic cells (CACs) is decreased in dyslipidemia. Action to Control Cardiovascular Risk in Diabetes found the associations between blood lipid levels and hard retinal exudation [61–63]. The total serum cholesterol or the LDL-C of the patients is increased at baseline, and retinal hard exudation is more likely to occur in the Early Treatment Diabetic Retinopathy Study (ETDRS) [64]. Klein and colleagues evaluate the correlations between the serum level of blood lipids in a five-year followed up cohort. A correlation between DR and the total cholesterol/HDL-C ratio is found, confirming that cholesterol-lowering treatment may delay DR progression [65]. The Hoorn study [66] evaluates the risk factors for DR in 2484 Caucasians aged between 50 and 74 years. The results demonstrate that the prevalence of DR is positively associated with body mass index (BMI), serum cholesterol, and triglyceride levels. In addition, elevated levels of plasma total cholesterol and LDL-C are associated with the occurrence and development of retinal hard exudation. To evaluate the risk factors for diabetic microvascular and macrovascular complications, Nazimek-Siewniak and colleagues [67] investigate the associations between the serum levels of fasting blood glucose, total cholesterol, triglycerides, blood pressure, and BMI with the development of DR in 2175 newly diagnosed type 2 diabetes patients. It is found that elevated total cholesterol significantly increased the risk of developing proliferative retinopathy in diabetic patients. Hadjadj et al. report that high triglycerides are independent predictors of renal and retinal complications in patients with type 1 diabetes without end-stage renal disease [68].

It is further reported by the Diabetes Control and Complications Trial (DCCT) that the total HDL-C ratio and LDL-C concentration are predictors for the development of CSME and hard exudation. Hyperlipidemia may increase the risk of CSME and hard retinal exudation, whereas lipid-lowering treatment in patients with type 1 diabetes may reduce the risk of CSME [69]. On the other hand, LDL is found to be an independent risk factor for DR [70], which is in line with the findings compared with simvastatin alone. HDL-C correlates negatively with the occurrence of DR, PDR, and DME in a cohort study in patients with T2DM [71].

Although traditional lipid profiles are found to be associated with the pathogenesis of DR, the conclusive link is still controversial. The correlation between the serum level of total cholesterol and HDL with DR and retinal hard exudative was not found associated with the serum level of total cholesterol and HDL by the Wisconsin Epidemiological Study of Diabetic Retinopathy (WESDR) [72]. The FIELD study [54] enrolled a total of 9995 T2DM patients aged from 50 to 75 years. The patients are followed up for 5 years to evaluate whether long-term use of fenofibrate, the peroxisome proliferator-activated receptor alpha agonist lipid-lowering therapy, could reduce DR progression and the number of laser treatments. The participants receiving fenofibrate (200 mg/d) exhibited a 31% reduction of reduced incidence of DR or progressed to DME in the first laser treatment requirements compared with the placebo group. The Action to Control Cardiovascular Risk in Diabetes (ACCORD) trial is a randomized, multicenter study. Among the 10,251 middle-aged and older participants with T2MD, a subgroup of 2856 subjects were evaluated for the effects of the intensive or standard treatment for glycemia, dyslipidemia, or systolic blood-pressure control at 4 years on the progression of DR. The results showed that at 4 years, the rate of progression of DR was 6.5% with fenofibrate in comparison with 10.2% of the placebo [73]. However, no conclusive relationship between the lipid effects of fenofibrate and the presence or progression of DR was found in both FIELD and ACCORD studies; Wong et al. suggested that the beneficial effects of fenofibrate on DR may be through regulating the levels of apos [74]. Hadjadj et al. also found that apoA1 is correlated negatively with DR, while apoB and apoB/apoA1 ratios are correlated positively with DR [68], which is consistent with others, showing that serum apoB and apoB/apoA ratios are the most important risk factors for PDR and CSME [59].In summary, current guidelines suggest that the use of lipid-lowering drugs as adjuvant therapy can control diabetes-related microvascular complications [58, 75]. However, in certain large epidemiological studies, such as DCCT, EDIC, and WESDR, there is no direct association between the progression of DR and the levels of peripheral blood lipids. It is speculated that retinal-specific mechanisms may play an important role in the progression of DR caused by cholesterol [76], which remains to be clarified in the future. Although several researchers suggest that LDL, HDL, and apo are related to DR in varying degrees, no clear markers exist for the prediction of the occurrence and development of DR. Further research on the association between dyslipidemia and DR could provide additional evidence for the prevention of the development DR. More recently, the application of the nontraditional lipid marker apo has been continuously explored in the detection of lipid-associated disease, and it is expected that further breakthroughs will be achieved in the near future.

5. LXR and Diabetic Retinopathy

LXR is not only involved in the regulation of lipid metabolism but also considered a part of the insulin signaling pathway, which is involved in the process of glucose metabolism [22]. Activation of LXR regulates the systemic inflammatory response by promoting cholesterol metabolism and inhibiting the inflammatory response. LXRβ polymorphisms with type 2 diabetes mellitus and obesity are also evidenced recently [77]. Figure 1 summarizes the effects of the LXR pathway and LXR agonist in the pathogenesis of DR.

It is speculated that LXR may participate in the development of DR through the following mechanisms (Figure 2).

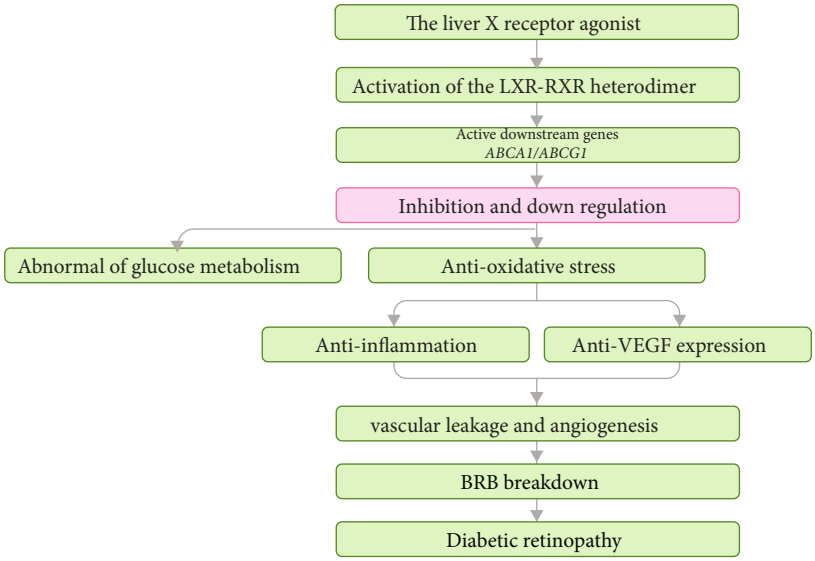

Figure 2: The liver X receptor agonist and diabetic retinopathy. This flow diagram illustrates the regulatory mechanism of activation of LXR signaling by the LXR agonist in DR. LXR: liver X receptor; BRB: blood-retinal breakdown; RXR: retinoid X receptor; DR: diabetic retinopathy.

5.1. Regulation of Glucose Metabolism. LXR participates in the regulation of lipid metabolism and acts as an insulin sensitizer, playing a significant role in glucose metabolism. LXR can be activated with glucose in the liver, which is an endogenous ligand of LXR [78]. Furthermore, LXR inhibits endogenous glucose production, converts excess glucose to glycogen or fatty acids, and stores these molecules in the adipose tissue [79]. Glucose transporter GLUT4 plays a key role in insulin-mediated glucose uptake in adipose tissues. Impairment of GLUT4 is associated with obesity and type 2 diabetes. The promoter of GLUT4 is a direct target gene of LXR. LXR agonists upregulate GLUT4 in adipocytes and promote peripheral glucose uptake [9]. In animal models of diabetes, the LXR agonists GW-3965 and T0901317 significantly reduce blood glucose levels in hyperglycemic mice, improving insulin sensitivity, inhibiting the hepatic synthesis of glycogen, and reducing glucose output [80, 81]. In summary, as a transcription switch, LXR integrates glucose metabolism and lipid metabolism and may be involved in the development of DR.

5.2. Anti-inflammation. Inflammation and oxidative stress are considered important pathological mechanisms of DR. Increased retinal or systemic inflammatory factors in DR patients or animals are reported. Oxidative stress is responsible for the inhibition of inflammation and oxidative stress, which prevents the development of DR significantly [82, 83]. Because activation of LXR inhibits inflammatory response *via* promoting cholesterol metabolism, LXR is considered to be one of the key receptors that regulate systemic inflammation [13, 84]. Anti-inflammatory mechanisms of LXR include transrepression, posttranscriptional level regulation, and inhibition of inflammatory factor expression via regulating lipid metabolism. Activation of LXR inhibits the activity of transcription factors, such as NF-κB, to block NF-κB-dependent inflammatory factors [85], regulating the expression of inflammatory factors via posttranscriptional mechanisms. Activation of LXR further inhibits the expression levels of the inflammatory factors *via* regulating lipid metabolism [86]. This is supported by the finding that oral administration of LXR agonists significantly prevents DR development and reduces inflammatory cells in the retina via downregulating oxidative stress genes in an STZ-induced diabetic model [13]. LXR is also found to normalize reverse cholesterol transport and prevent diabetes-induced inflammation in retinal cells. Activation of LXR reduces the number of pro-inflammatory macrophages and prevented DR-like pathology. The aforementioned findings suggest that LXR agonists may prevent diabetic vascular disease by inhibiting the inflammatory response and oxidative stress.

5.3. Inhibition of Angiogenesis. Vascular endothelial growth factor (VEGF) is a specific mitogenic protein secreted by endothelial cells, with the VEGF family of VEGF-A, B, C, D, and E and placental growth factor (PlGF). These VEGFs activate the downstream cascade after binding to VEGF receptors (VEGFR-1, VEGFR-2, and VEGFR-3).

VEGF-A is the most abundant and biologically active form among the VEGF family in tissues. Upregulation of VEGF in retinal vascular endothelial cells leads to an increase in the permeability of capillaries, which subsequently breaks down the blood-retinal barrier and acceleration of neovascularization and eventually exacerbates the progression of DR [87].

LXR agonists improve cholesterol metabolism and inhibit human umbilical vein vascular endothelial cell proliferation and migration, as well as formation of luminal structures *via* downregulating VEGF2 l [88]. Activation of the LXR receptor is found to suppress angiogenesis via induction of apoD in human umbilical vein endothelial cells [89]. It is also found that LXR activation reduces angiogenesis by impairing lipid raft localization and signaling of VEGF receptor 2. Furthermore, VEGF-A can be upregulated in the presence of LDL, suggesting that VEGF-A synergizes the

effects of LDL contributing to the progression of atherosclerosis [90]. Therefore, further exploration of the association between VEGF expression, LXR pathway, and cholesterol metabolism may aid the identification of new targets for DR intervention.

6. LXR Agonist Modulates Diabetic Retinopathy Pathophysiology

LXR has been proved to be the novel therapeutic target in both animal models and humans. Synthetic oxysterol as the gene-selective LXR modulator mediates transcriptional activation of ABCA1 gene expression with minimal effects on SREBP-1c both in vitro and in vivo in mice [91]. Selective LXRα and LXRβ increased HDL cholesterol and increased liver triglycerides in wild-type mice, induced ABCA1 expression, and stimulated cholesterol efflux in macrophages from both LXRα- and LXRβ-deficient mice [92].

Synthetic chemical agonists of LXT have been shown efficacious for inhibition of DR in diabetic animal models. However, due to the adverse effect profile, including hypertriglyceridemia and hepatic steatosis, the trials were halted [93, 94]. N,N-Dimethyl-3β-hydroxy-cholenamide (DMHCA) is a synthetic oxysterol with shortened sidechain and amide moiety which exhibits only limited activity for increasing hepatic SREBP-1c mRNA and does not stimulate triglyceride synthesis and alter circulating plasma triglycerides in comparison with known nonsteroidal LXR agonists [95]. Cell-based studies also indicate that this selective modulator inhibits cholesterol accumulation. DMHCA has been shown to rescue retinal and BM dysfunction in diabetes, thereby restoring retinal structure, function, and cholesterol homeostasis [95]. DMHCA has been tested in patients with advanced solid malignancies and lymphoma and with refractory malignancies [96].

There are also several ongoing clinical trials of DMHCA targeting on DR. An observational study is being carried out to investigate if LXR activation can restore cholesterol homeostasis in the diabetic retina and rescue diabetes-induced bone marrow dysfunction to sustain circulating angiogenic cells (CAC) and macrophages (ClinicalTrials.gov Identifier: NCT03403686).

7. Perspective

Previous studies have confirmed an inextricable link between abnormal cholesterol metabolism and the development of DR. Further research on lipid metabolites, such as the identification of cholesterol and nontraditional lipid markers, will aid the clarification of their role in disease development and provide new intervention directions for the preventive diagnosis and treatment of DR. All of this is expected to become a novel research hotspot with regard to the prevention and treatment of DR.

In summary, the current literature suggests that the RCT pathway plays an important role in the process of cholesterol metabolism. Recently, several studies have examined the interaction of LXR thoroughly with its agonists in an attempt to provide potential directions for clinical transformation. At present, a variety of artificial LXR agonists have been synthesized. However, since LXR agonists are applied to the whole body, they may upregulate SREBP-1c expression and produce related undesired adverse reactions, including induction of adipogenesis, hypertriglyceridemia, and liver steatosis. Although there are no safe and effective LXR agonists for clinical application yet, the development of LXR selective receptor agonists might promote the identification of novel LXR agonists that do not alter liver and plasma triglyceride levels. LXR agonists could be tailored therapeutical targets in the treatment of DR and other diseases with abnormal cholesterol metabolism in the near future.

Abbreviations

ABCA1: ATP-binding cassette subfamily A member 1
ABCG1: ATP-binding cassette subfamily G member 1
ACCORD: Action to Control Cardiovascular Risk in Diabetes
Apo: Apolipoproteins
BMD: Bone marrow-derived
BMI: Body mass index
CAC: Circulating angiogenic cells
CETP: Cholesterol ester transfer protein
CM: Chylomicrons
CSME: Clinical significant macular edema
CY7PA: Cholesterol 7α hydroxylase
DMHCA: N-Dimethyl-3β-hydroxy-cholenamide
DR: Diabetic retinopathy
ETDRS: Early Treatment Diabetic Retinopathy Study
GLUT4: Glucose transporter type 4
HDL: High-density lipoprotein
LDL: Low-density lipoprotein
LXR: Liver X receptor
PlGF: Placental growth factor
RCT: Cholesterol reverse transport
RXR: Retinoid X receptor
VEGF: Vascular endothelial growth factor
VEGFR: VEGF receptors
VLDL: Very low-density lipoprotein
WESDR: Wisconsin Epidemiological Study of Diabetic Retinopathy.

Data Availability

This review did not include any original data.

Conflicts of Interest

All authors declare that the research was conducted in the absence of any commercial or financial relationships that could be construed as a potential conflict of interest.

Acknowledgments

This work is supported by the National Natural Science Foundation of China (Grant 81570850, Grant 81170859, and grant 82070988) and the Ministry of Science and Technology Foundation of China (Grant 2016YFC1305604).

References

[1] P. L. Yeagle, "Modulation of membrane function by cholesterol," *Biochimie*, vol. 73, no. 10, pp. 1303–1310, 1991.

[2] A. H. Payne and D. B. Hales, "Overview of steroidogenic enzymes in the pathway from cholesterol to active steroid hormones," *Endocrine Reviews*, vol. 25, no. 6, pp. 947–970, 2004.

[3] J. P. Incardona and S. Eaton, "Cholesterol in signal transduction," *Current Opinion in Cell Biology*, vol. 12, no. 2, pp. 193–203, 2000.

[4] E. Czuba, A. Steliga, G. Lietzau, and P. Kowiański, "Cholesterol as a modifying agent of the neurovascular unit structure and function under physiological and pathological conditions," *Metabolic Brain Disease*, vol. 32, no. 4, pp. 935–948, 2017.

[5] M. S. Brown and J. L. Goldstein, "Receptor-mediated control of cholesterol metabolism," *Science*, vol. 191, no. 4223, pp. 150–154, 1976.

[6] J. L. Betters and L. Yu, "NPC1L1 and cholesterol transport," *Febs Letters*, vol. 584, no. 13, pp. 2740–2747, 2010.

[7] H. Zhou, K. C. B. Tan, S. W. M. Shiu, and Y. Wong, "Cellular cholesterol efflux to serum is impaired in diabetic nephropathy," *Diabetes/Metabolism Research and Reviews*, vol. 24, no. 8, pp. 617–623, 2008.

[8] R. Ohashi, H. Mu, X. Wang, Q. Yao, and C. Chen, "Reverse cholesterol transport and cholesterol efflux in atherosclerosis," *Qjm*, vol. 98, no. 12, pp. 845–856, 2005.

[9] B. A. Laffitte, L. C. Chao, J. Li et al., "Activation of liver X receptor improves glucose tolerance through coordinate regulation of glucose metabolism in liver and adipose tissue," *Proceedings of the National Academy of Sciences of the United States of America*, vol. 100, no. 9, pp. 5419–5424, 2003.

[10] C. Hong and P. Tontonoz, "Liver X receptors in lipid metabolism: opportunities for drug discovery," *Nature Reviews Drug Discovery*, vol. 13, no. 6, pp. 433–444, 2014.

[11] D. J. Peet, B. A. Janowski, and D. J. Mangelsdorf, "The LXRs: a new class of oxysterol receptors," *Current Opinion in Genetics & Development*, vol. 8, no. 5, pp. 571–575, 1998.

[12] B. Balasubramanian, H.-J. Kim, R. A. Mothana, Y. O. Kim, and N. A. Siddiqui, "Role of LXR alpha in regulating expression of glucose transporter 4 in adipocytes – Investigation on improvement of health of diabetic patients," *Journal of Infection and Public Health*, vol. 13, no. 2, pp. 244–252, 2020.

[13] S. Hazra, A. Rasheed, A. Bhatwadekar et al., "Liver X receptor modulates diabetic retinopathy outcome in a mouse model of streptozotocin-induced diabetes," *Diabetes*, vol. 61, no. 12, pp. 3270–3279, 2012.

[14] P. J. Willy, K. Umesono, E. S. Ong, R. M. Evans, R. A. Heyman, and D. J. Mangelsdorf, "LXR, a nuclear receptor that defines a distinct retinoid response pathway," *Genes & Development*, vol. 9, no. 9, pp. 1033–1045, 1995.

[15] T. Jakobsson, E. Treuter, J.-Å. Gustafsson, and K. R. Steffensen, "Liver X receptor biology and pharmacology: new pathways, challenges and opportunities," *Trends in Pharmacological Sciences*, vol. 33, no. 7, pp. 394–404, 2012.

[16] L. Zhou, H. Y. Choi, W.-P. Li, F. Xu, and J. Herz, "LRP1 controls cPLA2 phosphorylation, ABCA1 expression and cellular cholesterol export," *PLoS One*, vol. 4, no. 8, article e6853, 2009.

[17] S. L. Sabol, H. B. Brewer Jr., and S. Santamarina-Fojo, "The human ABCG1 gene: identification of LXR response elements that modulate expression in macrophages and liver," *Journal of Lipid Research*, vol. 46, no. 10, pp. 2151–2167, 2005.

[18] T. Yoshikawa, H. Shimano, M. Amemiya-Kudo et al., "Identification of liver X receptor-retinoid X receptor as an activator of the sterol regulatory element-binding protein 1c gene promoter," *Molecular & Cellular Biology*, vol. 21, no. 9, pp. 2991–3000, 2001.

[19] S. B. Joseph, B. A. Laffitte, P. H. Patel et al., "Direct and Indirect Mechanisms for Regulation of Fatty Acid Synthase Gene Expression by Liver X Receptors," *Journal of Biological Chemistry*, vol. 277, no. 13, pp. 11019–11025, 2002.

[20] E. P. Ratliff, A. Gutierrez, and R. A. Davis, "Transgenic expression of CYP7A1 in LDL receptor-deficient mice blocks diet-induced hypercholesterolemia," *Journal of Lipid Research*, vol. 47, no. 7, pp. 1513–1520, 2006.

[21] P. A. Mak, B. A. Laffitte, C. Desrumaux et al., "Regulated Expression of the Apolipoprotein E/C-I/C-IV/C-II Gene Cluster in Murine and Human Macrophages:," *Journal of Biological Chemistry*, vol. 277, no. 35, pp. 31900–31908, 2002.

[22] A. M. L. Pettersson, B. M. Stenson, S. Lorente-Cebrián et al., "LXR is a negative regulator of glucose uptake in human adipocytes," *Diabetologia*, vol. 56, no. 9, pp. 2044–2054, 2013.

[23] P. A. Edwards, M. A. Kennedy, and P. A. Mak, "LXRs;: Oxysterol-activated nuclear receptors that regulate genes controlling lipid homeostasis," *Vascular pharmacology*, vol. 38, no. 4, pp. 249–256, 2002.

[24] J. J. Repa, K. E. Berge, C. Pomajzl, J. A. Richardson, H. Hobbs, and D. J. Mangelsdorf, "Regulation of ATP-binding Cassette Sterol Transporters ABCG5 and ABCG8 by the Liver X Receptors α and β," *Journal of Biological Chemistry*, vol. 277, no. 21, pp. 18793–18800, 2002.

[25] Y.-F. Hong, H. Kim, H. S. Kim, W. J. Park, J. Y. Kim, and D. K. Chung, "Lactobacillus acidophilus K301 inhibits atherogenesis via induction of 24 (S), 25-epoxycholesterol-mediated ABCA1 and ABCG1 production and cholesterol efflux in macrophages," *PLoSOne*, vol. 11, no. 4, article e0154302, 2016.

[26] J. Fan, R. Q. Zhao, C. Parro et al., "Small molecule inducers of ABCA1 and apoE that act through indirect activation of the LXR pathway," *Journal of Lipid Research*, vol. 59, no. 5, pp. 830–842, 2018.

[27] P. Seeree, T. Janvilisri, T. Kangsamaksin, R. Tohtong, and S. Kumkate, "Downregulation of ABCA1 and ABCG1 transporters by simvastatin in cholangiocarcinoma cells," *Oncology Letters*, vol. 18, no. 5, pp. 5173–5184, 2019.

[28] M. Thiriet, *Hyperlipidemias and obesity*, 2018.

[29] A. M. Vaughan and J. F. Oram, "ABCG1 redistributes cell cholesterol to domains removable by high density lipoprotein but not by lipid-depleted apolipoproteins," *Journal of Biological Chemistry*, vol. 280, no. 34, pp. 30150–30157, 2005.

[30] T. Langmann, J. Klucken, M. Reil et al., "Molecular cloning of the human ATP-binding cassette transporter 1 (hABC1): evidence for sterol-dependent regulation in macrophages," *Biochemical & Biophysical Research Communications*, vol. 257, no. 1, pp. 29–33, 1999.

[31] H. H. Hassan, M. Denis, L. Krimbou, M. Marcil, and J. Genest, "Homeostasie cellulaire du cholesterol dans les cellules endotheliales vasculaires," *Canadian Journal of Cardiology*, vol. 22, Supplement B, pp. 35B–40B, 2006.

[32] N. Terasaka, S. Yu, L. Yvan-Charvet et al., "ABCG1 and HDL protect against endothelial dysfunction in mice fed a high-cholesterol diet," *Journal of Clinical Investigation*, vol. 118, no. 11, pp. 3701–3713, 2008.

[33] L. Rohrer, P. M. Ohnsorg, M. Lehner, F. Landolt, F. Rinninger, and A. von Eckardstein, "High-density lipoprotein transport through aortic endothelial cells involves scavenger receptor BI and ATP-binding cassette transporter G1," *Circulation Research*, vol. 104, no. 10, pp. 1142–1150, 2009.

[34] E. A. Fisher, J. E. Feig, B. Hewing, S. L. Hazen, and J. D. Smith, "High-density lipoprotein function, dysfunction, and reverse cholesterol transport," *Arteriosclerosis, Thrombosis, and Vascular Biology*, vol. 32, no. 12, pp. 2813–2820, 2012.

[35] J. W. Lee, E. F. Moreira, and I. R. Rodriguez, "Oxysterols induce the expression of ABCA1 and ABCG1 in cultured RPE cells," *Investigative Ophthalmology & Visual Science*, vol. 49, no. 13, 2008.

[36] F. Storti, G. Raphael, V. Griesser et al., "Regulated efflux of photoreceptor outer segment-derived cholesterol by human RPE cells," *Experimental Eye Research*, vol. 165, pp. 65–77, 2017.

[37] F. Storti, K. Klee, V. Todorova et al., "Impaired ABCA1/ABCG1-mediated lipid efflux in the mouse retinal pigment epithelium (RPE) leads to retinal degeneration," *Elife*, vol. 8, article e45100, 2019.

[38] B. A. Laffitte, J. J. Repa, S. B. Joseph et al., "LXRs control lipid-inducible expression of the apolipoprotein E gene in macrophages and adipocytes," *Proceedings of the National Academy of Sciences of the United States of America*, vol. 98, no. 2, pp. 507–512, 2001.

[39] N. Zelcer and P. Tontonoz, "Liver X receptors as integrators of metabolic and inflammatory signaling," *Journal of Clinical Investigation*, vol. 116, no. 3, pp. 607–614, 2006.

[40] V. I. Zannis, A. Chroni, and M. Krieger, "Role of apoA-I, ABCA1, LCAT, and SR-BI in the biogenesis of HDL," *Journal of Molecular Medicine*, vol. 84, no. 4, pp. 276–294, 2006.

[41] H. Saito, P. Dhanasekaran, D. Nguyen et al., "α-Helix Formation Is Required for High Affinity Binding of Human Apolipoprotein A-I to Lipids," *Journal of Biological Chemistry*, vol. 279, no. 20, pp. 20974–20981, 2004.

[42] J. Ribalta, J.-C. Vallvé, J. Girona, and L. Masana, "Apolipoprotein and apolipoprotein receptor genes, blood lipids and disease," *Current Opinion in Clinical Nutrition & Metabolic Care*, vol. 6, no. 2, pp. 177–187, 2003.

[43] L. Zhu, M. Parker, N. Enemchukwu et al., "Combination of apolipoprotein-A-I/apolipoprotein-A-I binding protein and anti-VEGF treatment overcomes anti-VEGF resistance in choroidal neovascularization in mice," *Communications Biology*, vol. 3, no. 1, p. 386, 2020.

[44] A. Uchida, S. K. Srivastava, D. Manjunath et al., "Impact of Drusen burden on incidence of subclinical CNV with OCTA," *Ophthalmic Surgery, Lasers Imaging Retina*, vol. 51, no. 1, pp. 22–30, 2020.

[45] S. D. Lee and P. Tontonoz, "Liver X receptors at the intersection of lipid metabolism and atherogenesis," *Atherosclerosis*, vol. 242, no. 1, pp. 29–36, 2015.

[46] O. Briand, V. Touche, S. Colin et al., "Liver X Receptor Regulates Triglyceride Absorption Through Intestinal Downregulation of Scavenger Receptor Class B, Type 1," *Gastroenterology*, vol. 150, no. 3, pp. 650–658, 2016.

[47] J. Davignon, R. E. Gregg, and C. F. Sing, "Apolipoprotein E polymorphism and atherosclerosis," *Arteriosclerosis*, vol. 8, no. 1, pp. 1–21, 1988.

[48] E. H. Corder, A. M. Saunders, W. J. Strittmatter et al., "Gene dose of apolipoprotein E type 4 allele and the risk of Alzheimer's disease in late onset families," *Science*, vol. 261, no. 5123, pp. 921–923, 1993.

[49] Y. Cheng, J. Li, Z. Shuai, and S. Xiaochuan, "Apo E4 influences growth cone of neuronal axon through ERK signal pathway," *Journal of Third Military Medical University*, vol. 34, 2012.

[50] C.-I. Lin, C.-N. Chen, P.-W. Lin, and H. Lee, "Sphingosine 1-phosphate regulates inflammation-related genes in human endothelial cells through $S1P_1$ and $S1P_3$," *Biochemical & Biophysical Research Communications*, vol. 355, no. 4, pp. 895–901, 2007.

[51] Y. Wang, P. M. Rogers, C. Su, G. Varga, K. R. Stayrook, and T. P. Burris, "Regulation of Cholesterologenesis by the Oxysterol Receptor, LXRα," *Journal of Biological Chemistry*, vol. 283, no. 39, pp. 26332–26339, 2008.

[52] I. Björkhem and S. Meaney, "Brain cholesterol: long secret life behind a barrier," *Arteriosclerosis, Thrombosis, and Vascular Biology*, vol. 24, no. 5, pp. 806–815, 2004.

[53] S. J. Fliesler, R. Florman, L. M. Rapp, S. J. Pittler, and R. K. Keller, "In vivo biosynthesis of cholesterol in the rat retina," *Febs Letters*, vol. 335, no. 2, pp. 234–238, 1993.

[54] S. J. Fliesler, "Retinal degeneration in a rat model of Smith-Lemli-Opitz Syndrome: thinking beyond cholesterol deficiency," in *Retinal Degenerative Diseases*, vol. 664 of Advances in Experimental Medicine and Biology, , pp. 481–489, Springer, 2010.

[55] V. M. Elner, "Retinal pigment epithelial acid lipase activity and lipoprotein receptors: effects of dietary omega-3 fatty acids," *Transactions of the American Ophthalmological Society*, vol. 100, pp. 301–338, 2002.

[56] N. Tserentsoodol, J. Sztein, M. Campos et al., "Uptake of cholesterol by the retina occurs primarily via a low density lipoprotein receptor-mediated process," *Molecular Vision*, vol. 12, pp. 1306–1318, 2006.

[57] A. Misra, S. Kumar, N. Kishore Vikram, and A. Kumar, "The role of lipids in the development of diabetic microvascular complications: implications for therapy," *American Journal of Cardiovascular Drugs*, vol. 3, no. 5, pp. 325–338, 2003.

[58] A. Keech, P. Mitchell, P. Summanen et al., "Effect of fenofibrate on the need for laser treatment for diabetic retinopathy (FIELD study): a randomised controlled trial," *The Lancet*, vol. 370, no. 9600, pp. 1687–1697, 2007.

[59] R. Crosby-Nwaobi, I. Chatziralli, T. Sergentanis, T. Dew, A. Forbes, and S. Sivaprasad, "Cross talk between lipid metabolism and inflammatory markers in patients with diabetic retinopathy," *Journal of Diabetes Research*, vol. 2015, Article ID 191382, 9 pages, 2015.

[60] S. S. Hammer, E. Beli, N. Kady et al., "The mechanism of diabetic retinopathy pathogenesis unifying key lipid regulators, sirtuin 1 and liver X receptor," *EBioMedicine*, vol. 22, pp. 181–190, 2017.

[61] M. Sasaki, R. Kawasaki, J. E. Noonan, T. Y. Wong, E. Lamoureux, and J. J. Wang, "Quantitative measurement of hard exudates in patients with diabetes and their associations with serum lipid levels," *Investigative Ophthalmology & Visual Science*, vol. 54, no. 8, pp. 5544–5550, 2013.

[62] A. Gupta, V. Gupta, S. Thapar, and A. Bhansali, "Lipid-lowering drug atorvastatin as an adjunct in the management of diabetic macular edema," *American Journal of Ophthalmology*, vol. 137, no. 4, pp. 675–682, 2004.

[63] E. Papavasileiou, S. Davoudi, R. Roohipoor et al., "Association of serum lipid levels with retinal hard exudate area in African Americans with type 2 diabetes," *Graefe's Archive for Clinical*

and Experimental Ophthalmology, vol. 255, no. 3, pp. 509–517, 2017.

[64] E. Y. Chew, M. L. Klein, F. L. Ferris 3rd et al., "Association of elevated serum lipid levels with retinal hard exudate in diabetic retinopathy. Early Treatment Diabetic Retinopathy Study (ETDRS) report 22," *Archives of Ophthalmology*, vol. 114, no. 9, pp. 1079–1084, 1996.

[65] B. Klein, R. Klein, and S. Moss, "Is serum cholesterol associated with progression of diabetic retinopathy or macular edema in persons with younger-onset diabetes of long duration?," *American Journal of Ophthalmology*, vol. 128, no. 5, pp. 652–654, 1999.

[66] H. A. van Leiden, J. M. Dekker, A. C. Moll et al., "Blood pressure, lipids, and obesity are associated with retinopathy: the hoorn study," *Diabetes Care*, vol. 25, no. 8, pp. 1320–1325, 2002.

[67] B. Nazimek-Siewniak, D. Moczulski, and W. Grzeszczak, "Risk of macrovascular and microvascular complications in type 2 diabetes: results of longitudinal study design," *Journal of Diabetes & Its Complications*, vol. 16, no. 4, pp. 271–276, 2002.

[68] S. Hadjadj, B. Duly-Bouhanick, A. Bekherraz et al., "Serum triglycerides are a predictive factor for the development and the progression of renal and retinal complications in patients with type 1 diabetes," *Diabetes & Metabolism*, vol. 30, no. 1, pp. 43–51, 2004.

[69] B. Miljanovic, R. J. Glynn, D. M. Nathan, J. E. Manson, and D. A. Schaumberg, "A prospective study of serum lipids and risk of diabetic macular edema in type 1 diabetes," *Diabetes*, vol. 53, no. 11, pp. 2883–2892, 2004.

[70] T. Y. Wong, N. Cheung, W. T. Tay et al., "Prevalence and risk factors for diabetic retinopathy: the Singapore Malay Eye Study," *Ophthalmology*, vol. 115, no. 11, pp. 1869–1875, 2008.

[71] P. P. Toth, R. J. Simko, S. R. Palli, D. Koselleck, R. A. Quimbo, and M. J. Cziraky, "The impact of serum lipids on risk for microangiopathy in patients with type 2 diabetes mellitus," *Cardiovascular Diabetology*, vol. 11, no. 1, p. 109, 2012.

[72] B. E. Klein, S. E. Moss, R. Klein, and T. S. Surawicz, "The Wisconsin Epidemiologic Study of Diabetic Retinopathy: XIII. Relationship of Serum Cholesterol to Retinopathy and Hard Exudate," *Ophthalmology*, vol. 98, no. 8, pp. 1261–1265, 1991.

[73] ACCORD Study Group and ACCORD Eye Study Group, "Effects of medical therapies on retinopathy progression in type 2 diabetes," *New England Journal of Medicine*, vol. 363, no. 3, pp. 233–244, 2010.

[74] T. Y. Wong, R. Simó, and P. Mitchell, "Fenofibrate - a potential systemic treatment for diabetic retinopathy?," *American Journal of Ophthalmology*, vol. 154, no. 1, pp. 6–12, 2012.

[75] M. Elam, L. Lovato, and H. Ginsberg, "The ACCORD-lipid study: implications for treatment of dyslipidemia in type 2 diabetes mellitus," *Clinical Lipidology*, vol. 6, no. 1, pp. 9–20, 2011.

[76] M. B. Sasongko, T. Y. Wong, T. T. Nguyen et al., "Serum apolipoproteins are associated with systemic and retinal microvascular function in people with diabetes," *Diabetes*, vol. 61, no. 7, pp. 1785–1792, 2012.

[77] K. Solaas, V. Legry, K. Retterstol et al., "Suggestive evidence of associations between liver X receptor β polymorphisms with type 2 diabetes mellitus and obesity in three cohort studies: HUNT2 (Norway), MONICA (France) and HELENA (Europe)," *BMC Medical Genetics*, vol. 11, no. 1, p. 144, 2010.

[78] R. Grempler, S. Günther, K. R. Steffensen et al., "Evidence for an indirect transcriptional regulation of glucose-6-phosphatase gene expression by liver X receptors," *Biochemical & Biophysical Research Communications*, vol. 338, no. 2, pp. 981–986, 2005.

[79] N. Mitro, P. A. Mak, L. Vargas et al., "The nuclear receptor LXR is a glucose sensor," *Nature*, vol. 445, no. 7124, pp. 219–223, 2007.

[80] G. Cao, Y. Liang, C. L. Broderick et al., "Antidiabetic Action of a Liver X Receptor Agonist Mediated By Inhibition of Hepatic Gluconeogenesis," *Journal of Biological Chemistry*, vol. 278, no. 2, pp. 1131–1136, 2003.

[81] A. Grefhorst, T. H. van Dijk, A. Hammer et al., "Differential effects of pharmacological liver X receptor activation on hepatic and peripheral insulin sensitivity in lean and ob/ob mice," *American Journal of Physiology Endocrinology & Metabolism*, vol. 289, no. 5, pp. E829–E838, 2005.

[82] W. Zhang, H. Liu, M. al-Shabrawey, R. W. Caldwell, and R. B. Caldwell, "Inflammation and diabetic retinal microvascular complications," *Journal of Cardiovascular Disease Research*, vol. 2, no. 2, pp. 96–103, 2011.

[83] R. A. Kowluru, M. Kanwar, P.-S. Chan, and J. P. Zhang, "Inhibition of retinopathy and retinal metabolic abnormalities in diabetic rats with AREDS-based micronutrients," *Archives of ophthalmology*, vol. 126, no. 9, pp. 1266–1272, 2008.

[84] M. H. Faulds, C. Zhao, and K. Dahlman-Wright, "Molecular biology and functional genomics of liver X receptors (LXR) in relationship to metabolic diseases," *Current Opinion in Pharmacology*, vol. 10, no. 6, pp. 692–697, 2010.

[85] S. B. Joseph, A. Castrillo, B. A. Laffitte, D. J. Mangelsdorf, and P. Tontonoz, "Reciprocal regulation of inflammation and lipid metabolism by liver X receptors," *Nature Medicine*, vol. 9, no. 2, pp. 213–219, 2003.

[86] N. M. de Wit, J. Vanmol, A. Kamermans, J. J. A. Hendriks, and H. E. de Vries, "Inflammation at the blood-brain barrier: The role of liver X receptors," *Neurobiology of Disease*, vol. 107, pp. 57–65, 2017.

[87] P. Romero-Aroca, M. Baget-Bernaldiz, A. Pareja-Rios, M. Lopez-Galvez, R. Navarro-Gil, and R. Verges, "Diabetic macular edema pathophysiology: vasogenic versus inflammatory," *Journal of Diabetes Research*, vol. 2016, Article ID 2156273, 17 pages, 2016.

[88] A. Noghero, A. Perino, G. Seano et al., "Liver X receptor activation reduces angiogenesis by impairing lipid raft localization and signaling of vascular endothelial growth factor receptor-2," *Arteriosclerosis, Thrombosis, and Vascular Biology*, vol. 32, no. 9, pp. 2280–2288, 2012.

[89] C.-J. Lai, H.-C. Cheng, C.-Y. Lin et al., "Activation of liver X receptor suppresses angiogenesisviainduction of ApoD," *Faseb Journal Official Publication of the Federation of American Societies for Experimental Biology*, vol. 31, no. 12, pp. 5568–5576, 2017.

[90] A. M. Kivelä, M. H. Dijkstra, S. E. Heinonen et al., "Regulation of endothelial lipase and systemic HDL cholesterol levels by SREBPs and VEGF-A," *Atherosclerosis*, vol. 225, no. 2, pp. 335–340, 2012.

[91] E. M. Quinet, D. A. Savio, A. R. Halpern, L. Chen, C. P. Miller, and P. Nambi, "Gene-selective modulation by a synthetic oxysterol ligand of the liver X receptor," *Journal of Lipid Research*, vol. 45, no. 10, pp. 1929–1942, 2004.

[92] E. G. Lund, L. B. Peterson, A. D. Adams et al., "Different roles of liver X receptor α and β in lipid metabolism: Effects of an α-

selective and a dual agonist in mice deficient in each subtype," *Biochemical Pharmacology*, vol. 71, no. 4, pp. 453–463, 2006.

[93] J. W. Chisholm, J. Hong, S. A. Mills, and R. M. Lawn, "The LXR ligand T0901317 induces severe lipogenesis in the db/db diabetic mouse," *Journal of Lipid Research*, vol. 44, no. 11, pp. 2039–2048, 2003.

[94] T. G. Kirchgessner, P. Sleph, J. Ostrowski et al., "Beneficial and adverse effects of an LXR agonist on human lipid and lipoprotein metabolism and circulating neutrophils," *Cell Metabolism*, vol. 24, no. 2, pp. 223–233, 2016.

[95] C. P. Vieira, S. D. Fortmann, M. Hossain et al., "Selective LXR agonist DMHCA corrects retinal and bone marrow dysfunction in type 2 diabetes," *JCI Insight*, vol. 5, no. 13, article e137230, 2020.

[96] M. M. Mita, A. C. Mita, B. Chmielowski et al., "Pharmacodynamic and clinical activity of RGX-104, a first-in-class immunotherapy targeting the liver-X nuclear hormone receptor (LXR), in patients with refractory malignancies," *Journal of Clinical Oncology*, vol. 36, 15_suppl, pp. 3095–3095, 2018.

Hindawi
Journal of Diabetes Research
Volume 2021, Article ID 8766517, 10 pages
https://doi.org/10.1155/2021/8766517

Research Article

Segmentation of Laser Marks of Diabetic Retinopathy in the Fundus Photographs Using Lightweight U-Net

Yukang Jiang,[1,2] Jianying Pan,[1] Ming Yuan,[2] Yanhe Shen,[2] Jin Zhu,[2] Yishen Wang,[1] Yewei Li,[2] Ke Zhang,[2] Qingyun Yu,[2] Huirui Xie,[1] Huiting Li,[1] Xueqin Wang,[2,3,4] and Yan Luo[1]

[1]*State Key Laboratory of Ophthalmology, Image Reading Center, Zhongshan Ophthalmic Center, Sun Yat-Sen University, Guangzhou 510060, China*
[2]*Department of Statistical Science, School of Mathematics, Southern China Research Center of Statistical Science, Sun Yat-Sen University, Guangzhou 510275, China*
[3]*Department of Statistics and Finance, School of Management, University of Science and Technology of China, Hefei, Anhui 230026, China*
[4]*Xinhua College, Sun Yat-Sen University, Guangzhou 510520, China*

Correspondence should be addressed to Xueqin Wang; wangxq20@ustc.edu.cn and Yan Luo; luoyan2@mail.sysu.edu.cn

Received 29 May 2021; Revised 3 September 2021; Accepted 24 September 2021; Published 19 October 2021

Academic Editor: Honghua Yu

Diabetic retinopathy (DR) is a prevalent vision-threatening disease worldwide. Laser marks are the scars left after panretinal photocoagulation, a treatment to prevent patients with severe DR from losing vision. In this study, we develop a deep learning algorithm based on the lightweight U-Net to segment laser marks from the color fundus photos, which could help indicate a stage or providing valuable auxiliary information for the care of DR patients. We prepared our training and testing data, manually annotated by trained and experienced graders from Image Reading Center, Zhongshan Ophthalmic Center, publicly available to fill the vacancy of public image datasets dedicated to the segmentation of laser marks. The lightweight U-Net, along with two postprocessing procedures, achieved an AUC of 0.9824, an optimal sensitivity of 94.16%, and an optimal specificity of 92.82% on the segmentation of laser marks in fundus photographs. With accurate segmentation and high numeric metrics, the lightweight U-Net method showed its reliable performance in automatically segmenting laser marks in fundus photographs, which could help the AI assist the diagnosis of DR in the severe stage.

1. Introduction

Diabetic retinopathy (DR) is one of the most common complications of diabetes and the leading cause of irreversible visual loss globally [1]. For patients who have developed severe DR, panretinal photocoagulation (PRP) is one of the main treatments to reduce the risk of blindness. Laser marks are the scars left after retinal laser treatments. Identifying the position of laser marks on fundus photographs provides information of the received retinal laser treatment and thus is significant for the assistance of R3A and R3S DR stage grading in the Diabetic Eye Screening Guidance of the National Health Service (NHS) in the United Kingdom (UK) [2]. The R3A is classified as active proliferative DR (PDR) with at least one of the following active proliferate DR characteristics: new vessels on disc, new vessels elsewhere, preretinal or vitreous hemorrhage, and preretinal fibrosis with or without tractional detachment. The R3S is classified as the a stable stage of PDR after panretinal laser treatment and can present stable preretinal fibrosis, but without any other active proliferate DR characteristics [3]. The stable R3S status with panretinal laser marks can be distinguished from an active R3A, and the treatments of these two stages are different [2]. Laser marks appearing on nasal

proximity to optic disc no closer than 500 microns, on temporal proximity to macular center no closer than 3000 microns, and at the superior/inferior limit that no further posterior than 1 burn within the temporal arcades, are believed to be the signal of receiving PRP [4]. Patients diagnosed as R3S could be monitored in the annual screen, while the active treatments such as PRP or intravitreal injection of anti-VEGF drug should be received by patients diagnosed as R3A [2]. Moreover, determining the position of laser marks is of great importance to patients with DR for the follow-up treatment. For instance, many patients may not complete all laser photocoagulation at one treatment and need to receive laser photocoagulation several times because of the progress of their disease or personal tolerance. Besides, if patients are detected new active proliferate lesions on the retina even with the presence of laser marks, their DR gradings may revert to R3A, and the patients may be urged to receive active treatments [2, 5]. In automatic retinal diagnostic systems, the existence of laser marks on the fundus photographs may hinder the further retinal image assessment [6]. Hence, segmenting laser marks in fundus photograph images becomes clinically important.

Traditional detections [6–8] and deep learning methods [9] have put effort into detecting the existence of laser marks. However, they do not give enough attention to the exact locations of laser marks on the fundus photograph images. The traditional methods, which make full use of morphological characteristics related to laser marks for detection, in a sense offer the candidate regions of laser marks, but the extraction of candidate regions tends to be relatively poor with irregular boundaries. The deep learning method, which is a state-of-the-art machine learning technique that has shown its superiority in the diagnosis of some diseases [10–12], especially the DR screening in the field of ophthalmology [13–16], extracts features directly from images for detection and attains relatively high detective accuracy, but it does not provide interpretable explanations for its decisions [17, 18]. Also, it has long been a challenge to include medical knowledge within machine learning algorithms, especially within the deep learning algorithms [11, 18, 19]. Deficient attention to segmenting laser marks in fundus images may also in part result in difficulty attaining image data accurately annotated by well-trained ophthalmologists. So far, there are no public fundus photograph datasets annotating laser marks pixel by pixel. Thus, few studies have been involved in the segmentation of laser marks in fundus photograph images.

In this study, a deep learning method, the light version of U-Net [20], named lightweight U-Net, was adapted to segment laser marks in fundus photographs using the dataset we proposed. The lightweight U-Net inputted a fundus image and outputted the probability map localizing the potential area of laser marks. Furthermore, to meliorate the segmentation maps, we introduced two postprocessing procedures developed from clinical practice. These procedures further improved the segmentation accuracy of the prediction. The well-performed model would be of great help for ophthalmologists serving as an essential component of the DR computer-aided diagnosis system.

2. Materials and Methods

2.1. Datasets. The fundus photographs with laser marks in this dataset were RGB images in a JPG or JPEG format and obtained from the Image Reading Center of Zhongshan Ophthalmic Center, Sun Yat-Sen University, China. The fundus photographs were collected from the clinical department of Zhongshan Ophthalmic Center, or the DR screening charity project of Lifeline Express in China, or the internet public data. A set of 154 fundus photographs with laser marks comprised of two subdatasets: one contains 84 images manually segmented by experienced graders at the Image Reading Center only once, and the other contains the rest 70 images manually and independently segmented by three experienced graders at the Image Reading Center. Since the manual segmentation of 84 images in the first dataset was relatively coarse, which might lead to a less precise estimation, we only used it in the pretraining session.

For the second dataset containing 70 images, the three experienced graders were asked to mark all the pixels ensured as laser marks. The gold standards of the images were labeled by at least two graders. Since this subdataset had more precise manual segmentations, it was used to construct the formal data set. These 70 fundus photographs with gold standards were randomly divided into the formal training set with 50 images and the testing set with 20 images, respectively.

In our dataset, the microaneurysms, retinal hemorrhages, hard exudates, soft exudates, venous beading, intraretinal microvascular abnormality, NVE/NVD, fibrous proliferation, preretinal hemorrhage, vitreous hemorrhage, and tractional retinal detachment were detected in about 95.71%, 98.57%, 70.00%, 12.86%, 0.00%, 11.43%, 5.71%, 2.86%, 1.43%, 0.00%, and 0.00% of the 70 images, respectively. Besides, among all 154 fundus photographs, 75.97% are at the R3S stage, 3.25% are at the R3A stage, and the remaining 20.78% are photos that are at other stages. And 51.30% of the images are with PRP, and 42.21% are with partial retinal laser marks. All of the laser marks in our data were at the late stage.

It should be noted that every image collected in the dataset was used to make clinical diagnoses, leading to the characteristic inconsistency of these images because photos were acquired by more than one specific camera model, such as CIRRUS, Cobra, and Canon. Shot by various types of cameras, the images had different resolutions (ranging from 1116×1080 pixels to 4928×3264 pixels), fields-of-views (from 45 to 60 degrees), hues (whitish, yellowish, reddish, etc.), centers of the fundus images (either macula lutea or optic disc (OD), pupil diameters, and so on. All these variations contributed to the diversity of our dataset, enabling a more generalized and robust deep learning algorithm for laser marks segmentation.

2.2. Image Preprocessing and Augmentation. It was essential to preprocess the images to summarize the commonness artificially because fundus photographs in the image dataset varied in size, resolution, and hue due to the multiplicity of camera devices. Preprocessing helped diminishing differences in the intrinsic feature distributions.

First, images were all resized to 512×512 pixels. The next three steps were successively implemented on each channel to eliminate the outputted overall tone brightness variance among images. The Z-score standardization, resulting in an image with a mean of 0 and a variance of 1, was calculated using the following formula:

$$z_{ijk} = \frac{x_{ijk} - \mu_{jk}}{\sigma_{jk}}, \quad i = 1, 2, \cdots, N^{(\text{img})}, j = 1, 2, \cdots, p, k = 1, 2, 3, \tag{1}$$

where $N^{(\text{img})}$ is the total number of images in the training set, p is the number of pixels in a channel of an image (for a 512×512 image, the number of pixels p is 262144), and $k = 1, 2, 3$ represents the three channels (red, green, blue) of an image. And x_{ijk} represents the jth pixel value in the kth channel of the ith image, $\mu_{jk} = \sum_i x_{ijk}/N^{(\text{img})}$, and $\sigma_{jk} = \sqrt{\sum_i (x_{ijk} - \mu_{jk})^2/N^{(\text{img})}}$ is the mean and the standard deviation of the corresponding pixel points of all images in the training set, respectively. The outcome z_{ijk} is the adjusted value of that specific pixel.

Inner image minimum-maximum normalization then followed, aiming to rescale the gray values into a scale of 0 to 255. This process was enabled by

$$v_{ijk} = \frac{z_{ijk} - \min\limits_{j=1,\cdots,p}(z_{ijk})}{\max\limits_{j=1,\cdots,\text{p}}(z_{ijk}) - \min\limits_{j=1,\cdots,p}(z_{ijk})} \times 255, \quad i = 1, \cdots, N^{(\text{img})}, j = 1, \cdots, p, k = 1, 2, 3, \tag{2}$$

where z_{ijk} is obtained in the previous step, and $\min\limits_{j=1,\cdots,p}(z_{ijk})$ and $\max\limits_{j=1,\cdots,p}(z_{ijk})$ stand for the minimum and maximum value of z_{ijk} in the kth channel of ith image, respectively. And v_{ijk} is the final value restricted in the range between 0 and 255.

The contrast limited adaptive histogram equalization (CLAHE) [21] and the gamma correction ($\gamma = 1/1.2$) [22] were conducted sequentially to enhance the contrast in the image. The grayscale values were then divided by 255 to transform them back to the 0 and 1 range. By performing these preprocessing steps on all three channels separately and then combining them back together, the contrast could be effectively enhanced between the laser marks and background while feature discrepancies caused by camera models would be weakened (Figure 1).

The random cropping technique was applied to effectually augment the training set due to data scarcity [23]. A total of 500,000 patches were extracted from the formal training set that contained 50 fundus images. Completely black patches extracted from the peripheral black area that contained no information would be excluded. As a result, from each training image, 10,000 randomly centered patches with 48×48 pixels in size were extracted. This size was chosen because the patches of the size were able to determine whether there were one or two laser marks in the images, thus enabling the network to learn the characteristics of these specific lesions. The corresponding ground truth label patches were also extracted (Figure 1) to match the augmented training set. In the testing process, we cropped the images into pieces 48×48 pixels in size, a coherent size to the training ones. Unlike the training set where the central locations were randomly chosen, a sliding operation with stride 5 (five pixels were moved each time) was adopted in the testing set to clip the patches. Although some parts of the original images were repeatedly seized, i.e., the patches overlapped, it benefitted the accuracy of the prediction, as a single-pixel might be predicted several times. The patches cropped at the right or lower margins might not be of size 48×48 because of the sliding operation; as to these images of incompatible sizes, we used a zero padding strategy on that specific margin (or those margins) to preserve the marginal information. In our case, a total of 3364 patches could be attained from one image. The modified testing set with a size of 48×48 pixels was fed into the trained lightweight U-Net. The predicted outcomes of the patches were then placed back to create the integral prediction maps of the original images. The final integral outcomes that the algorithms would present for each image were prediction maps with each pixel indicating the probability of being diagnosed as laser marks, calculated by the sum of the prediction results divided by the frequency of being predicted.

2.3. A Lightweight U-Net Model Development. The lightweight U-Net structure was proposed by Wang et al. [24], who used this structure for the segmentation of retinal vessels in single-channel images. Our model resembled the structure of Wang et al., and we applied this method to segment the laser marks of the fundus photographs.

The U-Net structure mainly consisted of two paths: the "mutually inverse" contracting path and the expansive path. On each path, dense convolutional bocks, comprising two convolutional layers followed by rectified linear unit (ReLU) layers, were joined by either downsampling operations (on the contracting path) or upsampling operations (on the expansive path).

And the main change from the U-Net to the lightweight U-Net was that we downscaled the original network into a three-scaled network, meaning that there were only five dense convolutional blocks within the entire structure. We further adjusted hyperparameters in the structure:

(1) The number of feature channels at every block has been halved compared to the U-Net

(2) The padding strategy was adapted in every convolutional operation for storing the marginal information

(3) Dropout layers (with probability = 0.2) were introduced between two successive convolutional layers to prevent overfitting

In the structure proposed by Wang et al., they used convolutional filters with a size of 3×3 and a striding step of 2 to down-sample the feature maps, but our model simply

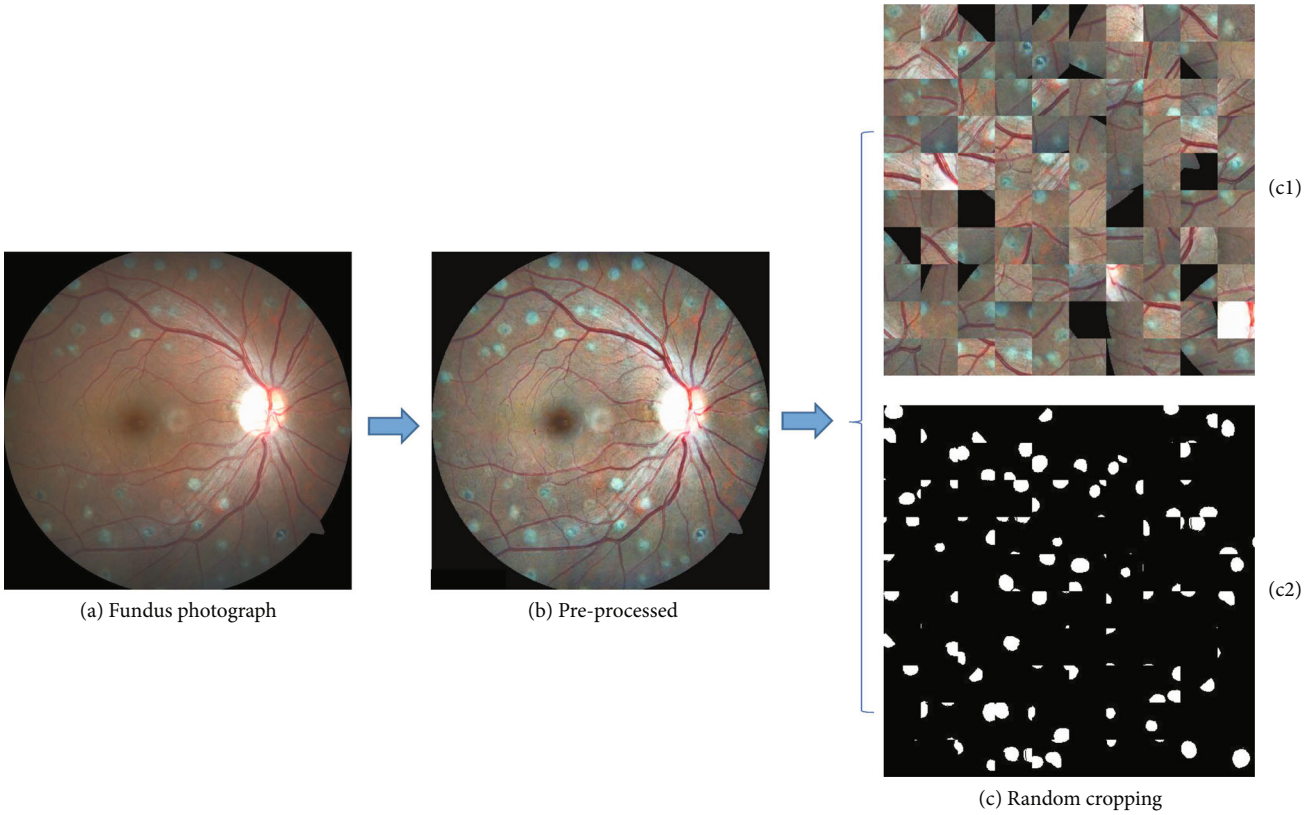

(a) Fundus photograph (b) Pre-processed (c) Random cropping

Figure 1: Presentation of the preprocessing and data augmentation session. (a) A sample from the training set. (b) The matching preprocessed image. (c) The examples of the randomly cropped patches (c1) and the corresponding labeled patches (c2).

used the max-pooling operations with filters of size 2×2 to downsize the feature maps. Figure 2 vividly shows the structure of the lightweight U-Net. The detailed parameters of the layers are also presented in Figure 2.

We used the transfer learning technique for parametric initialization before formally training the networks with images containing accurately labeled laser marks. We first pretrained the modified lightweight U-Net with the DRIVE dataset [25], a fundus image dataset with a total of 40 images annotating vessels. Likewise, 40 images in DRIVE went through the data preprocessing, and augmentation procedures mentioned above before being used for pretraining. Although DRIVE was not built for the segmentation of laser marks, using it to pretrain the network did help accelerate the convergence of parameters and obtain more accurate results because both datasets shared similar characteristics [26]. Subsequently, we pretrained the lightweight U-Net with the 84 roughly labeled fundus images. This helped the network to grasp a coarse cognition of laser marks.

Our extended training set was randomly divided into batches, each possessing 128 patches. Ten percent of the samples of a batch was split apart for validation. The stochastic gradient descent (SGD) was applied for parameter optimization by minimizing the loss function. The loss function in this segmentation task was a pixel-wise categorical crossentropy, which computed the following formula over the final feature maps:

$$R = -\sum_{i=1}^{N}\sum_{k=1}^{K} y_{ik} \log f_k(x_i), \tag{3}$$

where N indicates the total number of pixels within a batch, i.e., N = batch size × pixel number per patch, K denotes the number of classes, and y_{ik} and $f_k(x_i)$ represent the ground truth label and the predicted probability of the x_i pixel in the kth class, respectively. Network parameters (weights) saved for testing were the weights that minimized the loss function evaluated in the validation set.

2.4. Postprocessing Procedures. PRP surgeries generally follow certain standards, and there are several standards directly related to positioning and screening laser marks on fundus images in clinical practice. Here are two examples:

(i) Lasers should not be beamed within the OD and a diameter range of the OD

(ii) Lasers should not be beamed within 1500 microns from the macular fovea

We developed two postprocessing procedures to denoise the prediction maps based on these standards. Below is a sketchy description of the algorithms.

As to the first standard, all the "suspected laser marks" at the ODs and their peripheries are not laser marks. Thus, it is necessary to eliminate the false-positive judgments around

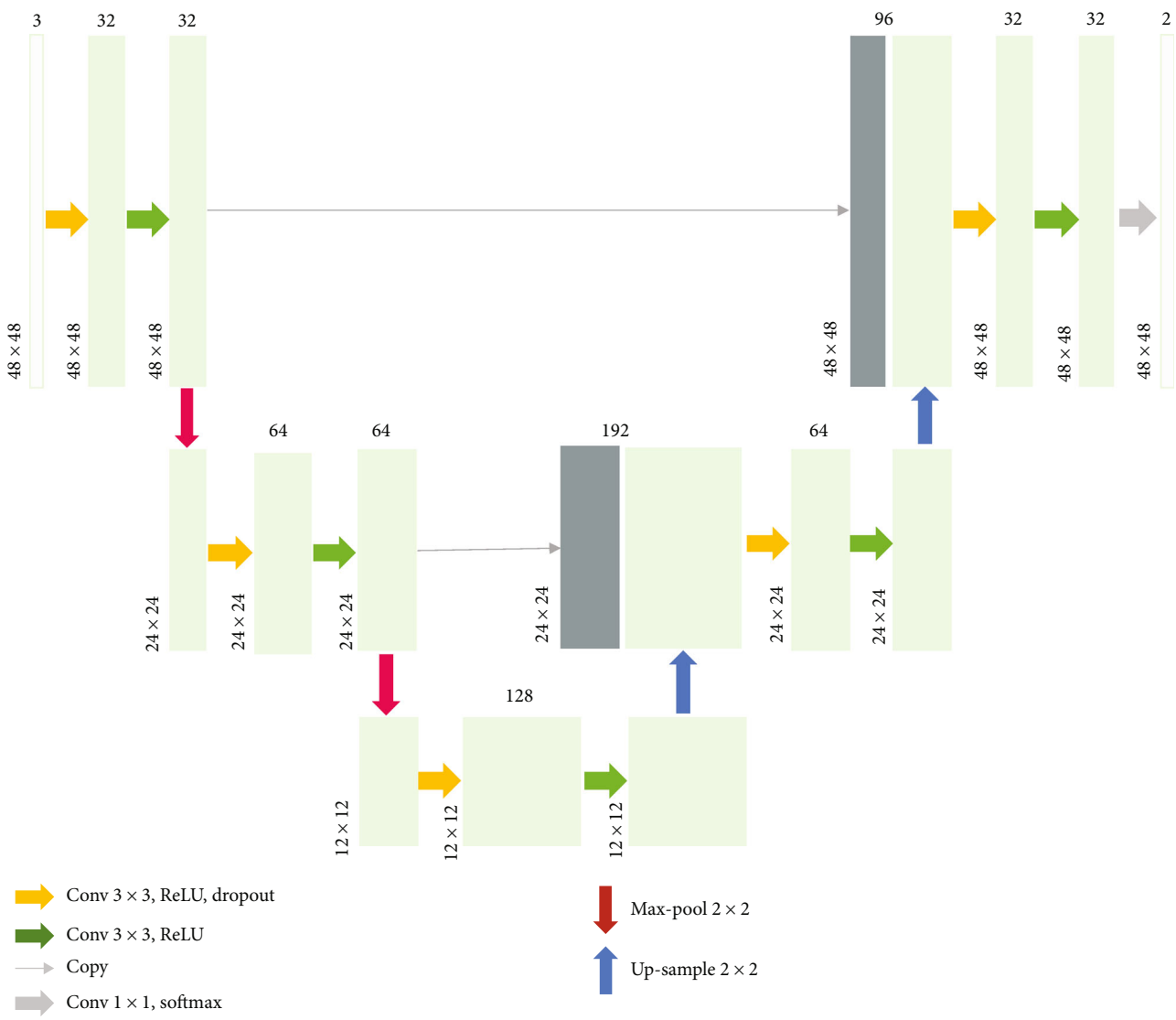

Figure 2: The lightweight U-Net architecture. Each green box corresponded to a multichannel feature map. The number of channels was denoted on top of the boxes. The *x*-*y* size was provided at the lower left edge of the box. Gray boxes represented copied feature maps. The arrows denoted the different operations.

the ODs. To do this, we first located the ODs and then erased the positive decisions within an elliptical area at and around the ODs. We applied a deep learning method to locate the ODs. The deep learning structure and training process were identical to the lightweight U-Net, except that it was pretrained only on the DRIVE dataset and then trained on the fundus images with ODs manually segmented. This fundus photograph dataset annotating ODs was collected and annotated at the Image Reading Center of Zhongshan Ophthalmic Center. The predicted OD area on each segmentation map was determined as the largest connected domain on the binary prediction graph, where the division threshold of the binary prediction graph from the grayscale output was set to be 0.5 empirically. This method has proven effective in locating and segmenting this anatomic structure in our prior experiment on an inhouse image dataset: evaluating on the inhouse testing set, the area under the receiver operating characteristic curve (AUC) was 0.9997, and the sensitivity, specificity, and accuracy were 93.90%, 99.90%, and 99.81%, respectively. The major and minor axes of elliptical areas that would be covered over the ODs were determined by 1.8 times the maximal *x*-axis and *y*-axis lengths of the predicted OD.

As to the second standard, what we did was highly analogous. The macular region was first oriented through morphological features using the method proposed by Jiang et al. [27], and then the area around the macular region was covered. To erase more impertinent noises, the area covered was macular-centered squares whose sides were 80 pixels long. Both manipulations served as the backend processes to further optimize the prediction results. The flowchart of the postprocessing is presented in Figure 3.

2.5. Hyperparameter Setting for Model Training. The initial learning rate was 1×10^{-3} with a learning rate reduce the factor of 0.3 for every ten consecutive epochs without

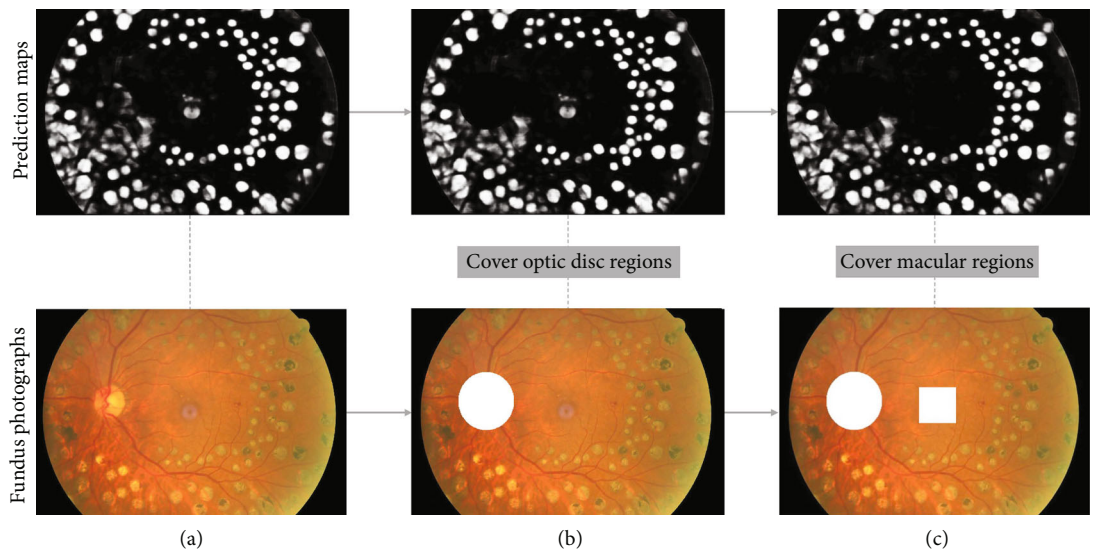

Figure 3: The flowchart of the postprocessing procedures. The top row presented the prediction maps after each step, and the bottom row showed the corresponding procedures on the fundus photographs. (a) The raw prediction map coming from the lightweight U-Net structure and the corresponding fundus image. (b) The prediction map and the fundus image after an elliptic region around the optic disc were covered. (c) The prediction map and the fundus image after the optic disc and macula region were covered.

improvement in validation accuracy. The onset of an early stop was when validation accuracy did not improve in 40 consecutive epochs.

2.6. Statistical Analysis of Model Performances. Statistical analyses were performed using Python 3.6.5 (Wilmington, Delaware, USA), which was also used for image processing and the lightweight U-Net experiments. Grayscale images were provided as the outcomes of the algorithms, as some shallow shades between bright domains might inform graders of coalesces of laser marks. To evaluate the performances of the lightweight U-Net and its combination with two postprocessing procedures, evaluation metrics were calculated. We drew the receiver operating characteristic (ROC) curves and computed the AUC. Besides, we presented the optimal pairs of sensitivity and specificity on the ROC curves. The optimal choices were based on Youden's index [28], defined as the sum of sensitivity and specificity subtracted by 1, i.e.,

$$\text{Youden's index} = \text{sensitivity} + \text{specificity} - 1. \quad (4)$$

Dice similarity coefficient (DSC) can show the percentage of the overlap areas between two set (the prediction map and the manual segmentation map). It equals twice the number of elements in the intersection of both set divided by the sum of the number of elements in each set. The corresponding formula is as follows:

$$\text{DSC} = \frac{2\text{TP}}{2\text{TP} + \text{FP} + \text{FN}}, \quad (5)$$

where *TP*, *FP*, *FN* represent the number of pixels correctly segmented as laser marks (true positive), pixels falsely segmented as laser marks (false positive), and pixels falsely detected as background (false negative), respectively.

3. Results

Before using the proposed dataset, we did a fivefold crossvalidation to verify the randomness in selecting the training set and the testing set. The 70 elaborately labeled images were randomly divided into five folds, and each fold contained 14 images. Then, one of the five folds was selected to be the testing set, and the other four folds were the training set in the following validation experiment. The ROC curves of the five crossvalidation experiments without postprocessing procedures and the mean ROC curves were presented in Figure 4. The maximum and minimum AUCs were 0.9833 and 0.9706, respectively. The interval formed by these two extreme AUC values covered 0.9798, indicating that the original division of the training set and the testing set were relatively random.

For the model evaluation, ROC curves of predictions through the lightweight U-Net alone and with the postprocessing procedures were presented in Figure 5. The optimal pairs of sensitivity and specificity on the ROC curves and the pixel-wise accuracies corresponding to them were shown in Table 1, which contained the results on a test set trained by lightweight U-Net and the net with postprocessing. The AUC for the 20 testing images was 0.9824 for the lightweight U-Net structure with the postprocessing procedures, which increased the AUC index by 0.26% compared with the AUC for the structure without these procedures. The best sensitivity, specificity, and accuracy for the lightweight U-Net with the postprocessing procedures were 94.16%, 92.82%, and 92.90%, respectively, attaining a, respectively, 0.61%, 0.66%, and 0.65% rise compared to those of the light structure without postprocessing procedures. And the DSC

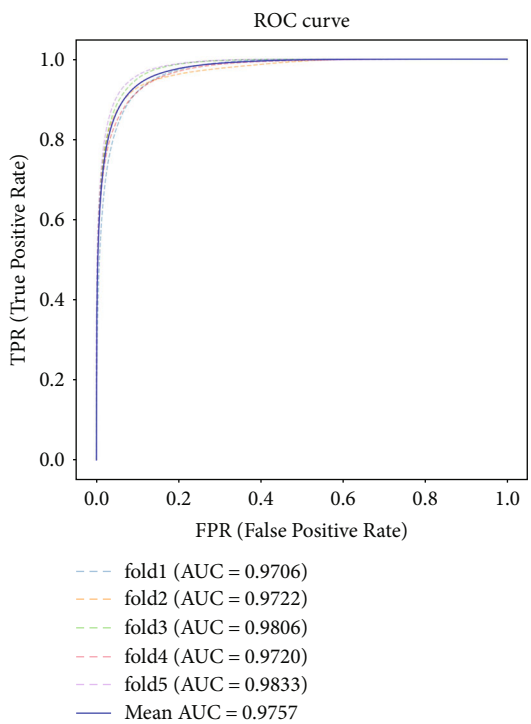

Figure 4: The ROC curves of the 5-fold crossvalidation experiments. The x-axis represented the false-positive rate, i.e., 1-specificity, and the y-axis represented the true-positive rate, i.e., sensitivity. The area under the curves (AUCs) were calculated, which were presented on the bottom right of the figure. The mean ROC curve, which was plotted with a solid line, and its AUC (namely, mean AUC) were also presented.

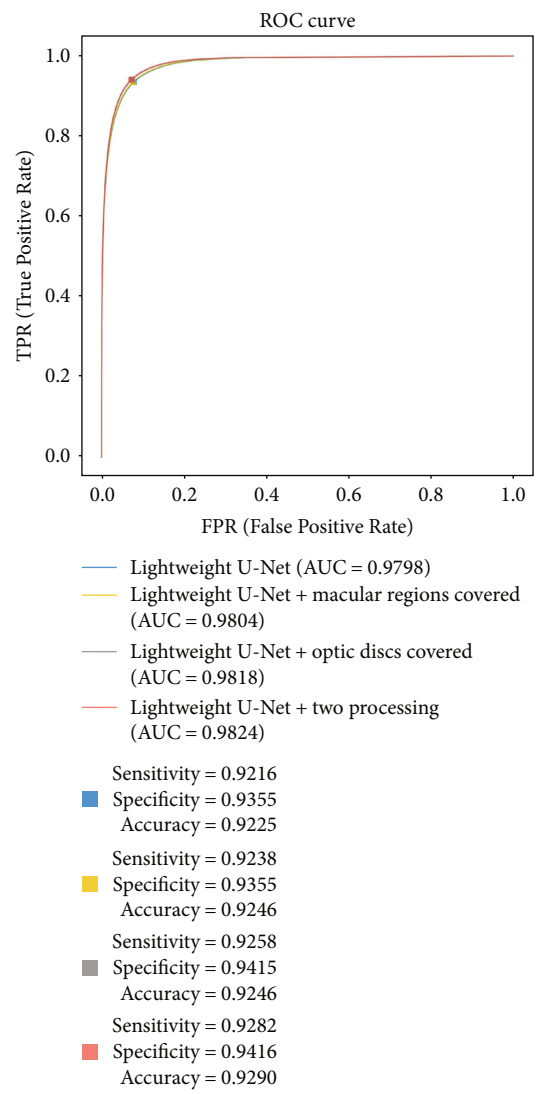

Figure 5: The ROC curves of the lightweight U-Net, the lightweight U-Net with either postprocessing procedure, and with both postprocessing procedures. The x-axis represented the false-positive rate, i.e., 1-specificity, and the y-axis represented the true-positive rate, i.e., sensitivity. The area under the curve (AUC) was also calculated, which was presented on the bottom right of the figure. The optimal pair of sensitivity and specificity chosen based on Youden's index were also marked on the curve, and the precise numeric values were presented on the right side.

also verified the results that the postprocessing procedures brought in a small advance. The small scale of improvement might result from the low probability of noises around ODs and macular regions. The effect of the postprocessing procedures on the evaluation metrics was not as great as the effect on the display of the segmentation results. Examples of the raw prediction images generated from the lightweight U-Net and the corresponding postprocessed prediction images were shown in Figure 6. After postprocessing procedures, noises at and around the ODs and macular regions were removed, leaving clearer and more accurate segmentation results. Finally, an algorithm according to the definition of PRP for diagnosing was designed, and the prediction results were used to verify in the test set. Through the prediction of laser marks, the sensitivity, specificity, and accuracy of our algorithm are 80%, 100%, and 90%, respectively.

Both the quantitative evaluations and the predicted maps showed that the combination with prior medical knowledge improved the performance of the deep learning algorithm and thus could achieve a good result even with a small amount of data.

4. Discussion

To the best of our knowledge, we first developed the lightweight U-Net, a deep learning algorithm used to segment the laser marks in fundus photographs in the present study. Traditional methods also focus on the detection of laser marks from fundus photos [6–8]. On the one hand, some details in the reported methods, such as some key parameters, are not clearly provided in the articles; so, we cannot use the accurate parameters to get good performance results. On the other hand, the segmentation of laser marks by traditional morphological methods is relatively poor and rough, for the morphological methods do not extract the candidate regions exactly. On the contrary, the deep learning method can well learn the essential features of retinal laser lesions by training on a well-labeled dataset and perform better than the morphological methods [29]. The neural network was trained and evaluated on the dataset of novel

Table 1: Comparison of methods on the proposed dataset.

Architecture	Sensitivity $= \frac{TP^*}{TP + FN^\dagger}$	Specificity $= \frac{TN^\ddagger}{TN + FP^\S}$	Accuracy $= \frac{TP + TN}{TP + FP + TN + FN}$	DSC	AUC
Lightweight U-Net	93.55%	92.16%	92.25%	70.59%	0.9798
Lightweight U-Net with macular regions covered	93.55%	92.38%	92.46%	70.76%	0.9804
Light weight U-Net with optic discs covered	94.15%	92.58%	92.68%	71.01%	0.9818
Lightweight U-Net with both post-processing procedures	94.16%	92.82%	92.90%	71.18%	0.9824

*TP: the number of pixels correctly classified as laser marks; †FN: the number of pixels mistakenly classified as background; ‡ TN: the number of pixels correctly classified as background; § FP: the number of pixels mistakenly classified as laser marks.

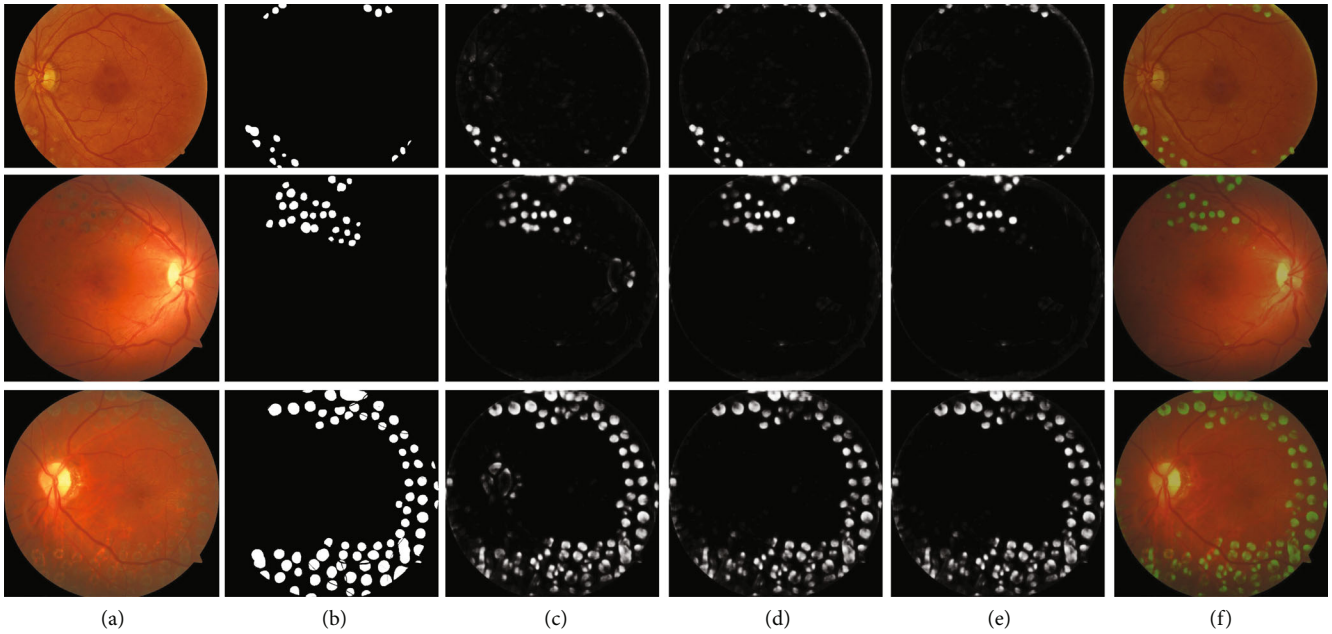

Figure 6: Dataset and prediction result presentation. Each row represented a sample in the testing sets and its corresponding processed results. (a) Laser marks showed in the fundus photographs of patients with DR. (b) The ground truth labels of laser marks in the testing images. (c) The raw predictions for laser marks made by the lightweight U-Net. (d) The predictions for laser marks made by the lightweight U-Net after optic disc areas were covered. (e) The postprocessed lightweight U-Net showed more accurate outcomes in the segmentation of laser makers. (f) The merge of postprocessed prediction maps and the original fundus photographs.

fundus photographs with laser marks in this study. Moreover, two postprocessing procedures developed from clinical standards of the PRP surgery were combined with the lightweight U-Net to further improve the segmentation results. Both the high numerical metrics and grayscale output images showed the lightweight U-Net could be used to set apart the laser marks on the fundus images, thus providing visible explanations of computer aid systems for DR diagnosis.

The biggest challenge of AI is the interpretability of deep learning algorithms. When a deep learning model detects a fundus photograph as an image with DR, it always gives out the diagnosis without providing more interpretable reasons why it made the decision. In this study, we first adopted a convolutional neural network designed for image segmentation, the lightweight U-Net, to detect laser marks from fundus photographs. This network assigned class labels to every pixel of the images and the pixel-based method to some extent visualized the diagnosis of the R3S stage of DR. The segmentation probability maps provided not only the suspected locations of laser marks but the valuable information for ophthalmologists, who could fully consider the comprehensive conditions of the patients and thus could provide more accurate and suitable cares and adjust the treatment regimens for the patient with DR. The focal or grid laser marks due to diabetic macular edema in our data were relatively lighter, smaller, and less pigment than the laser spots in other parts of the retina. While the experienced graders in our study marked all kinds of laser marks including the focal or grid laser marks accurately, we combined different laser marks images together for the training of the deep learning algorithm. Thus, it would not reduce the accuracy of segmentation in the test set. Combined with the additional algorithm, PRP could be accurately diagnosed according to the segmentation of laser marks, and the diagnostic accuracy of PRP on the test set was 90%, assisting the interpretative diagnosis of R3S. All the laser marks with the different color or size used for segmentation in this study

were from the fundus photographs of patients with DR. However, the features of retinal laser marks treated different diseases are similar, and the algorithm in our study could also make accurate predictions for laser markers in the fundus photographs of patients with retinal vein occlusion or peripheral retinal breaks.

Another major challenge in building computer-aided diagnosis systems is that medical knowledge is difficult to merge with deep learning algorithms. Combining prior medical knowledge undoubtedly improves the decision accuracy of a deep learning model. The present work addressed this challenge by collaborating the results of multimodels, which was to postprocess the segmentation results of the lightweight U-Net. According to clinical practices that the areas around OD and macular regions do not allow the presence of laser marks, we applied a similar deep network structure to cover the elliptic area containing the OD and a classical morphological operation to locate macular regions and then denoised around them. These two procedures were rooted in clinical practices and made the results closer to reality. The coverage of ODs and their peripheries improved the lightweight U-Net results more than the coverage of macular regions, which might be because ODs and laser marks shared more morphological characteristics, resulting in more misclassification around the optic disc areas for the lightweight U-Net model. The combination with the postprocessing procedures did not require graders a great effort to label a large amount of laser mark. With a relatively small amount of data for training, along with the cooperation with other models, the refined results containing a priori medical experience could be obtained. The postprocessing procedures derived from the clinical practices in this study increased the efficiency of the lightweight U-Net. The result concatenation from multiple models in our study was a simple but effective way to incorporate medical knowledge.

There were still several limitations in our study. First, our model showed its high reliability in distinguishing most laser marks from retinas, but it was still hard to differentiate some noises sharing similar morphological characteristics. Therefore, we will try to adjust the image tone in preprocessing and coalesce local information with global information in the future. Second, the number of fundus photographs in the training set was still relatively small. With more training images from diverse populations, the model would be more robust and accurate.

5. Conclusions

This study developed the postprocessed lightweight U-Net to accurately and reliably segment laser marks in fundus photographs for the AI-assisted diagnosis of DR in the different stage, potentially reducing the workload of oculists in various fundus diseases to some extent in the near future.

Data Availability

Original data and corresponding labels of training and test set are publicly available as attachments.

Conflicts of Interest

The authors declare that they have no conflicts of interests.

Authors' Contributions

Y. Jiang, J. Pan, and M. Yuan contributed equally as the first authors.

Acknowledgments

This study was supported by the National Natural Science Foundation of China (Grant No. 81770971), National Natural Science Foundation of Guangdong Province, China (Grant No. 2020A1515010617) to Dr. Y. Luo, the Open Research Funds of the State Key Laboratory of Ophthalmology (Grant No. 2019KF02), and National Natural Science Foundation of China (Grant No. 11771462) to Dr. X. Wang.

References

[1] A. W. Stitt, T. M. Curtis, M. Chen et al., "The progress in understanding and treatment of diabetic retinopathy," *Progress in Retinal and Eye Research*, vol. 51, pp. 156–186, 2016.

[2] D. Taylor, "Diabetic eye screening Revised grading Definitions," 2012.

[3] D. Broadbent, "Diabetic retinopathy: fundamentals for primary care," *Diabetes & Primary Care*, vol. 15, no. 4, 2013.

[4] E. K. Deschler, J. K. Sun, and P. S. Silva, "Side-effects and complications of laser treatment in diabetic retinal Disease," *Taylor & Francis*, vol. 29, no. 5-6, pp. 290–300, 2014.

[5] Ophthalmologists, T. R. C. O., "Diabetic Retinopathy Guidelines," in *Definition of Diabetic Retinopathy*, vol. 1, The Royal College of Ophthalmologists, 2012.

[6] F. Tahir, M. U. Akram, M. Abbass, and A. A. Khan, "Laser marks detection from fundus images," in *2014 14th International Conference on Hybrid Intelligent Systems*, pp. 147–151, Kuwait, 2014.

[7] F. Tahir, M. U. Akram, M. Abbas, and A. A. Khan, "Detection of laser marks from retinal images for improved diagnosis of diabetic retinopathy," *International Journal of Computer Information Systems and Industrial Management Applications*, vol. 7, pp. 130–136, 2015.

[8] E. Sousa, J. G. R. Almeida, C. M. Oliveira, and L. A. da Silva Cruz, "Automatic detection of laser marks in retinal digital fundus images," in *2016 24th European Signal Processing Conference (EUSIPCO)*, pp. 1313–1317, Budapest, Hungary, 2016.

[9] Q. Wei, X. Li, H. Wang, D. Ding, W. Yu, and Y. Chen, "Laser scar detection in fundus images using convolutional neural networks," in *Computer Vision-ACCV2018. 14th Asian Conference on Computer Vision. Revised Selected Papers: Lecture Notes in Computer Science*, Perth, WA, Australia, 2019.

[10] Y. LeCun, Y. Bengio, and G. Hinton, "Deep learning," *Nature*, vol. 521, no. 7553, pp. 436–444, 2015.

[11] J. M. Son, J. Y. Shin, H. D. Kim, K. H. Jung, K. H. Park, and S. J. Park, "Development and validation of deep learning models for screening multiple abnormal findings in retinal fundus images," *Ophthalmology*, vol. 127, no. 1, pp. 85–94, 2020.

[12] Y. Tong, W. Lu, Y. Yu, and Y. Shen, "Application of machine learning in ophthalmic imaging modalities," *Eye and Vision*, vol. 7, no. 1, pp. 1–15, 2020.

[13] Z. Gao, J. Li, J. Guo, Y. Chen, Z. Yi, and J. Zhong, "Diagnosis of diabetic retinopathy using deep neural networks," *IEEE Access*, vol. 7, pp. 3360–3370, 2019.

[14] M. D. Abràmoff, P. T. Lavin, M. Birch, N. Shah, and J. C. Folk, "Pivotal trial of an autonomous AI-based diagnostic system for detection of diabetic retinopathy in primary care offices," *Npj Digital Medicine*, vol. 1, no. 1, 2018.

[15] V. Gulshan, L. Peng, M. Coram et al., "Development and validation of a deep learning algorithm for detection of diabetic retinopathy in retinal fundus photographs," *Jama-Journal of the American Medical Association*, vol. 316, no. 22, pp. 2402–2410, 2016.

[16] G. Lim, V. Bellemo, Y. Xie, X. Q. Lee, M. Y. T. Yip, and D. S. W. Ting, "Different fundus imaging modalities and technical factors in AI screening for diabetic retinopathy: a review," *Eye and Vision*, vol. 7, no. 1, pp. 1–13, 2020.

[17] A. V. Varadarajan, R. Poplin, K. Blumer et al., "Deep learning for predicting refractive error from retinal fundus images," *Investigative Ophthalmology & Visual Science*, vol. 59, no. 7, pp. 2861–2868, 2018.

[18] F. Li, Z. Liu, H. Chen, M. Jiang, X. Zhang, and Z. Wu, "Automatic detection of diabetic retinopathy in retinal fundus photographs based on deep learning algorithm," *Transitional Vision Science & Technology*, vol. 8, no. 6, p. 4, 2019.

[19] Z. Xie, T. Ling, Y. Yang, R. Shu, and B. J. Liu, "Optic disc and cup image segmentation utilizing contour-based transformation and sequence labeling networks," *Journal of Medical Systems*, vol. 44, no. 5, pp. 1–13, 2020.

[20] O. Ronneberger, P. Fischer, and T. Brox, "U-net: convolutional networks for biomedical image segmentation," in *International Conference on Medical Image Computing & Computer-assisted Intervention*, vol. 9351, pp. 234–241, Munich, Germany, 2015.

[21] S. M. Pizer, E. P. Amburn, J. D. Austin et al., "Adaptive histogram equalization and its variations," *Computer Vision, Graphics, and Image Processing*, vol. 39, no. 3, pp. 355–368, 1987.

[22] C. Poynton, *Digital video and HDTV: algorithms and interfaces*, Morgan Kaufmann Publishers, San Francisco, 2003.

[23] F. Girard, C. Kavalec, and F. Cheriet, "Joint segmentation and classification of retinal arteries/veins from fundus images," *Artificial intelligence in medicine*, vol. 94, pp. 96–109, 2019.

[24] W. Xiancheng, L. Wei, M. Bingyi et al., "Retina blood vessel segmentation using a U-net based convolutional neural," in *International Conference on Data Science*, Beijing, China, 2018.

[25] J. Staal, M. D. Abramoff, M. Niemeijer, M. A. Viergever, and B. van Ginneken, "Ridge-based vessel segmentation in color images of the retina," *IEEE Transactions on Medical Imaging*, vol. 23, no. 4, pp. 501–509, 2004.

[26] N. Tajbakhsh, J. Y. Shin, S. R. Gurudu et al., "Convolutional neural networks for medical image analysis: full training or fine tuning?," *IEEE Transactions on Medical Imaging*, vol. 35, no. 5, pp. 1299–1312, 2016.

[27] Y. Jiang, J. Pan, Y. Shen et al., "A Fast and Effective Method of Macula Automatic Detection for Retina Images," 2020, https://arxiv.org/abs/2010.03122.

[28] W. J. Youden, "Index for rating diagnostic tests," *Cancer*, vol. 3, no. 1, pp. 32–35, 1950.

[29] L. Wang, J. Gu, Y. Chen et al., "Automated segmentation of the optic disc from fundus images using an asymmetric deep learning network," *Pattern Recognition*, vol. 112, article 107810, 2021.

Hindawi
Journal of Diabetes Research
Volume 2021, Article ID 3825155, 8 pages
https://doi.org/10.1155/2021/3825155

Research Article

Nomogram Prediction Model for Diabetic Retinopathy Development in Type 2 Diabetes Mellitus Patients: A Retrospective Cohort Study

Xiaomei Chen,[1] **Qiying Xie**,[1] **Xiaoxue Zhang**,[1] **Qi Lv**,[1] **Xin Liu**,[1] **and Huiying Rao**[1,2]

[1]*Department of Ophthalmology, Fujian Provincial Hospital North Branch, Fujian Provincial Geriatric Hospital, Fuzhou, China*
[2]*Department of Ophthalmology, Fujian Provincial Hospital, Fuzhou, China*

Correspondence should be addressed to Huiying Rao; rhydoctor@163.com

Received 28 July 2021; Revised 23 August 2021; Accepted 26 August 2021; Published 21 September 2021

Academic Editor: Honghua Yu

Background. This study is aimed at investigating the systemic risk factors of diabetic retinopathy and further establishing a risk prediction model for DR development in T2DM patients. *Methods*. This is a retrospective cohort study including 330 type 2 diabetes mellitus (T2DM) patients who were followed up from December 2012 to November 2020. Multivariable cox regression analysis identifying factors associated with the hazard of developing diabetic retinopathy (DR) was used to construct the DR risk prediction model in the form of nomogram. *Results*. 50.6% of participants (mean age: 58.60 ± 10.55) were female, and mean duration of diabetes was 7.09 ± 5.36 years. After multivariate cox regression, the risk factors for developing DR were age (HR 1.068, 95%Cl 1.021-1.118, $P = 0.005$), diabetes duration (HR 1.094, 95%Cl 1.018-1.177, $P = 0.015$), HbA1c (HR 1.411, 95%Cl 1.113-1.788, $P = 0.004$), albuminuria (HR 6.908, 95%Cl 1.794-26.599, $P = 0.005$), and triglyceride (HR 1.554, 95%Cl 1.037-2.330, $P = 0.033$). The AUC values of the nomogram for predicting developing DR at 3-, 4-, and 5-year were 0.854, 0.845, and 0.798. *Conclusion*. Combining age, diabetes duration, HbA1c, albuminuria, and triglyceride, the nomogram model is effective for early recognition and intervention of individuals at high risk of DR development.

1. Introduction

Diabetic retinopathy (DR) is known to be one of the most common microvascular complications of type 2 diabetes mellitus (T2DM) [1]. As the leading cause of vision loss among adults, DR results in nearly 4.8% of 37 million cases of blindness globally [2]. Recent studies related to DR prevalence in China have shown that approximately 9.4%–43.1% of patients with diabetes were diagnosed with DR [3]; with about 113.9 million Chinese adults with diabetes [4], this could be translated into extremely high prevalence of DR in China. However, DR is always symptomless before it enters the late-stage [5]. As DR seriously endangering human health as well as economic sustainability of the national health system, screening for DR is increasingly crucial for individuals of saving vision and for society of saving costs associated with visual impairment and blindness [6, 7]. Nevertheless, the massive population of China as well as a high prevalence of diabetes and relatively insufficient number of clinicians highlight a huge challenge confronting with widespread DR screening. Hence, with the burden of DR on health system becoming increasingly heavy, how to solve the DR screening problem in Chinese medical environment becomes more and more important.

As one of the complications of T2DM, DR is an ocular manifestation of systemic microvascular disease, which means that the development of DR is often accompanied by the development of systemic risk factors and the

exacerbation of other diabetic complications. Previous studies have indicated that DR is commonly accompanied by various comorbidities including dyslipidemia, chronic kidney disease, hypertension, hyperglycemia, and anemia [8–10]. Consistent with this notion, diverse researches have also demonstrated multiple different systemic risk factors for DR, such as urine albumin-to-creatinine ratio (UACR), low-density lipoprotein (LDL), apolipoprotein, and hemoglobin A1c (HbA1c) [8, 11, 12]. These findings provide evidence that these easily obtained systemic factors may be capable to be used in building an inexpensive, accurate, and convenient DR development prediction model, therefore, assisting DR screening. Nonetheless to our knowledge, such models have not been extensively explored or used for predicting DR development.

Since the burden of a rising population of T2DM will be increasingly unstoppable, especially in China of a remarkable low doctor-to-patient ratio, prevention is intensely required to reduce the occurrence of associated complications like DR. For this reason, our research tended to build a prediction model for DR development using a nomogram approach, based on the systemic risk factors.

2. Methods

2.1. Study Population. This retrospective cohort study was conducted on 330 patients in Fujian Provincial Geriatric Hospital. All medical information in the cohort study was collected from the electronic medical records. Inpatients who were diagnosed as T2DM [13] (ICD-10-CM: E11.900) with contemporaneous ophthalmology consultation records between December 1, 2012, and November 30, 2020, were included in this research. Cases were excluded if the following situations existed at baseline: (1) any clinical signs of DR of both eyes, (2) any other diseases affecting the ocular circulation (e.g., refractive error ≤ -3 diopters, glaucoma, retinal vascular occlusion, and eye trauma), and (3) any severe systemic diseases (e.g., cerebral infarction, myocardial infarction, and history of dialysis). Participant was followed up until the first time that DR was diagnosed; otherwise, the last follow-up was selected as individual endpoint in patients without signs of DR in the follow-up period. The flowchart of Figure 1 demonstrated the distribution of study participants. The research was conducted according to the Declaration of Helsinki and approved by the Research Ethics Committee of Fujian Provincial Geriatric Hospital (registration number: 2020-03-01). Informed written consent was obtained from each study participant.

2.2. Data Collection at Baseline. Demographics data (gender, age), medical history (duration of T2DM), physical data (height, weight, and blood pressure), and laboratory parameters were collected at the baseline. The body mass index (BMI) was calculated as weight in kilograms divided by height in meters squared. Blood pressure (BP, mmHg) was measured using a sphygmomanometer after 30 mins of rest. Laboratory parameters included hemoglobin (Hb, g/dL), hematocrit (Hct, %), fasting plasma glucose (FPG, mg/dL), HbA1c (%), serum creatinine (Scr, mg/dL), serum albumin (ALB, g/L), serum total protein (TP, g/L), LDL (mg/dL), triglyceride (TRIG, mg/dL), total cholesterol (TC, mg/dL), and albuminuria (measured qualitatively). Hypertension was defined as systolic blood pressure (SBP) $\geq$ 140 mmHg, diastolic blood pressure (DBP) $\geq$ 90 mmHg, antihypertensive drugs usage, or self-reported history of hypertension. Estimated glomerular filtration rate (eGFR) was calculated using the CKD-EPI creatinine equation [14]: $141 \times \min\left(\mathrm{Scr}/\kappa, 1\right)^{\alpha} \times \max\left(\mathrm{Scr}/\kappa, 1\right)^{-1.209} \times 0.993^{\mathrm{age}} \times 1.018$ (if female), among which κ is 0.9 for males or 0.7 for females, α is -0.411 for males or -0.329 for females, max indicates the maximum of 1 or Scr/κ, and min indicates the minimum of 1 or Scr/κ. All blood and urine samples were collected before 08:00 am.

2.3. Evaluation of DR Development at Endpoint. The primary outcome of the cohort endpoint was development of DR. DR assessments were conducted using image evaluation system (2-field fundus photograph) by qualified graders and were reviewed by a retinal professor (H.R.) if two graders held opposing opinions. DR was confirmed if existence of the following retinal lesions [15]: microaneurysms, hard exudates, intraretinal hemorrhagic dots, soft exudates, venous beading, intraretinal microvascular abnormality, neovascularization, preretinal hemorrhage, or vitreous hemorrhage. One eye with the worst retinopathy of the subjects was selected to determine the presence of DR. DR development was defined as DR in any stage at the endpoint of cohort, including nonproliferative diabetic retinopathy and proliferative diabetic retinopathy, while non-DR development was defined as no any signs of DR of both eyes at the endpoint.

2.4. Statistical Analysis. Statistical analyses were performed using SPSS software version 26.0 (Chicago, Illinois, USA) and R software version 4.1.0 (The R Foundation for Statistical Computing). All data was tested for normality using Shapiro-Wilk test and histograms. Normally distributed continuous data were demonstrated as mean ± SD, while nonnormally distributed continuous data as (medians, interquartile ranges (IQR)), and categorical data as number and percentage (%). Independent t-test was used to compare normally distributed continuous data, while Mann-Whitney U test for nonnormally distributed continuous data and chi-square test for categorical data. Cox regressions were conducted using "survival" R package. The outcomes of Cox regressions were expressed as hazard ratios (HRs), confidence interval stated at 95% (95% CI), and P value. The nomogram was plotted using "rms" R package, while receiver-operating characteristic (ROC) analyses determining the performance of nomogram to predict DR risk was conducted using "survivalROC" R package. All statistical tests were two-sided with P value < 0.05 as statistically significant.

3. Results

3.1. Participant Characteristics. This retrospective hospital-based cohort study was conducted for a follow-up period

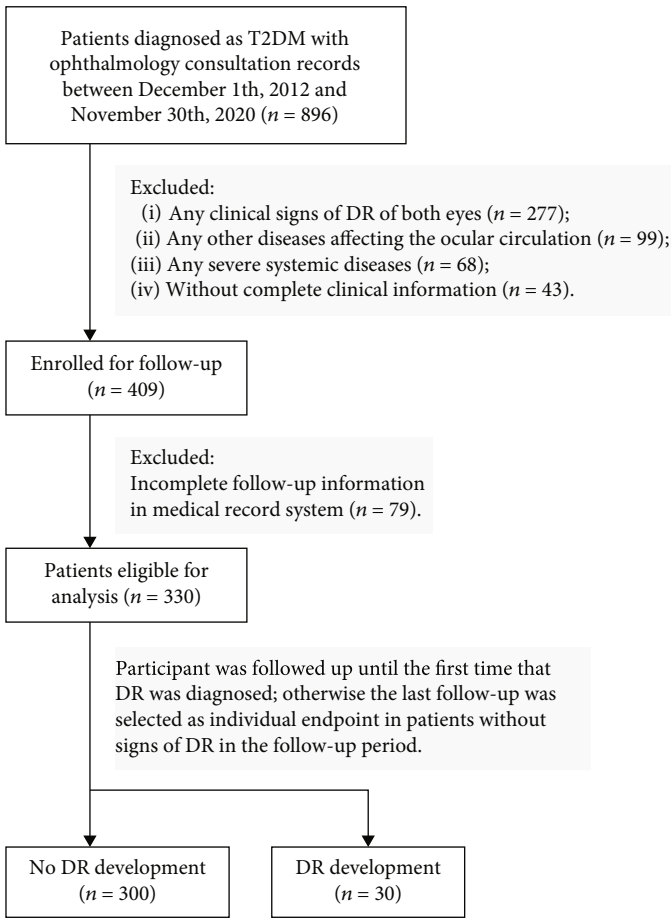

Figure 1: The distribution of study participants. T2DM: type 2 diabetes mellitus; DR: diabetic retinopathy.

with a mean time of 3.66 ± 1.90 years. The mean age of enrolled participants (167 females and 163 males) was 58.60 ± 10.55 years, with the mean duration of T2DM of 7.09 ± 5.36 years.

During the follow-up, 30 participants were found developments into DR (9.1%), while other 300 ones (90.9%) remained non-DR development. The baseline characteristics of these two groups were shown in Table 1. Participants who developed into DR were older at baseline (non-DR development 58.33 years old vs. DR development 61.30 years old) and more likely to be female (non-DR development 51.7% vs. DR development 40.0%), despite not statistically significant. The median (IQR) duration of T2DM for participants developed into DR was 9.5 (8.0) year, significantly longer than that without DR development, which was 6.0 (9.0) years ($P < 0.01$). Patients with DR development were more likely to have hyperglycemia manifested as higher HbA1c and FPG (both $P < 0.05$). In addition, the discrepancy in the incidence of albuminuria appears great between these two groups ($P < 0.01$). Moreover, the level of Scr and TRIG also significantly increased in the groups developed into DR (both $P < 0.05$). Nevertheless, other clinical parameters including BMI, BP, eGFR, TP, ALB, HGB, HCT, TC, LDL, and medication of oral hypoglycemic, insulin, antihypertension, and lipid-lowering remained comparable between these two groups ($P > 0.05$).

3.2. DR Development and Risk Factors. To address the risk factors of DR development, we further performed the cox regression analyses between DR development and clinical parameters with three different models (Table 2). Among them, model 1 was a univariate cox regression, model 2 was a multivariate regression with age and sex as covariates, and model 3 was a multivariate regression adjusted by all variables entered into the regression. Model 1 and model 2 demonstrated that age, HbA1c, albuminuria, Scr, ALB, FPG, and TRIG were significantly correlated with DR development (all $P < 0.05$). After controlling for all covariates, our results provided further evidence that the following factors may play essential roles in the development of DR: age (HR 1.068, 95% CI 1.021-1.118, $P = 0.005$), diabetes duration (HR 1.058, 95% CI 1.018-1.177, $P = 0.015$), HbA1c (HR 1.411, 95% CI 1.113-1.788, $P = 0.004$), albuminuria (HR 6.908, 95% CI 1.794-26.599, $P = 0.005$), and TRIG (HR 1.554, 95% CI 1.037-2.330, $P = 0.033$).

3.3. Nomogram Model Predicting DR Development. To reach the high ability of DR prediction, the independent risk factors including age, diabetes duration of DR, HbA1c, albuminuria, and triglyceride screened from multivariate cox regression analysis of model 3 were combined to establish a highly accurate developing DR prediction nomogram (Figure 2(a)). The 3-, 4-, and 5-year overall risk of individual

Table 1: Characteristics of DR nondevelopment group and DR development group.

Characteristics	Non-DR development ($n = 300$)	DR development ($n = 30$)	P value
Age (years)	58.33 ± 10.64	61.30 ± 9.31	†0.142
Sex (female)	155 (51.7%)	12 (40.0%)	‡0.223
Diabetes duration (years)	6.00, 9.00	9.50, 8.00	§0.009**
BMI (kg/m^2)	25.62 ± 3.63	25.72 ± 3.55	†0.889
HBP	123 (41.0%)	13 (43.3%)	‡0.804
SBP (mmHg)	127.81 ± 17.28	130.03 ± 18.97	†0.505
DBP (mmHg)	76.03 ± 11.96	75.9 ± 11.08	†0.953
HbA1c (%)	7.23 ± 1.55	8.38 ± 2.26	†0.010*
Albuminuria (+~+++)	11 (3.7%)	5 (16.7%)	‡0.002**
Scr (mg/dL)	84.89 ± 23.84	103.49 ± 43.64	†0.028*
eGFR (mL/min/1.73 m^2)	79.11 ± 21.27	71.82 ± 29.60	†0.197
TP (g/L)	70.74 ± 6.08	70.3 ± 8.88	†0.794
ALB (g/L)	44.29 ± 4.17	42.8 ± 5.47	†0.071
HGB (g/dL)	134.12 ± 15.51	137.57 ± 19.7	†0.259
HCT (%)	39.05 ± 4.23	39.58 ± 5.75	†0.523
FPG (mg/dL)	6.89, 2.55	7.81, 5.82	§0.023*
TC (mg/dL)	4.27 ± 0.89	4.05 ± 1.01	†0.204
LDL (mg/dL)	2.50 ± 0.75	2.34 ± 0.74	†0.260
TRIG (mg/dL)	1.31, 1.00	1.89, 1.32	§0.011*
Oral hypoglycemic	265 (88.3%)	28 (93.3%)	‡0.408
Insulin (unit)	15.00, 27.00	16.50, 20.00	§0.743
Antihypertension	94 (31.3%)	10 (33.3%)	‡0.822
Lipid-lowering	224 (74.7%)	21 (70.0%)	‡0.577

Results are expressed as mean ± SD, percentages, or as medians, IQR; P values were compared by independent t-test, Mann-Whitney U test or χ^2 test as appropriate. *$P < 0.05$, **$P < 0.01$.†Values for comparisons between groups by independent samples t-test. ‡Values for comparisons between groups by χ^2 test. §Values for comparisons between groups by Mann-Whitney U test. DR: diabetic retinopathy; BMI: body mass index; HBP: hypertension; SBP: systolic blood pressure; DBP: diastolic blood pressure; HbA1c: hemoglobin A1c; Scr: serum creatinine; eGFR: estimated glomerular filtration rate; TP: total protein; ALB: serum albumin; HGB: hemoglobin; HCT: hematocrit; FPG: fasting plasma glucose; TC: total cholesterol; LDL: low-density lipoprotein; TRIG: triglyceride.

DM patients developing DR could be predicted by the nomogram. The great power in predicting DR developing of DM patients was reflected by the time-dependent receiver-operating characteristics (tROC) curve analysis of the nomogram (Figure 2(b)), which showed AUCs for DR prediction models of 3-, 4-, and 5-year were 0.854, 0.845, and 0.798, respectively. Therefore, the systemic factor-based nomogram possibly will help clinicians predict the 3-,4-, and 5-year overall risk of developing DR in patients with DM individually and accurately.

4. Discussions

Through this retrospective cohort study, we found several systemic factors including age, duration of diabetes, HbA1c, albuminuria, and TRIG held significant associations with DR development, which remained statistically significant after adjusting for confounding factors. Based on these significant independent systemic variables identified in the multivariate cox regression, we further established a nomogram to formulate a new predictive tool for evaluating risk of DR development after 3-, 4-, and 5-year, which was implied considerable accurate from the AUC analyses.

For the present, Early Treatment Diabetic Retinopathy Study (ETDRS) 7-standard fields color retinal photographs and fundus slit-lamp examination are still the gold standard for DR screening [16, 17]. However, some evident deficiencies are present in the above DR screening modalities: complex of ETDRS photographs and time-consuming of fundus slit-lamp examination, which make them impractical for such large-scale screening in China. Thus, unconventional options are indispensable to circumvent these problems. Some current literatures suggested that the ultrawide-field (UWF) retina imaging providing a single image covering up to 200° of fundus could also be used as a reliable DR screening tool [18]. Data from other studies showed that different quantitative metrics derived from optical coherence tomography (OCT) or optical coherence tomography angiography (OCTA) may be considered as potential discriminant indicators of stage of DR [19]. Nevertheless, the above methods were also hindered by several practical problems, such as cost prohibitive and sophisticated analyses.

Table 2: Cox regression for DR development with clinical characteristics. †Model 1: univariate cox regression. ‡Model 2: age and sex were adjusted by each other; all other variables were adjusted by age and sex. §Model 3: all variables were entered into this multivariate regression analysis model. The outcomes of Cox regressions were expressed as HRs, 95% CI, and P value. $^{*}P < 0.05$, $^{**}P < 0.01$. DR: diabetic retinopathy; BMI: body mass index; SBP: systolic blood pressure; DBP: diastolic blood pressure; HbA1c: hemoglobin A1c; Scr: serum creatinine; eGFR: estimated glomerular filtration rate; TP: total protein; ALB: serum albumin; HGB: hemoglobin; HCT: hematocrit; FPG: fasting plasma glucose; TC: total cholesterol; LDL: low-density lipoprotein; TRIG, triglyceride.

Characteristics	†Model 1		Model 2		Model 3	
	HR (95%Cl)	P value	HR (95%Cl)	P value	HR (95%Cl)	P value
Age (years)	1.036 (0.997–1.077)	0.067	1.041 (1.001–1.082)	0.043*	1.068 (1.021–1.118)	0.005**
Sex (female)	0.601 (0.289–1.249)	0.173	0.544 (0.260–1.139)	0.107	1.058 (0.349–3.209)	0.920
Diabetes duration (years)	1.058 (0.993–1.127)	0.080	1.046 (0.982–1.114)	0.163	1.094 (1.018–1.177)	0.015*
BMI (kg/m^2)	0.992 (0.893–1.103)	0.886	1.005 (0.897–1.126)	0.929	0.988 (0.867–1.126)	0.856
SBP (mmHg)	1.008 (0.988–1.029)	0.429	1.006 (0.986–1.025)	0.572	1.007 (0.984–1.031)	0.564
HbA1c (%)	1.297 (1.129–1.489)	<0.001**	1.406 (1.206–1.640)	<0.001**	1.411 (1.113–1.788)	0.004**
Albuminuria (+~+++)	4.804 (1.789–12.895)	0.002**	4.952 (1.826–13.430)	0.002**	6.908 (1.794–26.599)	0.005**
Scr (mg/dL)	1.013 (1.005–1.021)	0.002**	1.011 (1.001–1.020)	0.022*	1.003 (0.990–1.016)	0.634
TP (g/L)	0.969 (0.917–1.024)	0.263	0.967 (0.915–1.022)	0.232	1.000 (0.926–1.080)	0.993
ALB (g/L)	0.889 (0.821–0.962)	0.004**	0.875 (0.805–0.952)	0.002**	0.895 (0.768–1.044)	0.157
HGB (g/dL)	1.012 (0.990–1.034)	0.281	1.010 (0.984–1.037)	0.445	1.067 (0.965–1.179)	0.205
HCT (%)	1.038 (0.958–1.125)	0.358	1.022 (0.929–1.123)	0.658	0.890 (0.625–1.268)	0.520
FPG (mg/dL)	1.126 (1.047–1.211)	0.001**	1.133 (1.058–1.213)	<0.001**	1.038 (0.931–1.158)	0.500
TC (mg/dL)	0.796 (0.532–1.191)	0.267	0.903 (0.591–1.380)	0.637	0.738 (0.327–1.668)	0.465
LDL (mg/dL)	0.725 (0.450–1.169)	0.187	0.818 (0.501–1.338)	0.424	0.727 (0.296–1.787)	0.487
TRIG (mg/dL)	1.371 (1.058–1.778)	0.017*	1.488 (1.125–1.969)	0.005**	1.554 (1.037–2.330)	0.033*

Nomogram is considered to be a dependable and practical predictive tool that is capable of generating quantitative probabilities of specific clinical events by incorporating multiple prognostic parameters [20]. The form of nomogram fulfills our desire for a clinically and biologically consolidated model and simultaneously enables our demands for personalized medicine. Through such a form of nomogram, our research established and validated an innovative predictive model for the risk of DR development among individual with T2DM, based on five systemic metrics easy to measure. Recently, investigators have explored the ability of nomogram on DR risk prediction, which were instructive in DR screening: Zhuang et al. built nomogram models to predict the risk of DR and diabetic macular edema (DME) originated from duration of diabetes, urine albumin-to-creatinine ratio (UACR), and LDL [12]; Mo et al. developed an analogous risk nomogram of DR based on other seven systemic predictors [21]. However, researches on the subject have been mostly restricted to limited ability that were only able to predict the current risk of DR but not the future risks. It is been shown that the nomogram based on sex, age, duration of diabetes, and HbA1c could be used to predict NPDR development within 6 months, 1 year, and 3 years in type 1 diabetes mellitus (T1DM) population [22], but the utility of nomogram for predicting DR development in T2DM patients has not been well documented. In this cohort study, through the Cox regressions analyzing the relationships between systemic baseline characteristics and events of DR development at endpoint, we constructed the risk nomogram of DR development after 3, 4, and 5 years in T2DM patients. In addition to indicating the occurrence of DR, this risk prediction model can also guide T2DM patients when to undergo secondary DR screening in the future, thus extending the interval of individual reexamination and alleviating the screening burden.

Sustained hyperglycemia and diabetes duration are widely recognized major risk factors for DR. Our findings demonstrated that HbA1c and diabetes duration were substantially linked with DR development, which was consistent with prior researches [11, 23]. After T2DM is identified, excessively high blood sugar levels produce oxidative stress and microinflammation, which is thought to be a significant pathogenesis of T2DM and associated complications [24, 25]. With duration of the disease increasing and microinflammation developing constantly, the hazard for DR development grows undoubtedly. As a result, adequate blood glucose control, as well as early diagnosis and treatment of DR, is critical.

Albuminuria is a key biochemical biomarker that reflects renal function particularly in diabetic kidney disease (DKD) [26]. Since DR shares comparable etiology with DKD [10, 27], metabolic markers of impaired renal function could not only reflect renal condition but also imply an indirect risk of DR. Multiple prior investigations have shown that albuminuria is a key factor for DR even when other systemic risk factors were controlled [12]. Therefore, albuminuria has also appeared to be highly related to the development of DR in our multivariate cox regression analyses and played an important role in the nomogram model.

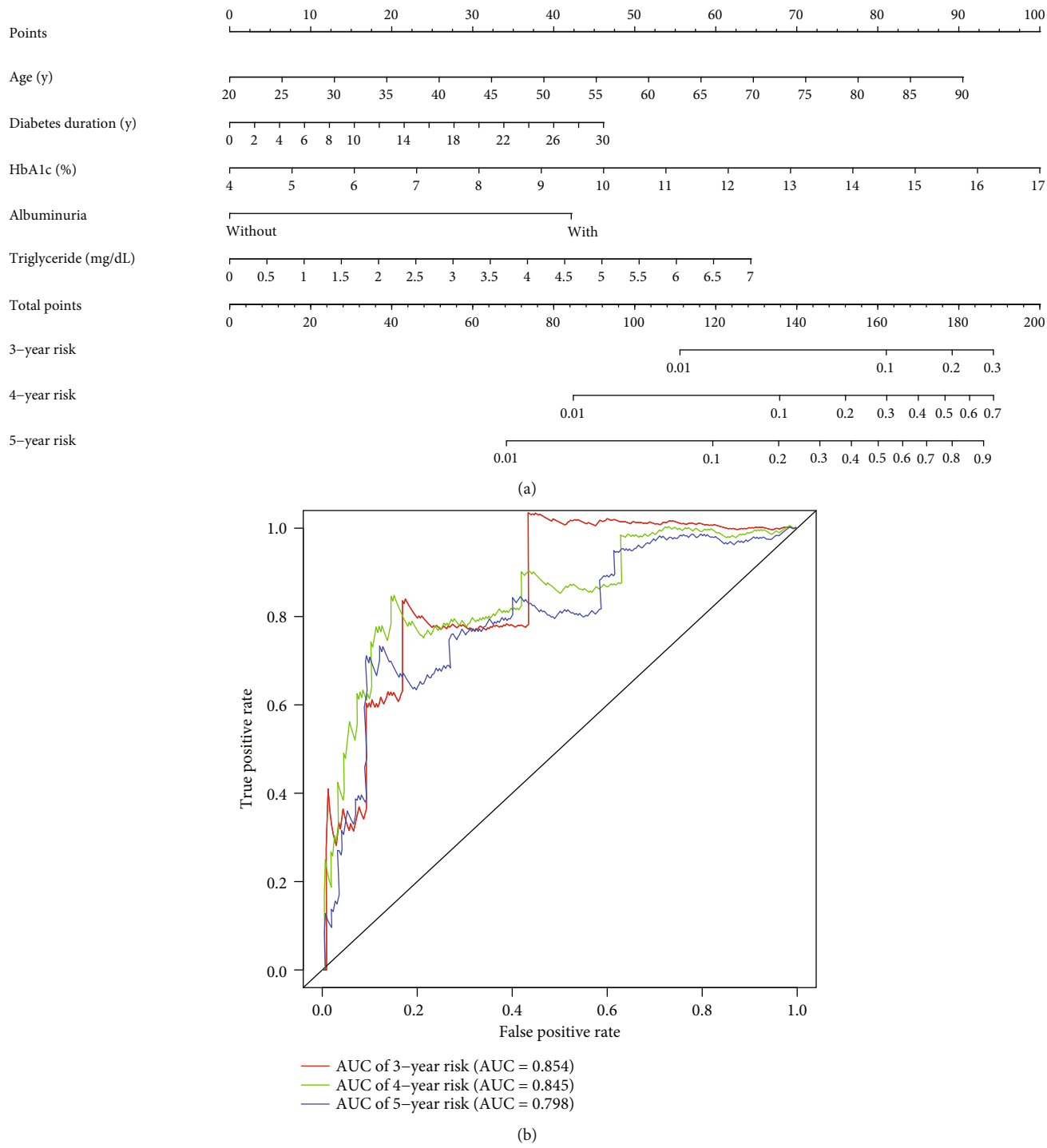

Figure 2: DR prediction model for T2DM patients. (a) Clinical parameter-based nomogram integrating age, diabetes duration, HbA1c, albuminuria, and triglyceride to predict 3-, 4-, and 5-year risks of DR development in patients with T2DM. (b) Time-dependent ROC curves of the nomogram showed AUCs for DR prediction models of 3, 4, and 5 years were 0.854, 0.845, and 0.798, respectively. HbA1c: hemoglobin A1c; AUC: area under the ROC curve; ROC: relative-operating characteristic.

Whereas the relationships between lipids and DR were relatively understudied compared to the above indicators, their link has been theorized for many years [8]. In terms of dyslipidemia, our analysis revealed that the development of DR was significantly correlated to TRIG levels. Growing evidences showed that dyslipidemia tends to worsen diabetic retinopathy by inducing inflammation and activating microglia rather than direct lipid extravasation [28] and that aberrant lipid clearance in diabetic retina may play a greater role in oxidative stress and nonenzymatic glycation [29]. Based on our results associated with dyslipidemia and DR, we believe that the clinically accessible and practical TRIG

measurement might be a significant indicator for the development of diabetic retinopathy.

Age was shown to be significantly positively associated with the development of DR in our cox regression analyses. This may be explained that age-related alterations in the retinal vasculature expedite the degradation of the retinal perfusion by causing the failure of autoregulation mechanism, which in normal conditions maintains a generally steady blood flow [30]. However, a review of researches revealed that the influence of age on DR remains controversial and varies depending on the populations being investigated. According to the UK Prospective Diabetic Study, older age was found to be a risk factor for DR advancement with a statistically significant relative ratio (RR) of 2.1 [31]. The results of the Wisconsin Epidemiological Study of Diabetic Retinopathy, on the other hand, revealed that older age was a protective factor for diabetic retinopathy [32]. We hypothesize that the confounders in diverse trials, such as variances in environmental, genetic, or lifestyle variables, as well as the type of patients screened, may explain the discrepancies in the influence of age for DR.

During a mean follow-up time of 3.66 ± 1.90 years, 30 (9.09%) of the 330 patients with T2DM included in this cohort eventually developed DR. However, the population included in the study were T2DM patients who had been hospitalized, indicating that they might have a stricter glycemic control regimen. In the real world, however, not all patients with T2DM follow such a rigorous regimen, and some individuals with T2DM may be unaware that they have T2DM until they are in the late stages of DR. This means that DR development may be more severe in the real world. However, even though the nomogram model in this study might be better at predicting DR development in T2DM patients who had an adequate treatment protocol, it still suggests how important DR screening and prevention are in T2DM patients.

To summarize, through the nomogram tool and five systemic factors easily accessible including age, diabetes duration, HbA1c, albuminuria, and triglyceride, we created a reliable prediction model that aided clinicians in the early recognition of individuals at high risk of DR development after 3, 4, and 5 years. Based on this model, clinicians and patients could also implement early medical interventions like as altering treatment scheme to decline the risk of DR. In other words, this quantitative framework was of great significance for disease management of DR in high-risk population, manifested in indicating and delaying the development of DR in T2DM.

There are still a few limitations in this study. Firstly, the lack of external validation is one of the significant limitations of our study. In this context, additional research is required to replicate and externally validate the findings of this study. Secondly, due to the limited sample size, the endpoint event in our cohort study was defined as DR development including both NPDR and PDR. Study's findings would have been more enriched if development of NPDR and PDR had been analyzed separately. Thirdly, because all data in this investigation were collected from a medical recording system or fundus color photography rather than fundus fluorescence angiography imaging, the DR diagnosis might lack strictness. The prediction model in this study may, however, remain generalized, and it is desired that future prospective studies can be carried out to assess the accuracy of this model in the real world and to further enhance it.

Data Availability

The data related to this article can be publicly available after the article accepted.

Conflicts of Interest

The authors declare that they have no conflicts of interest.

Authors' Contributions

X.C. and H.R. contributed to the conception and design of the study. X.C., Q.X., and X.Z. contributed to data collection, analysis, and/or interpretation. X.C. wrote the article. Q.L. and H.R. revised the manuscript. All the coauthors have read and approved the final article.

References

[1] Q. Shi, Y. Zhao, V. Fonseca, M. Krousel-Wood, and L. Shi, "Racial disparity of eye examinations among the U.S. working-age population with diabetes: 2002-2009," *Diabetes Care*, vol. 37, no. 5, pp. 1321–1328, 2014.

[2] S. Resnikoff, D. Pascolini, D. Etya'ale et al., "Global data on visual impairment in the year 2002," *Bulletin of the World Health Organization*, vol. 82, no. 11, pp. 844–851, 2004.

[3] X. Zhu, Y. Xu, L. Lu, and H. Zou, "Patients' perspectives on the barriers to referral after telescreening for diabetic retinopathy in communities," *BMJ Open Diabetes Research & Care*, vol. 8, no. 1, article e000970, 2020.

[4] Y. Xu, L. Wang, J. He et al., "Prevalence and control of diabetes in Chinese adults," *JAMA*, vol. 310, no. 9, pp. 948–959, 2013.

[5] S. S. Park, "Cell therapy applications for retinal vascular diseases: diabetic retinopathy and retinal vein occlusion," *Investigative Opthalmology & Visual Science*, vol. 57, no. 5, article ORSFj1, 2016.

[6] E. Agardh and P. Tababat-Khani, "Adopting 3-year screening intervals for sight-threatening retinal vascular lesions in type 2 diabetic subjects without retinopathy," *Diabetes Care*, vol. 34, no. 6, pp. 1318-1319, 2011.

[7] S. Y. Wang, C. A. Andrews, W. H. Herman, T. W. Gardner, and J. D. Stein, "Incidence and risk factors for developing diabetic retinopathy among youths with type 1 or type 2 diabetes throughout the United States," *Ophthalmology*, vol. 124, no. 4, pp. 424–430, 2017.

[8] M. B. Sasongko, T. Y. Wong, T. T. Nguyen et al., "Serum apolipoprotein AI and B are stronger biomarkers of diabetic retinopathy than traditional lipids," *Diabetes Care*, vol. 34, no. 2, pp. 474–479, 2011.

[9] C. J. Flaxel, R. A. Adelman, S. T. Bailey et al., "Diabetic retinopathy preferred practice pattern®," *Ophthalmology*, vol. 127, no. 1, pp. P66–P145, 2020.

[10] E. J. Barrett, Z. Liu, M. Khamaisi et al., "Diabetic microvascular disease: an endocrine society scientific statement," *The Journal*

of Clinical Endocrinology & Metabolism, vol. 102, no. 12, pp. 4343–4410, 2017.

[11] M. Lind, A. Pivodic, A. M. Svensson, A. F. Ólafsdóttir, H. Wedel, and J. Ludvigsson, "HbA1clevel as a risk factor for retinopathy and nephropathy in children and adults with type 1 diabetes: Swedish population based cohort study," *BMJ*, vol. 366, article l4894, 2019.

[12] X. Zhuang, D. Cao, D. Yang et al., "Association of diabetic retinopathy and diabetic macular oedema with renal function in southern Chinese patients with type 2 diabetes mellitus: a single-centre observational study," *BMJ Open*, vol. 9, no. 9, article e031194, 2019.

[13] K. G. M. M. Alberti, P. Z. Zimmet, and WHO Consultation, "Definition, diagnosis and classification of diabetes mellitus and its complications. Part 1: diagnosis and classification of diabetes mellitus provisional report of a WHO consultation," *Diabetic Medicine*, vol. 15, no. 7, pp. 539–553, 1998.

[14] A. S. Levey, L. A. Stevens, C. H. Schmid et al., "A new equation to estimate glomerular filtration rate," *Annals of Internal Medicine*, vol. 150, no. 9, pp. 604–612, 2009.

[15] T. Y. Wong, C. M. G. Cheung, M. Larsen, S. Sharma, and R. Simó, "Diabetic retinopathy," *Nature Reviews Disease Primers*, vol. 2, no. 1, article 16012, 2016.

[16] R. Taylor, L. Lovelock, W. M. Tunbridge et al., "Comparison of non-mydriatic retinal photography with ophthalmoscopy in 2159 patients: mobile retinal camera study," *BMJ*, vol. 301, no. 6763, pp. 1243–1247, 1990.

[17] J. A. Pugh, J. M. Jacobson, W. A. J. van Heuven et al., "Screening for diabetic retinopathy. The wide-angle retinal camera," *Diabetes Care*, vol. 16, no. 6, pp. 889–895, 1993.

[18] L. P. Aiello, I. Odia, A. R. Glassman et al., "Comparison of early treatment diabetic retinopathy study standard 7-field imaging with ultrawide-field imaging for determining severity of diabetic retinopathy," *JAMA Ophthalmology*, vol. 137, no. 1, pp. 65–73, 2019.

[19] S. Niu, C. Yu, Q. Chen et al., "Multimodality analysis of hyperreflective foci and hard exudates in patients with diabetic retinopathy," *Scientific Reports*, vol. 7, no. 1, p. 1568, 2017.

[20] V. P. Balachandran, M. Gonen, J. J. Smith, and R. P. DeMatteo, "Nomograms in oncology: more than meets the eye," *The Lancet Oncology*, vol. 16, no. 4, pp. e173–e180, 2015.

[21] R. Mo, R. Shi, Y. Hu, and F. Hu, "Nomogram-based prediction of the risk of diabetic retinopathy: a retrospective study," *Journal of Diabetes Research*, vol. 2020, Article ID 7261047, 9 pages, 2020.

[22] E. Y. C. Kang, F. S. Lo, J. P. Wang et al., "Nomogram for prediction of non-proliferative diabetic retinopathy in juvenile-onset type 1 diabetes: a cohort study in an Asian population," *Scientific Reports*, vol. 8, no. 1, article 12164, 2018.

[23] M. G. Kotoula, G. N. Koukoulis, E. Zintzaras, C. H. Karabatsas, and D. Z. Chatzoulis, "Metabolic control of diabetes is associated with an improved response of diabetic retinopathy to panretinal photocoagulation," *Diabetes Care*, vol. 28, no. 10, pp. 2454–2457, 2005.

[24] O. O. Oguntibeju, "Type 2 diabetes mellitus, oxidative stress and inflammation: examining the links," *International Journal of Physiology, Pathophysiology And Pharmacology*, vol. 11, no. 3, pp. 45–63, 2019.

[25] M. Halim and A. Halim, "The effects of inflammation, aging and oxidative stress on the pathogenesis of diabetes mellitus (type 2 diabetes)," *Diabetes & Metabolic Syndrome: Clinical Research & Reviews*, vol. 13, no. 2, pp. 1165–1172, 2019.

[26] M. C. Thomas, M. Brownlee, K. Susztak et al., "Diabetic kidney disease," *Nature Reviews Disease Primers*, vol. 1, no. 1, article 15018, 2015.

[27] Y. H. Chen, H. S. Chen, and D. C. Tarng, "More impact of microalbuminuria on retinopathy than moderately reduced GFR among type 2 diabetic patients," *Diabetes Care*, vol. 35, no. 4, pp. 803–808, 2012.

[28] Y. R. Chung, S. Y. Lee, Y. H. Kim, H. E. Byeon, J. H. Kim, and K. Lee, "Hyperreflective foci in diabetic macular edema with serous retinal detachment: association with dyslipidemia," *Acta Diabetologica*, vol. 57, no. 7, pp. 861–866, 2020.

[29] S. S. Hammer and J. V. Busik, "The role of dyslipidemia in diabetic retinopathy," *Vision Research*, vol. 139, pp. 228–236, 2017.

[30] D. Nagasato, Y. Muraoka, R. Osaka et al., "Factors associated with extremely poor visual outcomes in patients with central retinal vein occlusion," *Scientific Reports*, vol. 10, no. 1, article 19667, 2020.

[31] I. M. Stratton, E. M. Kohner, S. J. Aldington et al., "UKPDS 50: risk factors for incidence and progression of retinopathy in type II diabetes over 6 years from diagnosis," *Diabetologia*, vol. 44, no. 2, pp. 156–163, 2001.

[32] R. Klein, B. E. Klein, S. E. Moss, and K. J. Cruickshanks, "The Wisconsin epidemiologic study of diabetic retinopathy. XIV. Ten-year incidence and progression of diabetic retinopathy," *Archives of Ophthalmology*, vol. 112, no. 9, pp. 1217–1228, 1994.

Hindawi
Journal of Diabetes Research
Volume 2021, Article ID 2611250, 9 pages
https://doi.org/10.1155/2021/2611250

Research Article

Automated Grading of Diabetic Retinopathy with Ultra-Widefield Fluorescein Angiography and Deep Learning

Xiaoling Wang,[1] **Zexuan Ji**,[2] **Xiao Ma**,[2] **Ziyue Zhang**,[2] **Zuohuizi Yi**,[1] **Hongmei Zheng**,[1] **Wen Fan**,[3] **and Changzheng Chen**[1]

[1]*Eye Center, Renmin Hospital of Wuhan University, Wuhan, China*
[2]*School of Computer Science and Engineering, Nanjing University of Science and Technology, Nanjing, China*
[3]*Department of Ophthalmology, The First Affiliated Hospital of Nanjing Medical University, Nanjing, China*

Correspondence should be addressed to Wen Fan; fanwen@njmu.edu.cn and Changzheng Chen; whuchenchzh@163.com

Received 5 June 2021; Revised 7 August 2021; Accepted 19 August 2021; Published 9 September 2021

Academic Editor: Yijun Hu

Purpose. The objective of this study was to establish diagnostic technology to automatically grade the severity of diabetic retinopathy (DR) according to the ischemic index and leakage index with ultra-widefield fluorescein angiography (UWFA) and the Early Treatment Diabetic Retinopathy Study (ETDRS) 7-standard field (7-SF). *Methods*. This is a cross-sectional study. UWFA samples from 280 diabetic patients and 119 normal patients were used to train and test an artificial intelligence model to differentiate PDR and NPDR based on the ischemic index and leakage index with UWFA. A panel of retinal specialists determined the ground truth for our data set before experimentation. A confusion matrix as a metric was used to measure the precision of our algorithm, and a simple linear regression function was implemented to explore the discrimination of indexes on the DR grades. In addition, the model was tested with simulated 7-SF. *Results*. The model classification of DR in the original UWFA images achieved 88.50% accuracy and 73.68% accuracy in the simulated 7-SF images. A simple linear regression function demonstrated that there is a significant relationship between the ischemic index and leakage index and the severity of DR. These two thresholds were set to classify the grade of DR, which achieved 76.8% accuracy. *Conclusions*. The optimization of the cycle generative adversarial network (CycleGAN) and convolutional neural network (CNN) model classifier achieved DR grading based on the ischemic index and leakage index with UWFA and simulated 7-SF and provided accurate inference results. The classification accuracy with UWFA is slightly higher than that of simulated 7-SF.

1. Introduction

The number of people with diabetes mellitus has quadrupled globally in the past three decades, and diabetes mellitus is the ninth major cause of death [1]. With the increasing prevalence of diabetes mellitus in the community, diabetic retinopathy- (DR-) related visual impairment has become a serious public health issue [2]. The prevalence rate of DR in adults with diabetes aged 40 and older has been estimated to be 34.6% (93 million people) worldwide [3–5].

Diabetic patients have a disease course of more than 20 years, and more than 60% of patients will develop retinopathy [6]. Fundus examination of the retina constitutes part of the recommended routine physical examination of any adults with newly diagnosed diabetes and diabetic patients with a long disease course. Fundus fluorescence angiography (FFA) can clearly show retinal microaneurysm, nonperfusion areas, and neovascularization [7]. In particular, in eyes with complicated cataracts, FFA is routinely used to evaluate retinal vascular retinopathy.

The conventional Early Treatment Diabetic Retinopathy Study (ETDRS) 7-standard field (7-SF) montage FFA only images part of the fundus at a time. In recent years, ultra-widefield angiography (UWFA), capturing nearly 200°, has been used to image a wider retinal area, including the peripheral retina [8]. The significant advantage of UWFA is that it eliminates the need to stitch together several images to obtain a full fundus photograph, which is more convenient for clinical work. However, the lesions found beyond 7-SF by UWFA, and whether to take them into consideration when

evaluating the severity of DR confused many ophthalmologists including us. The concepts of ischemic index and leakage index were defined as the ratio of nonperfusion area and leakage area to total retina area in UWFA images, respectively [9, 10], and were introduced to quantitatively analyze the nonperfusion area and leakage area by UWFA. Several recent studies have shown that the severity of diabetic retinopathy is closely associated with the ischemic index and leakage index [10–14]. It is difficult to delineate or quantify the nonperfusion and leakage areas accurately manually. Given the large number of diabetes patients globally, this process is expensive and time-consuming. Therefore, artificial intelligence (AI) technology for rapid diagnosis and quantitative analysis for disease staging is urgently needed.

At present, with the rapid development of AI technology in the medical and health domain, AI technology has wide applications in ophthalmic imaging, such as fundus color photography and optical coherent tomography (OCT) [15–22]. For example, IDx-DR was the first authorized device to provide a screening decision without the need for a clinician to also interpret the image or results, making it usable by health care providers who may not normally be involved in eye care [22]. A few studies have reported the application of AI for FFA in DR patients, mainly to identify microaneurysms, nonperfusion areas, leakage, and laser spots [23, 24]. These algorithms depend on manual extraction for DR characterization. It is ineffective, measures only partial features of a single field of vision, and cannot comprehensively grade the disease; thus, its clinical application is limited. Ding et al. established algorithms to characterize prognostic anatomic structures in UWFA images, such as the optic disc or blood vessels [25]. To date, there has been no research on the application of AI models with UWFA to comprehensively evaluate disease staging.

Therefore, we created a fully automated algorithm in UWFA images using scalable deep learning methods and accurately identified nonperfusion and leakage areas in synthetic images to establish a prediction model to evaluate the severity of DR. The prediction model can make a preliminary judgment of the patient's condition immediately following examination.

2. Method

More than 5000 DR patients with UWFA examination between 2015 and 2020 from the eye center of Renmin Hospital of Wuhan University (Wuhan, China) were retrospectively reviewed. The exclusion criteria were as follows: eyes with opacity of refractive media, preretinal hemorrhage obscuring fluorescence, and treated eyes. Finally, 280 naive DR patients were included in this study, including 171 NPDR patients and 109 PDR patients. Additionally, 119 normal cases were included for model training and testing. The inclusion criterion of normal cases was eyes without any fundus disease. In total, 399 eyes were included in this study.

For the data divisions, we employed the 5-fold cross-validation to estimate the proposed method. Specifically, cases in each period were randomly divided into 5 groups. Five independent repeat experiments using each group as the test set and the remaining groups as the training set, respectively. In the training stage, the training images are augmented by flip, rotate, and translation.

2.1. Overview of the Pipeline. Classical generative adversarial network (GAN) methods generate fake images with general global similarity to real images. The adversarial strategy is employed in which the discriminator was gradually confused the output images of the generator with the real images. CycleGAN transfers the styles of images in the two domains to each other. The rule of cycle-consistent of CycleGAN expands fake image local consistency to real images. However, the expectation of style transfer in each semantic area is not balanced. In this study, lesion biomarkers are demanded to transfer to appearance of normal tissue, and the remaining should be transformed as little as possible.

A lesion attention enhanced generation approach, joint optimization of CycleGAN and convolutional neural network (CNN) classifier, leverages the automated grading of DR in this paper. The part of CycleGAN prefers to make the transformed image more like a real image of the target domain, and the part of classifiers prefers to constrain the transformed content to the relevant part of the category. In addition, the joint optimization approach extends the transformation of two domains to the discrimination of multiple categories.

The architecture of the joint optimization model is shown in Figure 1. Specifically, normal, NPDR, and PDR images are divided into two groups as normal domain and abnormal domain. Two groups of GANs (consists of generator and discriminator) translate the inputs into the two domains, separately, where the generator G_Y only outputs abnormal domain images and generator G_X only outputs normal domain images. When a fake image is fed into the other generator, the domain of the second generated image will transfer back to the real image. The cycle-consistent is the pixel level constraints between real image and the second generated image, which maintain the shape and spatial position of the tissue during style transfer. The two groups of GANs and the corresponding cycle-consistent make up a CycleGAN for the style transfer between normal image and abnormal image. However, none of GAN and cycle-consistent has the ability to distinguish grading of DR. Review the criterion of grading, local biomarkers are strong evidence for intuitive diagnosis. The difference image between real image and fake image reveals pseudobiomarkers with abnormal brightness. Classifiers for distinguishing the grading of difference images cooperate with CycleGAN to generate more category-specific results. Meanwhile, CycleGAN cooperates with classifiers to find more discriminative information.

In this study, all evaluation criteria are determined by the proposed unified model, which is supervised only by the image-level label. We qualitatively locate the abnormal area from the difference between the real image and the fake image and the auxiliary diagnosis from the results of the classifier. We quantitatively assessed the correlation between ischemia and leakage on the severity of DR.

2.2. Localization of Biomarkers. Accurate location is conducive to the discovery of potential biomarkers or lesion areas.

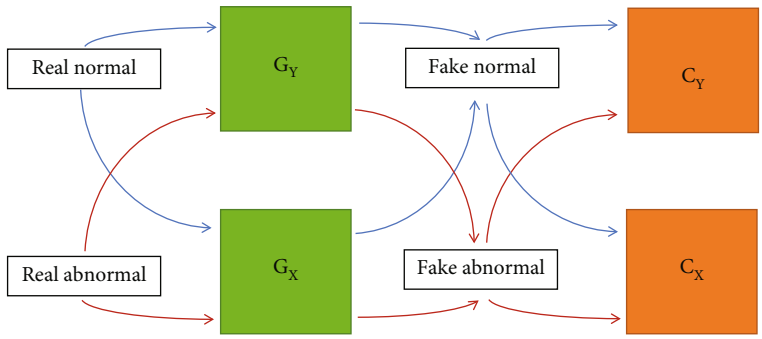

Figure 1: Joint optimization of CycleGAN and CNN classifier. A fixed CycleGAN with a pair of extended classifiers was designed to analyze the DR-related pathological characteristics. We defined the X domain as comprised of normal images and the Y domain as containing abnormal images. The generators G_X and G_Y mapped X and Y functions, respectively. When given a real X domain image as the input, the cycle consistency loss constrains the output of G_X to be consistent with the input, while a discriminator and a classifier cooperate to optimize the output of G_Y to approach domain Y. When the input is a real image of domain Y, the outputs of G_X and G_Y are opposite to the input of domain X.

The generator G_X of CycleGAN replaces biomarkers or diseased areas with fake normal tissue; that is, to generate a disease-free fake image corresponding to the real image whose appearance of abnormal areas primarily has been transformed. The generator G_Y of CycleGAN supplements local confusion similar to biomarkers in the real image to generate a fake abnormal image. The difference between fake image and real image shows the abnormal areas, thereby localizing the biomarkers or the lesion areas.

DR-related lesions show a clear difference in brightness from normal tissues in UWFA. In especial, leakage shows significant high brightness. The location of the leakage areas are extensively highlighted in the difference image. The generator G_X transfers an input image to a base normal template for localization. If the input is an abnormal image, ideally, the bright spots in the subtraction image would indicate the lesion areas. If taking a normal image as input, the output image should be similar to the input image, and the corresponding different image should be an approximately all-zero image.

2.3. Grade Classification. The difference between real image and fake image, i.e., subtraction image, is then fed into the CNN classifiers to diagnose the DR severity. The screening of all patients diagnosed 3 grades: normal, NPDR, and PDR. Actually, the classifier C_X corresponding generator G_X distinguishes all 3 grades, and the classifier C_Y corresponding generator G_Y only distinguishes whether a biomarker appears. Subtraction images focus the attention of the network more on the abnormal areas. A single CycleGAN model tends to perform a global average attention transfer process on the images. The joint optimization method enhances the transfer ability of category-related areas.

On the other hand, the G_X branch with classifier C_X extracts more valuable lesion areas to grade the severity of DR. Notice that the subtraction input is obtained from the input UWFA image and the generated fake image. Therefore, the path of G_X and C_X in the unified model is expanded to classify UWFA images end-to-end.

2.4. DR-Related Indexes. In this study, we quantitatively evaluated the ischemic index and leakage index in correlation with the severity of DR. Early-phase images (at 30 seconds–1 minute) were used to assess the ischemic index, and late-phase (at 5–7 minutes) images were used to assess the leakage index, separately. The abnormally dark areas and abnormally bright areas are biomarkers of nonperfusion area and leakage area, respectively, whose ratio to biological standard d^2 is ischemic index and leakage index, and the d^2 is determined by the square of the visible retina. As shown in Figure 2, the low brightness biomarkers, i.e., nonperfusion area on UWFA, are obtained from the real image and the fake image by an automatic detection algorithm. A minimum filter extracts the local low brightness distribution of an image which reveals the darker tissue or the nonperfusion area. In addition, there is a difficulty difference between detection of leakage and ischemia. To reduce some complexity, we used a more simple but effective method for leakage detection.

For a UWFA image, the leakage and vessels show the highest brightness, the perfusion area shows moderate brightness, and the nonperfusion area shows the lowest brightness. An eroding and dilating operation expands the brightness distribution of the perfusion area while the range of local moderate brightness distribution is maintained. Based on the fixed local moderate brightness distribution, the area with lower brightness in the corresponding position in the image is detected as a suspected nonperfusion area. The agreement of both the real image and fake image is the pseudononperfusion area. To combine the distribution of the nonperfusion area and the distribution of the whole dataset, each pseudoperfusion area was used as a pseudolabel to train a U-net. In addition, we employed a label smoothing strategy [26] to avoid the excessive consistency of pseudolabels. Therefore, the nonperfusion area can be automatically segmented by U-net from real images and fake images, and the ischemic index is the ratio of the ischemic area to d^2.

The bright biomarkers, i.e., leakage and microaneurysms on UWFA, are obtained from the results of localization and classification introduced in section A. As shown in Figure 2,

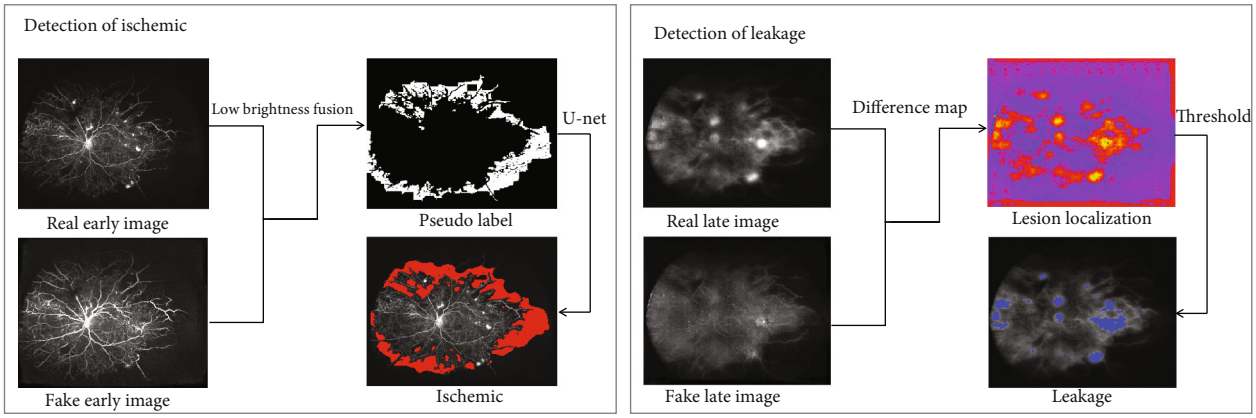

Figure 2: Detection of biomarkers. The low brightness biomarkers, i.e., nonperfusion areas on UWFA images, were obtained from the real image and the fake image by an automatic detection algorithm. A minimum filter extracts the local low brightness distribution of an image, which reveals the darker tissue or the nonperfusion area. The bright biomarkers, i.e., leakage and microaneurysms on UWFA images, are obtained from the results of localization and classification. The fake image is close to the normal image domain, where the abnormally bright areas are replaced by a lower brightness appearance. The difference image of the real image and fake image reveals the anomaly detection of leakage. A thresholding operation leverages the anomaly map to the segmentation of leakage. The leakage index is the ratio of the leakage area to d^2.

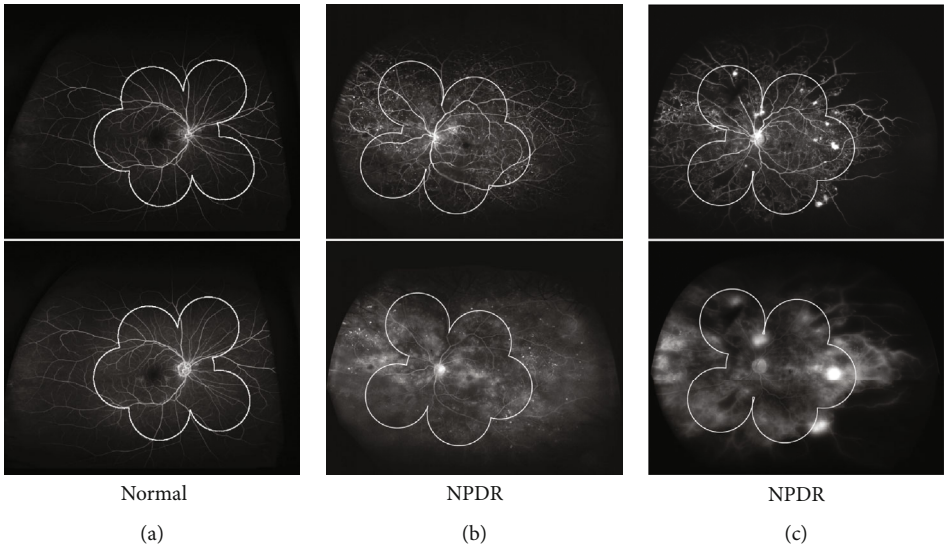

Figure 3: Comparison of the UWFA and simulated 7-SF. (a) UWFA showed wider retina than simulated 7-SF in the normal eye. (b) UWFA image on the early phase showed more nonperfusion in the peripheral retina than simulated 7-SF in the NPDR eye (upper), and more peripheral leakage was found on UWFA image than simulated 7-SF on the late phase (bottom). (c) UWFA image on the early phase showed more nonperfusion and neovascularization in the peripheral retina than simulated 7-SF in the PDR eye (top), and more peripheral leakage was found on UWFA image than simulated 7-SF on the late phase (bottom).

the fake image is close to the normal image domain, where the abnormally bright areas are replaced by lower brightness appearance. The difference image of real image and fake image reveals the anomaly detection of leakage. A thresholding operation leverages the anomaly map to the segmentation of leakage. The leakage index is the ration of leakage area to d^2.

3. Results

Two experts defined the location of the macula and the optic disc as a reference for quantitative comparison. Based on the location, the range of 7-SF is determined automatically [27], and the biological standard d^2 is determined by the square of visible retina. As shown in Figure 3, bright microaneurysms were widely distributed in the NPDR case, in which 7-SF could not be captured completely. A large nonperfusion area was located near the temporal retina in the PDR case, while 7-SF captured only the posterior pole perspective.

3.1. Classification. Three disease grades (normal, NPDR, and PDR) were inferred through the path of generator G_X and classifier C_X. In this section, we evaluated classification results to compare the advantages of UWFA images and traditional 7-stand field images. The original UWFA images

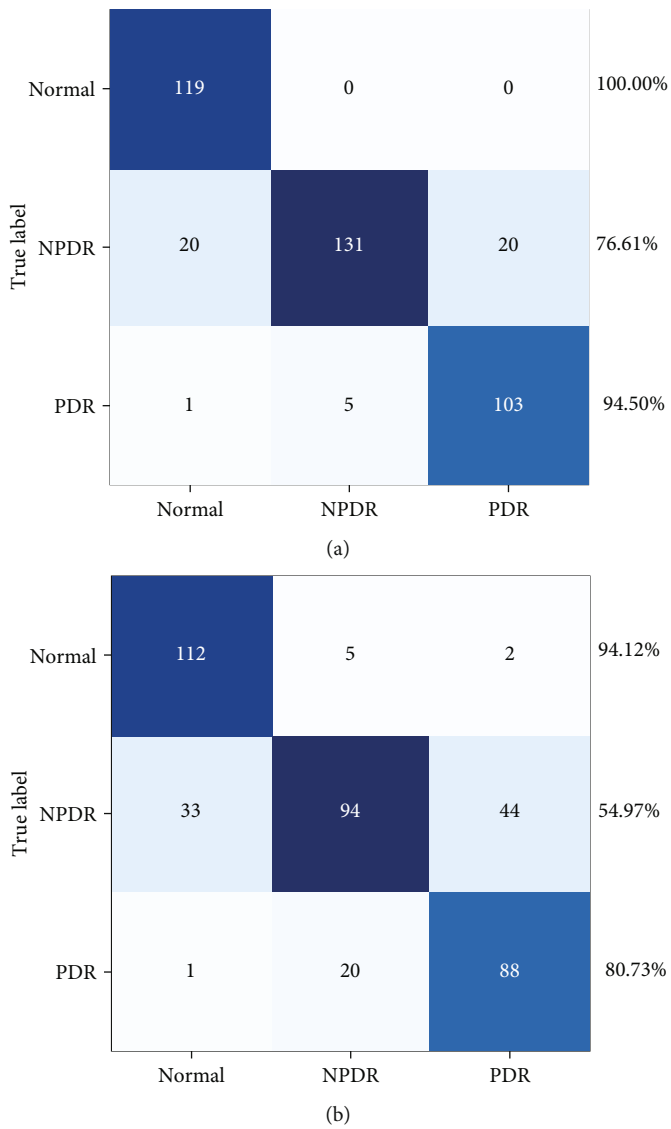

Figure 4: The confusion matrix of the classification results. The classification results of the original UWFA images achieved 100.00% accuracy for normal eyes, 94.50% for PDR, and 76.61% for NPDR, respectively. The classification results of the 7-SF images achieved 94.12% accuracy for normal eyes, 80.73% for PDR, and 54.97% for NPDR, respectively.

were used to quantitatively evaluate classification performance, and the images with the mask of the 7-stand field were used to the comparison experiment. Two experiments were trained with the same configuration. The classification results of the original UWFA images achieved 88.50% accuracy, and the images with masks achieved 73.68% accuracy. In general, the proposed model provides accurate inference results for disease classification.

In detail, Figure 4 shows the confusion matrix of the classification results. Normal cases are easy to distinguish both on the UWFA images and 7-SF images, even though all normal images are correctly identified on UWFA images. However, the classification accuracy for NPDR and PDR is more accurate on UWFA images, which demonstrates the advantage of a wider visual degree of the retinal range. For dataset, there are differences in the number of samples in each category. To balance the evaluation results, the kappa coefficient is calculated by the confusion matrixes. The original UWFA images achieved 0.827 while the images with masks achieved 0.608, which demonstrates that original UWFA images achieved very high classification consistency and much higher than images with masks.

3.2. Statistical Analysis of Indexes. Figure 5 shows the statistical analysis of the leakage index and ischemic index. The box-and-whisker plots show that both the ischemic index and leakage index are positively correlated with the severity of DR.

Based on the dual biomarker indexes, we implemented a simple linear regression function to explore the discrimination of indexes on the grades of DR, shown in Figure 6. Two thresholds were reached to classify DR severity grades, which achieved 76.8% accuracy. This demonstrates that there is a significant relationship between the biomarkers and the severity of DR.

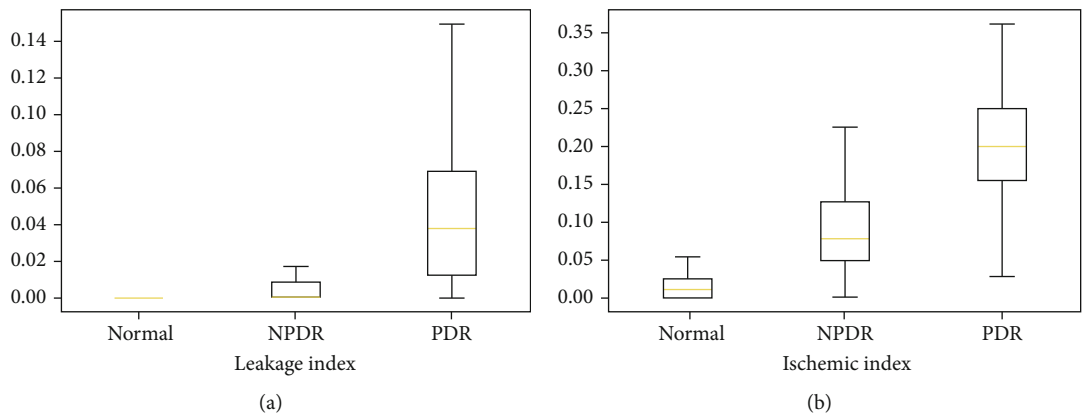

Figure 5: The box-and-whisker plots show that both the ischemic index and leakage index are positively correlated with the severity of DR.

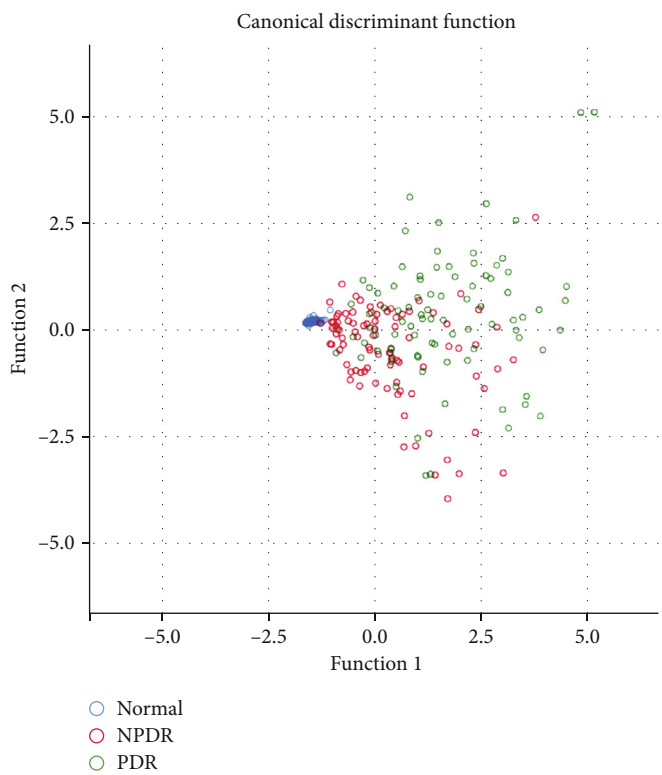

Figure 6: Canonical discriminant function. In the regression analysis, the arguments were ischemic area and leakage area, and the response variables were categories, i.e., normal, NPDR, and PDR. It demonstrates that there is a significant relationship between the biomarkers and the severity of DR.

Previous studies have verified the correlation between 2 indexes and the lesion grading. However, deep learning methods require accurate pixel level standards, and unsupervised methods can only extract one single feature. In this study, we perform a unified image level supervised model to implement location, classification, and indexes evaluation, concurrently. The verification results show that the conclusion of this study is basically consistent with the optimization of the CycleGAN and CNN model classifier. It means that this efficient model has great value in UWF data analysis.

4. Discussion

Seventy-five percent of DR patients live in underdeveloped areas with insufficient available specialists [28]. Consequently, millions of people are experiencing vision impairment without proper predictive diagnosis and eye care worldwide. A few global screening programs have been performed to prevent sight-threatening diseases from devastating; however, DR exists at too large a scale for such programs to be screened and managed efficiently on individual level. To address the

shortfalls of current diagnostic workflows, automated solutions for retinal disease diagnosis from screened and graded fundus images are urgently needed. AI technology has wide applications in fundus imaging, such as fundus color photography and optical coherent tomography (OCT) [15, 16, 22]. However, there were few applications of AI in fundus fluorescein angiography until recently, and AI was merely used to identifying vascular structures or fluorescein features [23–25, 29–31].

There are several reasons for this situation. First, fluorescein angiography examination is different from other static examinations, and it is dynamic with varying image collection times. Dye leakage, staining, and accumulation gradually appear over time. Therefore, it is difficult to maintain the homogeneity of the image. Second, when evaluating the fundus condition, a dozen or even more images from multiple orientations are required. These are the inherent requirements of angiography. Moreover, there are great differences in the fluorescein features and distributions of retinal diseases at different grades. All of the above reasons present a great challenge to the application of AI in fundus fluorescein angiography in DR.

With the development of AI technology, Pan et al. achieved multilabel recognition of a single vision field, including leakage, microaneurysm, neovascularization, nonperfusion area, and laser spot [24]. This model is closer to the actual clinical situation than the traditional single-label model. However, the scope of traditional angiography is limited, and a single image cannot be used to evaluate the overall situation of the fundus. Ultra-widefield images, which have a wide scope and collect a single image covering most of the fundus, increase the feasibility for the application of AI. Ding et al. adapted algorithms that realized the extraction of blood vessels and the identification of nonperfusion areas [25]. Nunez do Rio et al. segmented and quantified nonperfusion of retinal capillaries in UWFA based on deep learning [29]. However, neither of them achieved the goal of staging disease.

In this study, we did not extract and analyze any single features in UWFA images but focused on two indicators: ischemic index and leakage index. Diabetic retinopathy is a microvascular lesion, and the mechanism is clear [32]. The increase in retinal vascular permeability leads to the destruction of the blood-retinal barrier, causing fluid to leak from the blood vessel [33]. On the other hand, the destruction of endothelial cells leads to the occlusion of capillaries and the formation of ischemia without blood perfusion [6]. The above results showed the corresponding relationship between nonperfusion and leakage and the pathogenesis of diabetic retinopathy, and previous studies also indicated that the severity of DR is related to the ischemic index and leakage index [10–13]. We concluded that the ischemic index and leakage index are good evaluation factors for DR staging.

We proposed a unified generation model, to automatically detect and locate lesions by different category labels, extract nonperfusion and leakage in ultra-widefield images, and grade the grade categories of severity. This model enables us to mark and delineate lesions in batches automatically, while current standard practice consumes considerable manpower and time when performed manually. A GAN consists of a generator network and a discriminator network, which are trained alternately to achieve the goal of common optimization. The general guideline is to detect and locate the nonperfusion area and leakage area through the classical unpaired generating networks CycleGAN and CNN, respectively. CycleGAN can generate more realistic and reliable images with the help of cyclic consistency loss, and then the CNN classifier classifies the different images by subtracting the generated images from the real images. The discriminator and the generator obtain the local optimal solution in a confrontational way, and CycleGAN and the classifier cooperate to enhance the ability to generate results from the lesion area. After that, the prediction model could be used to differentiate NPDR and PDR based on the ischemic index and leakage index, which is in line with routine clinical diagnostics and has high credibility.

Intuitively, different severity of DR in UWFA corresponds to specific performance. And there is a specific clinical distinction between the biomarkers of severity. The collected clinical data in this study includes DR cases of different severity, where each period contains more than 100 cases. For training stage, the augmented training images supported the model to learn the potential features. The results show that the AI model can learn the biomarkers that are consistent with the disease regulars from our dataset.

Previous studies have obtained some encouraging results of some single indices of DR. However, different indices come from different models. A unified model that can obtain multiple indicators is meaningful for the study of multiple manifestations disease such as DR. To this end, this study tries to use an extended CycleGAN to discover the potential indices of DR. Besides, this model only needs the category labels, instead of the unavailable region labels of previous deep learning methods. The statistics of indices support the same conclusion as other studies, which demonstrates the feasibility of this model.

In addition, this study established a prediction model in simulated 7-SF for DR grading based on the leakage index and ischemic index. There is satisfactory accuracy in the recognition of normal eyes and PDR eyes in 7-SF. At the same time, we compared the predictive accuracy between the ultra-widefield vision images and the simulated 7-SF range and found that more lesions could be found on ultra-widefield vision images, and the predictive accuracy of UWFA was slightly better than that of 7-SF. Previous studies have shown that diabetic retinopathy lesions mainly involve the middle and posterior pole; most of the lesions appear in the 7-SF area, so ultra-widefield and 7-SF show some consistency [34]. With the increase in the severity of the disease, the posterior pole is increasingly vulnerable, and the possibility of its survival decreases. In summary, the algorithm is applicable for both UWFA and traditional 7-SF angiography images and performs better on UWFA images.

The following limitations of this study must be acknowledged. First, the training procedure was based on data collected from only one clinical center and may not be generalizable to the overall population with diabetes. Second, to obtain the leakage index and ischemic index

accurately, cases with preretinal hemorrhage and vitreous hemorrhage were excluded, so the universality of the model is limited and needs to be further optimized in the future. Additionally, there are distortions and differences in image brightness in UWFA images, which prevents the accurate extraction and quantification of the ischemic index and leakage index.

Overall, in this study, we adopted a deep learning model based on the ischemic index and leakage index in diabetic retinopathy staging for the first time, and the accuracy of the model was comparable to that of diagnoses made by resident doctors. If this model is widely adopted, it will bring great convenience to DR patients and clinicians. For example, this algorithm could be used as an intelligent UWFA image analysis system and an electronic medical report management system in hospitals. Patients can obtain AI diagnosis reports immediately after angiography examination and receive timely information on their condition. Meanwhile, such a tool could alleviate the workloads of trained specialists, allowing untrained technicians to screen and process many patients objectively without dependence on clinicians. Specifically, first, the classification results can provide a quick diagnosis, to assist doctors to quickly locate the image area that should be paid attention to and give a snapshot of DR severity classification. Additionally, it is convenient for doctors to manage and trace patient data, so as to better grasp the patient's condition and meet the needs of doctors' learning and scientific research. Last but not the least, these visual indexes are reasonable clinical auxiliary diagnostic indexes, which are classified on this basis, breaking the blind box dilemma of the application of imaging in artificial intelligence at this stage. In the future, we will continue to optimize the model, including classifying the images in the limited area of the posterior pole, image quality enhancement, and embedding a supplementary program in the model to identify vitreous hemorrhage and retinal hemorrhage. Finally, we hope that our model can be applied to general clinical situations and benefit doctors and patients in county hospitals and rural areas.

Data Availability

We have presented all our main data in the form of figures and additional files. The data used to support the conclusions of this study are available from the authors.

Ethical Approval

This research was approved by the local ethical committee (Clinical research ethics committee of Renmin Hospital of Wuhan University) under the number of WDRY2021-K034.

Consent

Given that this is a retrospective analysis, no patient consent was required.

Conflicts of Interest

No conflicting relationship exists for any author.

Authors' Contributions

Study design and conception were handled by X.W, W.F, and C.C. Analysis and interpretation were handled by all authors. Drafting of the article was handled by X.W, Z.J, X.M, Z.Z, Z.Y, H.Z, and C.C. Critical revision for intellectual content was handled by all authors. C.C had full access to all the data used in these analyses and takes full responsibility for the integrity of the data and the accuracy of the data analysis. All authors reviewed and accepted the submitted version of this manuscript. X.W is the first author; W.F and C.C are co-last authors of this paper.

Acknowledgments

The authors thank A'min Xu, MD, Lu He, MD, and Juejun Liu, MD, from Renmin Hospital of Wuhan University for image acquisition. This work was supported by the National Natural Science Foundation of China under Grant no. 62072241, in part by the Natural Science Foundation of Jiangsu Province under Grant no. BK20180069, in part by Six Talent Peaks Project in Jiangsu Province under Grant no. SWYY-056, and in part by Educational Research Foundation of Nanjing Medical University under Grant no. 2019LX044.

References

[1] Y. Zheng, S. H. Ley, and F. B. Hu, "Global aetiology and epidemiology of type 2 diabetes mellitus and its complications," *Nature Reviews Endocrinology*, vol. 14, no. 2, pp. 88–98, 2018.

[2] C. J. Flaxel, R. A. Adelman, S. T. Bailey et al., "Diabetic retinopathy preferred practice pattern®," *Ophthalmology*, vol. 127, no. 1, pp. P66–145, 2020.

[3] Y. Li, D. Teng, X. Shi et al., "Prevalence of diabetes recorded in mainland China using 2018 diagnostic criteria from the American Diabetes Association: national cross sectional study," *BMJ*, vol. 369, p. 369:m997, 2020.

[4] J. H. Kempen, B. J. O'Colmain, M. C. Leske et al., "The prevalence of diabetic retinopathy among adults in the United States," *Archives of Ophthalmology*, vol. 122, no. 4, pp. 552–563, 2004.

[5] X. Zhang, J. B. Saaddine, C. F. Chou et al., "Prevalence of diabetic retinopathy in the United States, 2005-2008," *Jama*, vol. 304, no. 6, pp. 649–656, 2010.

[6] T. Y. Wong, C. M. Cheung, M. Larsen, S. Sharma, and R. Simó, "Diabetic retinopathy," *Nature Reviews Disease Primers*, vol. 2, no. 1, p. 16012, 2016.

[7] E. M. Kohner and C. T. Dollery, "Fluorescein angiography of the fundus in diabetic retinopathy," *British Medical Bulletin*, vol. 26, no. 2, pp. 166–170, 1970.

[8] M. M. Wessel, G. D. Aaker, G. Parlitsis, M. Cho, D. J. D'Amico, and S. Kiss, "Ultra-wide-field angiography improves the detection and classification of diabetic retinopathy," *Retina*, vol. 32, no. 4, pp. 785–791, 2012.

[9] M. Singer, C. S. Tan, D. Bell, and S. R. Sadda, "Area of peripheral retinal nonperfusion and treatment response in branch

and central retinal vein occlusion," *Retina*, vol. 34, no. 9, pp. 1736–1742, 2014.

[10] J. P. Ehlers, A. C. Jiang, J. D. Boss et al., "Quantitative Ultra-Widefield Angiography and Diabetic Retinopathy Severity: An Assessment of Panretinal Leakage Index, Ischemic Index and Microaneurysm Count," *Ophthalmology*, vol. 126, no. 11, pp. 1527–1532, 2019.

[11] A. C. Jiang, S. K. Srivastava, M. Hu et al., "Quantitative ultra-widefield angiographic features and associations with diabetic macular edema," *Ophthalmology Retina*, vol. 4, no. 1, pp. 49–56, 2020.

[12] A. Jiang, S. Srivastava, N. Figueiredo et al., "Repeatability of automated leakage quantification and microaneurysm identification utilising an analysis platform for ultra-widefield fluorescein angiography," *The British Journal of Ophthalmology*, vol. 104, no. 4, pp. 500–503, 2020.

[13] N. Figueiredo, S. K. Srivastava, R. P. Singh et al., "Longitudinal panretinal leakage and ischemic indices in retinal vascular disease after aflibercept therapy: the PERMEATE study," *Ophthalmology Retina*, vol. 4, no. 2, pp. 154–163, 2020.

[14] A. S. Thomas, M. K. Thomas, A. P. Finn, and S. Fekrat, "Use of the ischemic index on widefield fluorescein angiography to characterize a central retinal vein occlusion as ischemic or nonischemic," *Retina*, vol. 39, no. 6, pp. 1033–1038, 2019.

[15] R. Kapoor, B. T. Whigham, and L. A. Al-Aswad, "Artificial intelligence and optical coherence tomography imaging," *Asia-Pacific Journal of Ophthalmology (Philadelphia, Pa)*, vol. 8, no. 2, pp. 187–194, 2019.

[16] D. S. W. Ting, L. R. Pasquale, L. Peng et al., "Artificial intelligence and deep learning in ophthalmology," *The British Journal of Ophthalmology*, vol. 103, no. 2, pp. 167–175, 2019.

[17] Z. Li, C. Guo, D. Nie et al., "Deep learning for detecting retinal detachment and discerning macular status using ultra-widefield fundus images," *Communications Biology*, vol. 3, no. 1, p. 15, 2020.

[18] J. Mao, Y. Shao, J. Lao et al., "Ultra-wide-field imaging and intravenous fundus fluorescein angiography in infants with retinopathy of prematurity," *Retina*, vol. 40, no. 12, pp. 2357–2365, 2020.

[19] Z. Li, C. Guo, D. Lin et al., "Deep learning for automated glaucomatous optic neuropathy detection from ultra-widefield fundus images," *British Journal of Ophthalmology*, 2020.

[20] Y. Ye, J. Mao, L. Liu, S. Zhang, L. Shen, and M. Sun, "Automatic diagnosis of familial exudative vitreoretinopathy using a fusion neural network for wide-angle retinal images," *IEEE Access*, vol. 8, pp. 162–173, 2020.

[21] M. Voets, K. Møllersen, and L. A. Bongo, "Reproduction study using public data of: development and validation of a deep learning algorithm for detection of diabetic retinopathy in retinal fundus photographs," *PLoS One*, vol. 14, no. 6, article e0217541, 2019.

[22] M. Savoy, "IDx-DR for diabetic retinopathy screening," *American Family Physician*, vol. 101, no. 5, pp. 307-308, 2020.

[23] K. Jin, X. Pan, K. You et al., "Automatic detection of non-perfusion areas in diabetic macular edema from fundus fluorescein angiography for decision making using deep learning," *Scientific Reports*, vol. 10, no. 1, p. 15138, 2020.

[24] X. Pan, K. Jin, J. Cao et al., "Multi-label classification of retinal lesions in diabetic retinopathy for automatic analysis of fundus fluorescein angiography based on deep learning," *Graefe's Archive for Clinical and Experimental Ophthalmology*, vol. 258, no. 4, pp. 779–785, 2020.

[25] L. Ding, M. H. Bawany, A. E. Kuriyan, R. S. Ramchandran, C. C. Wykoff, and G. Sharma, "A novel deep learning pipeline for retinal vessel detection in fluorescein angiography," *IEEE Transactions on Image Processing*, vol. 29, pp. 6561–6573, 2020.

[26] R. Müller, S. Kornblith, and G. Hinton, "When does label smoothing help?," 2019, https://arxiv.org/abs/1906.02629.

[27] Early Treatment Diabetic Retinopathy Study Research Group, "Grading Diabetic Retinopathy from Stereoscopic Color Fundus Photographs–An Extension of the Modified Airlie House Classification: ETDRS Report Number 10," *Ophthalmology*, vol. 98, no. 5, pp. 786–806, 1991.

[28] L. Guariguata, D. R. Whiting, I. Hambleton, J. Beagley, U. Linnenkamp, and J. E. Shaw, "Global estimates of diabetes prevalence for 2013 and projections for 2035," *Diabetes Research and Clinical Practice*, vol. 103, no. 2, pp. 137–149, 2014.

[29] J. M. Nunez do Rio, P. Sen, R. Rasheed et al., "Deep learning-based segmentation and quantification of retinal capillary non-perfusion on ultra-wide-field retinal fluorescein angiography," *Journal of Clinical Medicine*, vol. 9, no. 8, p. 2537, 2020.

[30] S. H. Rasta, S. Nikfarjam, and A. Javadzadeh, "Detection of retinal capillary nonperfusion in fundus fluorescein angiogram of diabetic retinopathy," *BioImpacts : BI*, vol. 5, no. 4, pp. 183–190, 2015.

[31] Y. Zheng, M. T. Kwong, I. J. C. MacCormick, N. A. Beare, and S. P. Harding, "A comprehensive texture segmentation framework for segmentation of capillary non-perfusion regions in fundus fluorescein angiograms," *PLoS One*, vol. 9, no. 4, article e93624, 2014.

[32] N. Cheung, P. Mitchell, and T. Y. Wong, "Diabetic retinopathy," *Lancet*, vol. 376, no. 9735, pp. 124–136, 2010.

[33] L. Z. Heng, O. Comyn, T. Peto et al., "Diabetic retinopathy: pathogenesis, clinical grading, management and future developments," *Diabetic Medicine : a journal of the British Diabetic Association*, vol. 30, no. 6, pp. 640–650, 2013.

[34] P. S. Silva, J. D. Cavallerano, J. K. Sun, J. Noble, L. M. Aiello, and L. P. Aiello, "Nonmydriatic ultrawide field retinal imaging compared with dilated standard 7-field 35-mm photography and retinal specialist examination for evaluation of diabetic retinopathy," *American Journal of Ophthalmology*, vol. 154, no. 3, pp. 549–559.e2, 2012.